Designing a Modular Approach for the Formation of Rhenium-functionalised Surfaces for SERS-based Sensing

Joshua N. Lea MChem

This dissertation is submitted for the degree of Doctor of Philosophy

May 2022

School of Chemistry

Declaration

This thesis has not been submitted in support of an application for another degree at this or any other university. It is the result of my own work and includes nothing that is the outcome of work done in collaboration except where specifically indicated. Many of the ideas in this thesis were the product of discussion with my supervisor Dr Nick C. Fletcher

Abstract

A modular approach has been designed for the synthesis of labelled nanoparticle films for targeted analyte detection using surface-enhanced Raman spectroscopy (SERS). Interfacial self-assembly of citrate-stabilised silver nanoparticles and photo-deposition of silver salts were employed as possible methods for the generation of reproducible SERS surfaces. The ability to label the platforms with the rhenium complex $[Re(L1)(CO)_3Br]$ where L1 is (2,2'-bipyridin-4-ylmethyl)-(1,2-dithiolan-3-yl)pentanoate were also made and assessed using SERS. The complex shows an ability to effectively label the structures via covalent interactions between the silver surface and the dithiol group of the ligand, evidenced by SERS. The complex can modify and position citrate stabilised nanoparticles at the interface between two immiscible liquids, demonstrating that the Re(I)-modified metal liquid-like films (MeLLFs) and surface-exposed nanosheets (SENS) provide a simple and reproducible method for the synthesis of labelled SERS active surfaces.

The $[Re(L1)(CO)_3Br]$ complex, also displayed a selective spectroscopic response to the presence of Hg^{2+} in solution which is believed to be Hg-facilitated Br removal and coordination of the solvent. This interaction was also observed using SERS after treating $[Re(L1)(CO)_3Br]$ functionalised MeLLFs and SENS with organic and aqueous solutions of Hg^{2+}. This is evidenced by observable changes to the Re–CO vibration and the appearance of a peak attributed to some form of Hg–Br interaction.

The Re(I) complex, $[Re(L2)(CO)_3(pyr)](PF_6)$ containing a bis-(benzimidazole)-4,4′-bipyridine, L2 showed individual photophysical responses to dihydrogen phosphate and acetate in solution. $H_2PO_4^-$ causes a sequential quenching while OAc^- causes a "switch off" of the emissive response. The $[Re(L2)(CO)_3(pyr)](PF_6)$ and $[Re(L2)(CO)_3(L3)](BF_4)$ complexes, where L3 is N-(4-pyridylmethyl)lipoamide also formed labelled MeLLF and SENS surfaces. Anion sensing was possible with the SENS films. SENS treated with $H_2PO_4^-$ showed changes to the complex fingerprint with additional peaks attributed to the anion. The detection of OAc^- is evidenced by an observed vibration and wavenumber shift of ligand specific vibrations attributed to the hydrogen bonding interaction between the complex and anion.

The complex, $[Re(L4)(CO)_3(L3)](BF_4)$ where L4 is dipyridophenazine was synthesised and used to form the interfacial MeLLF and SENS surfaces. Attempts at SERS detection using $[Re(L4)(CO)_3(L3)](BF_4)$ and $[Re(L2)(CO)_3(L3)](BF_4)$ SENS platforms for the detection of DNA were made using the SENS platforms. This was unsuccessful however, there is opportunity for further investigation.

Acknowledgements

I would like to thank my supervisor, Dr Nick Fletcher for all of his support. I will be forever grateful for all of his guidance and direction. You have always driven me to improve and succeed and none of this would have been possible without your input. To Dr Lorna Ashton, thank you for helping me garner the appreciation and understanding that I now have for Raman spectroscopy. To Drs Heather Montgomery, Stephen Bell and Yikai Xu, thank you for providing the foundations that this work is built upon.

Thank you to all the teachers and educators that took the time and effort to help me succeed. A notable mention to Dr S. Longshaw, Mr W. Atkins and Mrs A. Kuznir, without your help, I would never have found myself in a position to embark on a PhD.

Thank you to all my friends and colleagues at Lancaster University. I will always cherish the memories I made during my PhD and will always fondly remember my time here.

To my family, thank you for the consistent support, the motivational talks and convincing me to keep going when it really got tough. Thank you for never letting me quit and helping me through to the finish. To my partner Britt, I'm not sure I would have seen this through without all your love and support, I will be eternally grateful. To Ria, Rahul and Pashu, thank you for always being there and motivating me. Finally, a special mention to Tom, may this thesis forever hold your interest or at least until you fall asleep.

Contents

List of Abbreviations and Acronyms

AgNP	Silver Nanoparticle
ATR	Attenuated Total Reflectance
AuNP	Gold Nanoparticle
Bpy	2,2′-bipyridine
CM	Chemical Enhancement Mechanism
Ct	Calf thymus
DCM	Dichloromethane
DLVO	Derjaguin-Landau-Verwey-Overbeek
DMSO	Dimethylsulfoxide
DNA	Deoxyribonucleic Acid
EDL	Electric Double Layer
EDX	Energy-dispersive X-ray
EM	Electromagnetic Enhancement Mechanism
FTIR	Fourier Transform Infrared
GD	Glass Deposited
GERS	Graphene-enhanced Raman Spectroscopy
HOMO	Highest Occupied Molecular Orbital
HSA	Human Serum Albumin
IR	Infrared
L1	2,2'-bipyridin-4-ylmethyl-4-(1,2-dithiolan-3-yl)pentanoate
L3	N-(4-pyridylmethyl) lipoamide
L2	4,4'-bis(benzimidazole)bipyridine
L4	Dipyridophenazine
LC	Ligand Centred
LMCT	Ligand-to-metal-charge-transfer

LSPR	Localised Surface Plasmonic Resonance
LUMO	Lowest Unoccupied Molecular Orbital
MDMA	3,4-methylenedioxymethamphetamine
MeLLF	Metal Liquid-like Film
MeOH	Methanol
SERS	Surface-enhanced Raman Spectroscopy
MLCT	Metal-to-ligand charge-transfer
NMNP	Noble Metal Nanoparticle
NMR	Nuclear Magnetic Resonance
NP	Nanoparticle
PAH	Polycyclic Aromatic Hydrocarbon
PAL	Polyaromatic Ligand
PD	Photo-deposited
PEG	Poly(ethylene glycol)
PSA	Prostate Specific Antigen
RNA	Ribonucleic acid
RR	Resonance Raman
SEM	Scanning Electron Microscopy
SENS	Surface-exposed Nanosheets
SERS	Surface-enhanced Raman Spectroscopy
SERRS	Surface-enhanced Resonance Raman Spectroscopy
TAE	Tetraarylethylenes
TBA	Tetrabutylammonium
THF	Tetrahydrofuran
UV-Vis	Ultraviolet-visible

Introduction

Surface-enhanced Raman Spectroscopy and Functionalised Materials – An Overview

1.1 Introduction

Humanity's curiosity regarding the world around us has long driven the need to measure. This has influenced the development of sensing technologies that can monitor changes in our environment, detecting subtle differences and generating information. They help us to detect physiological differences in the human body, a notable example being the monitoring of blood sugar levels in patients with diabetes, allowing to take preventative measures thus reducing the risk of life threatening complications.[1, 2]

Chemical sensors, defined as a device that converts chemical information to a signal that can be observed, are fundamental for detection of a range of compounds in both biological and environmental settings, from disease biomarkers to explosive materials.[3-5] Colorimetric and fluorescence-based approaches have been widely used as they can be easy to perform and offer quick response times for relatively low cost in comparison to complex lab-based techniques.[6] However, these methods are not without their disadvantages; they are often solution-based and require on-site preparation that can be susceptible to conditional changes and sampling errors. These issues have led to the investigation of new approaches that are offer reproducibility with lower limits of detection that can also be taken out of the laboratory and used effectively in the real world.

Surface-enhanced Raman spectroscopy (SERS) utilises the characteristic properties of noble metal nanostructures to enhance the observed Raman scattering of an irradiated target. Consequently, SERS-active materials can be employed as novel sensors that detect molecules via the Raman fingerprint specific to the analyte in question. A significant advantage of SERS in comparison with colorimetric and fluorescence-based sensing is the quantity of spectral information that can be acquired (Fig. 1.1). However,

the obstacles that have prevented the widespread use of SERS sensing in real world applications are poor reproducibility and vulnerability to contamination.[7] This is particularly problematic due to the inherent high sensitivity of the technique. Furthermore, SERS sensing is often conducting using silver and gold nanoparticle shapes without any form of Raman reporting molecule bound to their surface. These label-free strategies are reliant on the analyte being in close proximity to the surface and, even then, it is somewhat limited by the Raman activity of the molecule, which in many cases can be quite small.

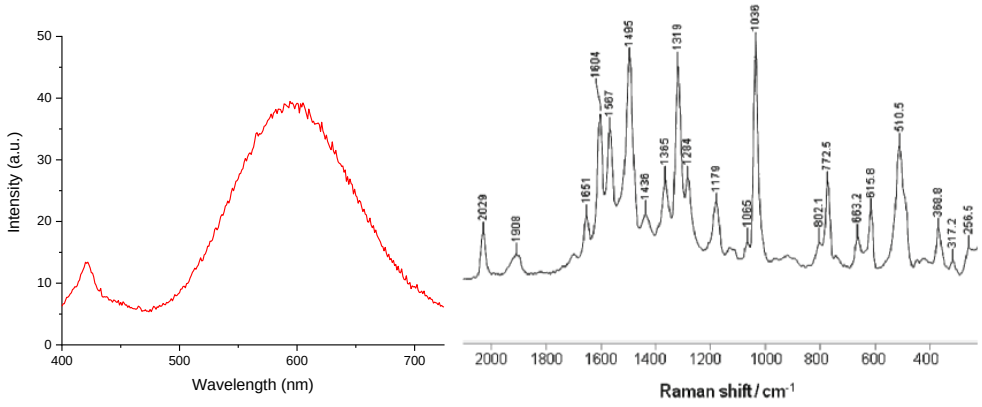

Figure 1.1: *The fluorescence spectrum (–) and SERS spectrum (–) of [Re(bpy)(CO)$_3$Br], highlighting the difference in spectral information obtained by the two techniques.*[8]

Resolving these issues are paramount if SERS-based sensing is to be successful. The comprehensive review of SERS by Langer *et al.* describes the current state of the technique and outlines what needs to be accomplished for it to considered in both a laboratory and real-world setting.[9] Some of the relevant concepts identified are the need for reproducible and rational design of substrate fabrication for targeted analysis in real environments. Certain limitations have already been overcome, for instance the problems of label-free sensing can be rectified to some degree through the integration of a molecular label to the SERS substrate. This functionalisation can provide a "spectral signpost" which can aid the observation of the target via molecular

interactions. Combining tailored molecular sensors with simply made SERS substrates could be a way to develop this technique so we can use it to its full potential

1.2 Interactions of Light and Matter

1.2.1 Absorption and Emission

Matter, when irradiated with light may absorb, scatter, or transmit the photons. These processes can provide us with meaningful information on the properties of the material. The absorption of light can induce energetic changes in a molecule. They exist in an initial or ground state and upon exposure to photons, can be excited to higher energetic states, if the energy of the photon corresponds to the energy gap between ground and excited states. The energy of the photon is determined by the wavelength, the relation of which is given by the following equation:

$$\boldsymbol{E = \frac{hc}{\lambda}} \qquad (\mathbf{1})$$

Where $\boldsymbol{E}$ is photon energy, $\boldsymbol{h}$ is Planck's constant, $\boldsymbol{c}$ is the speed of light in a vacuum and $\boldsymbol{\lambda}$ is the wavelength of the photon. Absorption spectroscopy is a collective term for techniques that measure the absorption of radiation and the transition between energy levels. As such, absorption spectroscopies can be performed using irradiation sources from across the electromagnetic spectrum with different wavelengths corresponding to different energetic changes. An example is UV-Vis spectroscopy which studies the electronic transitions of molecule that occur when irradiated with wavelengths of light through the UV and visible range. The energetic transitions in this instance correspond to the promotion of bonding and non-bonding electrons to higher energy orbitals.[10]

The relaxation of a molecule back to the ground state is also a subject of interest. This relaxation can occur through the emission of a photon of a corresponding wavelength.

Emission can be both stimulated and spontaneous and can occur via two processes, fluorescence, and phosphorescence.[10] these two processes are dependent on the spin multiplicity of the ground and the excited states (Fig. 1.2). The simplified Jablonski diagram illustrates the transitions of both processes. Fluorescence is a process involving non-radiative decay from the upper vibrational states before a radiative decay from the excited vibrational state back to the ground state. In this case, both states have the same multiplicity. The change in energy due to vibrational rearrangements processes mean that the photon released through fluorescence is lower in energy than the initial absorption. Phosphorescence initially begins with a similar non-radiative decay, however intersystem crossing from the singlet to a triplet state can occur if there is overlap between them. Non-radiative transitions continue in the triplet state until it can relax back to the ground state, resulting in the observed emission. As a result, phosphorescence has a longer lifetime as the multiplicity means the transition back to the ground state is spin-forbidden.

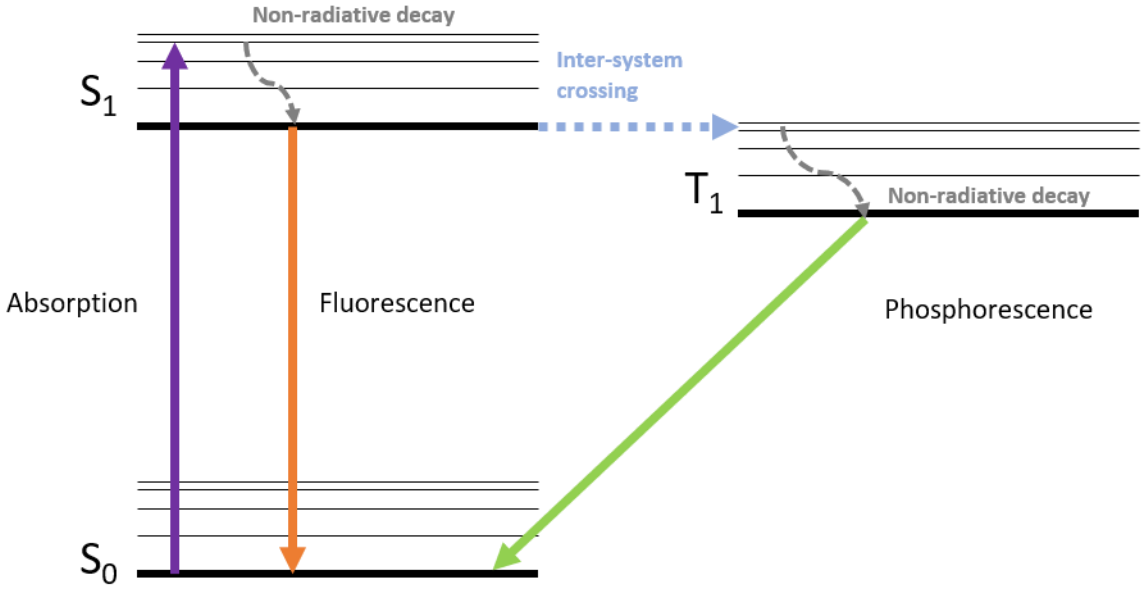

Figure 1.2: *A simplified Jablonski diagram that illustrates the processes of fluorescence and phosphorescence*

The fluorescence of a molecule, or fluorophore, is associated with the structural components of the molecule in question. Inducing changes to a fluorophore is the basis for fluorescent sensing. The review by de Silva *et al.* offers a comprehensive view on the mechanisms responsible.[11] Fluorescent sensing has become incredibly diverse with systems showing recognition of target analytes ranging from heavy metals to explosives.[12-15] This topic will be discussed in greater detail in a later section.

1.2.2 Scattering Processes

Another interaction between light and matter is scattering. Scattering occurs when a photon distorts or polarizes the electron cloud of nuclei into an unstable virtual state followed by the quick re-emission of a photon. The unstable state often induces no movement in the nuclei therefore the scattered photon exists at similar energy. This is more commonly referred to as elastic or Rayleigh scattering (Fig. 1.3). In rare cases (1 in every 10^6-10^8 photons), this virtual state does induce movement in the nuclei which alters the energetic state of the molecule and the corresponding energy of the scattered photon. This is more commonly referred to as Raman scattering. Two forms exist which are dependent on the energetic origins of the molecule prior to irradiation. Stokes scattering is defined as the scattering that occurs when the molecule begins in the ground state. Anti-Stokes scattering is the scattering that occurs from a molecule that begins in a higher vibrational state.

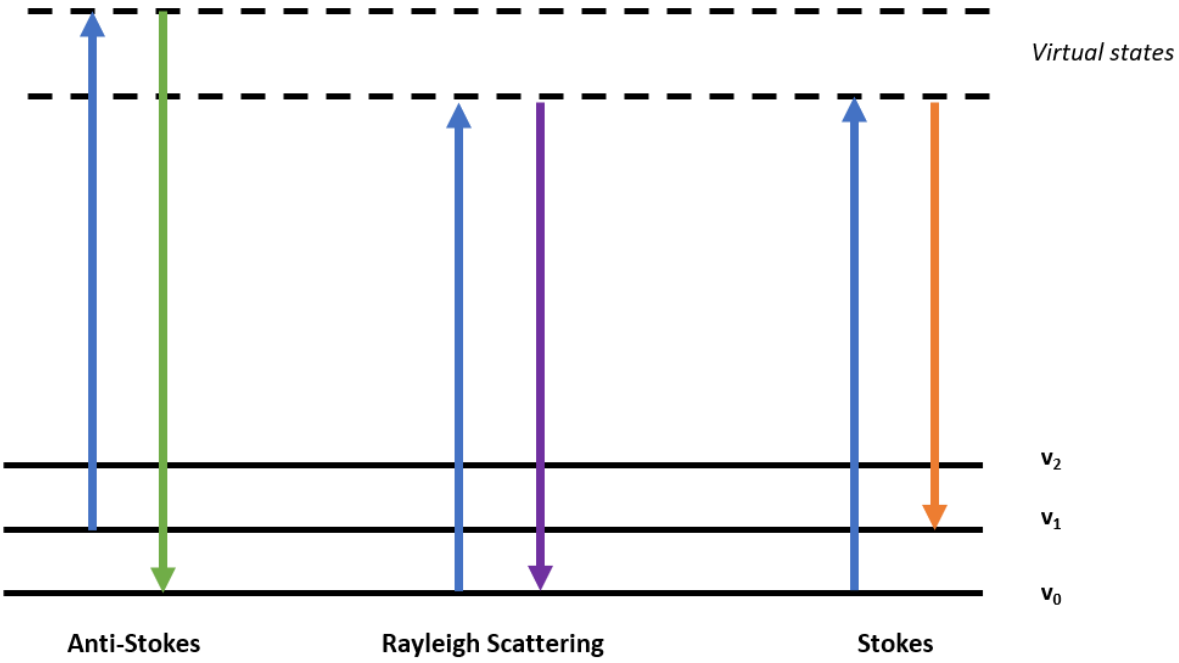

Figure 1.3: *A diagram displaying the origins of Stokes and anti-Stokes scattering.*

Raman scattering can be explained through classical theory.[16] The electric field strength, E of the electromagnetic wave changes with time t:

$$E = E_0 \cos 2\pi \nu_0 t \qquad (2)$$

E_0 and ν_0 correspond to the vibrational amplitude and the frequency of the laser respectively. When a diatomic molecule is irradiated by this light source, it induces an electric dipole moment, P:

$$P = \alpha E = \alpha E_0 \cos 2\pi \nu_0 t \quad (3)$$

α is a proportionality constant which is given as polarizability. If the molecule is vibrating with a frequency given by ν_m then q, the nuclear displacement, can be presented:

$$q = q_0 \cos 2\pi \nu_m t \qquad (4)$$

q_0 is the vibrational amplitude and when amplitude is low, α is a linear function of q and can be presented like so:

$$\alpha = \alpha_0 + \left(\frac{\partial \alpha}{\partial q}\right)_0 q_0 + \cdots \quad (5)$$

α_0 is the polarizability at the equilibrium position and $(\partial\alpha/\partial q)_0$ is the rate of change of α with respect to q at equilibrium. Combination of equations **2**, **3** and **4** gives:

$$P = \alpha_0 E_0 \cos 2\pi \nu_0 t + \frac{1}{2}\left(\frac{\partial \alpha}{\partial q}\right)_0 q_0 E_0 [\cos\{2\pi(\nu_0 + \nu_m)t\} + \cos\{2\pi(\nu_0 - \nu_m)t\}] \quad (6)$$

The first term of this final equation corresponds to the Rayleigh scattering frequency ($\alpha_0 E_0 \cos 2\pi \nu_0 t$). The Stokes and Anti-Stokes scattering vibrations are represented with respect to the difference in their frequency by the terms, $\cos\{2\pi(\nu_0 + \nu_m)t\}$and $\cos\{2\pi(\nu_0 - \nu_m)t\}$respectively. The intensity ratio of Stokes and Anti-Stokes is affected by the number of molecules existing in either the ground and excited states which can be determined using a Boltzmann relationship.[17]

$$\frac{N_n}{N_m} = \frac{g_n}{g_m} exp\left[\frac{-(E_n - E_m)}{kT}\right] \quad (7)$$

Where, N_m and N_n are the number molecules in the ground and excited vibrational energy states respectively, and g is the degeneracy. $(E_n - E_m)$ corresponds to the difference in energy between the vibrational level at temperature T. k is Boltzmann's constant.

Resonance Raman (RR) scattering occurs when the frequency of the incident radiation is close to the frequency of an electronic transition within the molecule resulting in increased scattering.[18] Schematic representations of RR and absorption are very similar as both involve the transition to an excited energetic state (Fig. 1.4).[16] However, a key difference with RR is that scattering is a much faster process and therefore different to absorption. This resonant state increases the Raman scattering, resulting in enhanced intensities relative to the normal Raman response. This enhancement is only available to the modes belonging to the chromophore in the target molecule. It is for this reason that RR is employed for the study of materials containing transition metals and more specifically, metal-containing biomolecules.[19] However care must be taken as the excited state generated in RR, can be problematic. The relaxation back to the ground state may also result in non-scattering processes such as fluorescence which can mask Raman active features.

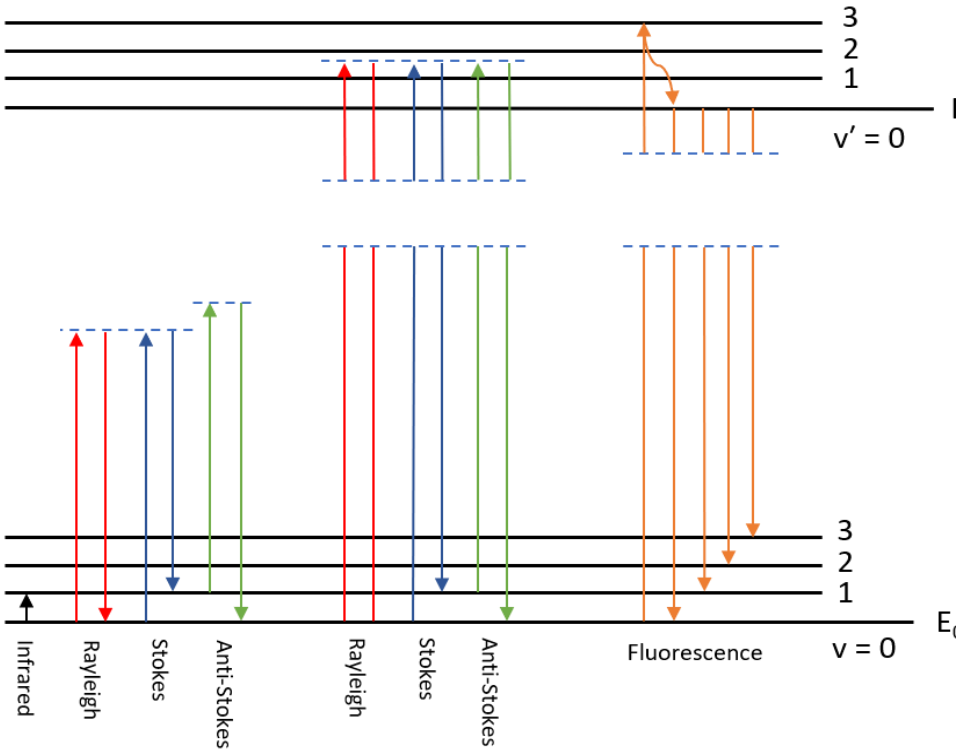

Figure 1.4: *A diagram to compare the energy levels of Raman, resonance Raman and fluorescence.*[16]

1.2.3 Surface-enhanced Raman Scattering

Raman scattering responses are considerably weaker than other optical processes as scattering occurs from approximately 1 photon in every 10^6 – 10^8 absorbed. This often results in Raman-active vibrations being unobserved or lost due to the fluorescence induced by irradiation. Resonance Raman does offer a degree of enhancement however, this is reliant on the frequency of the monochromatic incident light matching an electronic transition. Surface-Enhanced Raman Spectroscopy or SERS is the enhancement of Raman scattering processes resulting from an interaction between the molecule and an enhancing surface. When a molecule is in close proximity to a SERS-active surface, the scattering observed from that molecule is enhanced. The first instance of such enhancement was reported by Fleischmann *et al.* when they reported the Raman spectrum of pyridine adsorbed to a silver electrode however, the nature of the enhancement was not fully understood at the time. Further investigation led to what is now the commonly agreed theory of SERS which involves two distinct mechanisms, electromagnetic and chemical enhancement.[20-22] A brief overview of both mechanisms will be given here, however more complete presentations of enhancement theory can be found in the literature.[23-25]

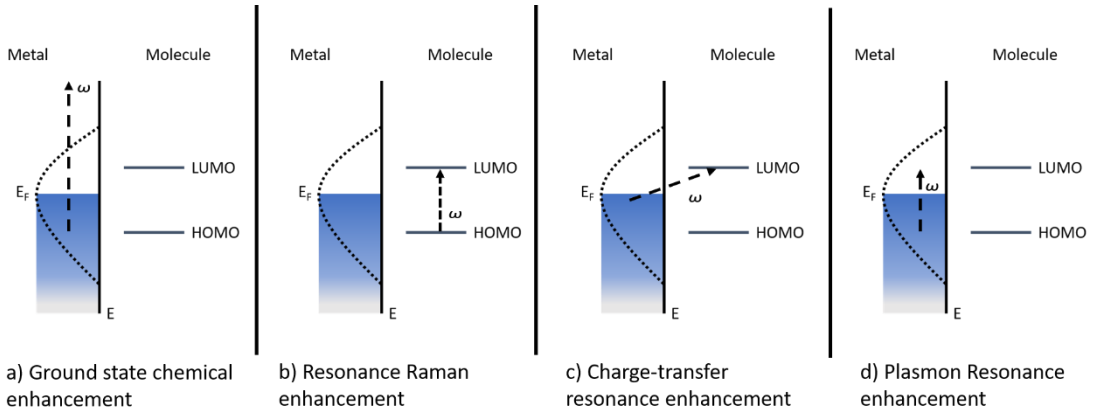

Figure 1.5: *A representation of the SERS enhancement contributions of both mechanisms. Reproduced from the article by Jenson, Aikens and Schatz.*[24]

1.2.3.1 The Electromagnetic Mechanism

The electromagnetic mechanism (EM) of SERS is a result of two enhancement contributions, more commonly referred to as the local field and the radiation enhancement.[21, 26, 27] Local field contributions utilise the electric field enhancement resulting from the excitement of oscillating delocalised electrons or surface plasmons situated at a metal surface by the incident light. This process can enhance the local field strength, E_{loc} of the molecule located at point r_m, given by the equation:

$$\boldsymbol{E_{loc}(\omega_0, r_m) = g_1(\omega_0, r_m) E_0(\omega_0)} \quad \textbf{(8)}$$

Where g_1 is the enhancement factor of the incident field strength E_0. This enhanced local field produces a stronger oscillating dipole at the Raman scattering frequency ω_r,:

$$\boldsymbol{P_m(\omega_0, r_m) = \alpha^I(\omega_R, r_0) E_{loc}(\omega_0, r_m)} \quad \textbf{(9)}$$

Where α^I is the Raman tensor specific to the molecule in question. The resulting power enhancement factor, M_{loc} at r_m is given by:

$$\boldsymbol{M_{loc}(\omega_0, r_m) = |g_1|^2 = \left| \frac{E_{loc}(\omega_0, r_m)}{E_0(\omega_0, r_m)} \right|^2} \quad \textbf{(10)}$$

This localised electromagnetic enhancement is therefore directly related to the localised surface plasmonic resonance (LSPR) of the material which is an intrinsic property of nanomaterials. Ag and Au nanostructures are popular choices for designing SERS-active surfaces because their LSPR sit within the visible and near-infrared region hence excitation can be readily achieved using laser sources. This LSPR is also dependant on the size and shape of the nanomaterial in question which has led to experimentation into nanoparticle synthesis.

Radiation enhancement also contributes to the overall enhancement that comprises the electromagnetic mechanism. The radiation characteristics of a dipole are affected by its immediate surroundings. The radiation enhancement factor M_{Rad} can be defined as the ratio of the power radiated in the nanoparticle environment P_{Rad}, with respect to a vacuum P_0 can be presented as:

$$M_{Rad}(\omega_0, r_m) = \frac{P_{Rad}}{P_0} \qquad (11)$$

Which can then be approximated using the optical reciprocity theorem:

$$M_{Rad}(\omega_0, r_m) \approx \left|\frac{E_{loc}(\omega_0, r_m)}{E_0(\omega_0, r_m)}\right|^2 \qquad (12)$$

The total enhancement resulting from both contributions at position r_m can be approximated by

$$EF(\omega_0, \omega_R, r_m) \approx \left|\frac{E_{loc}(\omega_0, r_m)}{E_0(\omega_0, r_m)}\right|^2 \times \left|\frac{E_{loc}(\omega_0, r_m)}{E_0(\omega_0, r_m)}\right|^2 \approx \left|\frac{E_{loc}(\omega_0, r_m)}{E_0(\omega_0, r_m)}\right|^4$$
$$\approx |E|^4 \qquad (13)$$

A more detailed breakdown of both the local field and radiation enhancement can be found in the work by Le Ru and Etchegoin, and other similar publications.[27-29]

1.2.3.2 The Chemical Enhancement Mechanism

The chemical enhancement mechanism (CM) of SERS are the enhancement contributions that are not a direct result of LSPR interactions but related to the interaction with the electronic properties of adsorbate-surface. Enhancement via CM is significantly smaller in comparison to EM, however the processes involved have accounted for observations that do not fit with LSPR related models including the SERS activity of materials like graphene.[30, 31] The contributions of CM can be divided into resonant and non-resonant interactions between the bound molecule and the surface. Non-resonant chemical enhancement is due to ground state interactions and are not associated with the excitation of the system.[32, 33]

The resonant contributions to chemical enhancement are related to the charge transfer and molecular resonances of the molecule–metal system are explained through Albrecht's work on resonant Raman scattering.[34] The first of the resonant contributions stems from the metal-adsorbate interaction when a molecule is in close proximity to the surface. A requirement is to have an energetic overlap between the Fermi level of the metal substrate, and either the highest occupied molecular orbital (HOMO) or the lowest unoccupied molecular orbital (LUMO) of the adsorbed molecule. Excitation can then result in electron/hole transitions between the surface and the adsorbate. This transient state and the resulting movement of electrons significantly alters the polarizability of the molecule resulting in enhancement.

The second contribution is the resonance Raman contribution where, as previously discussed, the frequency of the excitation light is resonant with a molecular transition. Lombardi and Birke account for both the charge-transfer and resonance Raman contributions giving a total or unified enhancement of resonant contributions, combining the molecular transition (***KI***) and the charge-transfer transition (***FK***).[24, 25]

$$\boldsymbol{R_{IFK}(\omega_0)} = \frac{\boldsymbol{\mu_{KI}\mu_{FK}h_{IF}\langle i|Q_k|f\rangle}}{\left((\boldsymbol{\epsilon_1(\omega)+2\epsilon_0})^2+\boldsymbol{\epsilon_2^2}\right)\left(\left(\boldsymbol{\omega_{FK}^2-\omega^2}\right)+\boldsymbol{\gamma_{FK}^2}\right)\left(\left(\boldsymbol{\omega_{IK}^2-\omega^2}\right)+\boldsymbol{\gamma_{IK}^2}\right)} \quad (\mathbf{14})$$

The denominator is the product of the three terms, the first of which, $\left((\boldsymbol{\epsilon_1(\omega)+2\epsilon_0})^2+\boldsymbol{\epsilon_2^2}\right)$, denotes the surface plasmon resonance at $\boldsymbol{\epsilon_1(\omega) = -2\epsilon_0}$ where $\boldsymbol{\epsilon_1}$ is the dielectric constant of the metal and $\boldsymbol{\epsilon_0}$ is the dielectric constant of the medium. The second term, $\left(\left(\boldsymbol{\omega_{FK}^2-\omega^2}\right)+\boldsymbol{\gamma_{FK}^2}\right)$, represents the contributions from the charge transfer resonance at $\boldsymbol{\omega = \omega_{FK}}$ of potential Fermi-energy transitions. Finally, the third term, $\left(\left(\boldsymbol{\omega_{IK}^2-\omega^2}\right)+\boldsymbol{\gamma_{IK}^2}\right)$, represents the molecular resonance at $\boldsymbol{\omega = \omega_{IK}}$ which is inherent to the molecule. The numerator that couples the resonances provides the selection rules for SERS. The term $\boldsymbol{h_{IF}\langle i|Q_k|f\rangle}$ where relates to the Herzberg-Teller contribution. $\boldsymbol{\mu_{KI}}$ and $\boldsymbol{\mu_{FK}}$ correspond to products of the dipole transition moments of the molecular transition (***KI***) and the charge-transfer transition (***FK***). The terms $\boldsymbol{\mu_{KI}}$ and $\boldsymbol{\mu_{FK}}$ are dependent on the orientation of the molecule with respect to the surface which is known to affect the observed SERS fingerprint of a given molecule.[35]

The fulfilment of the final term in the denominator, $\left(\left(\boldsymbol{\omega_{IK}^2-\omega^2}\right)+\boldsymbol{\gamma_{IK}^2}\right)$, means the process will be Surface-Enhanced Resonance Raman spectroscopy or SERRS. SERRS can present greater enhancement due to a coupling of the conventional SERS

mechanisms with regular resonance Raman enhancement. First reported in work investigating $[Ru(bpy)_3]^{2+}$ complexes adsorbed on silver electrodes, further development has led to the use of chromophoric dyes, such as rhodamine 6G, as Raman tags for assessing the full enhancement capabilities of SERS substrates.[36, 37] It is important to note that SERRS does not require the direct match between the incident beam frequency and the electronic transition which makes the technique more applicable.[38]

Molecular structures of biological relevance have been widely studied using conventional resonance Raman (RR) and that has translated into SERRS. The review by Kitahama and Ozaki discusses SERRS as a method to research an array of biological systems and how the scattering responses compare with the observed RR. They also detail how SERRS has been applied for the sensitive detection of hemezoin, a waste product of the malaria parasite, serving as an example for possible biomedical applications of the technique.[39] One advantage of SERRS is that the response is dominated by the bands associated with the chromophore. Additionally, the binding of optically active species to noble metal materials is known to quench fluorescence meaning signals that would usually not be visible, can be seen.[38]

1.3 The Nanoparticle

1.3.1 Introduction to Nanoparticle Synthesis

The prefix “nano” represents 10^{-9} of whatever unit of measurement it precedes so it is accepted that a nanoparticle (NP) has dimensions between 1 and 100 nm where 1 nm is equivalent to 1 $x10^{-9}$ m. Our understanding and appreciation of nanotechnology has grown significantly since it’s conceptualisation by Feynman in his lecture 1959 “There is plenty of room at the bottom”.[40] The construction of nanomaterials can be achieved by either “top down” or “bottom up” methods. Many reported nanoparticle syntheses align with the “bottom up” principles outlined by Drexler where larger structures are built from smaller components.[41] Taniguchi coined the term “Nanotechnology” also outlined the principle of “top down” approaches built upon miniaturisation and precision machining or larger structures.[42] Techniques such as lithography have been widely employed for many years, however such methods are reaching the limits of economic effectiveness and physical potential.[43]

The attraction of bottom up approaches lies with the simplicity and cost effectiveness they offer in comparison to top down methods and have now developed to the point where NPs can be generated from many different starting materials, both organic and inorganic in nature. Size and geometry can be controlled through manipulation of the experimental conditions which has resulted in the formation of various different shapes.[44] Control of size and geometry on nanoparticle structures is particularly important with respect to SERS as both parameters have significant impact on the wavelength of the associated LSPR. Such control can be established in many ways and one example is through synthetic control via the introduction of a stabilising agents that

provide shape control by limiting growth to one crystallographic face. Development of this principal has led to the synthesis of multicomponent and composite NP systems including cluster-like and star shaped nanoparticles along with core-shell and Janus nanoparticles.[45]

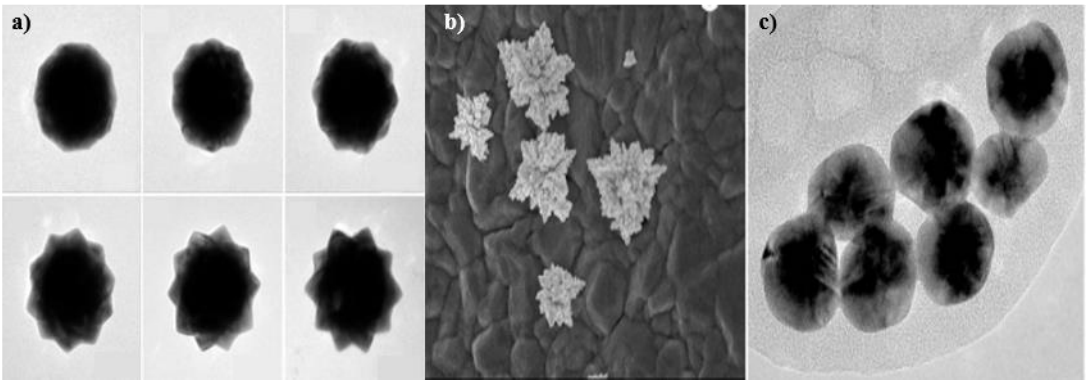

Figure 1.6: *a) TEM images of gold nanostars produced by varying the concentration of dimethylamine.[46] b) Quasi-fractral nanoparticles that are synthesised by modifying the temperature of procedure.[47] c) Core-shell Au@Ag nanoparticles made by the successive addition of $AgNO_3$ in the presence of ascorbic acid. Taken from literature.[46-48]*

1.3.2 LaMer Theory of Bottom up Nanoparticle Synthesis

Several mechanisms exist that offer explanations of the underlying processes of nucleation. The LaMer theory develops the classical nucleation ideas presented by Becker and Döring, and applies it to the concept of nanoparticle synthesis.[49-51] "Burst nucleation", as dictated by LaMer, can be broken down into three separate stages, the first of which is the generation of the nuclei through homogeneous nucleation processes (Fig. 1.7). With respect to noble metal nanoparticles (NMNPs), this is often the reduction of the metal salt or acid (Stage I). The concentration of nuclei will continue to increase where it will reach a critical supersaturation level until the activation energy of nucleation is surpassed. At this point, burst nucleation will begin, causing a decrease in the supersaturation level and the start of the growth (Stage II). Homogeneous nucleation does still occur however the newly formed nuclei now diffuse towards the

growing particle surface. It is at this point where nucleation become heterogeneous (Stage III). Heterogeneous nucleation is assumed to take place at areas where the effective surface energy is lower allowing for nucleation at that point.[52] In the case of NMNPs, evidence suggests that the growth pathway begins with the formation of smaller clusters which coalesce into the larger NPs.[49] Other theories exist that explain the growth mechanisms of other NP colloidal systems, however they are not discussed further here.[53-55]

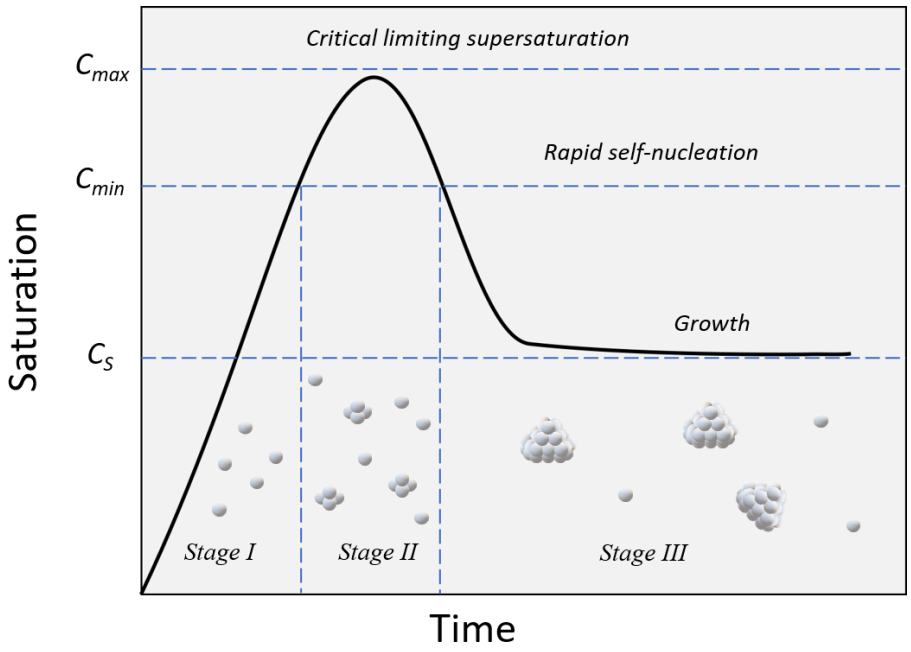

Figure 1.7: *A schematic diagram based on the original work by La Mer, displaying the three stages of nucleation.*[50, 52]

1.3.3 Stabilising the Colloidal Suspension

Stabilisation is an important factor in colloidal synthesis, providing control to the growth of the colloid. Uncontrolled growth will inevitably lead to an unstable suspension and agglomeration of the colloid resulting in sedimentation. Stability is achieved often through electrostatic stabilisation as a result of the surface charges present at the surface of the particle. Von Helmholtz first identified the electric double

layer that exists between a charged species or particle and the electrolyte surrounding it. The model was later significantly improved by Gouy and Chapman as the diffuse charge distribution was accounted for. They outlined that this charge distribution reduced exponentially as distance from the surface increased. The Stern-Graham model takes a slightly alternative look at this model by splitting it into two parts (Fig. 1.8). The first part being a layer of strongly adsorbed counterions on the surface and the second being the diffuse arrangement of counterions outlined by Gouy. This electric double layer results in the electrostatic repulsion that allows for particles to remain separate and avoid aggregation.

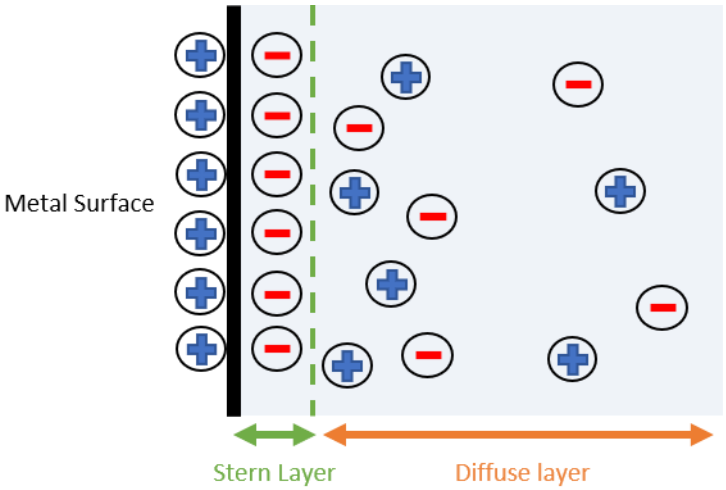

Figure 1.8: *A basic diagram illustrating the Gouy-Chapman-Stern-Graham electric double layer model the surface of a nanoparticle surface*

The Derjaguin-Landau-Verwey-Overbeek or DLVO theory states that the total force between colloidal nanoparticles, $\boldsymbol{W_{Total}}$ at an interparticle distance, $(\boldsymbol{D})$, is a balance between the attractive van der Waals forces, $\boldsymbol{W_a(D)}$, and the repulsive interactions generated by the electric double layer (EDL), $\boldsymbol{W_r(D)}$, resulting in the suspension of particles in the chosen media.[52].

$$\boldsymbol{W_{Total}(D) = W_a(D) + W_r(D)} \qquad \boldsymbol{(15)}$$

Van der Waals forces of attraction result from transient dipoles that can occur in a molecule which then induces a dipole in surrounding molecules. When approaching larger examples such as NPs, one must consider for all the interactions that occur within the large-scale system.[10, 52, 56] The Hamaker constant, where $\boldsymbol{\rho_1}$ and $\boldsymbol{\rho_2}$ is the number density of the two particles and $\boldsymbol{C}$, is the London coefficient, is a solution to this as it considers the interactions of two significantly larger, identical bodies;

$$A = \boldsymbol{\pi^2 \rho_1 \rho_2 C} \qquad (\mathbf{16})$$

This allows us to quantify the interaction potential between them. Where $\boldsymbol{W_a(D)}$ is the interaction energy between the two identical particles of radius, $\boldsymbol{R}$, at an interparticle distance, $\boldsymbol{D}$.

$$\boldsymbol{W_a(D) = -\frac{\pi^2 \rho_1 \rho_2 C R}{12D} = -\frac{AR}{12D}} \qquad (\mathbf{17})$$

The nanoparticle repulsive force, $\boldsymbol{W_r(D)}$, takes into account the thickness of the EDL, or Debye length, $\boldsymbol{\lambda = (\kappa^{-1})}$ and the distribution of the electric surface potential, $\boldsymbol{\psi}$, of each particle of radius, $\boldsymbol{R}$.[52]

$$\boldsymbol{W_r(D) = 2\pi\varepsilon\varepsilon_0 R\psi_\delta^2 exp(-\kappa D)} \qquad (\mathbf{18})$$

Where $\boldsymbol{D}$ is the interparticle distance, $\boldsymbol{\varepsilon}$ and $\boldsymbol{\varepsilon_0}$ are the dielectric constant and permittivity of a vacuum respectively. This means that equation (**14**) can be rewritten using equations, (**15**) and (**16**) to give:

$$\boldsymbol{W_{Total}(D) = W_a(D) + W_r(D) = -\frac{AR}{12D} + 2\pi\varepsilon\varepsilon_0 R\psi_\delta^2 exp(-\kappa D)} \qquad (\mathbf{19})$$

Plotting the resultant sum of the van der Waals attraction and the electrostatic repulsion with increasing distance results in the total interaction potential that exists between two species (Fig. 1.9). A noticeable maximum is observed at small distances which is the activation energy that prevents aggregation. The position of this maximum can be altered through change in the ion concentration. An increased counterion concentration results in a decrease in the EDL which in turn results in a loss of electrostatic repulsion meaning the colloid loses stability. Particle size also impacts colloid stability due to it proportionality with the repulsion potential therefore the DLVO potential increases with particle size.[56]

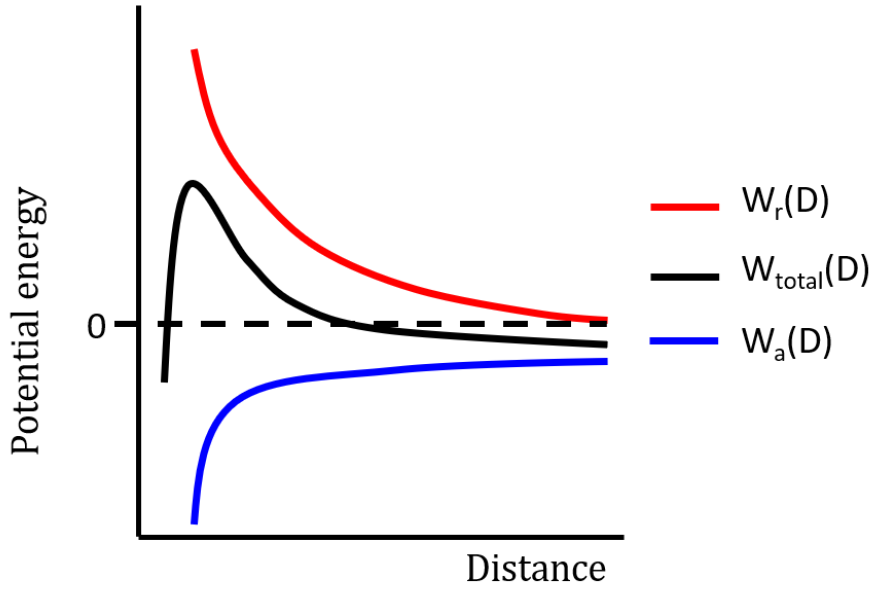

Figure 1.9: *A schematic representation of the total interaction, van der Waals attraction and electric double layer potentials.*[52]

The use of counterions and the electrostatic repulsion they generate has been highly beneficial with respect to noble metal NP synthesis. The most popular procedures for the formation of colloidal silver and gold nanoparticles are reliant on the reduction and stabilisation by trisodium citrate.[57, 58] An advantage of using citrate is that it reduces the metal precursor, encouraging seed formation and provides the stabilisation through the

formation of a surface potential. Size and shape control of such systems can be introduced through seed-mediated growth control methods that generates NPs that vary greatly in appearance.[59] Ascorbic acid also demonstrates a mildly reducing capability, however unlike citrate, it requires the presence of a secondary stabilising species to successfully stabilise a colloidal suspension.[60, 61]

1.3.4 Steric Stabilisation of Nanoparticle Colloids

Steric stabilisation can also be used to stabilise a nanoparticle against aggregation. This is achieved through the strong adsorption of larger molecules to the particle surface. By fully coating the NP, the attractive van der Waals forces are screened due to the interparticle distance created. With respect to the DLVO theory, sterics can be assumed to be an additional term that contributes to the overall repulsion potential and thereby contributing to the total interaction potential.[52]

$$\boldsymbol{W_{Total}(D) = W_a(D) + W_r(D) + W_{Sterics}} \qquad \boldsymbol{(20)}$$

For suitable steric stabilisation to be appropriate, a species should bind strongly to the surface and provide interparticle distance without initiating any other activity that may result in particle interaction. The most popular approach for the binding and stabilisation of NMNPs is the use of thiol containing species. It is believed that a strong covalent interaction exists between noble metal surfaces that is similar in strength to that of an Au-Au bond, allowing self-assembly of a thiolated monolayer.[62] The Brust-Schriffrin method is a notable example, using long chained organic thiols to strongly bind to gold nanoparticles (AuNPs).[63]

A possible disadvantage is the requirement of organic solvents and toxic reducing agents like $NaBH_4$ potentially limits further application of such systems in a biological setting.[64] Consequently, the capabilities of using the steric stabilisation of more biologically appropriate thiol containing compounds has been investigated. The use of thiolated poly(ethylene glycol)-NP systems are widely reported particularly in biomedical fields as poly(ethylene glycol) (PEG) improves the biocompatibility.[65-70] Functionalisation of such species requires the displacement of the citrate allowing for the adsorption of the binding moiety.[71] Other binding mechanisms do exist which has resulted in a diverse range of polymer stabilised nanoparticles that demonstrate interesting properties with recent reviews highlighting a range of possible catalytic, sensing and antimicrobial applications.[72-74] Additional examples of capping agents include oleyl amine and substances derived from biological entities which have enabled further functionalisation for adaptable applications.[75-77]

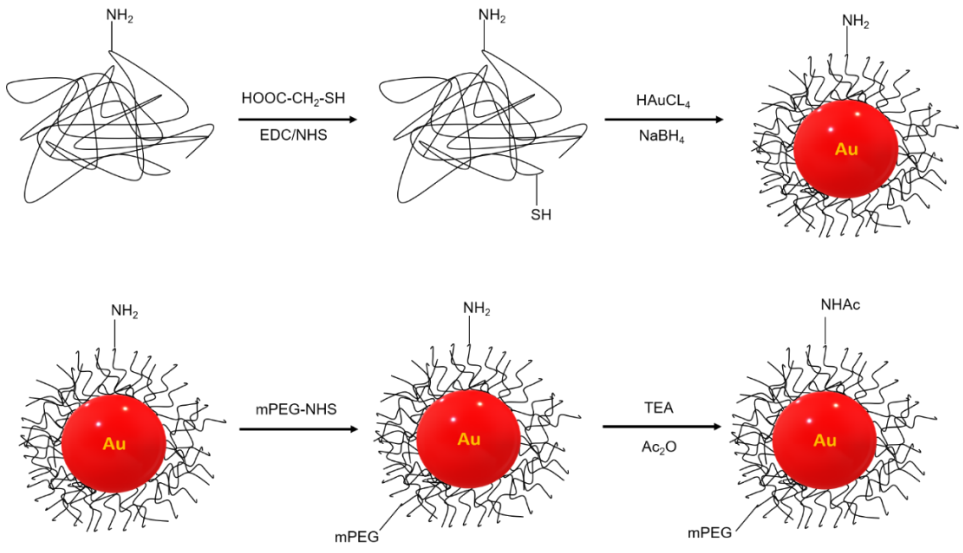

Figure 1.10: *The synthesis of PEG-functionalised AuNPs described by Zhang et al. Reproduced from literature.*[66]

1.4 SERS-based Sensing Using Functionalised Nanoparticles

SERS-based sensing and detection has profited greatly from noble metal nanostructures. Two main strategies exist defined by the interaction of the analyte with the SERS surface. Label-free methods are reliant on the target molecule being near the nanoparticle which when irradiated, generates a specific response of that particular molecule. This can be useful in a biomedical context when analysing larger molecules such as nucleic acids and proteins.[78] The second technique is built upon the ideas of surface functionalisation highlighted earlier, whereby a label is introduced to the nanoparticle surface that has a characteristic response. Detection occurs through interactions between the label and target and corresponding changes to the Raman spectrum of the label.[79] By attaching a variety of labelling species to nanoparticles, researchers have been able to use these methods for detection of different analytes.

Several systems have been designed for the control of pesticide and pollutant contamination in the environment. A polymer coated silver nanoparticle (AgNP) system described by Li *et al.* which is able to detect pyrethroid insecticides to a limit of 0.013 μmol L^{-1}.[80] Detection of the pesticide proceeds by the selective adsorption of the target molecule into cavities of the polymer coating where it can be recognised through a characteristic Raman band at 1595 cm^{-1}. Gold nanorods functionalised with cysteamine have also been employed for the sensitive detection of another popular pest control, acephate (Fig. 1.11).[81] The cysteamine-functionalised nanorods captures the target through formation of N-H-N bonds which is observed via the appearance of SERS peaks associated with acephate at 358, 400, 560 and 692 cm^{-1}. Both examples illustrate the practical potential for the detection of environmental contaminants in crops as measurement can be achieved in relatively short timeframes.

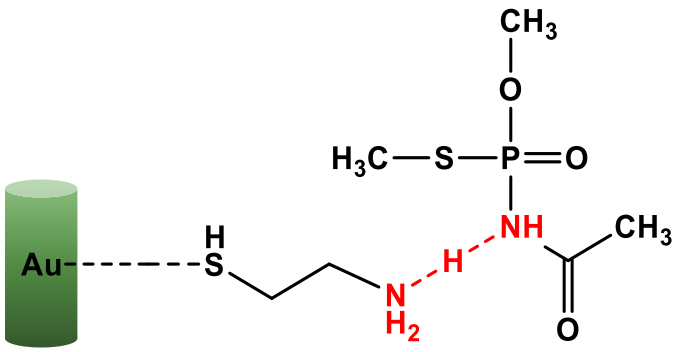

Figure 1.11: *A representation of the cysteamine capture of acephate proposed by Weng et al.*[81]

Heavy metal contaminants are another example that have been detected by SERS systems. Recently, a capillary system lined with 4,4'-bipyridyl functionalised AgNPs detects mercury ions.[82] The coordination of 4,4'-bipyridine with Hg^{2+} results in a dissociation of the bipyridine from the AgNP surface, leading to an observed decrease in the SERS response. Host-guest interactions can also be utilized for Hg^{2+} detection purposes. Wu, Yang and Wang detail the use of an azathia crown bound to Au@SiO_2 core-shell particles (Fig. 1.12).[83] Chelation of Hg^{2+} with the sensor is observed by the appearance of a peak corresponding to the newly formed Hg-S bond at 270 cm^{-1}.

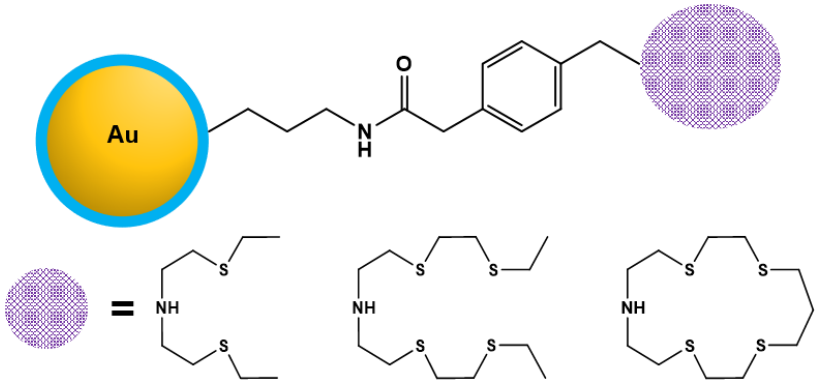

Figure 1.12: *A representation of the azathiacrown-NP system that has a host-guest interaction with* Hg^{2+}.[83]

Several procedures utilise complementary DNA interactions for Hg^{2+} sensing, displaying successful detection claiming sensitivities as low as 1 $x10^{-16}$ M.[84-86] The DNA binding interactions are induced by Hg^{2+} as it binds between the thymines situated

on the Raman label and the NP. An example of this is an oligonucleotide-functionalised magnetic silica@Au core shell nanoparticle system (Fig. 1.13).[87] The system relies on the presence of two NP structures, the thymine-rich core-shell nanoparticle that possesses a magnetic core and AuNPs with partially complementary sequences bound to the surface. The DNA@AuNP system also contains a Raman reporter for recognition of the interactions. The resulting composite formed after Hg^{2+} coordination can be removed magnetically and tested. Interestingly, the system can also be tuned for Ag^{+} detection by including cysteine-rich sequences meaning simultaneous detection can be achieved.

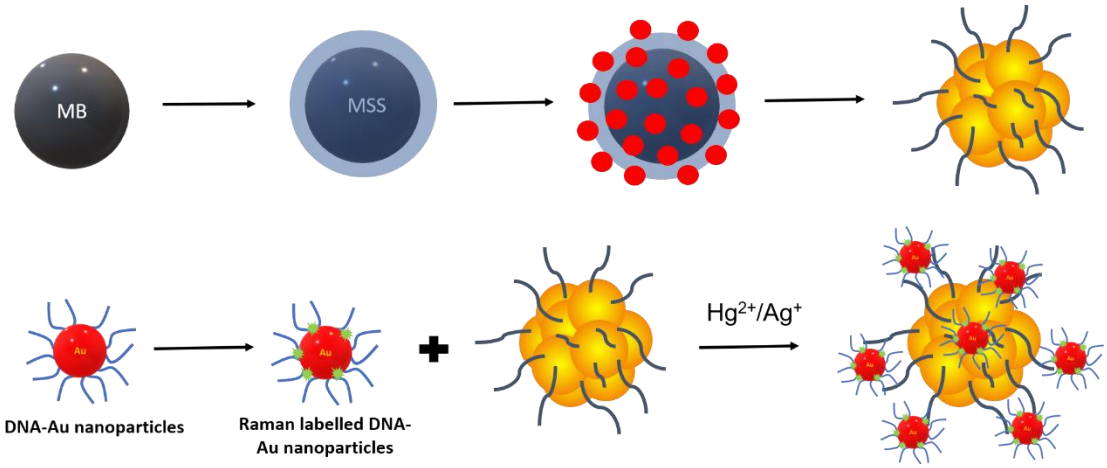

Figure 1.13: *A schematic representation of the synthesis of magnetic core-shell nanoparticle systems. Reproduced from literature.*[87]

Functionalised NPs have also been reported for the targeted SERS detection of biomarkers that are associated with a number of diseases. Improving the detection capabilities of such biomarkers could contribute greatly to the successful diagnosis of associated diseases. An aptamer-based sensor has demonstrated the capability to detect the prostate specific antigen (PSA), the blood level of which can be an indicator of prostate cancer.[88] The system is a core-satellite design that is centred around the association of AuNP satellite with a magnetic NP core and the presence of PSA induces dissociation via more favourable interactions with the satellite (Fig.1.14). The magnetic

core can be drawn from solution leaving the dissociated satellites in the supernatant where SERRS measurements can be taken. The change in SERRS intensity has a direct correlation with the concentration of PSA with the system displaying a limit of detection of 5.0 pg/ml.

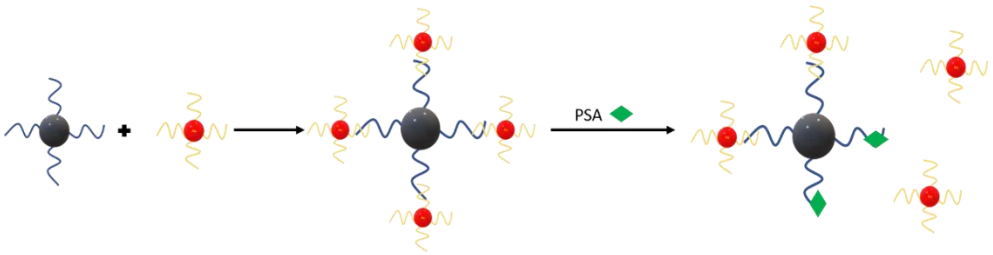

Figure 1.14: *A representation of the core-satellite system that shows an increased SERS enhancement after cleavage of the Au satellite from the nanoparticle upon the addition of PSA. Reproduced from literature.*[88]

A similar system that uses the core-satellite aptamer-functionalised NP blueprint has shown an ability to detect the presence of thrombin. Thrombin is involved with blood clotting and coagulation in the body however, there is also evidence to suggest that increased thrombin levels could be an indicator of Alzheimer's disease.[89, 90] Complementary aptamers link the core with labelled AuNPs but this link is disrupted by thrombin (Fig. 1.15). The core-thrombin species can be removed, at which point the SERS response of the suspension can be measured which is affected by the increase in labelled AuNPs to incredibly low levels of sensitivity.[91]

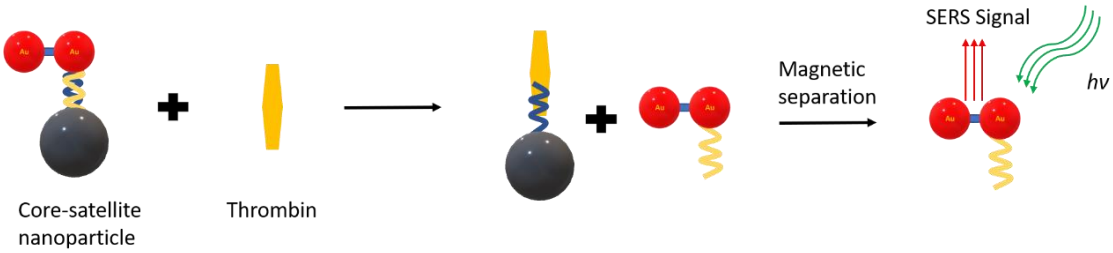

Figure 1.15: *A representation of the core-satellite system by Jiang et al. that detects the presence of thrombin through satellite separation. Adapted from literature.*[91]

1.5 Nanoparticle Substrate Assembly

1.5.1 The Theory of "Hot Spots"

Nanoparticle science has been expanding for several years, taking the nanoparticle and building larger structures that reproducible and have excellent SERS enhancement. Bringing NPs into close proximity creates areas of high SERS enhancement known as "hot spots", which is defined as the junction between two or more particles that possess a localised plasmon. The close proximity of the nanoparticles causes the overlap of the surface plasmons of both nanoparticles which in turn, causes an amplification of the electromagnetic field situated around and between the structures (Fig. 1.16). Factors such as the interparticle spacing and arrangement of the nanoparticles directly impact the overall coupling of the two EM fields with a corresponding effect on the overall signal enhancement.[92, 93] Initial observations were made independently by Kneipp *et al.* and followed closely by Nie and Emory. Both reported single molecule detection of dyes adsorbed to AgNPs and later work presented evidence that NP aggregates were the reason for this increased enhancement.[26, 94-97]

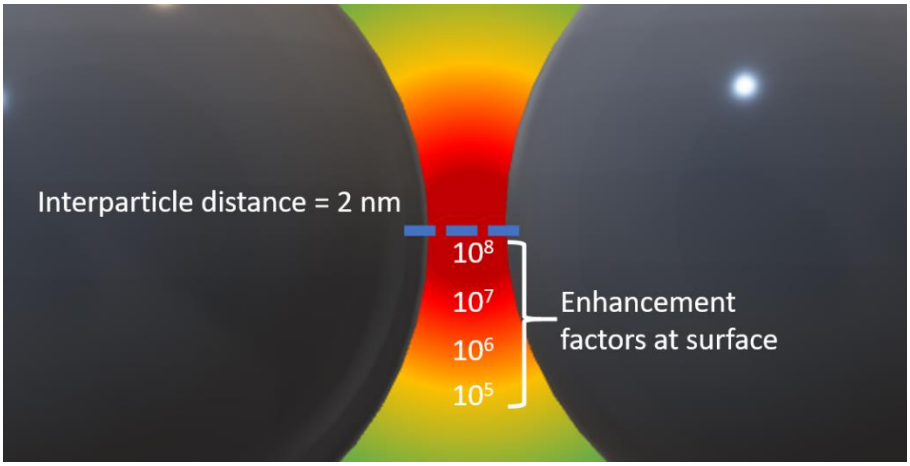

Figure 1.16: *The enhancement distribution factors that exist between two spherical nanoparticles. Adapted from the literature.*[26]

Early works focused predominately on the formation of NP aggregates from simple colloidal solutions, however there are drawbacks to this approach. Aggregation is a random process which affects the reproducibility of the system, and then locating the aggregates once formed also presents challenges. Researchers now seek to resolve these problems by bringing nanosized structures into close contact, aiming to improve reproducibility and utilise SERS hotspots more accurately. This has been achieved by employing methods such as lithography, which have the ability to write desired shapes and structures onto responsive materials, generating highly ordered arrays of nanohole and nanoshape platforms.[98-101] Despite the high enhancements that can be achieved with such platforms, the cost and requirements associated with lithographic techniques have restricted their widespread use. This has inspired investigation into more cost-effective approaches leading to a diverse range of techniques being reported.

1.5.2 Composite Materials for High SERS Enhancement

Composite materials that involve the growth or positioning of NMNPs on larger structures have seen considerable interest. Highly ordered architectures made from more structurally rigid materials have been incorporated into the development of SERS substrates. For a number of years, polymer scaffolds have been particularly popular as highlighted by the review from Rahim and Dong-Hwan.[102] The attractiveness of using polymers stems from the control offered in the fabrication steps. This allows for formation of ordered 2-dimensional and 3-dimensional structures such as brushes and fibres. Additionally, NMNPs can be readily immobilised onto these structures through bottom up procedures, which can also be fully characterised using microscopy techniques. This gives direct visualisation of the nanoparticles in close proximity, the requirement needed for “hot spot” enhancement.[102]

Sheng *et al.* and Karagoz *et al.* have provided recent examples of the polymer-nanoparticle composite materials.[103, 104] Both systems use Ag-functionalised polymer nanostructures that give suitable SERS enhancement whilst also displaying photocatalytic, self-cleaning capabilities. Polymer-metal hybrids possess the desired reproducibility and functionality that contribute to their potential as a SERS substrates. Deposition or growth of nanoparticle species onto pre-fabricated substrates often occurs through *in-situ* chemical reduction (Fig. 1.17). However, other techniques have been used. For instance, photocatalytic deposition has also been implemented for the growth of nanoparticle films and structures.[105, 106]

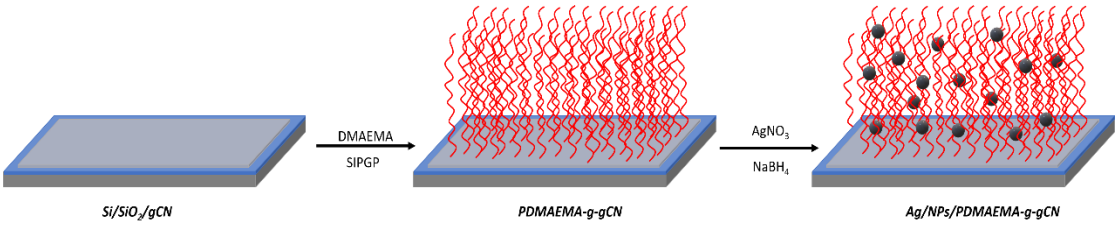

Figure 1.17: *The incorporation of AgNPs into large, ordered structures of polymer stands situated on a graphitic carbon nitride-silica substrate. Adapted from literature.*[103]

Metal deposition onto substrates featuring ordered polymer structures has been reported, most notably by the Van Duyne group.[107, 108] They initially detailed a technique that uses vapor deposition, and later show how it produced desirable SERS-responsive substrates with high levels of control. A similar technique of metal deposition onto a templated surfaces, is the formation of monodispersed nanosphere monolayers exemplified by Sabri *et al.* (Fig. 1.18a).[109] Their technique is similar to the nanosphere lithography approach detailed by the Van Duyne group however they employ electron beam (e-beam) lithography. This technique was taken and adapted further by Makam *et al.* creating a substrate for the ultrasensitive detection of mercury ions in water (Fig. 1.18b).[110] They use the e-beam substrate coated with a layer consisting of histidine conjugated perylene diimide units. These diimide moieties

introduce the Hg^{2+} sensitivity and the system has a reported detection limit of 60 $x10^{-18}$ M, demonstrating the sensing potential of such films.

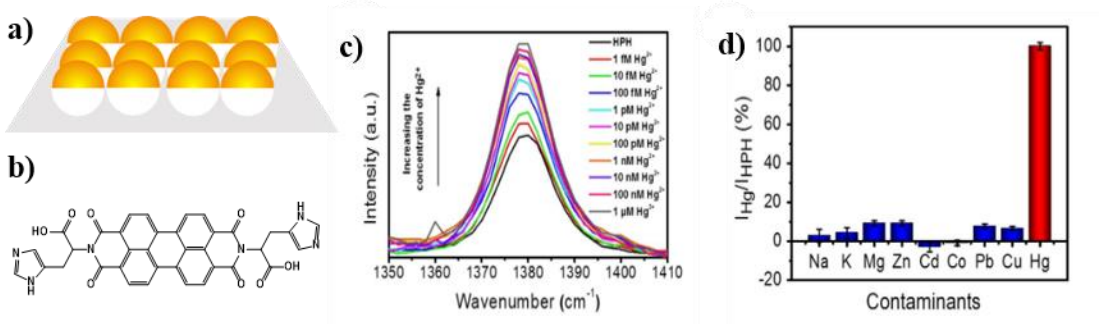

Figure 1.18: *a) A graphic showing the metal deposited surface formed using -beam lithography b) The histidine conjugated perylene diimide unit used to functionalise the surface. c) The observed change in relative intensity through Hg^{2+} interactions of a vibration originating from the ligand. d) The relative intensity change when subjected to other metal ions. Taken from literature.*[110]

Graphene, a carbon allotrope that exists as a planar hexagonal honeycomb structure, has displayed interesting properties that have also led to its widespread use in SERS science.[111, 112] It has shown an ability to quench fluorescence, improving the recognition of weaker Raman signals that may go unobserved due to interference.[113] More interestingly, graphene itself has demonstrated an ability to enhance Raman scattering of adsorbed dyes via chemical enhancement.[31, 112] The development of Graphene-enhanced Raman Spectroscopy or GERS has generated better understanding of chemical enhancement and continues to contribute to SERSs substrate development. Graphene has been utilised in various ways, as a substrate, as molecular spacers between nanoparticles and in NP decoration for sensing.[111, 114, 115]

A recent example from the literature uses graphene oxide (GO) as a spacer between AgNPs and AuNPs that shows sensitive levels of detection for polychlorinated biphenyl pollutants (Fig. 1.19).[116] The heightened enhancement from such systems stems from additional enhancement contributions from the GO and hot spot enhancement provided through the spacing. Detection is possible due to π- π interactions that occur between

the graphene layer and the organic species. An analogous system achieves the detection of polycyclic aromatic hydrocarbons through similar interactions.[117]

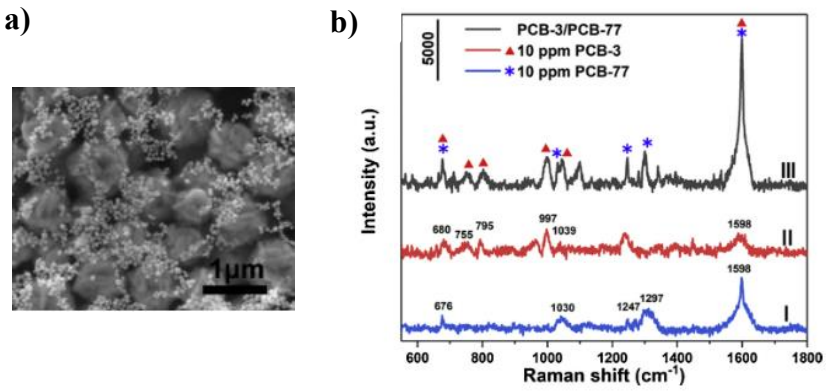

Figure 1.19: *a) A SEM image of their AgNP-GO-AuNP substrate described by Zhang et al. and b) the SERS spectrum obtained using the surface to detect two forms of polychlorinated biphenyls. Taken from literature.*[116]

Other semiconductor materials display enhancement capabilities which in turn has also led to their incorporation into hybrid composite materials. Further information can be found in a number of recent reviews.[118, 119] A noteworthy example is the work produced by Yilmaz *et al.* where they describe an organic semiconductor that possesses incredibly high enhancement factors (Fig. 1.20).[120] Deposition of closely packed AuNPs onto the surface further increases the possible enhancement. The authors report an incredibly low detection limit of $<10^{-21}$ mole for methylene blue.

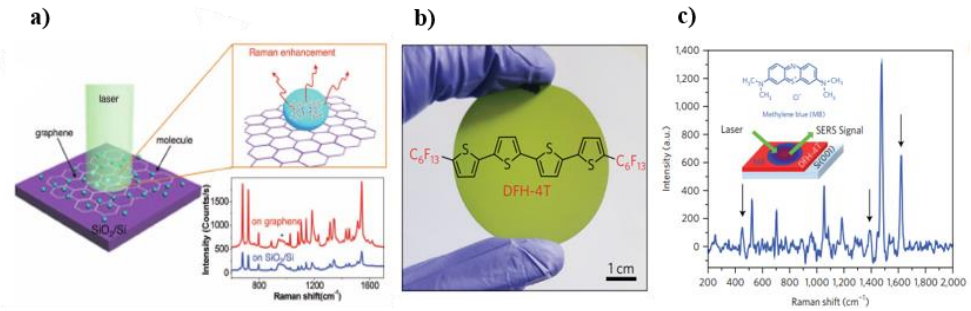

Figure 1.20: *a) An illustration of graphene enhancement with the spectra of phthalocyanine deposited on graphene (red) and SiO_2/Si (blue).*[31] *b) The organic semiconductor described in the work by Yilmaz et al. and c) the SERS of methylene blue from just the semiconductor surface. Taken from literature.*[120]

1.5.3 Self-assembled Nanoparticle Systems

Self-assembly is another approach that has generated significant interest in recent years. The recent review conducted by Hu *et al.* demonstrates the wide variety of techniques that have been explored for producing in-plane anisotropic films using nanostructures that differ in both shape and composition.[121] Additionally, Langmuir-Blodgett techniques have been implemented for the production of thin films using spherical and rod-shaped particles with procedural modifications allowing tunable plasmonic responses meaning SERS performance can be optimised.[122-124] Additionally, other reported methods include the controlled evaporation of polymer-functionalised NP films and drop casting of the interface.[125-127]

Self-assembled noble metal nanostructures can be generated through modification of both the NP surface and the environment.[122-124] Nanoparticles functionalised with DNA have shown an ability to assemble through complementary bridging between the DNA strands of neighbouring NPs. Different architectures developed using this approach included monolayer films, dimers and more complex NP-clustered nanocages.[128, 129] Recently, the positional control of nanorod and spherical dimers was described by Lloyd *et al.*[130] The orientation and positioning of DNA-functionalised Au nanorods and nanoparticles could be controlled though altering the deposition and drying times, giving three conformers; tip-on, side-on and on-top. The approach yields individual structures however the authors describe possible expansion that would give more complex multiparticle species. Another example of self-assembly through DNA functionalisation has been demonstrated by Li *et al.* who illustrate the *in-situ* formation NR dimers inside cells (Fig 1.21).[131] The orientational control available through this

procedure has successfully shown an ability to bind and detect microRNA within the cell.

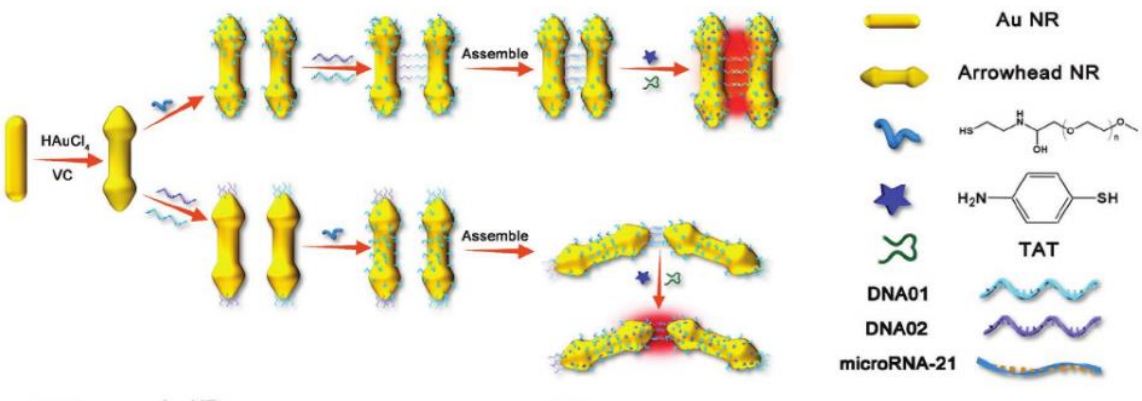

Figure 1.21: *DNA induced self-assembly of different orientations of arrowhead Au nanoroad dimers. Taken from literature.*[131]

1.5.4 Nanoparticle Assembly at Liquid-Liquid Interfaces

An attractive method for the formation of larger assemblies is the positioning of NP structures at liquid-liquid interfaces. Colloidal particles at water-oil interfaces is a key concept for multiple disciplines, including the work described in this thesis. The Free energy model for particle assembly offers a suitable description of how stability is achieved for a charge neutral species situated at a water-oil interface. [132, 133] An interface between immiscible liquids forms due to repulsive interactions between the two layers. The adsorption of a charge-neutral particle at this interface results in a decrease of the interfacial energy, making it energetically favourable. This interfacial free energy, $\boldsymbol{\Delta G}$ is directly related to both the contact angle, $\boldsymbol{\theta}$ of the particle and the interfacial tension, $\boldsymbol{\gamma_{OW}}$ between the two liquids.

$$\boldsymbol{\Delta G = \pi R^2 \gamma_{OW}(1 + cos\theta)} \qquad \boldsymbol{(21)}$$

The highest attachment energy is when $\boldsymbol{\theta}$ =90° and any significant movement away from this value massively impacts the ability for immobilisation at the interface. $\boldsymbol{\Delta G}$ is also proportional to $\boldsymbol{R^2}$ meaning particle size is a controlling element. The study by Lin *et al.* demonstrates that as size and the corresponding interfacial energy decreases, thermal energy is sufficient to induce the displacement of the nanoparticle back into the bulk phase.[134]

Charged-stabilised particles and the electric double layer (EDL) responsible for their stability introduce greater complexity into the system. Pieranski shows that the EDL is disrupted when a particle is situated at a water-air interface which is due to surface stabilising agents being unable to cross the interfacial boundary.[135] This dissociation results in an asymmetric charge distribution at the nanoparticle surface, inducing a dipole that contributes to long-range repulsion in the non-aqueous phase (Fig.1.22). Aveyard *et al.* illustrated that this repulsion is also applicable to particles situated at a water-oil interface.[136] The exhibited long-range coulombic repulsion gives considerable separation of the nanoparticles at the interface. However, this repulsion can be depleted through the addition of NaCl to the colloidal suspension.

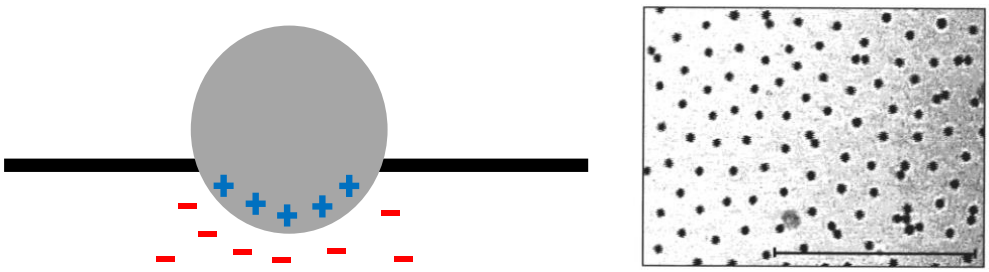

Figure 1.22: *A schematic representation of the asymmetric disruption of the electric double layer and the observed distancing of latex particles as a result of coulombic repulsion. Taken from literature.*[135, 136]

The thermodynamic model for the self-assembly of charged nanoparticles has been presented by Reincke *et al*. which reiterates that reducing surface charge density is the key to interfacial NP self-assembly.[137] To date, numerous strategies have effectively situated NMNPs at water-oil interface, forming Metal Liquid-like Films or MeLLFs. Early reports describe the use of surfactant and metal polypyridyl complexes as stabilising agents through surface interactions resulting in MeLLF formation.[138, 139] The displacement of charge stabilisers with charge-neutral, organic agents has also been widely investigated. Specific examples include thiol- and nitrogen-containing species that bind to the nanoparticle surface thereby altering the relative hydrophobicity, inducing interfacial placement.[140-142] Other approaches involve the introduction of hydrophilic salts or competitive solvents like ethanol which sufficiently alter the surface charge causing interfacial adsorption. Mechanical methods like centrifugation have also been successful.[143-147]

A notable approach is the addition of lipophilic tetrabutylammonium (TBA) salts that induce MeLLF formation as reported by members of the Bell group.[148] TBA salts "promote" the nanoparticle to the interface through screening of the surface charge similarly to NaCl, and it does not modify the surface like organic species. An attractive element of TBA salts is that surface charge is screened on both sides of the interface due to the hydrophobic nature of the TBA^+ counter ion (Fig. 1.23).

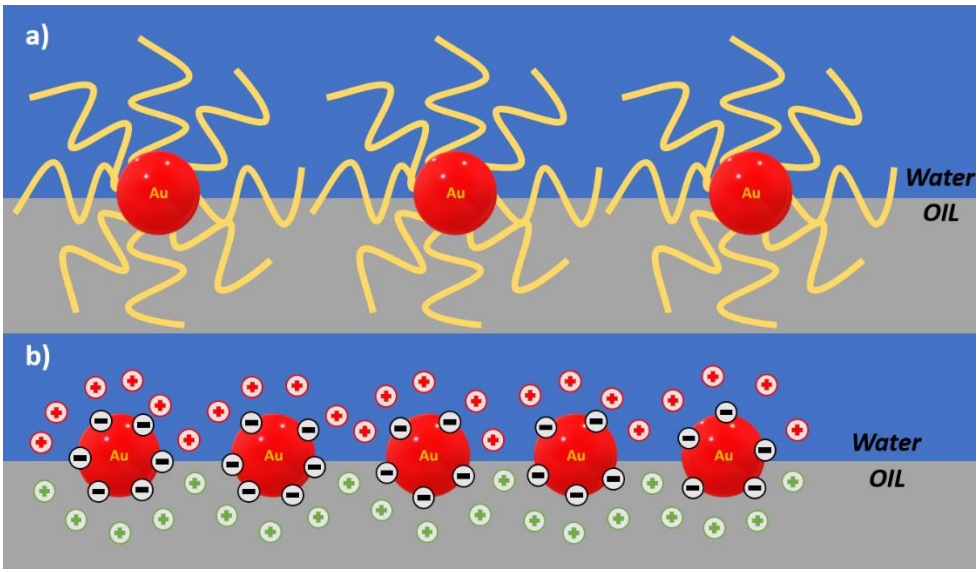

Figure 1.23: *A schematic representation of a) modification and b) promotion stabilises nanoparticles at a liquid-liquid interface as demonstrated by Xu et al. It demonstrates how TBA salts can effectively stabilise nanoparticles at both sides of the interface. Adapted from literature.*[148]

Further development of the TBA promoted MeLLFS has produced Surface-exposed Nanoparticle Sheets or SENS. A polymer support envelops the fraction of the particle that is immersed in the organic layer as is dissolves meaning one half of the nanoparticle is still chemically and physically accessible (Fig. 1.24).[149] The advantage of this is the attractive SERS-enhancing properties of the liquid-liquid films are translated to a solid substrate which is more robust and easier to handle.

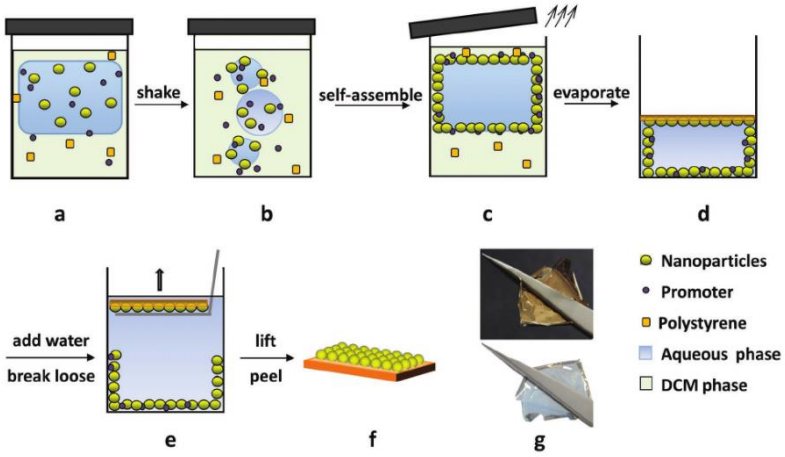

Figure 1.24: *An Illustration of the fabrication procedure for the SENS taken from the work by Xu et al. a-c) The formation and assembly of the MeLLF followed by d) the evaportation of the polymer containing organic solution. e) The film floats upon the addition of water and can then be extracted. Taken from literature.*[149]

1.5.5 Sensing Using Interfacial Films

The review by Fan *et al*. discusses the recent advances in SERS in an analytical setting and detail how interfacial films have already demonstrated widespread sensing capabilities.[150] One example, described by Cecchini *et al*. is the use polyaromatic ligand (PAL) species being used to form interfacial films that possess a SERS-responsive interaction with Hg^{2+}.[151] The complexation between the PAL and Hg^{2+} causes π-stacking interactions with the PAL-NP can be tracked through changes in the SERS response. The work presented by Mao *et al.* demonstrates the rapid on-the-spot drug detection using interfacial films.[126] The authors describe the interfacial positioning of Au nanorods at the interface between cyclohexane and water that isolate targets from both the aqueous and organic layers during film formation. The presence of the drugs ketamine, and 3,4-methylenedioxymethamphetamine (MDMA) on the surface is seen via the observation of their respective SERS fingerprints (Fig. 1.25).

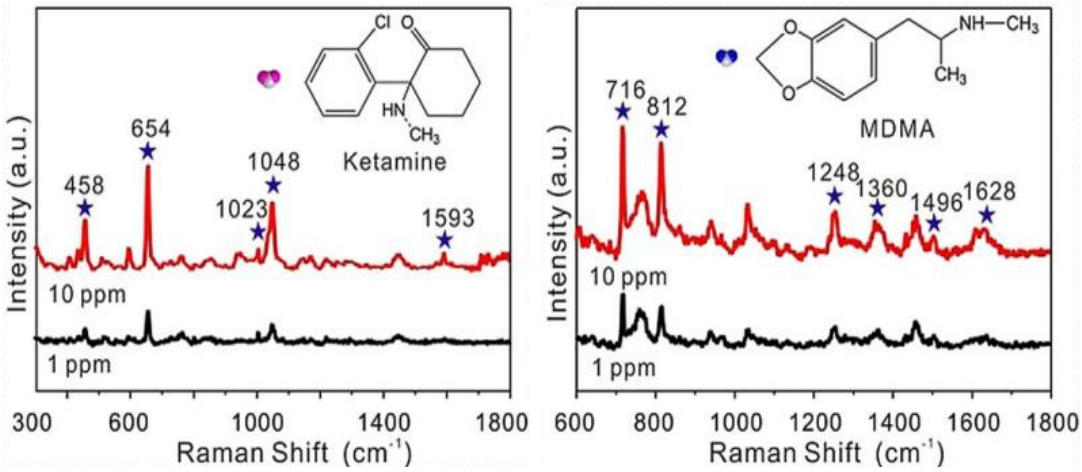

Figure 1.25: *The SERS spectra of ketamine and MDMA observed on the surface of an Au nanorod interfacial film as reported by Mao et al. Taken from literature.*[126]

A recent example is the work by Li *et al.* that describes interfacial assembly of Au nanorods, isolated onto silicon wafer for the detection of thiram in soil samples.[152] This label-free approach forms the densely packed array of nanorods add sensing is achieved by dropping the solution of containing the target species. In this case, it is the supernatant after washing soil samples contaminated with the fungicide, thiram and recognition is made through identification of the 1380 cm^{-1} peak owing to the CH_3 bending and C–N stretching (Fig. 1.26).

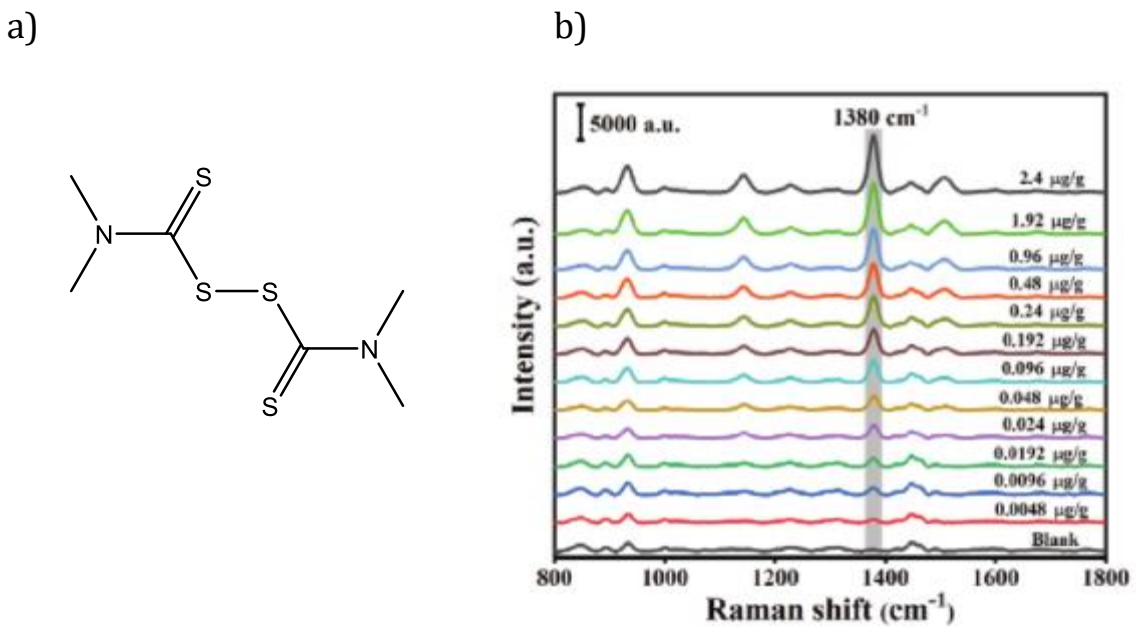

Figure 1.26: *a) The structure of the fungicide, thiram and b) the SERS spectrum of thiram at given concentrations, highlighting the peak at 1380 cm^{-1}. Taken from literature.*[152]

1.6 Rhenium-based Sensing Materials

IUPAC defines a chemical sensor to be a device that transforms chemical information, originating from a chemical reaction of an analyte into an analytically useful signal (Fig. 1.27). Furthermore, the type of device can be described by the operating principle of the transducer. The structure of a chemical sensor can be generally regarded two functional components responsible for recognition and reporting with a high degree of sensitivity and selectivity.[153] Gründler provided a contemporary reflection on the topic of chemical sensors as a whole, including the different sensing categories and potential applications that exist.[154] Fluorescent sensors are chemical devices that exhibit a change in the observed fluorescence when induced by chemical interactions occurring between the sensing species and the desired target. Recognition and monitoring of pH, anionic/cationic pollutants, explosive precursors and biologically important species through such design has been present for many years.[155]

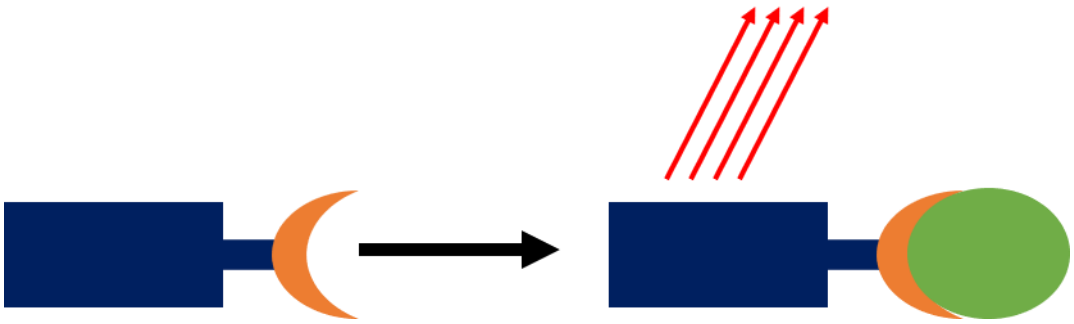

Figure 1.27: *A basic illustration of a fluorescent sensor. The binding of a target can either initiate or change the luminescent output of the sensor.*

1.6.1 Rhenium Complexes for Sensing

The structures of fluorescent chemical sensors are wide-ranging with organic macrocyclic molecules and quantum dots of different compositions all displaying responsive applications.[156-158] Luminescent organometallic rhenium complexes have been of interest for molecular recognition as they hold significant advantages including versatility and high photostability. Polypyridyl tricarbonyl rhenium(I) complexes possess long-lived excited states, attributed to metal-to-ligand charge transfer. The photophysical properties of these complexes can be tuned through ligand modification which also allows the incorporation of other functional components into the system.[159] This is highlighted by the work of K-W Lo who has reported numerous Re(I) polypyridyl complexes for biological sensing (Fig.1.28).[160] This adaptability has already proven beneficial in a biological context as tricarbonyl Re complexes have been employed as imaging probes and photoresponsive agents for photodynamic therapy.[160, 161]

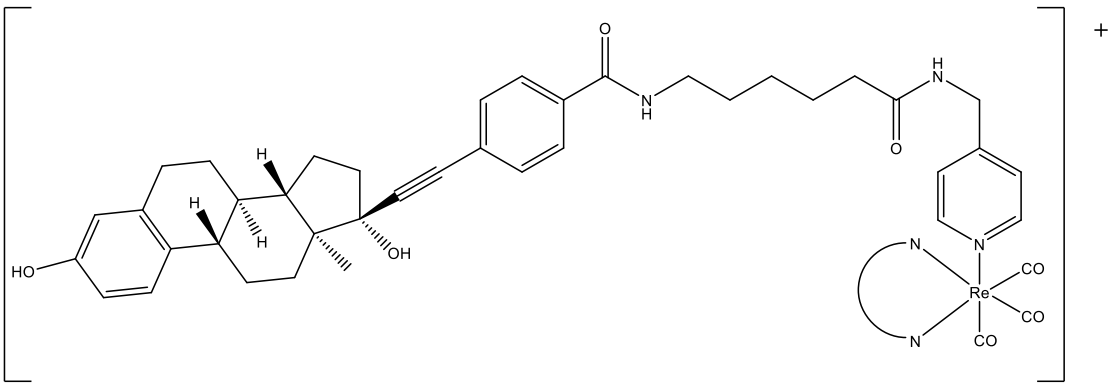

Figure 1.28: *One of the polypyridyl Re(I) complexes reported by Kenneth Kam-Wing Lo that displays luminescent changes upon binding with estrogen receptor α .*[160]

Recent reports illustrate the versatility of Re(I) complexes as tailored ligand design allows for the targeted sensing of a diverse range of molecules, reflected in the work by Gabr and Pigge.[162, 163] They describe the synthesis of numerous functionalised Re(I) complexes using tetraarylethylenes (TAE) as a molecular framework to incorporate different functionalities into the system (Fig 1.29a). One example of these TAE-functionalised Re(I) complex is tailored for a specific binding interaction with human serum albumin (HSA) which is signified by enhanced luminescence coupled with a blue shift.[162] This complex in question, contains two indole groups which have a known affinity for HSA, in the arene positions (Fig. 1.29b). Binding with HSA occurs at the indole-benzodiazepine site via the indole functionalities on the probe. They also report the synthesis of another complex, this time containing (oligo)thiophene units which are able to bind to amyloid fibrils (Fig.1.29c). Interactions between the complex and the fibrils result in significant enhancement of the observed luminescence with a red shift of the emission wavelengths from 386 to 494 nm.

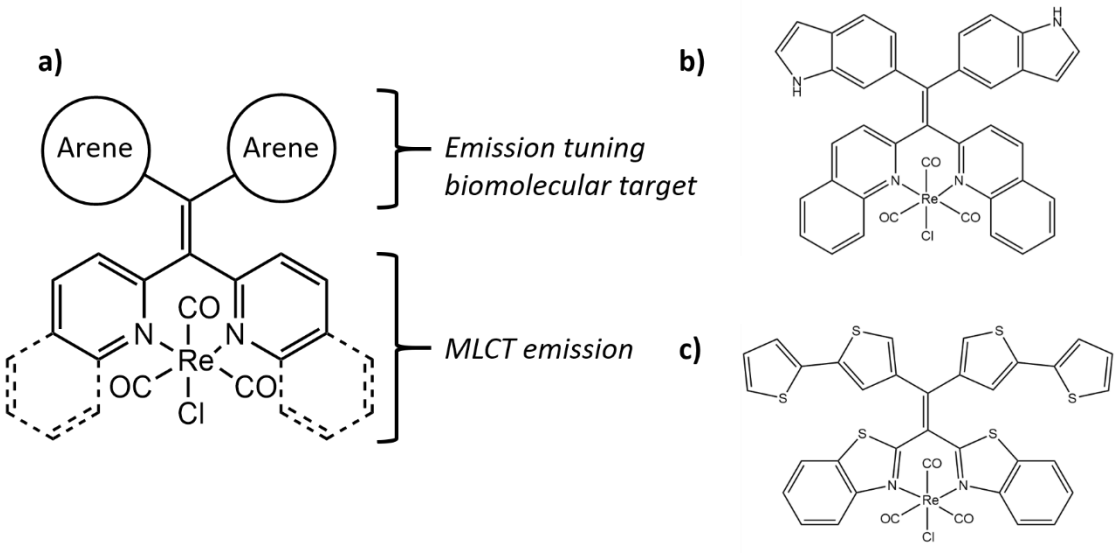

Figure 1.29: *a) The TAE-functionalised complex design that can be tailored for specific interactions. b) The indole-containing complex for HSA detection and b) the (oligo)thiophene-containing complex that binds to amyloid fibrils. Adapted from literature.*[162, 163]

Sathish *et al*. also demonstrate how ligand design can be tailored for the detection of specific targets.[164] They describe a binuclear Re(I) species that presents host-guest activity with polycyclic aromatic hydrocarbons (PAHs) (Fig. 1.30). The dinuclear complex contains napthylvinylpyridine structures that can form CH-π interactions with PAHs. The absorption and emission response of the PAH changes with continual addition of the Re(I) species. A ground state complex is formed as the two species interact and subsequent charge transfer from the electron-rich guest molecule gives enhanced absorption and fluorescence quenching.[164] Additionally, these binuclear complexes have also shown to be excellent probes for the sensing nitroaromatics and a number of different biomolecular structures.[165-168]

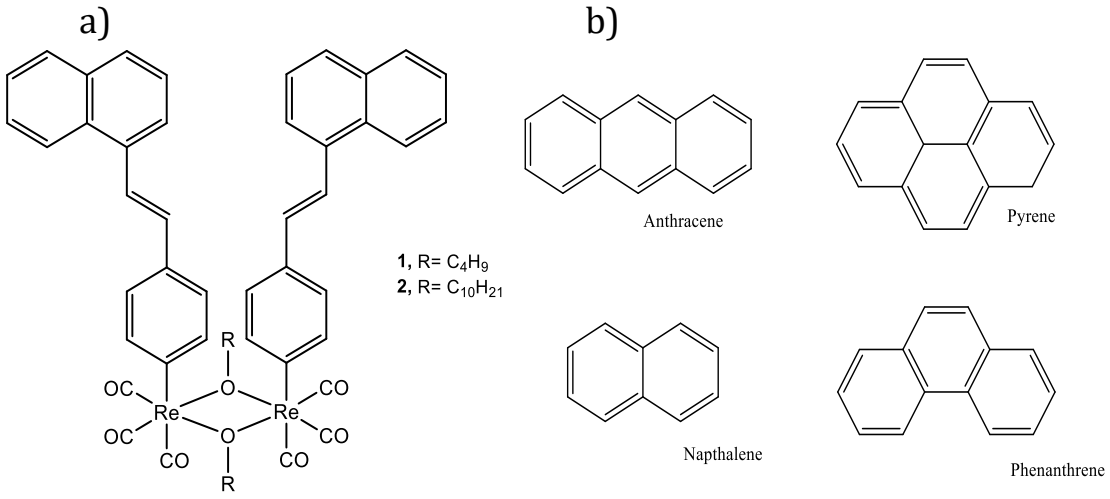

Figure 1.30: *a) The binuclear complex reported by Sathish et al. that can target b) the polycyclic aromatic hydrocarbons.*[164-168]

Functionalised Re(I) complexes are also known to display excellent levels of selectivity as highlighted by work published by Das and Rajak.[169] A bidentate ligand comprising of a Schiff base formed from anthraldehyde and aminoquinoline displays selective with the CN^- ion through a proposed interaction with the imine bond generating an adduct (Fig. 1.31). This can be observed through a ratiometric changes to both the absorption

and fluorescence responses of the complex which are not seen when screened against other anions.

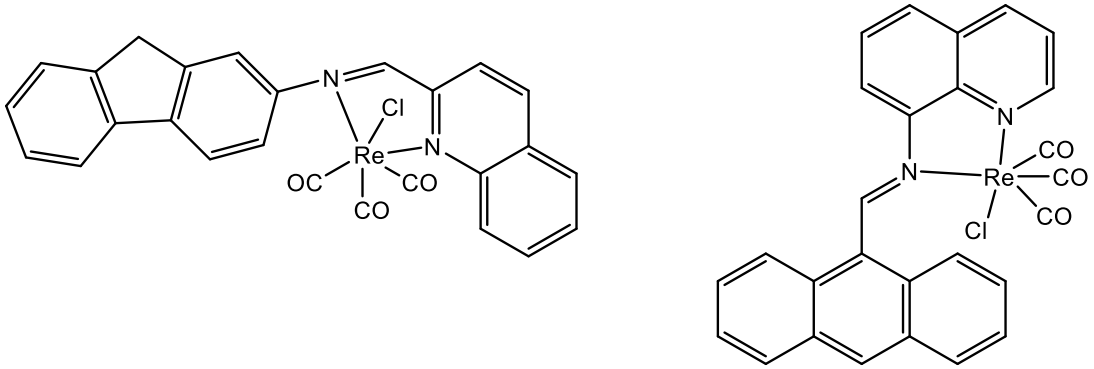

Figure 1.31: *The rhenium complexes reported by Das and Rajak that show change in both absorption and emission behaviour upon the addition of* CN^-*.*[168]

High levels of selectivity are also evident in the rhenium sensor described by Ramdass *et al.* which also involves Schiff base type ligands, this time comprising of a substituted aminophenol and bipyridine.[170] C=N isomerization controls the photophysical responses of these structures, and the introduction of Cu^{2+} into the system inhibits this isomerisation resulting in an observed enhancement of the luminescence (Fig. 1.32). The presence of other metallic cations induced relatively little or no optical response to the complex.

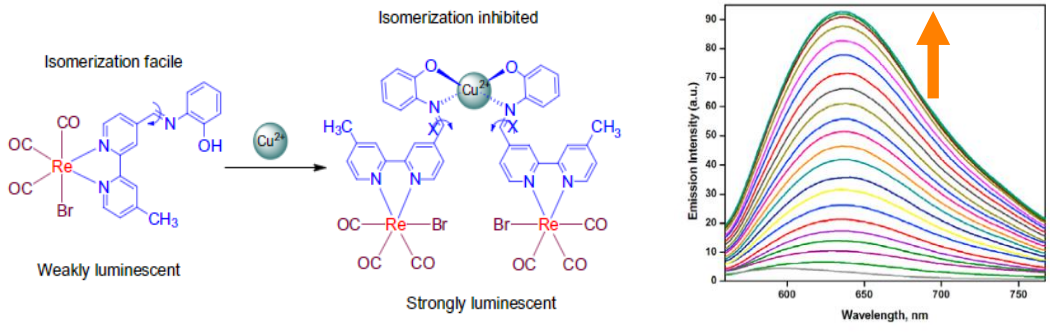

Figure 1.32: *The proposed mechanism of* Cu^{2+} *binding presented by Ramdass et al. and the ratiometric response luminescent response induced by increasing concentrations of* Cu^{2+}*. Taken from literature.*[170]

1.6.2 Composite Rhenium Sensing Materials

There have also been attempts to incorporate rhenium complexes with solid supports for the generation of hybrid sensing materials. The work by Zhang *et al.* describe how silica substrates doped with polypyridyl Re(I) complexes display a fluorescence quenching response when in the presence of oxygen.[171-173] More recently, Re complexes functionalised with aminophenanthroline have been incorporated into polymers which in turn, display a ratiometric response to the presence of O_2 (Fig. 1.33).[174]

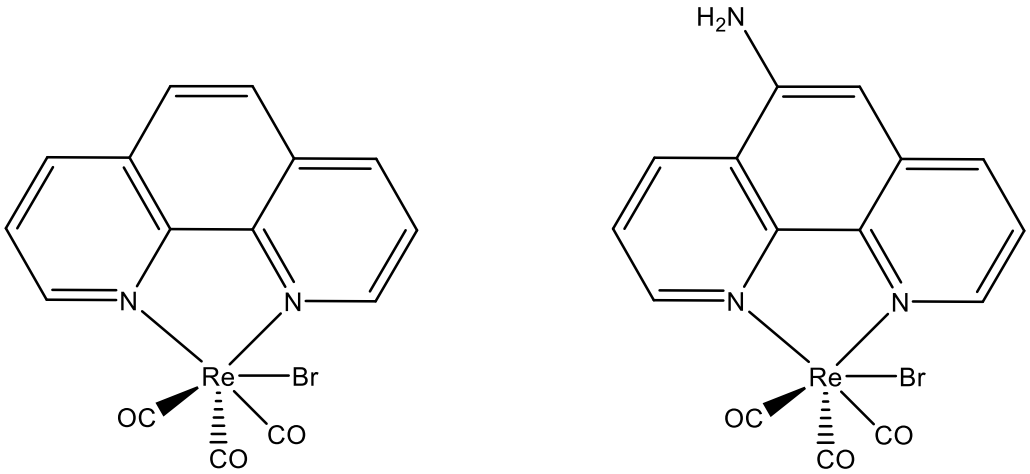

Figure 1.33: *The Re(I) complexes functionalised with phenanthroline and aminophenanthroline used for ratiometric oxygen sensing.*[174]

The use of rhenium complexes for emissive sensing purposes has been well reported yet their use in SERS related devices remains limited. Rhenium-functionalised noble metal nanoparticles have been reported however more work has been conducted with other transition metal complexes. The recent review by Quintana, Cifuentes and Humphrey gives an excellent account of the wider picture on transition metal nanoparticle hybrids.[175] The extensive research that currently exists, focuses on other metal centres, particularly ruthenium and iron complexes.[175] Nonetheless, the synthesis of Re-functionalised NMNPs has been reported using differing approaches. Pérez-Mirabet *et al.* describe the complexation of Re centres with the stabilising monolayer

of mercaptopropionic acid situated on the surface of both silver and gold nanoparticles.[176] Hallet *et al.* also describe the synthesis of luminescent gold nanoparticles that use a pyridyl thioesters to bind to rhenium centres to a the NP surface.[177] Additionally, the group led by Yam have detailed the use of lipoic tails as a means to binding tricarbonyl Re complexes to the surface of noble metal nanoparticles (Fig. 1.34).[178] Interestingly, the reported hybrid nanoparticles display a luminescent response to presence of esterase in solution that is prompted by the cleavage of the Re(I) complexes by the enzyme.

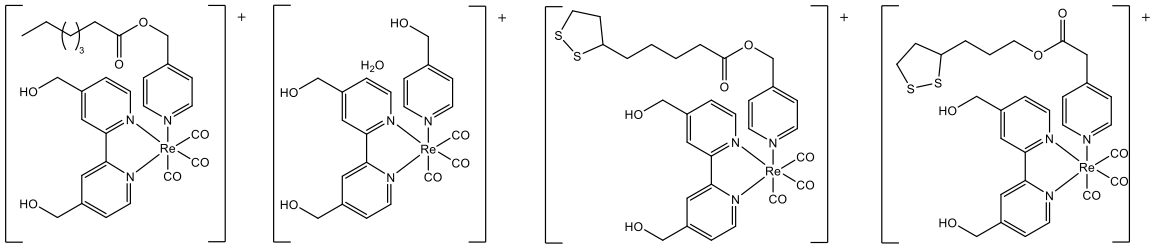

Figure 1.34: *The complexes that display a switching on of fluorescence caused by esterase cleavage of the rhenium centre from the nanoparticle.*[178]

Vlčková *et al.* reported the SERS response of polypyridyl tricarbonyl rhenium complexes in the early nineties and presented early ideas on the binding interaction between Re(I) metal complexes and nanoparticles.[179] Previous work by members of the Fletcher group have investigated the SERS response of rhenium complexes bound to AgNPs through a lipoic-bipyridyl ligands (Fig. 1.35). They concluded that the presence of the rhenium centre acts as a sensitizer and therefore contributing additional enhancement through a SERRS response.[180] Additionally, they conclude that the SERRS response is affected by the orientation of the complex relative to the surface, evidenced by prominent intensities attributed to the complex, changing with concentration.

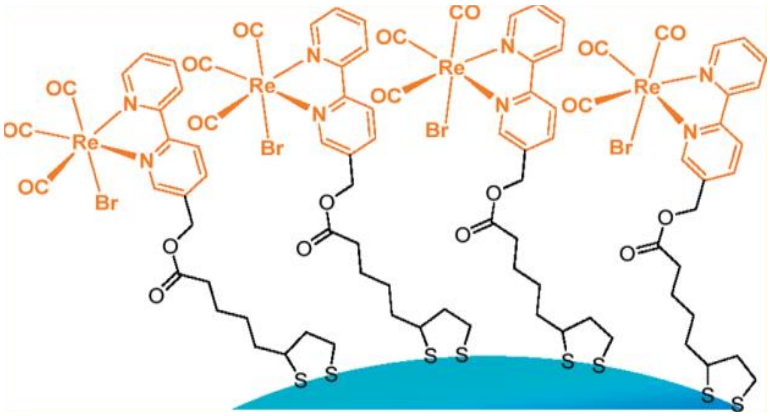

Figure 1.35: *An illustration featured in the work by Montgomery et al. demonstrating the position of their reported rhenium complex on the surface of a nanoparticle. Taken from literature .*[180]

The vibrational stretch attributed to the Re-carbonyl vibration is particularly useful in the work by Lin *et al.* who have developed a silica-coated gold nanorod system labelled with a Re complex.[181] The system possesses selective detection capabilities for tumour-related DNA by chelating Re functionalised nanorods through target-specific interactions. The authors report that this chelation interaction can be monitored with the measuring of signal intensity of the peak corresponding to the metal-centred carbonyls at 2113 cm^{-1}. This response is only generated when the label and the target are complimentary, demonstrating selectivity. This presents evidence that Re-functionalised nanoparticle hybrids have potential applications as SERS diagnostic and sensing tools.

1.7 Aims and Objectives

Currently, SERS sensing devices exist that detect wide ranging analytes from disease biomarkers to environmental pollutants. They demonstrate the huge potential that SERS holds. There has also been a movement towards generating highly ordered SERS substrates to improve the reproducibility and enhancement abilities. However, unlike the NP systems, most larger substrates rely on label-free sensing as the incorporation of a sensing species is difficult, often involving additional experimental steps. Composite materials such as NP-polymer systems are restricted by either size constraints or simply because other species bound to the nanoparticle surface are necessary for substrate fabrication. Films derived from the interfacial positioning of nanoparticles are formed through the manipulation of either the hydrophobicity or screening of surface charge. Such films offer a potential pathway for the development of functionalised SERS-active films so long as the surface species satisfies the requirements of interfacial positioning.

The sensing abilities of luminescent rhenium-centred organometallics using fluorescent responses are well known, however their application as SERS sensors has yet to be realised. There are examples that exist where such complexes have been adsorbed to a noble metal surface. The implication is that Re-NMNP hybrids for SERS sensing are within the realm of possibility. The use of such complexes may also generate greater enhancement via SERRS-based contributions. Additionally, rhenium complexes may also possess the ability to position nanoparticles at a liquid-liquid interface. This means that highly ordered, reproducible films that offer sensitive and selective sensing activity could be realised.

To this end, it is expected that tricarbonyl Re(I) complexes that possess specific analyte interactions via the chelation of tailored ligands can be bound to the surface of noble metal nanoparticles. Furthermore, the interfacial positioning of the complex-NP hybrid can be encouraged, allowing for the formation of metal liquid-like films and subsequent derivatives. It is hoped that once formed, these films will enable the molecular recognition of the individual rhenium complex to be observed through changes to the SERS fingerprint. Moreover, the possible high enhancement capabilities of SERS platforms allow for single molecular sensing and the detection of molecules of biological importance. The overall result being the realisation of a modular approach, where luminescent Re(I) complexes can be tailored for targeted interactions and then employed for the labelling of a SERS-active substrate, thus creating a Re(I)-functionalised SERS sensor (Fig. 1.36).

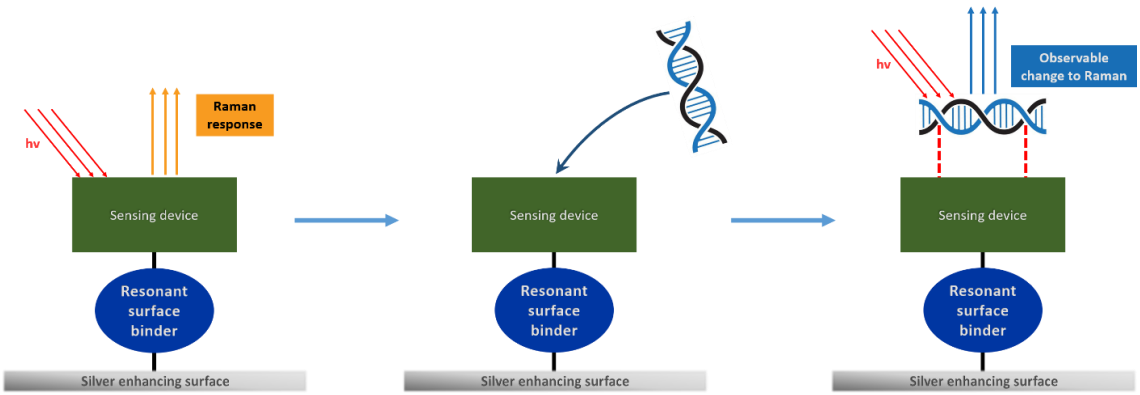

Figure 1.36: *A schematic diagram of the proposed design and use of a Re(I)-labelled SERS-active substrate for the detection of a specific analyte*

1.8 References

1. S. E. Clarke and J. R. Foster, *Br. J. Biomed. Sci.*, 2012, **69**, 83-93.
2. W. Li, W. X. Luo, M. Y. Li, L. Y. Chen, L. Y. Chen, H. Guan and M. J. Yu, *Front. Chem.*, 2021, **9**.
3. S. Abdul, T. Judit, F. Ilona and M. Nikoletta, in *Fundamentals of Nanoparticles*, eds. A. Barhoum and A. S. Hamdy Makhlouf, Elsevier, 2018, pp. 485-519.
4. Y. Y. Broza, X. Zhou, M. Yuan, D. Qu, Y. Zheng, R. Vishinkin, M. Khatib, W. Wu and H. Haick, *Chem. Rev.*, 2019, **119**, 11761-11817.
5. R. Liu, Z. Y. Li, Z. L. Huang, K. Li and Y. Lv, *Trac-Trends Anal. Chem.*, 2019, **118**, 123-137.
6. H. Sohrabi, A. Hemmati, M. R. Majidi, S. Eyvazi, A. Jahanban-Esfahlan, B. Baradaran, R. Adlpour-Azar, A. Mokhtarzadeh and M. de la Guardia, *TrAC, Trends Anal. Chem.*, 2021, **143**, 116344.
7. R. Shi, X. Liu and Y. Ying, *J. Agric. Food. Chem.*, 2018, **66**, 6525-6543.
8. H. J. Montgomery, PhD, Queen's University Belfast, 2011.
9. J. Langer, D. Jimenez de Aberasturi, J. Aizpurua, R. A. Alvarez-Puebla, B. Auguié, J. J. Baumberg, G. C. Bazan, S. E. J. Bell, A. Boisen, A. G. Brolo, J. Choo, D. Cialla-May, V. Deckert, L. Fabris, K. Faulds, F. J. García de Abajo, R. Goodacre, D. Graham, A. J. Haes, C. L. Haynes, C. Huck, T. Itoh, M. Käll, J. Kneipp, N. A. Kotov, H. Kuang, E. C. Le Ru, H. K. Lee, J.-F. Li, X. Y. Ling, S. A. Maier, T. Mayerhöfer, M. Moskovits, K. Murakoshi, J.-M. Nam, S. Nie, Y. Ozaki, I. Pastoriza-Santos, J. Perez-Juste, J. Popp, A. Pucci, S. Reich, B. Ren, G. C. Schatz, T. Shegai, S. Schlücker, L.-L. Tay, K. G. Thomas, Z.-Q. Tian, R. P. Van Duyne, T. Vo-Dinh, Y. Wang, K. A. Willets, C. Xu, H. Xu, Y. Xu, Y. S. Yamamoto, B. Zhao and L. M. Liz-Marzán, *ACS Nano*, 2020, **14**, 28-117.
10. P. W. Atkins, J. De Paula and J. Keeler, *Atkins' Physical Chemistry*, Oxford University Press, 2018.
11. A. P. de Silva, H. Q. N. Gunaratne, T. Gunnlaugsson, A. J. M. Huxley, C. P. McCoy, J. T. Rademacher and T. E. Rice, *Chem. Rev.*, 1997, **97**, 1515-1566.
12. A. P. Demchenko, *Introduction to Fluorescence Sensing*, Springer Science & Business Media, 2008.
13. Z. Guo, S. Park, J. Yoon and I. Shin, *Chem. Soc. Rev.*, 2014, **43**, 16-29.
14. H. N. Kim, W. X. Ren, J. S. Kim and J. Yoon, *Chem. Soc. Rev.*, 2012, **41**, 3210-3244.
15. X. Sun, Y. Wang and Y. Lei, *Chem. Soc. Rev.*, 2015, **44**, 8019-8061.
16. J. R. Ferraro, *Introductory Raman Spectroscopy*, Elsevier, 2003.
17. E. Smith and G. Dent, *Modern Raman Spectroscopy: A Practical Approach*, John Wiley & Sons, 2019.
18. R. J. H. Clark and T. J. Dines, *Angew. Chem. Int. Ed.*, 1986, **25**, 131-158.
19. R. R. Crichton and R. O. Louro, in *Practical Approaches to Biological Inorganic Chemistry*, eds. R. R. Crichton and R. O. Louro, Elsevier, Oxford, 2013, pp. 161-177.
20. M. Fleischmann, P. J. Hendra and A. J. McQuillan, *J. Chem. Soc., Chem. Commun.*, 1973, 80-81.
21. D. L. Jeanmaire and R. P. Van Duyne, *J. Electroanal. Chem. Interfacial. Electrochem.*, 1977, **84**, 1-20.
22. M. G. Albrecht and J. A. Creighton, *J. Am. Chem. Soc.*, 1977, **99**, 5215-5217.
23. M. Moskovits, *Rev. Mod. Phys.*, 1985, **57**, 783-826.
24. L. Jensen, C. M. Aikens and G. C. Schatz, *Chem. Soc. Rev.*, 2008, **37**, 1061-1073.
25. J. R. Lombardi and R. L. Birke, *J. Phys. Chem. C*, 2008, **112**, 5605-5617.
26. P. G. Etchegoin and E. Le Ru, *Phys. Chem. Chem. Phys.*, 2008, **10**, 6079-6089.
27. E. C. Le Ru and P. G. Etchegoin, *Principles of Surface-Enhanced Raman Spectroscopy : and Related Plasmonic Effects*, Elsevier, Amsterdam ; Boston, 1st edn., 2009.

28. S.-Y. Ding, E.-M. You, Z.-Q. Tian and M. Moskovits, *Chem. Soc. Rev.*, 2017, **46**, 4042-4076.
29. R. Pilot, R. Signorini and L. Fabris, in *Metal Nanoparticles and Clusters: Advances in Synthesis, Properties and Applications*, ed. F. L. Deepak, Springer International Publishing, Cham, 2018, pp. 89-164.
30. K. Kneipp, *J. Phys. Chem. C*, 2016, **120**, 21076-21081.
31. X. Ling, L. Xie, Y. Fang, H. Xu, H. Zhang, J. Kong, M. S. Dresselhaus, J. Zhang and Z. Liu, *Nano Lett.*, 2010, **10**, 553-561.
32. S. M. Morton, E. Ewusi-Annan and L. Jensen, *Phys. Chem. Chem. Phys.*, 2009, **11**, 7424-7429.
33. S. M. Morton and L. Jensen, *J. Am. Chem. Soc.*, 2009, **131**, 4090-4098.
34. A. C. Albrecht, *J. Chem. Phys.*, 1961, **34**, 1476-1484.
35. J. A. Creighton, *Surf. Sci.*, 1983, **124**, 209-219.
36. A. A. Stacy and R. P. Van Duyne, *Chem. Phys. Lett.*, 1983, **102**, 365-370.
37. P. Hildebrandt and M. Stockburger, *J. Phys. Chem.*, 1984, **88**, 5935-5944.
38. G. McNay, D. Eustace, W. E. Smith, K. Faulds and D. Graham, *Appl. Spectrosc.*, 2011, **65**, 825-837.
39. Y. Kitahama and Y. Ozaki, *Analyst*, 2016, **141**, 5020-5036.
40. R. P. Feynman, *California Institute of Technology, Engineering and Science magazine*, 1960.
41. K. E. Drexler, *Proc. Nat. Acad. Sc.*, 1981, **78**, 5275-5278.
42. N. Taniguchi, *Proc. ICPE*, 1974.
43. P. Iqbal, J. A. Preece and P. M. Mendes, *Supramolecular Chemistry: From Molecules to nanomaterials*, 2012.
44. L. Marks and L. Peng, *J. Phys.: Condens. Matter*, 2016, **28**, 053001.
45. M. Benelmekki, in *Designing Hybrid Nanoparticles*, Morgan & Claypool Publishers, 2015.
46. W. Niu, Y. A. A. Chua, W. Zhang, H. Huang and X. Lu, *J. Am. Chem. Soc.*, 2015, **137**, 10460-10463.
47. R. E. Darienzo, O. Chen, M. Sullivan, T. Mironava and R. Tannenbaum, *Mater. Chem. Phys.*, 2020, **240**, 122143.
48. A.-M. Hada, M. Potara, S. Suarasan, A. Vulpoi, T. Nagy-Simon, E. Licarete and S. Astilean, *Nanotechnology*, 2019, **30**, 315701.
49. N. T. K. Thanh, N. Maclean and S. Mahiddine, *Chem. Rev.*, 2014, **114**, 7610-7630.
50. V. K. L. Mer, *Ind. Eng. Chem. Res.*, 1952, **44**, 1270-1277.
51. R. Becker and W. Döring, *Annalen der Physik*, 1935, **416**, 719-752.
52. J. Polte, *CrystEngComm*, 2015, **17**, 6809-6830.
53. M. A. Watzky and R. G. Finke, *Chem. Mater.*, 1997, **9**, 3083-3095.
54. W. Ostwald, *Z. Phys. Chem.*, 1900, **34**, 495-503.
55. E. E. Finney and R. G. Finke, *J. Colloid Interface Sci.*, 2008, **317**, 351-374.
56. K. Holmberg, D. O. Shah and M. J. Schwuger, *Handbook of Applied Surface and Colloid Chemistry*, John Wiley & Sons, 2002.
57. P. Lee and D. Meisel, *J. Phys. Chem.*, 1982, **86**, 3391-3395.
58. J. Turkevich, P. C. Stevenson and J. Hillier, *Discuss. Faraday Soc.*, 1951, **11**, 55-75.
59. T. K. Sau and A. L. Rogach, *Adv. Mater.*, 2010, **22**, 1781-1804.
60. Y. Qin, X. Ji, J. Jing, H. Liu, H. Wu and W. Yang, *Colloids. Surf. A. Physicochem. Eng. Asp.*, 2010, **372**, 172-176.
61. Z. Khan, T. Singh, J. I. Hussain and A. A. Hashmi, *Colloids. Surf. B. Biointerfaces.*, 2013, **104**, 11-17.
62. H. Häkkinen, *Nat. Chem.*, 2012, **4**, 443-455.
63. M. Brust, M. Walker, D. Bethell, D. J. Schiffrin and R. Whyman, *J. Chem. Soc., Chem. Commun.*, 1994, 801-802.
64. T. Kunoh, M. Takeda, S. Matsumoto, I. Suzuki, M. Takano, H. Kunoh and J. Takada, *ACS Sustain. Chem. Eng.*, 2018, **6**, 364-373.

65. N. Leopold, V. Chiş, N. E. Mircescu, O. T. Marişca, O. M. Buja, L. F. Leopold, C. Socaciu, C. Braicu, A. Irimie and I. Berindan-Neagoe, *Colloids. Surf. A. Physicochem. Eng. Asp.*, 2013, **436**, 133-138.
66. Y. X. Zhang, S. H. Wen, L. Z. Zhao, D. Li, C. C. Liu, W. B. Jiang, X. Gao, W. T. Gu, N. Ma, J. H. Zhao, X. Y. Shi and Q. H. Zhao, *Nanoscale*, 2016, **8**, 5567-5577.
67. A. Silvestri, L. Polito, G. Bellani, V. Zambelli, R. P. Jumde, R. Psaro and C. Evangelisti, *J. Colloid Interface Sci.*, 2015, **439**, 28-33.
68. L. K. Lin, A. Uzunoglu and L. A. Stanciu, *Small*, 2018, **14**, 1702828.
69. K. Yang, L. Pan, L. Gong, Q. Liu, Z. Li, L. Wu and Y. He, *Microchim. Acta*, 2018, **185**, 95.
70. S. Al Shehab, R. El Kurdi and D. Patra, *Microchem. J.*, 2020, **153**, 104382.
71. S. Y. Lin, Y. T. Tsai, C. C. Chen, C. M. Lin and C. H. Chen, *J. Phys. Chem. B*, 2004, **108**, 2134-2139.
72. M. Rahimi, E. B. Noruzi, E. Sheykhsaran, B. Ebadi, Z. Kariminezhad, M. Molaparast, M. G. Mehrabani, B. Mehramouz, M. Yousefi, R. Ahmadi, B. Yousefi, K. Ganbarov, F. S. Kamounah, V. Shafiei-Irannejad and H. S. Kafil, *Carbohydr. Polym.*, 2020, **231**.
73. F. Laghrib, M. Bakasse, S. Lahrich and M. A. El Mhammedi, *Mater. Sci. Eng. C*, 2020, **107**.
74. Z. B. Shifrina, V. G. Matveeva and L. M. Bronstein, *Chem. Rev.*, 2020, **120**, 1350-1396.
75. M. Aslam, L. Fu, M. Su, K. Vijayamohanan and V. P. Dravid, *J. Mater. Chem.*, 2004, **14**, 1795-1797.
76. M. Chen, Y.-G. Feng, X. Wang, T.-C. Li, J.-Y. Zhang and D.-J. Qian, *Langmuir*, 2007, **23**, 5296-5304.
77. Z. Bao and C. Q. Lan, *Colloids. Surf. B. Biointerfaces.*, 2019, **184**, 110519.
78. X.-S. Zheng, I. J. Jahn, K. Weber, D. Cialla-May and J. Popp, *Spectrochim. Acta, Part A*, 2018, **197**, 56-77.
79. S. Schlücker, *ChemPhysChem*, 2009, **10**, 1344-1354.
80. H. Li, X. Wang, Z. Wang, J. Jiang, Y. Qiao, M. Wei, Y. Yan and C. Li, *New J. Chem.*, 2017, **41**, 14342-14350.
81. S. Weng, W. Zhu, P. Li, H. Yuan, X. Zhang, L. Zheng, J. Zhao, L. Huang and P. Han, *Food Chem.*, 2020, **310**, 125855.
82. Y. Zhao, Y. Yamaguchi, Y. Ni, M. Li and X. Dou, *Spectrochim. Acta, Part A*, 2020, **233**, 118193.
83. Y. Wu, L. Yang and Q. Wang, *ChemistryOpen*, 2017, **6**, 201-205.
84. Q. Zou, X. Li, T. Xue, S. Mo, Q. Su and J. Zheng, *Anal. Sci.*, 2019, **35**, 493-498.
85. Z. Duan, X. Zhang, T. Ye, X. Zhang, S. Dong, J. Liu, X. Xiao and C. Jiang, *ACS Appl. Mater. Interfaces.*, 2018, **10**, 25737-25743.
86. Y. Wu, T. Jiang, Z. Wu and R. Yu, *Biosens. Bioelectron.*, 2018, **99**, 646-652.
87. M. Liu, Z. Wang, S. Zong, H. Chen, D. Zhu, L. Wu, G. Hu and Y. Cui, *ACS Appl. Mater. Interfaces.*, 2014, **6**, 7371-7379.
88. K. Yang, Y. Hu, N. Dong, G. Zhu, T. Zhu and N. Jiang, *Biosens. Bioelectron.*, 2017, **94**, 286-291.
89. H. Akiyama, K. Ikeda, H. Kondo and P. L. McGeer, *Neuroscience Letters*, 1992, **146**, 152-154.
90. P. Grammas, P. G. Samany and L. Thirumangalakudi, *J. Alzheimer's Dis.*, 2006, **9**, 51-58.
91. N. J. Jiang, T. F. Zhu and Y. J. Hu, *Microchim. Acta*, 2019, **186**, 8.
92. P. Nordlander, C. Oubre, E. Prodan, K. Li and M. Stockman, *Nano Lett.*, 2004, **4**, 899-903.
93. K. L. Wustholz, A.-I. Henry, J. M. McMahon, R. G. Freeman, N. Valley, M. E. Piotti, M. J. Natan, G. C. Schatz and R. P. Van Duyne, *J. Am. Chem. Soc.*, 2010, **132**, 10903-10910.
94. S. L. Kleinman, R. R. Frontiera, A.-I. Henry, J. A. Dieringer and R. P. Van Duyne, *Phys. Chem. Chem. Phys.*, 2013, **15**, 21-36.

95. K. Kneipp, Y. Wang, H. Kneipp, L. T. Perelman, I. Itzkan, R. R. Dasari and M. S. Feld, *Phys. Rev. Lett.*, 1997, **78**, 1667-1670.
96. S. Nie and S. R. Emory, *Science*, 1997, **275**, 1102.
97. A. M. Michaels, M. Nirmal and L. Brus, *J. Am. Chem. Soc.*, 1999, **121**, 9932-9939.
98. S. Kasani, K. Curtin and N. Wu, 2019, **8**, 2065.
99. P. Zheng, S. K. Cushing, S. Suri and N. Wu, *Phys. Chem. Chem. Phys.*, 2015, **17**, 21211-21219.
100. M. Jung, J.-H. Kim and Y.-W. Choi, *J, Nanomater.*, 2018, **2018**.
101. T. Wang, J. Zhang, P. Xue, H. Chen, S. Ye, S. Wang, Y. Yu and B. Yang, *J. Mater. Chem. C. Mater.*, 2014, **2**, 2333-2340.
102. F. A. Rahim and K. Dong-Hwan, *Nano Today*, 2016, **11**, 415-434.
103. W. B. Sheng, W. Li, D. M. Tan, P. P. Zhang, E. Zhang, E. Sheremet, B. Schmidt, X. L. Feng, R. D. Rodriguez, R. Jordan and I. Amin, *ACS Appl. Mater. Interfaces.*, 2020, **12**, 9797-9805.
104. S. Karagoz, N. B. Kiremitler, M. Sakir, S. Salem, M. S. Onses, E. Sahmetlioglu, A. Ceylon and E. Yilmaz, *Ecotoxicol. Environ. Saf.*, 2020, **188**.
105. A. Mills, G. Hill, M. Stewart, D. Graham, W. E. Smith, S. Hodgen, P. J. Halfpenny, K. Faulds and P. Robertson, *Appl. Spectrosc.*, 2004, **58**, 922-928.
106. X. H. Li, G. Y. Chen, L. B. Yang, Z. Jin and J. H. Liu, *Adv. Funct. Mater.*, 2010, **20**, 2815-2824.
107. J. C. Hulteen and R. P. V. Duyne, *J. Vac. Sci. Technol. A*, 1995, **13**, 1553-1558.
108. C. L. Haynes and R. P. Van Duyne, *J. Phys. Chem. B*, 2001, **105**, 5599-5611.
109. Y. M. Sabri, A. E. Kandjani, S. J. Ippolito and S. K. Bhargava, *ACS Appl. Mater. Interfaces.*, 2015, **7**, 1491-1499.
110. P. Makam, R. Shilpa, A. E. Kandjani, S. R. Periasamy, Y. M. Sabri, C. Madhu, S. K. Bhargava and T. Govindaraju, *Biosens. Bioelectron.*, 2018, **100**, 556-564.
111. H. Lai, F. Xu, Y. Zhang and L. Wang, *J. Mater. Chem. B. Mater.*, 2018, **6**, 4008-4028.
112. W. Xu, N. Mao and J. Zhang, *Small*, 2013, **9**, 1206-1224.
113. L. Xie, X. Ling, Y. Fang, J. Zhang and Z. Liu, *J. Am. Chem. Soc.*, 2009, **131**, 9890-9891.
114. W. Fan, Y. H. Lee, S. Pedireddy, Q. Zhang, T. Liu and X. Y. Ling, *Nanoscale*, 2014, **6**, 4843-4851.
115. J. Quan, J. Zhang, J. Li, X. Zhang, M. Wang, N. Wang and Y. Zhu, *Carbon*, 2019, **147**, 105-111.
116. C.-Y. Zhang, B.-C. Zhao, R. Hao, Z. Wang, Y.-W. Hao, B. Zhao and Y.-Q. Liu, *J. Hazard. Mater.*, 2020, **385**, 121510.
117. X. Wang, Q. Xu, X. Hu, F. Han and C. Zhu, *Spectrochim. Acta, Part A*, 2020, **228**, 117783.
118. B. Yang, S. Jin, S. Guo, Y. Park, L. Chen, B. Zhao and Y. M. Jung, *ACS Omega*, 2019, **4**, 20101-20108.
119. X. X. Han, W. Ji, B. Zhao and Y. Ozaki, *Nanoscale*, 2017, **9**, 4847-4861.
120. M. Yilmaz, E. Babur, M. Ozdemir, R. L. Gieseking, Y. Dede, U. Tamer, G. C. Schatz, A. Facchetti, H. Usta and G. Demirel, *Nat. Mater.*, 2017, **16**, 918.
121. H. Hu, S. Wang, X. Feng, M. Pauly, G. Decher and Y. Long, *Chem. Soc. Rev.*, 2020, **49**, 509-553.
122. W. Li, X. Zhao, Z. Yi, A. M. Glushenkov and L. Kong, *Anal. Chim. Acta*, 2017, **984**, 19-41.
123. B. H. Nguyen, V. H. Nguyen and H. N. Tran, *Adv. Nat. Sci.: Nanosci. Nanotechnol.*, 2016, **7**, 033001.
124. J. Chen, L. Guo, B. Qiu, Z. Lin and T. Wang, *Mater. Chem. Front.*, 2018, **2**, 835-860.
125. N. Yang, T. You, Y. Gao, S. Lu and P. Yin, *Langmuir*, 2019, **35**, 4626-4633.
126. M. Mao, B. Zhou, X. Tang, C. Chen, M. Ge, P. Li, X. Huang, L. Yang and J. Liu, *Chem. Eur. J.*, 2018, **24**, 4094-4102.

127. M. Prusková, V. Sutrová, M. Šlouf, B. Vlčková, J. Vohlídal and I. Šloufová, *Langmuir*, 2017, **33**, 4146-4156.
128. D. Caprara, F. Ripanti, A. Capocefalo, A. Sarra, F. Brasili, C. Petrillo, C. Fasolato and P. Postorino, *Colloids. Surf. A. Physicochem. Eng. Asp.*, 2020, **589**, 124399.
129. Y. Li, Z. Liu, G. Yu, W. Jiang and C. Mao, *J. Am. Chem. Soc.*, 2015, **137**, 4320-4323.
130. J. A. Lloyd, Y. Liu, S. H. Ng, T. Thai, D. E. Gómez, A. Widmer-Cooper and U. Bach, *Nanoscale*, 2019, **11**, 22841-22848.
131. C. Li, S. Li, A. Qu, H. Kuang, L. Xu and C. Xu, *Adv. Funct. Mater.*, 2020, **30**, 2001451
132. S. Levine, B. D. Bowen and S. J. Partridge, *Colloids Surf.*, 1989, **38**, 325-343.
133. B. P. Binks and S. O. Lumsdon, *Langmuir*, 2000, **16**, 8622-8631.
134. Y. Lin, H. Skaff, T. Emrick, A. D. Dinsmore and T. P. Russell, *Science*, 2003, **299**, 226.
135. P. Pieranski, *Phys. Rev. Lett.*, 1980, **45**, 569-572.
136. R. Aveyard, J. H. Clint, D. Nees and V. N. Paunov, *Langmuir*, 2000, **16**, 1969-1979.
137. F. Reincke, W. K. Kegel, H. Zhang, M. Nolte, D. Wang, D. Vanmaekelbergh and H. Möhwald, *Phys. Chem. Chem. Phys.*, 2006, **8**, 3828-3835.
138. D. Yogev and S. Efrima, *J. Phys. Chem.*, 1988, **92**, 5754-5760.
139. K. C. Gordon, J. J. McGarvey and K. P. Taylor, *J. Phys. Chem.*, 1989, **93**, 6814-6817.
140. B. Vlckova, S. M. Barnett, T. Kanigan and I. S. Butler, *Langmuir*, 1993, **9**, 3234-3238.
141. S. E. J. Bell, J. J. McGarvey, S. J. Rigby and D. G. Walmsley, *J. Raman Spectrosc.*, 1991, **22**, 763-769.
142. H. Duan, D. Wang, D. G. Kurth and H. Möhwald, *Angew. Chem. Int. Ed.*, 2004, **43**, 5639-5642.
143. M. P. Cecchini, V. A. Turek, J. Paget, A. A. Kornyshev and J. B. Edel, *Nat. Mater.*, 2013, **12**, 165-171.
144. F. Reincke, S. G. Hickey, W. K. Kegel and D. Vanmaekelbergh, *Angew. Chem. Int. Ed.*, 2004, **43**, 458-462.
145. P.-P. Fang, S. Chen, H. Deng, M. D. Scanlon, F. Gumy, H. J. Lee, D. Momotenko, V. Amstutz, F. Cortés-Salazar, C. M. Pereira, Z. Yang and H. H. Girault, *ACS Nano*, 2013, **7**, 9241-9248.
146. V. A. Turek, L. N. Elliott, A. I. Tyler, A. Demetriadou, J. Paget, M. P. Cecchini, A. R. Kucernak, A. A. Kornyshev and J. B. Edel, *ACS Nano*, 2013, **7**, 8753-8759.
147. B. Su, J.-P. Abid, D. J. Fermín, H. H. Girault, H. Hoffmannová, P. Krtil and Z. Samec, *J. Am. Chem. Soc.*, 2004, **126**, 915-919.
148. Y. Xu, M. P. Konrad, W. W. Y. Lee, Z. Ye and S. E. J. Bell, *Nano Lett.*, 2016, **16**, 5255-5260.
149. Y. Xu, M. P. Konrad, J. L. Trotter, C. P. McCoy and S. E. J. Bell, *Small*, 2017, **13**, 1602163.
150. M. Fan, G. F. S. Andrade and A. G. Brolo, *Anal. Chim. Acta*, 2020, **1097**, 1-29.
151. M. P. Cecchini, V. A. Turek, A. Demetriadou, G. Britovsek, T. Welton, A. A. Kornyshev, J. D. Wilton-Ely and J. B. Edel, *Adv. Opt. Mater.*, 2014, **2**, 966-977.
152. X. Li, X. Lin, S. Lin, S. Zhou, G. Fang, H. Zhao, L. Wang and S. Cong, *Adv. Mater. Interfaces*, 2021, **8**, 2100412.
153. A. Hulanicki, S. Glab and F. Ingman, *Pure Appl. Chem.*, 1991, **63**, 1247-1250.
154. P. Gründler, *ChemTexts*, 2017, **3**, 16.
155. O. S. Wolfbeis, *J. Mater. Chem.*, 2005, **15**, 2657-2669.
156. E. B. Veale and T. Gunnlaugsson, *Annu. Rep. Prog. Chem., Sect. B: Org. Chem.*, 2010, **106**, 376-406.
157. M. J. Molaei, *Anal. Meth.*, 2020, **12**, 1266-1287.
158. Y. L. Yang, G. B. Mao, X. H. Ji and Z. K. He, *J. Mater. Chem. B. Mater.*, 2020, **8**, 9-17.

159. N. C. Fletcher and M. C. Lagunas, in *Molecular Organometallic Materials for Optics*, eds. H. Bozec and V. Guerchais, Springer Berlin Heidelberg, Berlin, Heidelberg, 2010, pp. 143-170.
160. K. K.-W. Lo, *Acc. Chem. Res.*, 2015, **48**, 2985-2995.
161. S. Hostachy, C. Policar and N. Delsuc, *Coord. Chem. Rev.*, 2017, **351**, 172-188.
162. 1..
163. M. T. Gabr and F. C. Pigge, *Chem. Eur. J.*, 2018, **24**, 11729-11737.
164. V. Sathish, M. M. Krishnan, M. Velayudham, P. Thanasekaran, K.-L. Lu and S. Rajagopal, *Spectrochim. Acta, Part A*, 2019, **222**, 117160.
165. V. Sathish, E. Babu, A. Ramdass, Z.-Z. Lu, T.-T. Chang, M. Velayudham, P. Thanasekaran, K.-L. Lu, W.-S. Li and S. Rajagopal, *RSC Adv.*, 2013, **3**, 18557-18566.
166. V. Sathish, E. Babu, A. Ramdass, Z.-Z. Lu, M. Velayudham, P. Thanasekaran, K.-L. Lu and S. Rajagopal, *Talanta*, 2014, **130**, 274-279.
167. V. Sathish, A. Ramdass, Z.-Z. Lu, M. Velayudham, P. Thanasekaran, K.-L. Lu and S. Rajagopal, *Inorg. Chem. Commun.*, 2016, **73**, 49-51.
168. V. Sathish, A. Ramdass, Z.-Z. Lu, M. Velayudham, P. Thanasekaran, K.-L. Lu and S. Rajagopal, *J. Phys. Chem. B*, 2013, **117**, 14358-14366.
169. T. Das and K. K. Rajak, *J. Organomet. Chem.*, 2020, **908**, 121098.
170. A. Ramdass, V. Sathish, E. Babu, M. Velayudham, P. Thanasekaran and S. Rajagopal, *Coord. Chem. Rev.*, 2017, **343**, 278-307.
171. J. Zhang, Y. Cui, B. Gao, G. Hu and Q. Jiang, *Sens. Actuators, B*, 2016, **223**, 806-819.
172. X. Yang and Y. Li, *Spectrochim. Acta, Part A*, 2016, **153**, 746-753.
173. L. Liu, Y. Yang and J.-s. Feng, *Sens. Actuators, B*, 2017, **253**, 310-316.
174. E. Valdés, M. Cepeda-Plaza, G. Günther, A. Vega, R. Palacios, M. L. Gómez and N. Pizarro, *Dyes and Pigments*, 2020, **172**, 107787.
175. C. Quintana, M. P. Cifuentes and M. G. Humphrey, *Chem. Soc. Rev.*, 2020, **49**, 2316-2341.
176. L. Pérez-Mirabet, S. Surinyach, J. Ros, J. Suades and R. Yáñez, *Mater. Chem. Phys.*, 2012, **137**, 439-447.
177. A. J. Hallett, P. Christian, J. E. Jones and S. J. A. Pope, *Chem. Commun.*, 2009, 4278-4280.
178. M.-J. Li, X. Liu, M.-J. Nie, Z.-Z. Wu, C.-Q. Yi, G.-N. Chen and V. W.-W. Yam, *Organometallics*, 2012, **31**, 4459-4466.
179. B. Vlckova, P. Matejka, J. W. M. van Outersterp, T. L. Snoeck and D. J. Stufkens, *Inorg. Chem.*, 1994, **33**, 2132-2136.
180. H. J. Montgomery, D. Pelleteret, S. E. J. Bell and N. C. Fletcher, *Inorg. Chem.*, 2011, **50**, 2738-2747.
181. D. Lin, T. Gong, S. Qiu, Q. Wu, C.-Y. Tseng, K. V. Kong, G. Chen and R. Chen, *Chem. Commun.*, 2019, **55**, 1548-1551.

Chapter 2

Experimental Methods and Procedures

2.1 Instrumentation

2.1.1 NMR Spectroscopy

^{1}H and ^{13}C spectra were recorded using a Bruker AVANCE III 400 and Bruker Fourier 300. Spectra were recorded at standard room temperature and pressure (298 K and 1 atm) using trimethysilane as an internal standard. All spectra were conducted in deuterated solvent.

2.1.2 UV-Vis, Emission and IR Spectroscopy

UV-Visible spectra were recorded on an Agilent Technologies Cary 60 UV-Vis spectrometer. Emission spectra was recorded using an Agilent Technologies Cary Eclipse Fluorescence Spectrophotometer. IR spectra were recorded on an Agilent Technologies Cary 630 FTIR spectrometer with the attenuated total reflectance (ATR) attachment. Stock solutions of all reagents were prepared and spectroscopic measurements were conducted as sequential titrations. Spectra were recorded at standard room temperature and pressure (298 K and 1 atm), using a quartz cell with a path length of 1 cm.

2.1.3 Scanning Electron Microscopy and X-ray Energy Dispersive Spectroscopy

Scanning electron microscopic imaging and corresponding X-ray energy dispersive spectroscopy was conducted using a JEOL JSM-7800F coupled to an X-Max50, Silicon Drift detector. Additional SEM imaging was conducted in collaboration with Queen's University Belfast, using a Quanta FEG 250.

2.1.4 Mass Spectrometry and Elemental Analysis

Mass spectrometry was conducted by Dr David Rochester, a using Shimadzu LCMS-IT-TOF mass spectrometer. Elemental analysis was conducted using a Vario MICRO Cube – CHNS analysis instrument.

2.1.5 Raman Spectroscopy

The majority of Raman experiments featured in this work was conducted using the Raman InVia System (Renishaw plc, Wooton-Under edge U.K.) with 532 and 785 nm wavelength lasers unless stated otherwise. The laser power of the 532 and 785 nm lasers when operating at 100% are 15 mW and 20 mW respectively. Additional spectra were also collected in collaboration with Queen's University, Belfast using an Avalon Raman Station equipped with a 100 mW 785 nm laser, a Perkin Elmer Raman Micro 200 Raman Microscope equipped with a 785 nm diode laser. Spectra were recorded at standard room temperature and pressure (298 K and 1 atm).

2.2 Materials

4,4′-Bis(benzimidazole)bipyridine (L2) and dipyridophenazine (L4) were supplied by C. J. Howells and N. C. Fletcher and used as supplied. All materials were purchased from either Fisher Scientific or Sigma-Aldrich and used as received. Laboratory grade solvents were used for synthesis unless stated otherwise. HPLC grade solvents were used for UV-vis, emission and Raman measurements. DCM was dried over $MgSO_4$ overnight and distilled under N_2.

Complex and Analyte solutions were freshly prepared prior to SERS experiments. Calf thymus (Ct) DNA supplied by Sigma Aldrich, was diluted in Tris Buffer (5 mM Tris-

HCl, 50 mM NaCl, 7.2 pH) and allowed to equilibrate overnight at 4 °C. The concentration of the ct-DNA per base pair was determined spectroscopically using the extinction coefficient at 260 nm of 6600 molar base^{-1} cm^{-1} dm^3 gave a ratio of UV absorbance at 260 and 280 nm of ca. 1.6 : 1. The ct-DNA stock solution concentration expressed in bases was 127 mM which was then diluted to 127 µM.

2.1 - Synthesis

2.1.1 - Ligand Synthesis

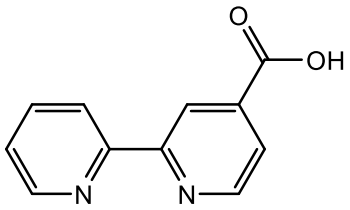

2,2'-Bipyridine-4-carboxylic acid[1,2]

Synthesis was carried out according to literature.[1,2] 4-Methyl-2,2'-bipyridine (10 g, 0.59 mol) was added to concentrated sulfuric acid (150 ml) with stirring. Potassium dichromate (25 g 0.85 mol) was added and the reaction mixture was cooled to 0°C and left to stir for 30 minutes. The temperature was then increased to 100°C and left to stir for 6 hours. The reaction mixture was precipitated with the addition of water and collected. The pH of the filtrate was adjusted to approximately 3.5 using 1 M aqueous HCL. A white solid was collected by filtration. Yield = 4.26 g 36.1% Characterisation in accordance with literature.[1,2] ^{1}H NMR DMSO 400 MHz δ 7.51 (1H ddd *J*= 7.7, 4.8, 1.0 Hz) 7.87 (1 H dd *J*= 4.8, 1.7 Hz) 7.99 (1H td *J* =7.7, 1.7 Hz) 8.43 (1H d *J* = 7.7 Hz) 8.74 (1H d *J* = 4.8, 1.7 Hz) 8.84 (1H bs) 8.88 (1H dd *J*=4.9, 1.0 Hz)

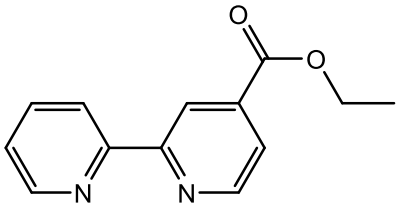

4-Ethoxycarbonyl-2,2'-bipyridine[3]

Synthesis was used according to literature.[3] 2,2′-Bipyridine-4-carboxylic acid (3 g 15 mmol) was refluxed in $SOCl_2$ (60 ml) for 3 hours followed by removal by vacuum distillation. The acyl chloride was then dissolved in dry THF (40 ml), dry ethanol (40 ml) and triethylamine (0.2 ml) and stirred for 16 hours under N_2. Solid was removed via Celite® filtration and the filtrate was washed with water and dried with $MgSO_4$. Solvent was removed, giving a white solid. Yield = 2.78 g 80.9% Characterisation in accordance with literature.[3] ^{1}H NMR $CDCl_3$ 400 MHz δ 1.46 (3H, t) 4.77 (2H, q) 7.37 (1H ddd *J*= 8.7, 4.8, 1.1 Hz) 7.86 (1 H td *J*= 7.8, 1.7 Hz) 7.90 (1H dd *J* =4.9, 1.7 Hz) 8.44 (1H dt *J*=8.0, 1.1 Hz) 8.75 (1H d *J* = 4.8, 1.7, 0.8 Hz) 8.84 (1H dd *J* = 4.9, 0.8 Hz) 8.95 (1H dd *J* =1.5, 0.8 Hz)

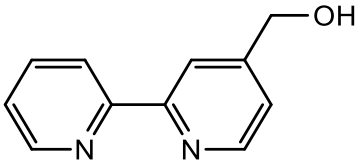

4-Hydroxymethyl-2,2'-bipyridine[4-6]

Synthesis was carried out according to literature.[4-6] 4-Ethoxycarbonyl-2,2′-bipyridine (2.50 g 0.012 mmol) and $NaBH_4$ (5.56 g 0.15 mol) was added to dry ethanol (45 ml) and stirred for 2 days at room temperature. Water (100 ml) was added and the solvent was removed. The resultant residue was dissolved in water and extracted into DCM (5x50 ml). The organic layer was dried with $MgSO_4$ followed by filtering and removal of solvent giving a brown oil as a product. Yield = 1.44 g 70.6% Characterisation in

accordance with reported data.[4-6] ^{1}H NMR $CDCl_3$ 400 MHz δ 4.67 (2H, s) 7.22 (1H dd *J*= 4.7, 0.7 Hz) 7.25 (1 H ddd *J*= 8.6, 4.7, 2.6 Hz) 7.75 (1H td *J* =7.9, 1.8 Hz) 8.24 (1H s) 8.27 (1H d *J* = 7.9 Hz) 8.49 (1H d *J* = 5.0 Hz) 8.57 (1H d *J* =4.3 Hz)

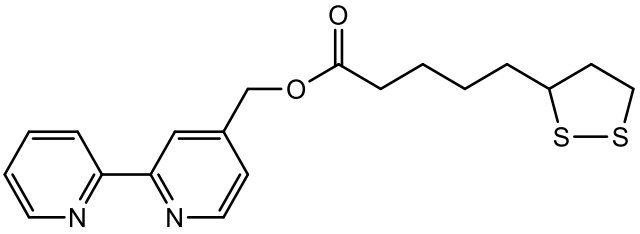

2,2'-(Bipyridin-4-ylmethyl)-(1,2-dithiolan-3-yl)pentanoate L1[6]

Synthesis was adapted from literature.[6] 4-Hydroxymethyl-2,2'-bipyridine (0.100 g 0.537 mmol) and thioctic acid (0.1109 g, 0.537 mmol) were dissolved in dry DCM (45 ml) and stirred for 45 min at 0°C. Dicyclohexylcarbodiimide (DCC) (0.1663 g, 0.806 mmol) and 4-dimethylaminopyridine (DMAP) (0.198 g, 1.621 mmol) dissolved in dry DCM was then added and stirred for 1 hr at 0°C and for 24 hrs at room temperature. The resulting solution was washed with water and the organic residues dried over $MgSO_4$. The solvent was removed and the product was purified by silica column chromatography, collecting the 1st major fraction (eluent 59:39:2 hexane: ethyl acetate: triethylamine) as a pale yellow oil. Yield 0.1344 g, 66.8%. ^{1}H NMR 300 MHz, $CDCl_3$ δ 1.43-1.54 (2H, m, CH_2), 1.64-1.73 (4H, m, 2CH_2), 1.81-1.93 (1H, m, CH_2), 2.36-2.46 (1H, m, CH_2), 2.44 (2H, t, *J* = 7.5 Hz, CH_2), 3.03-3.19 (2H, m, CH_2), 3.49-3.59 (1H,m, CH_2), 5.20(1H, s), 7.27 (1H, dd, *J* = 5.0, 1.8 Hz, CH_2, CH^{5}), 7.31 (1H, ddd, *J* = 7.6, 4.8, 1.2 Hz, $CH^{5'}$), 7.71 (1H, ddd, *J* = 8.0, 7.6, 1.8 Hz, $CH^{4'}$), 8.37 (1H, bs, CH^{3}), 8.40 (1H, ddd, *J* = 8.0, 1.8, 1.2 Hz, $CH^{3'}$), 8.66 (1H, dd, *J* = 4.9, 0.9 Hz, CH^{6}), 8.68 (1H, ddd, *J* = 4.9, 1.8, 0.9 Hz, $CH^{6'}$); ^{13}C NMR 75 MHz, $CDCl_3$ δ 24.6 (CH_2) 28.7 (CH_2), 33.9 (CH_2), 34.6 (CH_2),38.5 (CH_2),40.2 (CH_2), 56.3 (CH), 64.4 (CH_2), 119.3 (CH), 121.2

(CH),122.0 (CH), 123.9 (CH),137.0 (CH), 146.0 (Q), 149.2 (CH), 149.5 (CH), 155.8 (Q), 156.5 (Q), 173.0 (Q); ES-MS: 375.2 $[M]^+$ Elemental analysis found (calculated): $C_{19}H_{22}O_2N_2S_2$·: C: 60.78 (61.08), H: 7.57 (6.45), N: 6.79 (7.39), S: 14.91 (14.82).

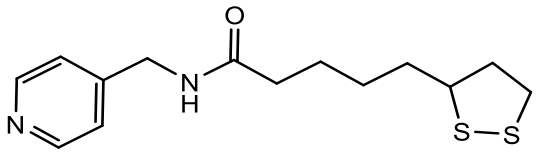

N-(pyridyl-4-methyl)lipoamide, L3 [7]

Synthesis was carried out according to literature.[7] Thioctic acid (826 mg, 4 mmol) and triethylamine (0.56 ml, 4 mmol) were stirred in THF (20 ml) at 0 °C for 5 mins, followed by the addition of $SOCl_2$ (0.8 ml 4 mmol) and left to stir for 15 minutes. 4-Picolylamine (0.452 ml, 3.3 mmol) was added and left to stir for 16 hrs. The solvent was removed and the product was redissolved in DCM and washed with 5% $NaHCO_3$ aqueous solution (3 x 15 ml) and brine solution (3 x 15 ml). Solvent was removed and purified using silica column chromatography with a 5% MeOH:DCM eluent, retrieving the 2nd band. Yield= 349.2 mg, 30% Characterisation was in accordance with the literature.[7] ^{1}H NMR 400 MHz $CDCl_3$ δ 8.49 (2H, d *J* = 6.1 Hz), 7.21 (2H, d *J* = 6.1 Hz), 6.73 (1H, bs), 4.43 (2H, d), 3.55 (1H, m), 3.11 (2H, m), 2.43 (1H, m), 2.33 (2H, t), 1.89 (1H, m), 1.66 (4H, m), 1.48 (2H, m).

2.1.2 – Metal Complex Synthesis

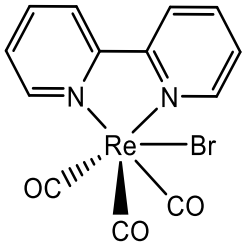

[Re(bpy)(CO)$_3$Br]

Synthesis was carried out according to literature.[8] $Re(CO)_5Br$ (100 mg 0.24 mmol) was refluxed with 2,2′-bipyridine (38.4 mg 0.25 mmol) in toluene (40 ml) for 16 hrs giving a yellow solution. The reaction was left to cool at room temperature. Reaction solvent was reduced in volume (<5 ml) and the product was precipitated with petroleum ether (20 ml). Yellow powder was captured via Hirsch filtration. Yield 73.3 mg 57% Characterisation was in accordance with the literature.[8]

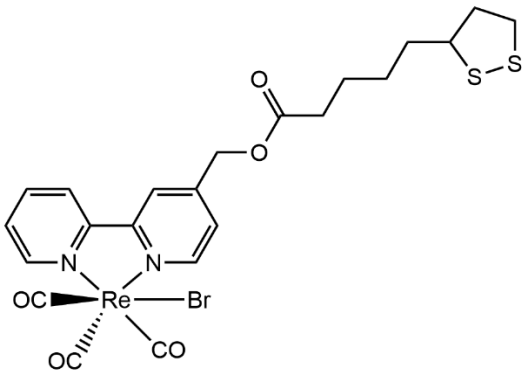

[Re(L1)(CO)$_3$Br][9]

Synthesis was adapted from literature.[9] [$Re(CO)_5Br$] (0.150 g, 0.37 mmol) was refluxed in toluene (20 ml) with L1 (0.160 g, 0.460 mmol) under a N_2 atmosphere for 18 h. The

volume of solvent was reduced (approximately 5 ml) causing the precipitation of the product, which was collected by filtration and washed with diethyl ether (3 x 10 ml) and dried in air. Yield 0.206 g, 72%. ^{1}H NMR 300 MHz, $CDCl_3$ δ 1.48-1.58 (2H, m), 1.70-1.80 (4H, m), 1.88-1.98 (1H, m), 2.45-2.52 (1H, m), 2.52 (2H, t, *J* = 7.5 Hz), 3.10-3.24 (2H, m), 3.56-3.63 (1H, m), 5.31(1H, s), 7.51 (1H, dd, *J* = 5.6, 1.6 Hz), 7.58 (1H, ddd, *J* = 7.6, 5.4, 1.2 Hz), 8.11 (1H, ddd, *J* = 8.0, 7.6, 1.7 Hz), 8.16 (1H, bs), 8.25 (1H, d, *J* = 8.0 Hz), 9.07 (1H, d, *J* = 5.4 Hz), 8.68 (1H, ddd, *J* = 4.8, 1.7, 0.9 Hz); ^{13}C NMR 75 MHz, $CDCl_3$ δ 24.6 (CH_2) 28.7 (CH_2), 33.8 (CH_2), 34.5 (CH_2),38.5 (CH_2),40.3 (CH_2), 56.3 (CH), 63.5 (CH_2), 121.5 (CH), 123.2 (CH),125.4 (CH), 127.3 (CH),138.9 (CH), 148.7 (Q), 153.4 (CH), 153.4 (CH), 155.4 (Q), 155.9 (Q), 172.7 (Q), 196.6 (Q); MS-ES: m/z 747 $[M+Na]^+$, 645 $[M-Br]^+$, 723 $[M-H]^-$. Elemental analysis found (calculated): $ReC_{22}H_{22}O_5N_2S_2Br$ $(NaBr)_{0.25}$: C: 35.16 (35.25), H: 2.74 (2.95), N: 3.94 (3.73), S: 8.73 (8.55). IR: 1739.3 (C=O), 1902.4, 2021.5 (3x ReC=O).

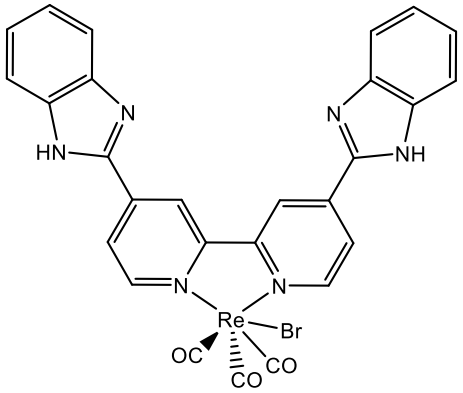

[Re(L2)(CO)$_3$Br]

$Re(CO)_5Br$ (150 mg 0.369 mmol) and 4,4′-bis(benzimidazole)bipyridine (L2) (143 mg 0.368 mmol) were ground to fine powders and added to DMSO (10 ml) and stirred at reflux for 24 hrs. The reaction mixture was precipitated by adding water (50 ml) and captured on Celite® and washed with water (2 x 15 ml) and dried in air. The product

was taken into THF (20 ml) and the solvent removed to give dark orange power. Yield: 160.9 mg 58.98% ^{1}H NMR 400 Hz CD_3CN δ 7.38 (2H t *J* = 8.0 Hz) 7.70 (2H t *J* = 7.0 Hz) 7.75 (2H d *J*= 7.8 Hz) 7.88 (2H d, *J* = 7.8 Hz) 8.45 (2H, dd *J* = 5.9, 1.6 Hz) 9.25 (2H t *J* = 5.9 Hz) 9.49 (2H s) 13.82 (2H bs). ^{13}C NMR and mass spectrometry was attempted but unsuccessful due to poor solubility.

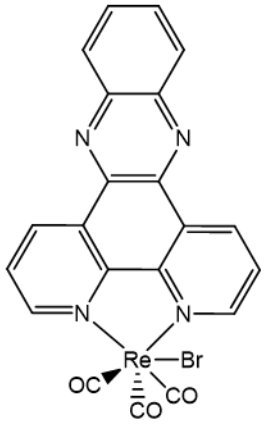

[Re(L4)(CO)$_3$Br][10]

Synthesis was carried out according to literature.[10] $Re(CO)_5Br$ (200 mg, 0.492 mmol) and dipyridophenazine (L4) (138 mg, 0.488 mmol) were dissolved in DMSO (10 ml) and stirred at reflux for 24 hrs. The product was precipitated with water (50 ml), collected using vacuum filtration and, washed with diethyl ether (3 x 15 ml). The product is a yellow powder. Yield 224.9 mg 72% **1**H NMR 400 MHz, $CDCl_3$ δ 8.05 (2H, m) 8.09 (2H m) 8.49 (2H, m) 9.49 (2H, dd, *J* = 8.3, 1.5 Hz) 9.90 (2H dd *J* = 5.2 Hz, 1.6 Hz). Characterisation in accordance with literature.[10]

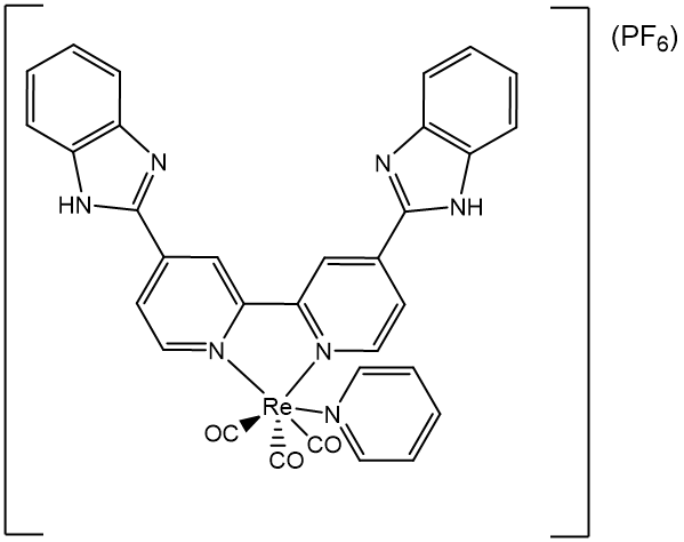

[Re(L2)(CO)$_3$(pyr)](PF$_6$)

Re(L2)(CO)$_3$Br (70 mg 0.172 mmol) was dissolved in THF with a large excess of $AgClO_4$ (40 mg, 0.192 mmol) and pyridine (5 ml, 62 mmol) was added. The reaction was stirred for 16 hrs. The reaction solution was filtered to remove insoluble impurities and the product precipitated with cold water (20 ml). Crude product was extracted into DCM and was washed with an aqueous solution of KPF_6 (20 ml) and dried. The solvent was removed via vacuum distillation. The brown product was redissolved into MeOH and precipitated with an aqueous solution of KPF_6 and collected by filtration. Yield 52.3 mg 41% IR (ATR): 1902 and 2025 (3x Re-CO) ^{1}H NMR 400 Hz CD_3CN δ 7.35 (2H td *J* = 7.7, 6.4, 1.1 Hz) 7.40 (2H dd *J* = 6.4, 3.2 Hz) 7.81 (2H m) 7.90 (1H m) 8.35 (2H, dd *J* = 6.4, 1.5 Hz) 8.41 (2H dd *J* = 5.6, 1.5 Hz) 9.25 (2H s) 9.38 (2H d *J* = 5.8 Hz). ^{13}C NMR and mass spectrometry was attempted but unsuccessful due to poor solubility.

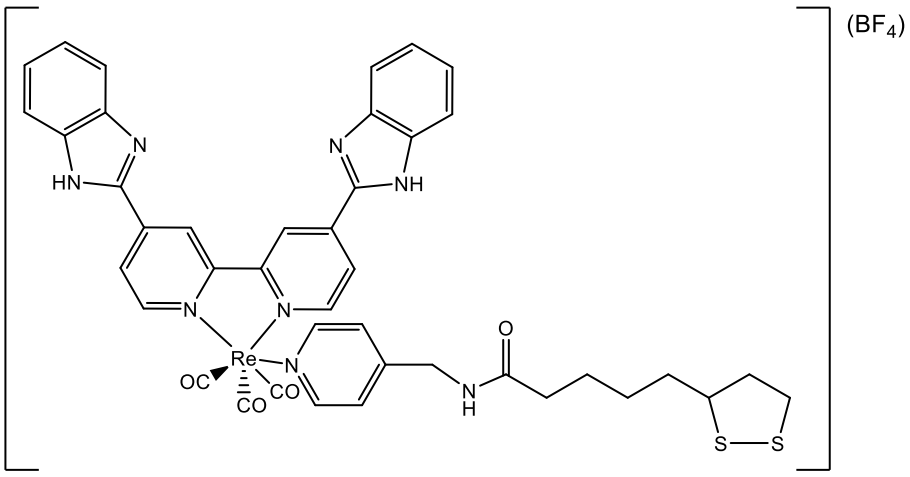

$[Re(L2)(CO)_3(L3)](BF_4)$[11]

Synthesis was adapted from literature.[11] [Re(L2)$(CO)_3$Br] (150 mg 0.144 mmol) was stirred at reflux in darkness in the presence of $AgBF_4$ (60 mg, 0.308 mmol) in acetonitrile (20 ml) for 16 hrs. The reaction was filtered and filtrate volume reduced (<5 ml). The resulting adduct was precipitated with diethyl ether (40 ml) and collected via filtration and washed with diethyl ether (3x 10 ml). This was redissolved in a 3:1 THF:MeOH (40 ml) solution and refluxed with L4 (10 mg 0.03 mmol) at reflux for 16 hrs. The reaction solvent was reduced in volume (≈1 ml) and the product precipitated with diethyl ether (30 ml) as an orange powder. Yield 8.3 mg 23.6 % ^{1}H NMR 400 Hz CD_3CN δ 1.53 (2H, m), 1.65 (4H, m), 1.79 (1H, m) 2.35 (2H, m), 2.43 (1H) 3.19 (2H, m), 3.56 (1H), 4.36 (2H, bs), 7.37 (2H bs) 7.78 (2H bs) 8.15 (2H s) 8.49 (2H, m) 8.55 (2H, bs) 8.69 (2H, bs) 9.25 (2H, s) 9.46 (2H, bs), 9.58 (2H). ^{13}C NMR and mass spectrometry was attempted but unsuccessful due to poor solubility.

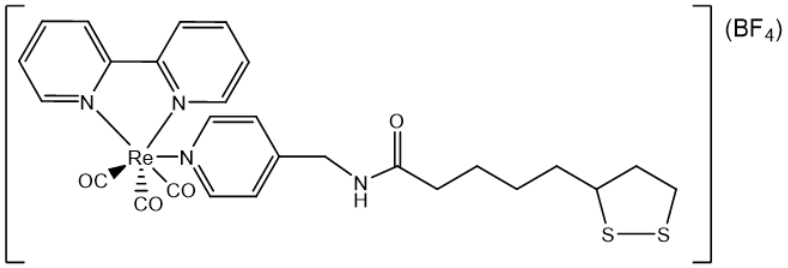

[Re(bpy)(CO)$_3$(L3)](BF$_4$) [11]

Synthesis was adapted from literature.[11] Re(bpy)(CO)$_3$Br (20 mg, 0.04 mmol) was stirred at reflux in CH_3CN (10 ml) in the presence of $AgBF_4$ (15 mg 0.7 mmol) for 16 hrs. The reaction mixture was then filtered and the volume of the filtrate was reduced (<5 ml). The resulting adduct was precipitated with cold diethyl ether (20 ml) and captured using filtration. The yellow solid was dissolved in 3:1 THF:MeOH (40 ml) with L3 (16 mg 0.05 mmol) and stirred for 16hrs. Solvent was removed and the residues were precipitated from acetone with diethyl ether (20 ml). Yield 28 mg 87.5% ^{1}H NMR 400 MHz CD_3CN δ 1.39 (2H, m), 1.59 (4H, m), 1.70 (2H, m) 1.91 (1H, m), 2.45 (1H, m), 3.16 (2H, m), 3.60 (1H), 4.27 (2H, d), 7.18 (2H d, *J* = 5.4 Hz), 7.81 (2H, m), 8.15 (2H d, *J* = 5.0 Hz), 8.30 (2H, td, *J*= 7.9, 1.5 Hz), 8.42 (2H, d, *J* = 8.3 Hz), 9.23 (2H, m). ^{13}C NMR and mass spectrometry was attempted but unsuccessful due to poor solubility.

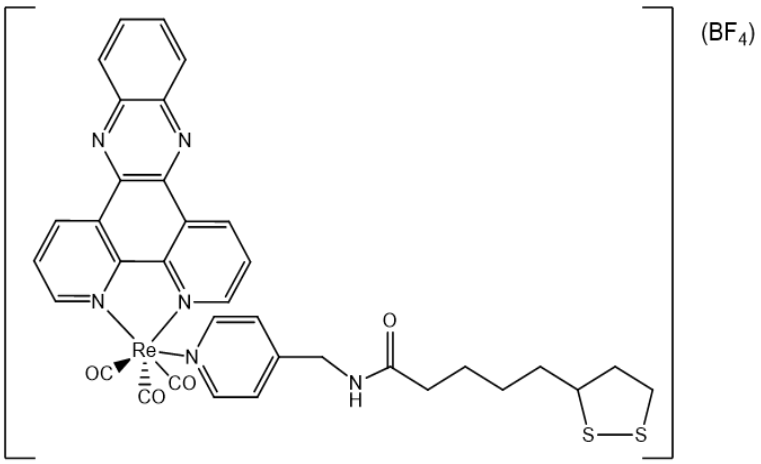

$[Re(L4)(CO)_3(L3)](BF_4)$ [10,11]

Synthesis was adapted from literature.[11] $Re(L4)(CO)_3Br$ (100 mg 0.158 mmol) was refluxed in CH_3CN (30 ml) in the presence of $AgBF_4$ (40 mg 0.205 mmol) for 24 hrs. The reaction mixture was filtered and volume of the filtrate was reduced and the adduct was precipitated with diethyl ether (30 ml). This was redissolved with L3 (48 mg, 0.162 mmol) in a 3:1 THF:MeOH (20 ml) and refluxed for 24 hrs. The solvent was removed and the solid material was precipitated from acetone with diethyl ether (30 ml). Yield: 95 mg 64% ^1H NMR 400 MHz, CD_3CN δ 1.59 (2H, m), 1.65 (4H, m), 2.12 (4H, m), 3.12 (2H, m), 3.72 (1H, m), 4.58 (2H, d, *J*= 5.9 Hz), 7.12 (2H, d, *J*= 5.9 Hz), 7.89 (2H, d, *J*= 5.9 Hz), 8.18 (2H, m), 8.30 (2H, m), 8.50 (2H, m), 8.62 (2H m), 9.92 (2H, dd, *J*= 8.3, 1.0 Hz). ^{13}C NMR and mass spectrometry was attempted but unsuccessful due to poor solubility.

2.1.3 – Nanoparticle Synthesis

Citrate Stabilised Ag Nanoparticles[12,13]

Prior to the nanoparticle synthesis, all glassware was cleaned with aqua regia and rinsed thoroughly with ultrapure water. Synthesis was carried out according to literature.[12,13] $AgNO_3$ (45 mg) was dissolved in ultrapure H_2O (250 ml) and was heated to reflux. A 1% aqueous sodium citrate solution (5 ml) was added over 30 s and refluxed for 90 min. before being cooled to room temperature. Vigorous stirring was present throughout. Formation of the nanoparticles was confirmed by an observed colour change from colourless to an opaque pale green colour. Ag NPs were characterised using UV-vis spectroscopy.

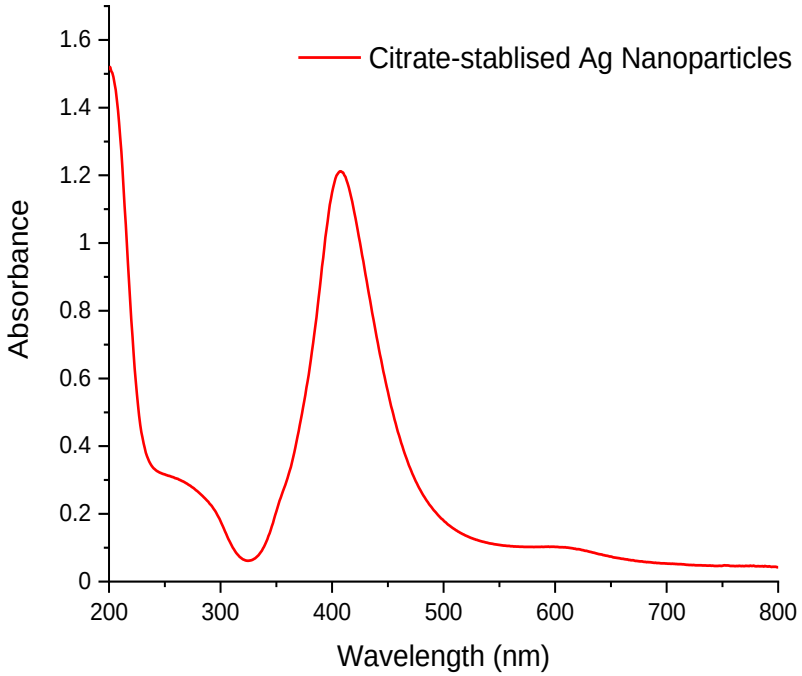

Figure 2.1: *The UV-vis spectrum of citrate stablised silver nanoparticles, showing an peak corresponding to the localised surface plasmonic resonance at 407 nm*

2.2 - Surface Preparation

2.2.1 – Metal Liquid-like Films

Metal Liquid-Like Films (MeLLFs) via Surface Modification[13-15]

Citrate-stabilised Ag nanoparticles (≈5 ml) were added to a 50 ml polypropylene centrifuge tube. A modifying compound in solution (100 µl) was added and gently shaken. DCM (≈4 ml) was added and shaken vigorously for 30 seconds or until a reflective emulsion formed, which coalesced to form the MeLLF. This was transferred to a polypropylene petri dish for Raman measurements. The modifying agent is specified in the following Chapters.

MeLLFs Formed via Promotion[13,16]

Citrate-stabilised Ag nanoparticles (≈5 ml) were added to a 50 ml polypropylene centrifuge tube. A 1 mM aqueous solution of TBA NO_3 (2 ml) and DCM (≈4 ml) was added. The centrifuge tube was then shaken vigorously for 30 seconds or until a reflective emulsion was formed which coalesced to form the MeLLF. This was then transferred to a polypropylene petri dish for Raman measurements.

"Picket Fence" Mixed Thiol MeLLFs[15]

Citrate-stabilised Ag nanoparticles (≈5 ml) were added to a 50 ml polypropylene centrifuge tube. A specified concentration of the $[Re(L1)(CO)_3Br]$ modifying solution (100 µl) and a 1 mM solution of the thiol (heptanethiol and thiophenol) (100 µl) was added and gently shaken. DCM (≈4 ml) was added and shaken vigorously for 30 seconds or until a reflective emulsion was formed which coalesced to form the MeLLF.

The concentrations of the [Re(L1)$(CO)_3$Br] solution are specified in the following chapters.

2.2.2 – Surface Exposed Nanosheets (SENS)

Surface Exposed Nanosheets (SENS) via Surface Modification

The modifying solution (100 µl) was added to citrate-stabilised Ag nanoparticles (≈5 ml). A polystyrene/DCM solution (3 ml, 0.06 g ml^{-1}) was added and shaken vigorously. The mixture was poured immediately into a polypropylene petri dish and sealed with a lid. The film was formed at the interface before the lid was removed and the DCM evaporated under ambient conditions. The dried film was cut away from the petri dish and water was added to float the film and transferred onto sticky tape.

SENS Formed via Promotion

SENS were fabricated according to a literature procedure.[17] A 1 mM aqueous TBA NO_3 solution (2 ml) was added to citrate-stabilised Ag nanoparticles (≈5 ml). A polystyrene/DCM solution (3 ml 0.06 g ml^{-1}) was added and shaken vigorously. The mixture was poured immediately into a polypropylene petri dish and sealed with a lid. The film was formed at the interface before the lid was removed and the DCM evaporated under ambient conditions. The dried film was cut away from the petri dish and water was added to float the film and transferred onto sticky tape.

2.2.3 Glass-deposited MeLLFs

Preparation of the glass deposited MeLLFs

0.1 M aqueous TBA HSO_4 solution (1 ml) was added to Ag NPs (4 ml) and then the mixture was shaken in the presence of DCM (3 ml). The resulting film was then extracted using needle and syringe and deposited onto glass slides and allowed to dry under ambient conditions. The resulting glass deposited MeLLFS were then stained with 1 mM solutions of the labelling compounds.

2.2.4 – Photodeposition

Photodeposited Ag Plates[18]

Diethylene glycol (7.5 g) and polyethylene glycol 600 MW (2.5 g) were dissolved in ethanol (40 ml). Titanium isopropoxide (5 g) was added and further stirred for 15 mins. The solution was spin coated onto ITO glass, spun at 1000 rpm for 30 seconds. This was followed by calcination at 450°C for 16 hrs. The plates were then immersed in 1 mM $AgNO_3$ methanolic solution (75:25 MeOH:H_2O) and irradiated using an unfiltered 8 W UV lamp with a 365 nm output for 30 minutes, removed from solution, washed with acetone and dried with compressed air.

2.3 Film-Analyte Interaction Experiments

2.3.1 Interaction of Ionic species using MeLLFs

The MeLLFs were formed initially using a specific modifying or promoting species (Section 2.2.1) followed by the addition of the analyte solution (100 µl) at a given concentration. The MeLLF was gently shaken, reformed and transferred to a polypropylene petri dish.

2.3.2 Sensing using SENS

The SENS were prefabricated with the desired modifying complex (Section 2.2.2), isolated on sticky tape. The analyte solution (100 μl) was dropped onto the film and the Raman measurements were taken.

2.4 – Raman Experiements

2.4.1 Data Processing

Data processing was carried out using Matlab (Version R2017a) using a locally sourced toolbox and the program, Spectragryph.[19] Baseline correction was done using an adaptive method and smoothing was done using triangular moving average of 4 intervals.

2.4.2 MeLLF Experiments

Static Raman measurements of the liquid-liquid interfacial films were taken using a 20x optic, taking 10 accumulations of 1 second exposures. Continuous scanning experiments were also conducted using a 20x optic, scanning from 200 to 3200 cm^{-1} using a 10 second exposure. 5-point spectra were then taken from different locations on the film and averaged. The same procedure was used for any experiments involving the interfacial films, including the “picket fence” MeLLFs and for analyte detection.

2.4.1.2 SENS Experiments

Static Raman measurements of the surface-exposed nanosheets were taken using a 50x optic, taking 10 accumulations of 1 second exposures. Continuous scanning experiments were taken using a 50x optic, scanning from 200 to 3200 cm^{-1} using a 10 second exposure. 5 point spectra from different locations on the film was taken and averaged. The same procedure was used for any experiments involving the interfacial films, including the "picket fence" SENS and for analyte detection.

2.4.1.3 Glass-deposited MeLLFs

Static Raman measurements of the glass deposited MeLLFs were taken using a 50x optic, taking 10 accumulations of 1 second exposures. Continuous scanning experiments were taken using a 50x optic, scanning from 200 to 3200 cm^{-1} using a 10 second exposure.

2.4.1.4 Photo-deposited Ag Plates

The Raman measurements of the photo-deposited Ag plates were taken using continuous scanning between the range 200 and 3200 cm^{-1} using a 10 second exposure.

2.4 - References

1. T. J. Huang and D. G. Brewer, *Can. J. Chem.*, 1981, **59**, 1689-1700.
2. N. C. Fletcher, M. Nieuwenhuyzen and S. Rainey, J. Chem. Soc., Dalton Trans., 2001, 2641-2648.
3. P. Paoprasert, S. Kandala, D. P. Sweat, R. Ruther and P. Gopalan, *J. Mater. Chem.*, 2012, **22**, 1046-1053.
4. S. G. Telfer, G. Bernardinelli and A. F. Williams, *Dalton. Trans.*, 2003, 435-440.
5. R. T. Brown, N. C. Fletcher, M. Nieuwenhuyzen and T. E. Keyes, *Inorg. Chim. Acta*, 2005, **358**, 1079-1088.
6. D. Pelleteret, PhD Thesis, Queen's University Belfast, 1997.
7. M. Abe, A. Inatomi and Y. Hisaeda, *Dalton. Trans.*, 2011, **40**, 2289-2298.
8. S. P. Schmidt, W. C. Trogler, F. Basolo, M. A. Urbancic and J. R. Shapley, *Inorganic syntheses: Reagents for transition metal complex and organometallic syntheses*, 1990, **28**, 160-165.
9. H. J. Montgomery, D. Pelleteret, S. E. J. Bell and N. C. Fletcher, *Inorg. Chem.*, 2011, **50**, 2738-2747.
10. F. L. Thorp-Greenwood, M. P. Coogan, L. Mishra, N. Kumari, G. Rai and S. Saripella, *New J. Chem.*, 2012, **36**, 64-72.
11. F. L. Thorp-Greenwood, J. A. Platts and M. P. Coogan, *Polyhedron*, 2014, **67**, 505-512.
12. P. Lee and D. Meisel, *J. Phys. Chem.*, 1982, **86**, 3391-3395.
13. Y. Xu, PhD Thesis, Queen's University Belfast, 2019.
14. B. Vlckova, S. M. Barnett, T. Kanigan and I. S. Butler, *Langmuir*, 1993, **9**, 3234-3238.
15. L. Faucher, E. F. Borra and A. M. Ritcey, *J. Nanosci. Nanotechnol.*, 2008, **8**, 3900-3908.
16. Y. Xu, M. P. Konrad, W. W. Lee, Z. Ye and S. E. Bell, *Nano Lett.*, 2016, **16**, 5255-5260.
17. Y. Xu, M. P. Konrad, J. L. Trotter, C. P. McCoy and S. E. J. Bell, *Small*, 2017, **13**, 1602163.
18. A. Mills, G. Hill, M. Stewart, D. Graham, W. E. Smith, S. Hodgen, P. J. Halfpenny, K. Faulds and P. Robertson, *Appl. Spectrosc.*, 2004, **58**, 922-928.
19. F. Menges, Spectragryph - optical spectroscopy software, Version 1.2.12, 2019, http://www.effemm2.de/spectragryph/.

Chapter 3

The Development of Rhenium-Functionalised Films

3.1 Introduction

Generating a suitably labelled SERS device for sensing and detection need to fulfil several parameters for it to be deemed effective. Firstly, the platform must be highly reproducible and ideally, the constituent steps of the synthetic procedure should produce samples that are chemically and physically identical. Addressing this remains an important part of the research into SERS science. Secondly, the platform should provide a high level of SERS enhancement for easy recognition of subtle changes occurring to the label itself. Another parameter to consider is the most effective way to introduce the labelling species and whether they can contribute to film formation or whether it needs to be introduced after the surface has been formed. The integration of a reporter molecule to a SERS active material has featured in numerous fields. Shan *et al.* highlight a number of examples where the presence of a reporting molecule bound to a plasmonic structure can be applied to a range of biomedical detection technologies.[1] The review features several molecules that have been used to bind to SERS surfaces using the thiol-noble metal affinity, also discussed in Chapter 1. This has allowed the development of reproducible functionalised SERS materials in both 2- and 3-dimensional forms.[2, 3]

The main objectives of this Chapter are to confirm that rhenium complexes can be employed to functionalise a noble metal nanostructure surface for surface-enhanced spectroscopic studies. An additional object is to establish a simple and reproducible method of forming a rhenium functionalised surfaces and evaluating which is the most suitable for detection applications.

3.2 Interfacial Films Comprised of Functionalised Nanoparticles

3.2.1 Brief Overview of the Synthesis

Ligand 2,2'-bipyridin-4-ylmethyl-4-(1,2-dithiolan-3-yl)pentanoate, L1 was synthesised using an adapted method using 4-methyl-2,2′-bipyridine in place of the previously reported example substituted at position 5.[4] Esterification of 4-hydroxymethyl-2,2'-bipyridine with thioctic acid was achieved using DCC coupling in the presence of DMAP. The subsequent complex, $[Re(L1)(CO)_3Br]$ was obtained by reacting L1 with bromopentacarbonylrhenium in toluene at reflux precipitated as a yellow solid following addition of acetone and diethyl ether in 72% yield. The product was characterised by ^1H NMR and IR spectroscopies.

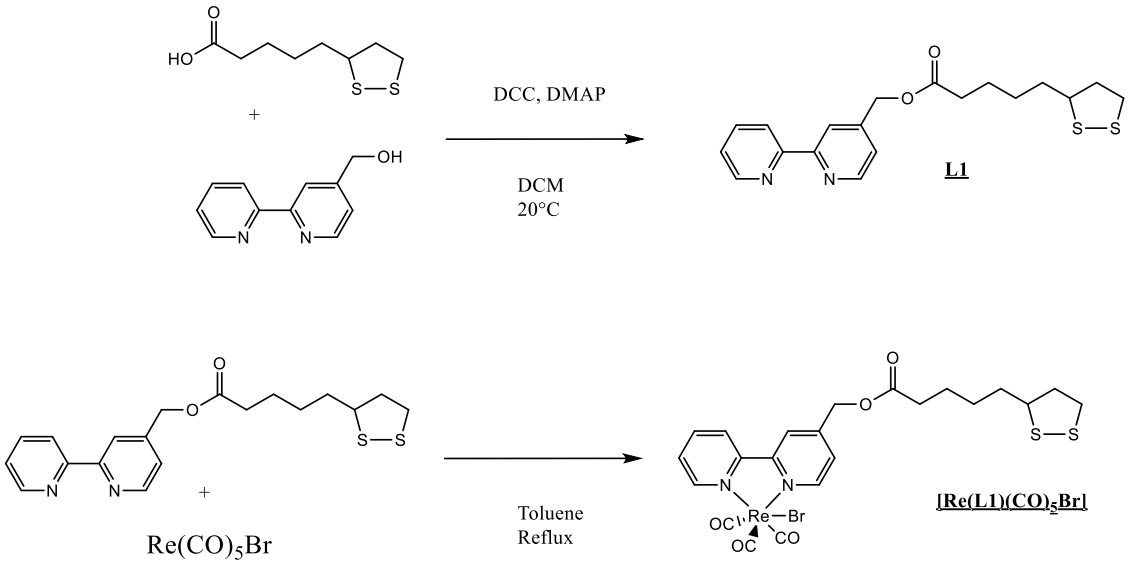

Figure 3.1: *A reaction schematic of the synthesis of the bipyridyl dithiolate ligand L1 (Yield 66.8%) and the formation of $[Re(L1)(CO)_3Br]$ (Yield 72%)*

3.2.2 Fabrication and SERS Responses of MeLLFs using Functionalised Nanoparticles

3.2.2.1 Aggregated Nanoparticles in the Presence of [Re(L1)(CO)$_3$Br]

[Re(L′)(CO)$_3$Br] functionalised Ag nanoparticles have previously been reported by the Fletcher group (Fig, 3.2a).[4] It has been shown that the simple aggregation of the nanoparticles with concentrated aqueous solutions of $MgSO_4$ in the presence of the [Re(L′)(CO)$_3$Br] complex gave a good SERS response of the resulting powder. It was anticipated that the slight positional difference of the functional tail on the bipyridine, from position 5 to 4, would not have any consequence on the observed spectroscopic response and the [Re(L1)(CO)$_3$Br] complex would display similar behaviour, confirming the original observations.

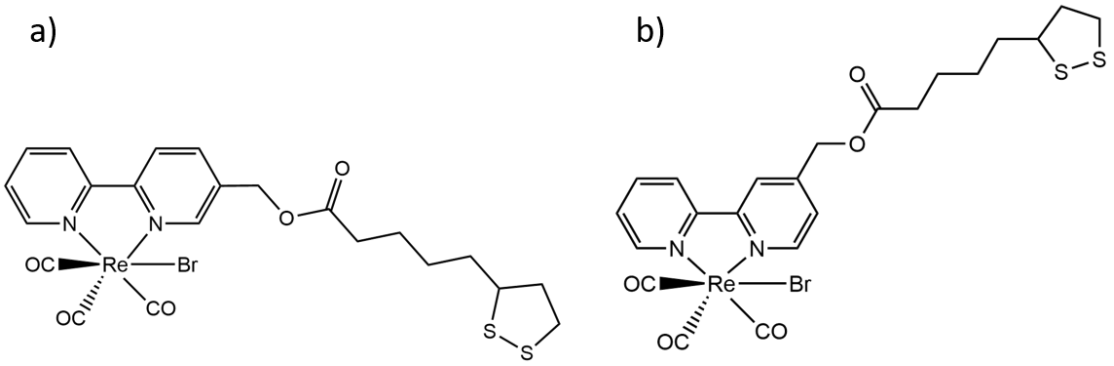

Figure 3.2: *The structures of a) [Re(L')(CO)$_3$Br] and b) [Re(L1)(CO)$_3$Br]*

Citrate stabilised nanoparticles were aggregated with a saturated aqueous solution of $MgSO_4$ in the presence of 0.1 mM acetonitrile solution of [Re(L1)(CO)$_3$Br]. The SERS spectrum of the resulting powder strongly resembles the expected response with the most recognisable feature being the peak situated at 509 cm^{-1} previously assigned to the Re-CO vibration (Fig. 3.3).[4] The Re-centred carbonyl stretches are also visible at 1902 and 2024 cm^{-1}. Another noticeable feature is the peak at 1034 cm^{-1} caused by the ring–

ring stretch of the bpy functional group with additional stretches at 1324, 1492, 1558 and 1605 cm^{-1} also attributed to the bpy component.

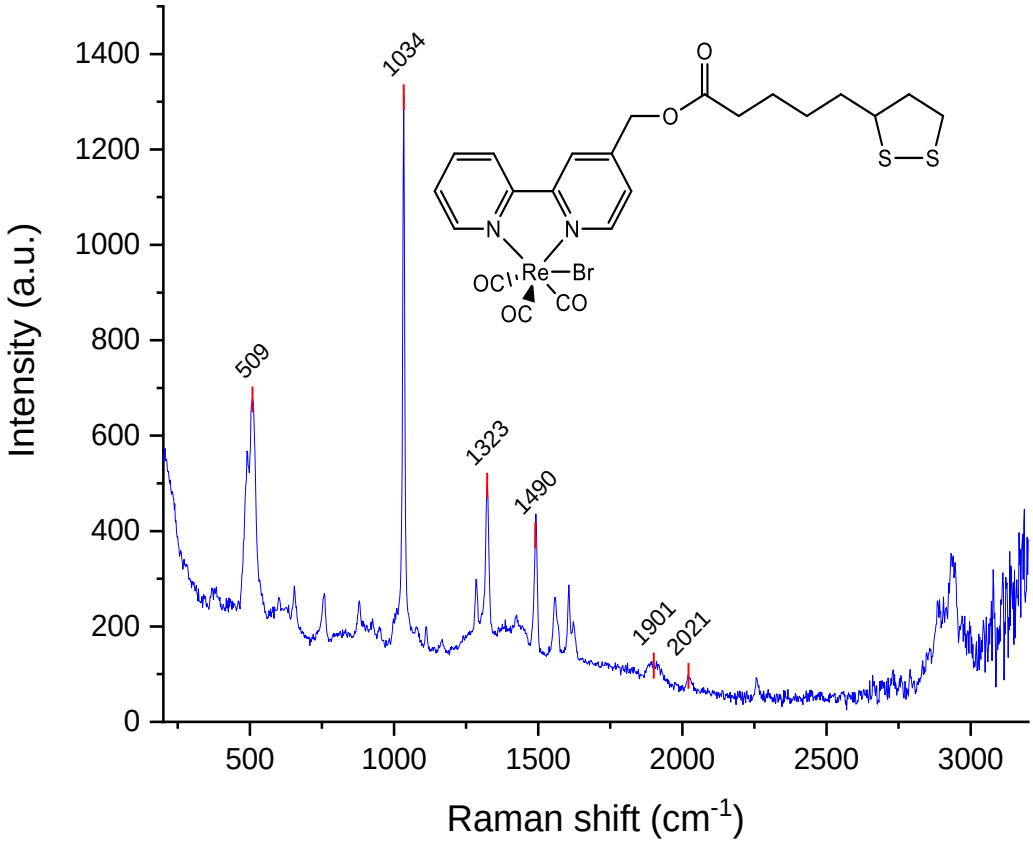

Figure 3.3: *The SERS spectrum of aggregated Ag nanoparticles in the presence of [Re(L1)(CO)$_3$Br]. Obtained at Queen's University Belfast, usingthe Avalon Raman Station, excited at 785 nm*

***Table 3.1**: The peak assignments for the SERS spectrum of aggregated nanoparticles in the presence of [Re(L1)(CO)$_3$Br]*

Wavenumber (cm^{-1})	Assignment
509	Re–C str.
655	Aliphatic C–S str.
756	Aliphatic C–S str.
881	CH_2 rocking
923	C–C str. (dithiolane ring)
1034	Ring–Ring str.
1285	Ring str. (C–C, C–N) + inter-ring stretching + C–H in-plane def.
1323	C–C inter-ring str. + in-plane C–H def.
1490	Ring str. (C–C, C–N) + inter-ring stretching + C–H in-plane def.
1559	Ring str. (C–C, C–N)
1606	Ring str. (C–C, C–N)
1624	Ring str. (C–C, C–N)
1901	Re–(C≡O) carbonyl str.
2021	
2887	Alkyl C–H str.
2095	C–H str. (Alkyl + dithiolane ring)

Stretching = str. Deformation = def.

3.2.2.2 Formation and SERS Response of Precursor Functionalised Metal Liquid-Like Films

The positioning of nanoparticles at liquid-liquid interfaces can be achieved through manipulation of the electrostatic forces between particles as discussed in Chapter 1.[5] It can also be achieved through the surface modification of the nanoparticle surface using a hydrophobic species. Lipoic acid derivatives have long been a popular choice for anchoring organic moieties to the surface of noble metal NPs.[6-8] Such compounds form bonds with the metal surface via the two sulfur atoms. It is believed that this, coupled with the presence of a hydrophobic metal centre, would allow the interfacial positioning of [Re(L1)(CO)$_3$Br] functionalised nanoparticles between two immiscible liquids. Forming a functionalised metal liquid-like film or MeLLF, can be achieved through vigorous shaking of colloidal nanoparticles in the presence of the modifying species and a chlorinated solvent. Methyl 5-(dithiolan-3-yl) pentanoate was used initially to

establish whether lipoic acid derivatives could be used as the modifier. The ester rather than the carboxylic acid was used to ensure that binding would proceed via Ag–S interactions on the nanoparticle surface and not via coordination through the carboxylic acid.

A MeLLF was formed via the standard procedure, using approximately 3 ml of a 1 mM acetone solution of the ester (Chapter 2. Section 2.2.1). The SERS spectrum of the resulting MeLLF contains vibrations corresponding to structural elements of the ester (Fig. 3.4). An intense band situated 600 cm^{-1} accompanied with the shoulder at 652 cm^{-1} is attributed to the in-phase and out-of-phase vibrations that occur on the two C-S bonds.[9] Possible evidence that binding is occurring, is the lack of an intense band in the region between 400-550 cm^{-1} that is distinctive of the S-S bond.[10] The implication is that the two sulfur atoms are no longer covalently bonded. The large vibration at 228 cm^{-1}, assigned to Ag-S interaction, suggests the molecule is anchored to the surface via the proposed interaction however this is tentative due to instrument limitations. The other significant contributions belonging to C-H bending and twisting modes, can be seen, along with the C=O stretching vibration observed at 1730 cm^{-1}. The broad peak at 2925 cm^{-1} is the asymmetric stretching of the CH_2 groups of the dithiolane ring along with C-H stretching vibrations.

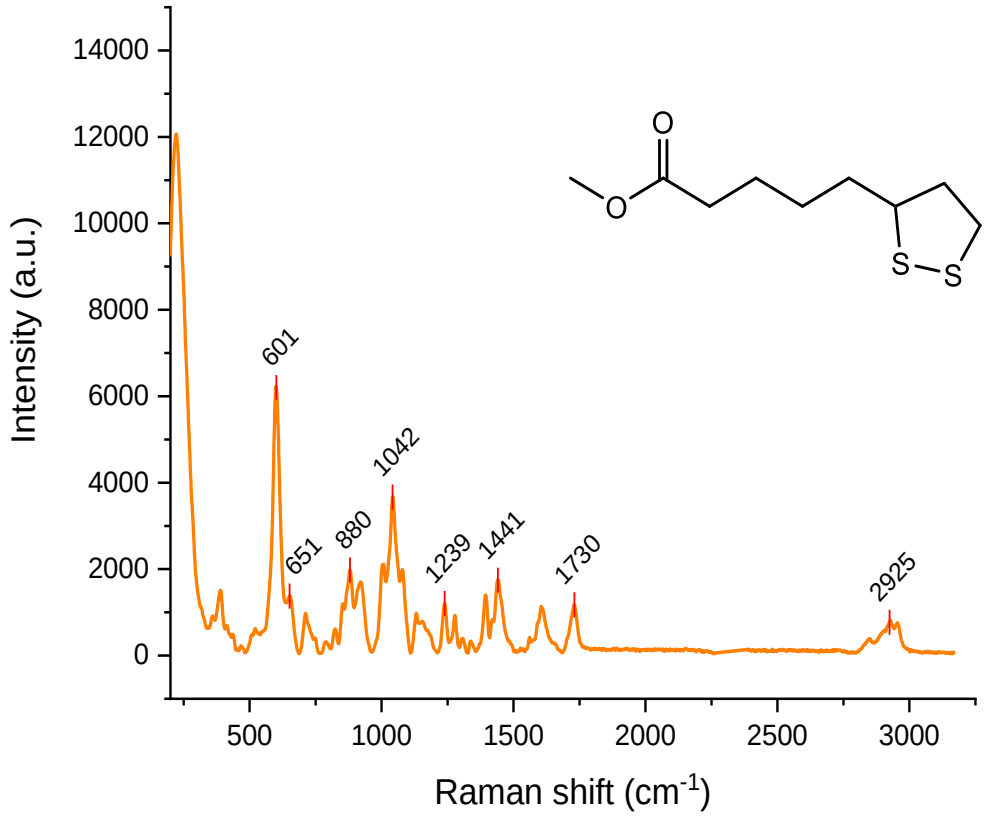

Figure 3.4: *The SERS spectrum of the methyl 5-(dithiolan-3-yl) pentanoate MeLLF*

Table 3.2*: The peak assignments for the SERS spectrum of a MeLLF formed with Methyl 5-(dithiolan-3-yl) pentanoate*

Wavenumber (cm^{-1})	Assignment
Methyl pentanoate	
601	Aliphatic C–S str.
651	Aliphatic C–S str.
711	CH rocking
880	Ring breathing
917	C–C str. (dithiolane ring)
1009	C–C str.
1042	Ring–Ring str.
1075	C–C str. + C–O str.
1239	Ring str. (C–C, C–N) + inter-ring str. + C–H in-plane def.
1277	CH_2 wagging
1394	CH_2 wagging
1441	CH_2 scissoring
1607	C=O str.
1730	
2925 (broad)	C–H str. (Alkyl + dithiolane ring)

Stretching = str. Deformation = def.

The use of the methyl dithiolate ester demonstrates that ligands derived from thioctic acid can form MeLLFs. An expectation therefore was that the bpy-dithiolate ligand, L1, would also successfully modify nanoparticles resulting in interfacial films. MeLLF formation with L1 was achieved according to the standard procedure (Chapter 2. Section 2.2.1), using L1 to modify Ag NPs. The presence of the bpy group is reflected in the resulting SERS response with the characteristic vibrations being prominent (Fig. 3.5). The strong peak at 997 cm^{-1} is attributed to the ring breathing mode, while the ring-ring stretch is adjacent at 1024 cm^{-1}. The aromatic C–H deformations are also visible at 1445 and 1486 cm^{-1} and the alkyl C–H vibrations are observed with a broad peak at 2923 cm^{-1}. The C-S stretch of the dithiolate tail at 616 cm^{-1} shifted to a higher wavenumber in comparison with the same vibration from the methyl ester.

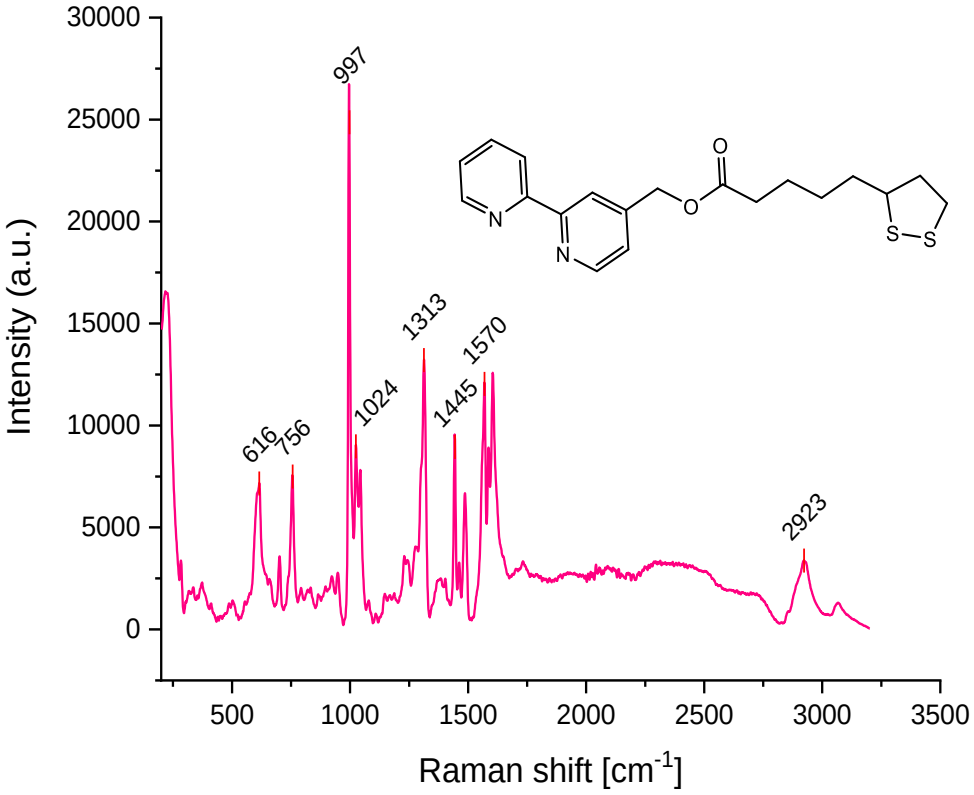

Figure 3.5: *The SERS spectrum of the MeLLF formed using the ligand, L1*

***Table 3.3**: The peak assignments for the SERS spectrum of a MeLLF formed using L1*

Wavenumber (cm^{-1})	Assignment
616	Aliphatic C–S str.
756	Aliphatic C–S str.
997	Ring breathing
1024	Ring–Ring str.
1285	Ring str. (C–C, C–N) + inter-ring str. + C–H in-plane def.
1313	C–C inter-ring str. + in-plane C–H def.
1445	Ring str. (C–C, C–N) + inter-ring str. + C–H in-plane def.
1570	Ring str. (C–C, C–N)
1606	Ring str. (C–C, C–N)
1624	Ring str. (C–C, C–N)
2923	C–H str. (Alkyl + dithiolane ring)

Stretching = str. Deformation = def.

3.2.2.3 Formation and SERS response of [Re(L1)(CO)$_3$Br] MeLLF

The SERS spectra of both the methyl and bipyridyl dithiol esters demonstrate the ability to form MeLLFs with reproducible responses through the modification of Ag nanoparticles with dithiol containing groups. To explore if MeLLF formation would be successful with the incorporation of the rhenium centre, MeLLFs were formed according to the standard procedure (Chapter 2. Section 2.2.1), using a 1 mM acetonitrile solution of [Re(L1)(CO)$_3$Br]. Addition of the complex results in a visible colour change of the nanoparticle solution and formation of the MeLLF is confirmed by the appearance of a reflective film at the interface (Fig. 3.6).

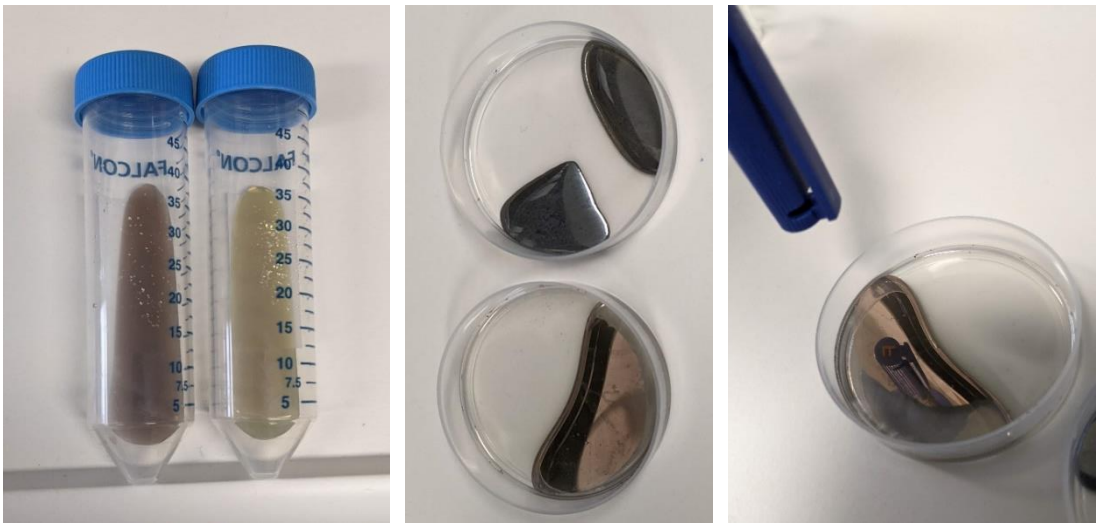

Figure 3.6: *Photographs of the Re(L1) functionalised nanoparticles and the subsequent MeLLF. Note the considerable darker colour after addition of the Re(L1) complex. The Re(L1) MeLLF has a bronze colour compared to the expected silver colour. Final picture demonstrates the highly reflective surface*

The SERS response of the MeLLF resulting from [Re(L1)$(CO)_3$Br] modification, possesses the vibrations inherent of rhenium tri-carbonyl complexes, evidenced by the Re-C vibration at 507 cm^{-1} and metal bonded CO stretches at 1909 and 2025 cm^{-1} respectively (Fig. 3.7). There are also distinct similarities between the spectrum from the MeLLF spectrum and the spectrum obtained via $MgSO_4$ nanoparticle aggregation (Fig. 3.7 insert). MeLLF formation using [Re(bpy)$(CO)_3$Br] complex was also attempted but this was judged not to successful. There is no observable colour change that occurs after addition of [Re(bpy)$(CO)_3$Br], suggesting that the complex is not modifying the surface. Increasing the volume of the [Re(bpy)$(CO)_3$Br] solution also did not result in any perceivable colour change and no MeLLFs were formed after shaking. The complex is charge neutral and does not possess a functionality that would bind with the nanoparticle therefore lacking the properties to influence the nanoparticle hydrophobicity sufficiently. This suggests that charge neutral rhenium complexes require some form of surface modifying group in order for MeLLF formation to occur, such as the bipyridyl thioctic ester moiety.

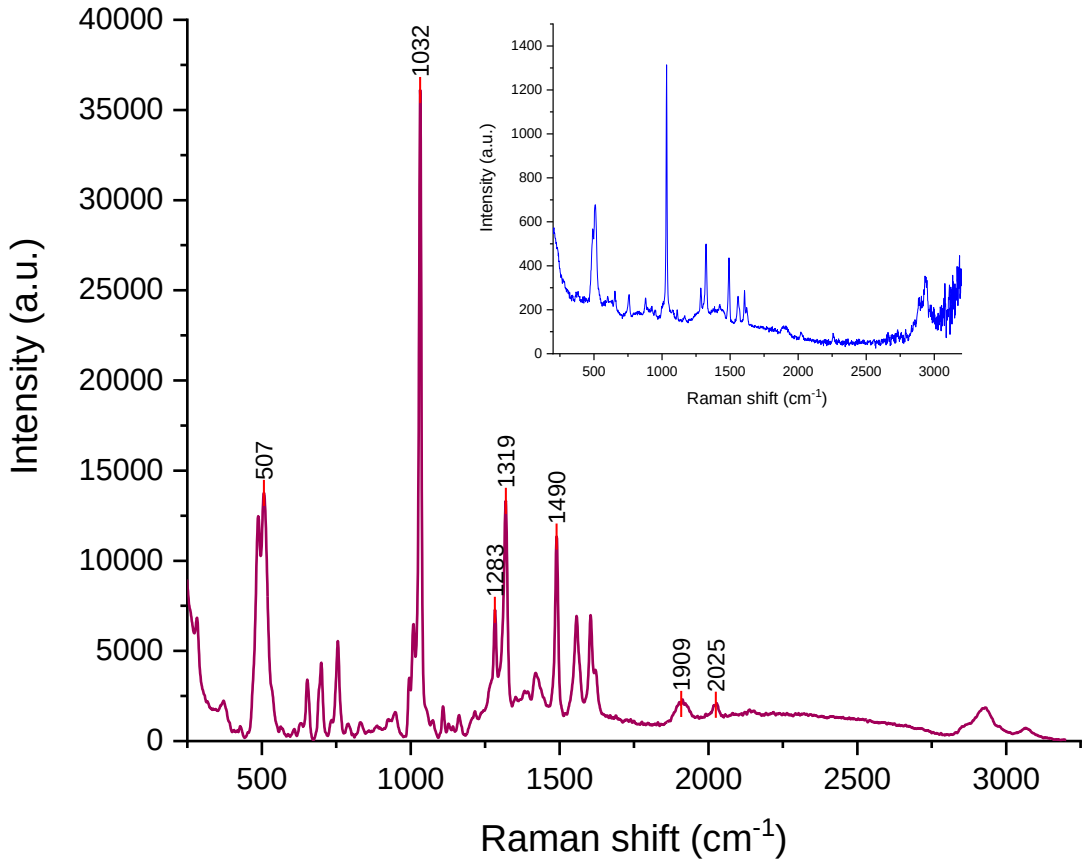

Figure 3.7: *The observed response from the MeLLF formed via functionalisation of nanoparticles using [Re(L1)(CO)$_3$Br]. Insert: The SERS spectrum of aggregated nanoparticles in the presence of [Re(L1)(CO)$_3$Br].*

Table 3.4*: The peak assignments for the SERS spectrum of a MeLLF formed using Re(L1)(CO)$_3$Br]*

Wavenumber (cm^{-1})	Assignment
509	Re–C str.
655	Aliphatic C–S str.
756	Aliphatic C–S str.
881	CH_2 rocking
923	C–C str. (dithiolane ring)
1034	Ring–Ring str.
1285	Ring str. (C–C, C–N) + inter-ring str. + C–H in-plane def.
1323	C–C inter-ring str. + in-plane C–H def.
1490	Ring str. (C–C, C–N) + inter-ring str. + C–H in-plane def.
1559	Ring str. (C–C, C–N)
1606	Ring str. (C–C, C–N)
1624	Ring str. (C–C, C–N)
1901	Re–(C≡O) carbonyl str.
2021	
2887	Alkyl C–H str.
2995	C–H str. (Alkyl + dithiolane ring)

Stretching = str. Deformation = def.

To summarise, a novel nanoparticle film functionalised with the [Re(L1)$(CO)_3$Br] complex has been formed which offers a proof of concept. This is evidenced by the SERS spectrum which exhibits the characteristic vibrations of the Re-CO group. It is assumed that the complex modifies the nanoparticle surface through Ag-S binding thus tuning the hydrophobicity of the surface sufficiently to allow for interfacial positioning.

3.3 Investigation of Hybrid Film Systems and SERS Studies

3.3.1 Initial Attempts at Films Formed Using Combinations of MeLLF-forming Species

Establishing that citrate stabilised Ag nanoparticles could be positioned at the interface between two immiscible liquids presented questions on the limitations of the methodology. One example is the role in which concentration of the rhenium complex has on film formation as it is particularly reliant on the sufficient modification of the nanoparticle surface. Additionally, an assumption was that the possible detection capabilities of the films would also be controlled by the concentration of the complex on the surface. Therefore, the lowest concentration at which film formation is achieved and that allows recognition of the Raman fingerprint of the complex could be recognised is an important parameter to consider. Film formation and SERS recognition has been demonstrated with a 1 mM solution of the complex (Section 3.2.2.3). Further investigations using solutions of decreasing concentrations of the [Re(L1)$(CO)_3$Br] showed the limitations of MeLLF formation to be of this order as it is not possible below a concentration of 0.1 mM to form a film. Below this, there is insufficient coverage of the complex on the nanoparticle surface, and the hydrophobicity of the colloidal nanoparticles is insufficient to position them at the solvent interface.

This prompted investigation into combining species that are known to induce interfacial positioning with lower concentrations of [Re(L1)$(CO)_3$Br]. Attempts at were made at forming a [Re(L1)$(CO)_3$Br] MeLLF using a $1x10^{-5}$ M solution of the complex in conjunction with an aliquot of an aqueous TBA NO_3 solution, therefore employing both a modifying and promoting species in the same system. The aim of this was to explore whether the limited surface coverage of the [Re(L1)$(CO)_3$Br] complex on the

nanoparticles could be mitigated by the presence of the promoting salt. This proved to be unsuccessful, as while a MeLLF was formed, the corresponding SERS spectrum did not feature any of the contributions that could be attributed to the rhenium complex.

3.3.2 MeLLFs Formed Using Mixed Thiol Modification

3.3.2.1 Mixed Thiol MeLLFs using [Re(L1)(CO)$_3$Br] and Heptanethiol

Another strategy to decrease the Re complex concentration on the surface could be the use of a secondary thiol in tandem with the complex. Monolayers of mixed thiols on AgNPs have been reported and it was hoped that building on this concept could potentially allow for recognition of the [Re(L1)(CO)$_3$Br] complex below 0.1 mM.[11, 12] A simple alkyl thiol could occupy the spaces between the much larger Re complex thus providing suitable coverage, orientating the complex away from the surface and tuning the NP's hydrophobicity accordingly (Fig. 3.8). Through this picket fence approach, so named as it was thought the surface on the nanoparticle would resemble a picket fence, could facilitate film formation and the recognition of the [Re(L1)(CO)$_3$Br] complex at much lower concentrations.

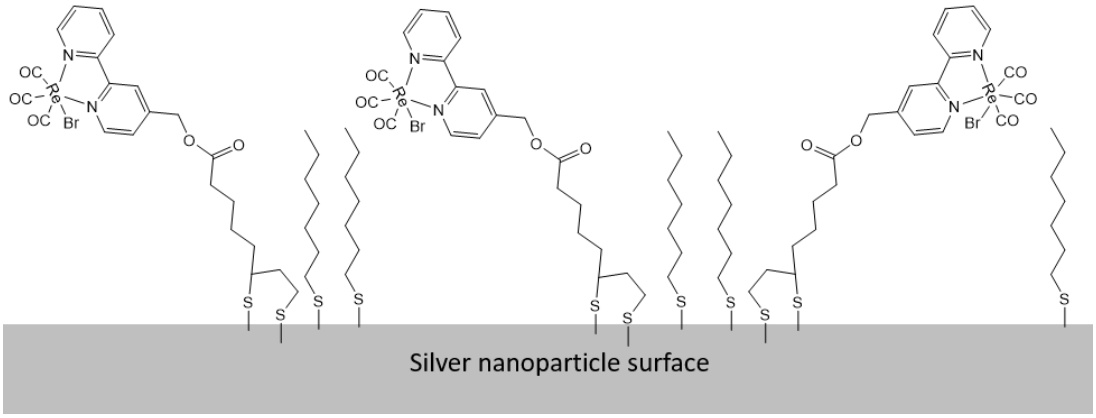

Figure 3.8: *A schematic representation of the mixed thiol nanoparticle surface formed in the "picket fence" approach*

1-Heptanethiol was used as the vibrational response should not obscure the noted Re-centred vibrations. An initial experiment showing that a MeLLF was successfully formed using the standard procedure (Chapter 2. Section 2.2.1), using a 1 mM acetonitrile solution of $CH_3(CH_2)_6SH$. The resulting SERS spectrum suggests that $CH_3(CH_2)_6SH$ is present as a strong vibration at 692 cm^{-1} is seen which is attributed to the C-S vibration (Fig. 3.9), is in close agreement with previously reported data.[13, 14] The alkyl C–C vibrations at 1016 and 1115 cm^{-1} are also visible and representative of the different conformational positions that can be adopted by the carbon atoms adjacent to the sulphur.[13-15] There are also no significant vibrations at 510 cm^{-1} which would mask the presence of the Re-C stretches.

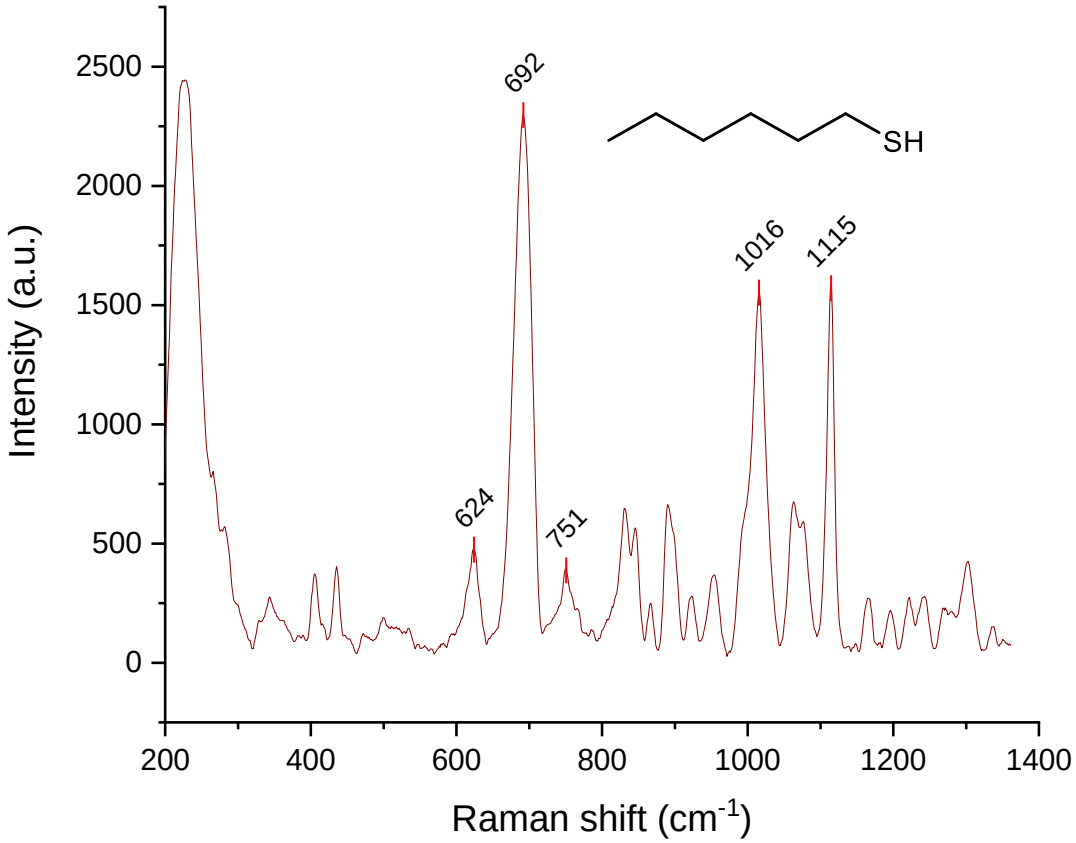

Figure 3.9: *The SERS spectrum of the 1-heptanethiol-functionalised MeLLF*

As heptanethiol can modify Ag NPs that interfacial films can be formed, it was anticipated that this would allow for the thiol to work in combination with the

[Re(L1)(CO)$_3$Br] complex. Using acetonitrile solutions of [Re(L1)(CO)$_3$Br] at concentrations lower than 0.1 mM, in sequentially decreasing increments, MeLLFs were formed using the standard procedure for "picket fence" MeLLFS (Chapter 2. Section 2.2.1). The resulting films appear to show the recognition of the [Re(L1)(CO)$_3$Br] at a concentration of 1x10^{-6} M with the Re-C band at 510 cm^{-1} present (Fig. 3.10). However, at this low complex concentration, the spectrum closely resembles that of the MeLLF formed with only $CH_3(CH_2)_6SH$, suggesting any [Re(L1)(CO)$_3$Br] features are masked by the thiol. As would be anticipated, as the complex concentration is reduced, the concentration of the heptanethiol remains effectively constant and so recognition below this is problematic as signal to noise ratio makes assignment of vibrations difficult. This result does however demonstrate that recognition of the [Re(L1)(CO)$_3$Br] complex is possible using a mixed-thiol system. Vibrations attributed to the Re-CO stretch are still visible at 510 cm^{-1} when the $CH_3(CH_2)_6SH$ is used in combination with a 1x10^{-5} M solution of the [Re(L1)(CO)$_3$Br] complex. This is comparable to 10^{-10} mols of the complex being present on the surface.

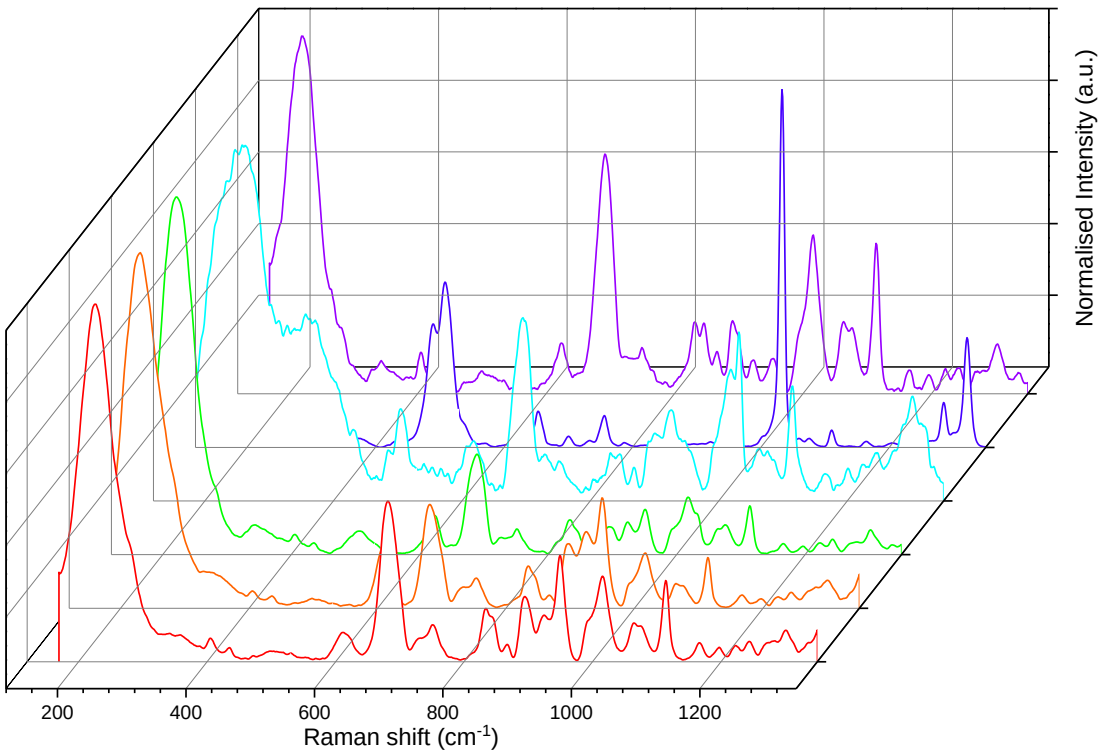

Figure 3.10: *The responses of the concentration dependence study on the "picket-fence" hybrid MeLLFs with comparison of the Re(L1) and 1-heptanethiol MeLLFs. Spectra identified by the concentration of [Re(L1)(CO)$_3$Br] used with CH$_3$(CH$_2$)$_6$SH. (–) 1 mM CH$_3$(CH$_2$)$_6$SH reference, (–) 0.1 mM [Re(L1)(CO)$_3$Br] reference, (–) 1x10^{-5} M [Re(L1)(CO)$_3$Br], (–) 1x10^{-6}M [Re(L1)(CO)$_3$Br], (–) 1x10^{-7} M [Re(L1)(CO)$_3$Br], (–) 1x10^{-8} M [Re(L1)(CO)$_3$Br]*

The SERS spectra of the "picket fence" films, using the decreasing concentrations of [Re(L1)(CO)$_3$Br], at higher wavenumbers show a peak situated at 1373 cm^{-1}. This is tentatively attributed to vibrations of the bpy unit, growing in and out with the [Re(L1)(CO)$_3$Br] concentration changes (Fig. 3.11). The nature of this vibration is unclear however it could be a result of orientation of the complex relative to the surface. It is possible that as concentration of the complex decreases, the metal centre positions closer to the metal surface where the metal centred carbonyls are situated close to the Ag NP surface (Fig. 3.11 insert). This vibration may be a result of the metal centred carbonyls interacting with the surface, assuming that the surface coverage permits the rhenium centre to be in close proximity to the film. SERS studies using the similar L′ complex in aggregated NP systems show changes to the SERS response as

concentration changes so it is plausible to assume the same behaviour would occur in this instance.[4] It is also possible that it is an indication of an orientational change of the heptane thiol. Computational modelling may be able to identify this peak, however such studies have not been undertaken yet.

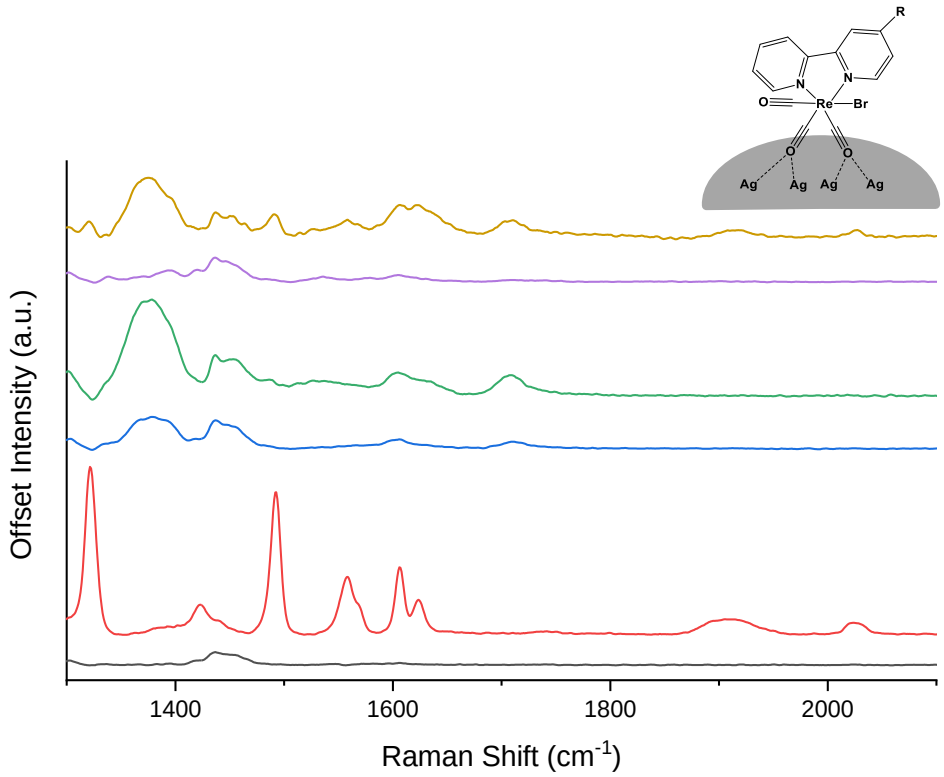

Figure 3.11: *The SERS spectra of the "picket fence" MeLLFs formed with [Re(L1)(CO)$_3$Br] complex solutions of differing concentration. 1x10^{-5}(–) 1x10^{-6} (–) 1x10^{-7} (–) 1x10^{-8} (–) 1mM [Re(L1)(CO)$_3$Br] (–) 1mM CH$_3$(CH$_2$)$_6$SH (–) Insert: the proposed interaction between the Re-CO groups and metal surface.*

3.3.2.2 Mixed Thiol MeLLFs using [Re(L1)(CO)$_3$Br] and Thiophenol

Thiophenol was also considered for use in a mixed thiol approach for the formation of a thiol-hybrid "picket-fence" MeLLF and were formed using decreasing concentrations addition of the [Re(L1)(CO)$_3$Br] with a constant concentration of thiophenol (Chapter 2. Section 2.2.1). The Re-C vibration is observed on the MeLLF using a 0.1 mM solution of [Re(L1)(CO)$_3$Br] (Fig. 3.12). However, the complex-specific vibrations are

overshadowed by thiophenol vibrations beyond 0.1 mM. Thiophenol is a popular SERS label because of its ability to form closely packed and ordered monolayers on metal surfaces. This means there could be competition for binding sites between thiophenol and the [Re(L1)(CO)$_3$Br] complex thus resulting in poor binding of the complex. The Raman response for a thiophenol surface is very strong owing to the highly ordered phenyl rings which would undoubtably make the recognition of anything else on the surface more challenging.[16-19]

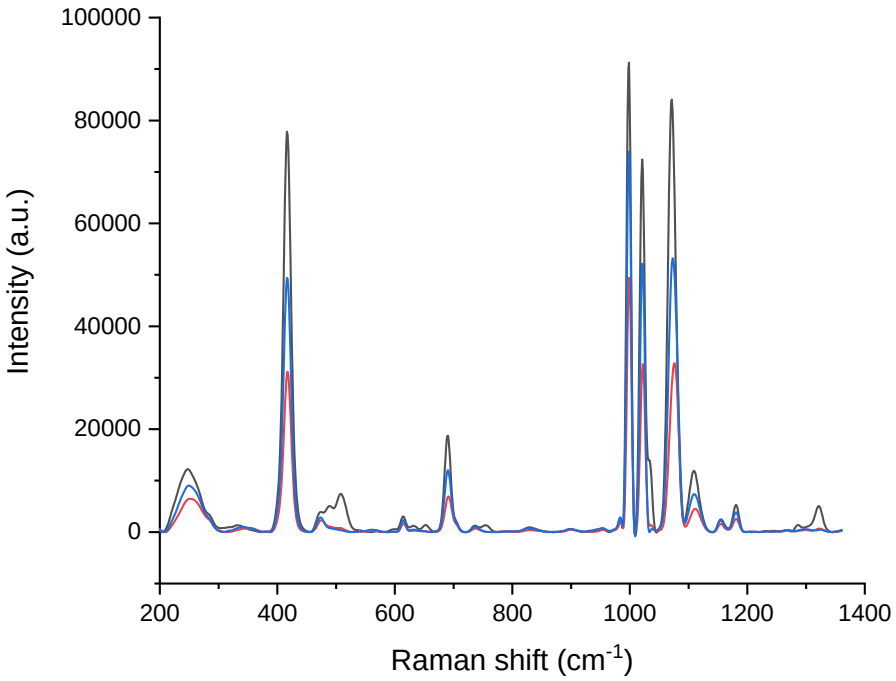

Figure 3.12: *The spectra obtained from the "picket fence" MeLLFs formed using varying concentrations of [Re(L1)(CO)$_3$Br] and thiophenol. Spectra identified by concentration of [Re(L1)(CO)$_3$Br] used; 1x10^{-4} M (–), 1x10^{-5} M (–), 1x10^{-6} (–)*

3.3.2.3 A Summary of "Picket-fence" MeLLFs

MeLLF formation using the mixed thiol, "picket-fence" approach does successfully form films that allow [Re(L1)$(CO)_3$Br] to be seen at concentrations lower than can be achieved using the complex alone. The "picket-fence" MeLLFs formed using [Re(L1)$(CO)_3$Br] and thiophenol allow the observation of the Re-CO vibrations when [Re(L1)$(CO)_3$Br] complex concentration of 0.1 mM solution. However, the fingerprint vibrations of [Re(L1)$(CO)_3$Br] complex are observed when forming a MeLLF using a $1x10^{-5}$ M complex solution in conjunction heptanethiol. Possible vibrations owing to the [Re(L1)$(CO)_3$Br] are also seen at $1x10^{-6}$ M but the signal to noise ratio becomes significant. Despite this, the heptanethiol: [Re(L1)$(CO)_3$Br] films demonstrate that sensing of the complex can be achieved at lower concentrations than solely using the [Re(L1)$(CO)_3$Br] complex. The implications are that improved sensing capabilities may be possible using mixed thiol systems but the methodology requires further investigation.

3.4 Development of Solid Films

3.4.1 Deposition of Promoted MeLLFs onto Glass and Labelling with [Re(L1)$(CO)_3$Br]

MeLLFs are advantageous as a SERS platform as their fabrication is relatively quick, simple and low cost. However, their fluid nature does have some inherent difficulties in their transportation, stability and handling. A possible way of rectifying these issues would be to isolate the MeLLFs on a solid platform, allowing for better control of the physical parameters and minimising the risks of film damage. A potential method to achieve this involved the deposition of the interfacial MeLLFs onto borosilicate glass slides. Glass-deposited (GD) MeLLFs were formed using TBA NO_3 promotion

followed by deposition onto glass slides and subsequent staining with the desired label (Chapter 2. Section 2.2.3).

3.4.1.1 Glass Deposited MeLLFs Stained with [Re(L1)(CO)$_3$Br] Precursors

Initial experiments on the GD-MeLLFs involved staining with 1 mM solutions of the ligand precursors, thioctic acid and bipyridine. The MeLLF stained with a 1 mM solution of thioctic acid presented incredibly broad peaks centred at 1551 cm^{-1} (Fig. 3.13a). The bending and twisting motions of the C-H bonds situated in the alkyl chain are expected in this region and the broadness of the peak maybe representative of numerous contributions. The peak at 657 cm^{-1} which are attributed to vibrational modes belonging to the C–S bond, indicating thioctic acid is present.[13, 14] The absence of a strong vibration belonging to a C–S–S–C group in the region between 500 and 550 cm^{-1}, implies the two sulfur atoms are not bound together and that the molecule is attached to the surface via the Ag-S bond.[20] There is possible observation of the Ag–S bond at 235 cm^{-1} however, instrument limits mean this a speculative conclusion. The vibration at 2912 cm^{-1} corresponds to the symmetrical and asymmetrical C-H of at alkyl tail, additionally stretches of the dithiolane ring CH_2. It is possible that the carboxylic acid group also interacts with the surface which would account for the difference between this spectrum and that of the methyl ester.

Staining with a 1 mM solution of 2,2′-bipyridine (bpy) provided greater insight into the efficacy of the deposited MeLLFs as a platform. The dominant features in the spectrum of the bpy stained glass deposited MeLLF can be attributed to the characteristic vibrational modes of bpy (Fig. 3.13b).[21] Additionally, the spectrum resembles a previously reported 2,2′-bipy-functionalised Ag MeLLF that was deposited on glass.[22] The in-plane ring vibrations are observed at 1603 and 1560 cm^{-1} and 1275 and 1322 cm^{-}

[1] with the most intense band attributed to the C-H deformation stretch at 1489 cm^{-1}. In addition, the ring–ring stretching mode is also visible at 1025 cm^{-1}.

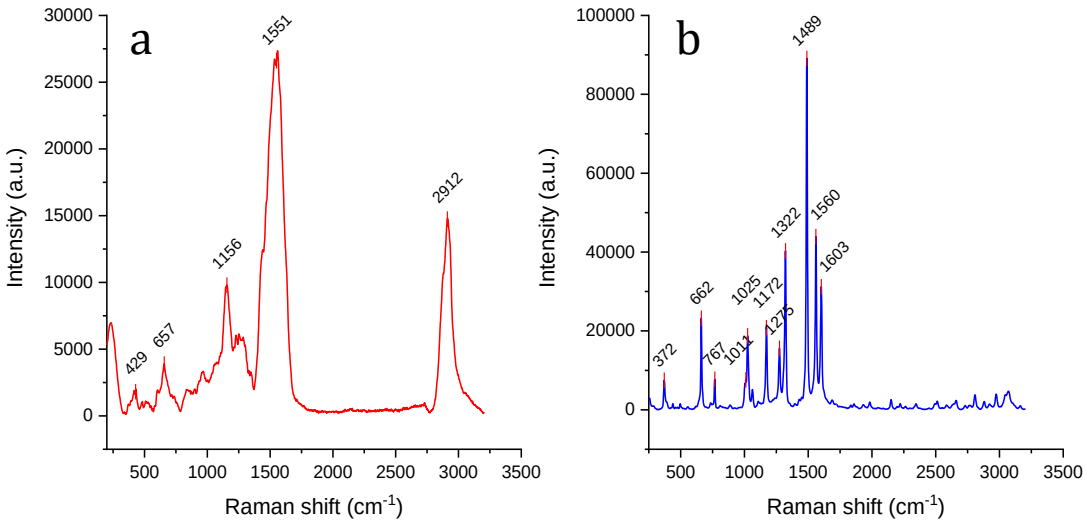

Figure 3.13: *The SERS spectrum of the GD-MeLLFs stained with A) thioctic acid and B) 2,2'-bipyridine*

The SERS spectrum of the GD-MeLLF stained with the bpy dithiolate ligand, L1, displays the component vibrations from both thioctic acid and bpy (Fig. 3.14). The peaks at 664 and 2923 cm^{-1} are assigned to the C–S of the dithiolate ring and the C–H stretches of the alkyl tail respectively. The broad peak around 1500 cm^{-1} is attributed to contributions from both functionalities. The sharper and more defined peaks that stem from it at 1490, 1559 and 1604 cm^{-1} are assigned to the in plane ring and C–H deformation vibrational modes of bipyridine. The weaker vibrations at 1027, 1170 and 1320 cm^{-1} are also considered to belong to the bpy group as they closely resemble the peaks observed from the glass deposited MeLLF stained with bpy.

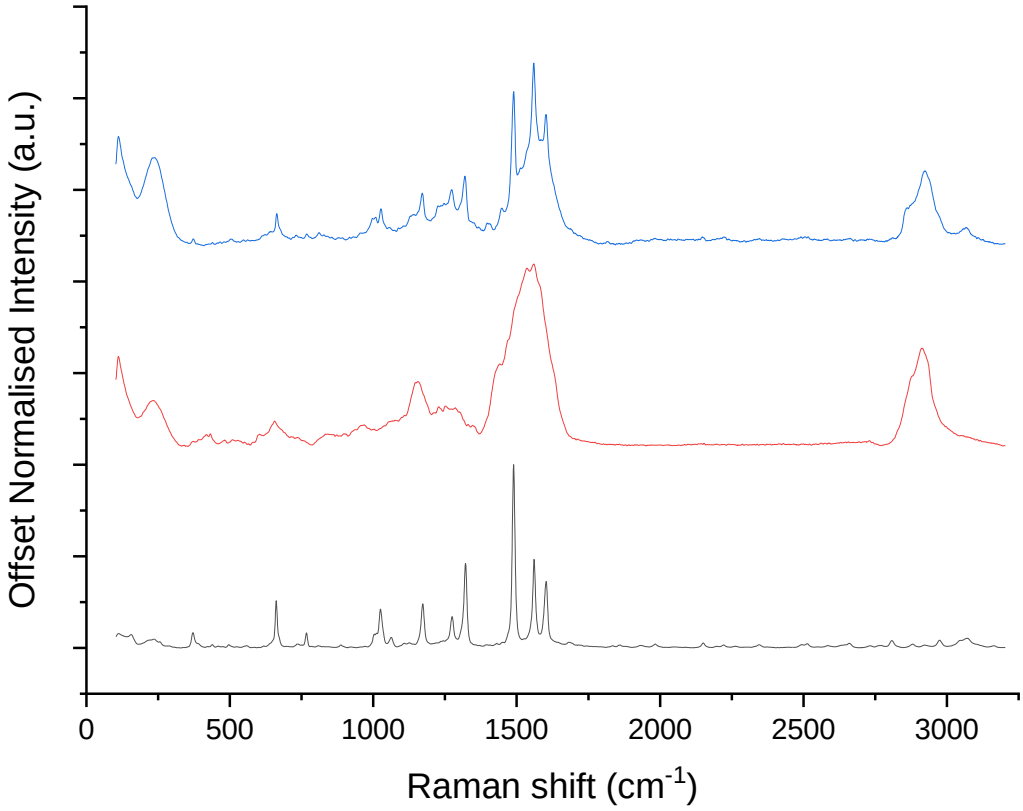

Figure 3.14: *Comparison of the SERS responses obtained via staining GD-MeLLFs with 1 mM 2,2'-bipyridine (–), thioctic acid (–), and the bipy-dithiolate ligand, (L1) (–)*

3.4.1.2 Glass Deposited MeLLFs Stained with [Re(L1)(CO)$_3$Br] Precursors

Staining of a glass deposited MeLLF with a 1x10^{-5} M solution of the [Re(L1)(CO)$_3$Br] complex was also attempted. Initially it was unclear from the Raman spectrum whether the complex was present on the surface (Fig. 3.15). The most dominant vibrations belong to the bipy and thioctic functionality while the expected vibrations owing to the Re-CO group were not immediately apparent. However weak vibrations that could be attributed to both the Re–C at 496 cm^{-1} and the metal CO modes at 1917 and 2019 cm^{-1} were observed close to the baseline (Fig. 3.14insert). It is possible that the peak situated at 558 cm^{-1} belongs to the S-S vibration within the dithiolane ring, suggesting the molecule is sat on the surface as opposed to directly bound to it.

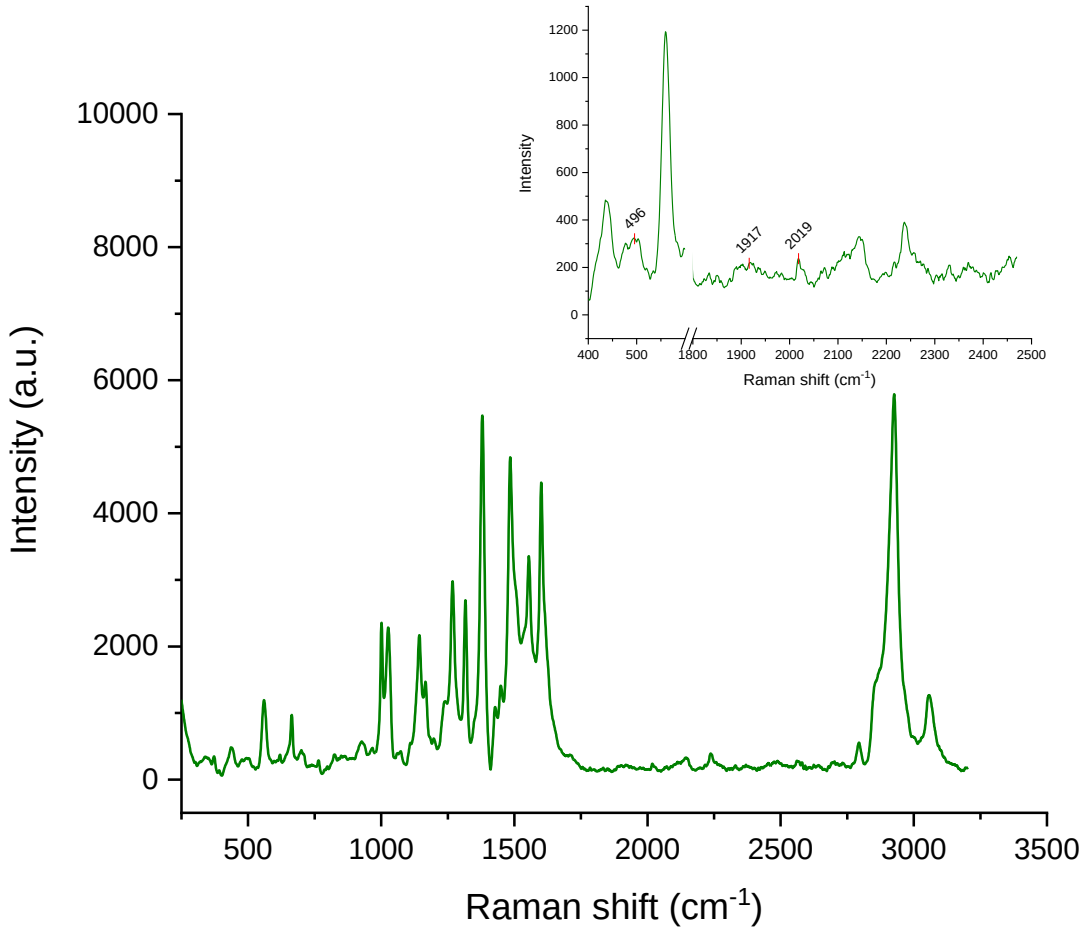

Figure 3.15: *The SERS spectrum of the GD-MeLLF stained with a 1 mM solution of [Re(L1)(CO)$_3$Br]. Insert: An expansion of the[Re(L1)(CO)$_3$Br] spectrum showing the Re–CO vibrations*

Staining with a 0.1 mM solution of the [Re(L1)(CO)$_3$Br] complex yielded better results, giving an assumed Re-CO vibration at 506 cm^{-1} (Fig. 3.16). The moderate vibration attributed to the S–S stretch at 558 cm^{-1} that was seen in the glass deposited MeLLF stained with a lower concentration of [Re(L1)(CO)$_3$Br] is no longer present. This, coupled with the vibration at 655 cm^{-1} that is assumed to be representative of a C–S mode suggest the binding of the complex to the NP surface. Comparisons of the responses from [Re(L1)(CO)$_3$Br] labelled MeLLFs formed via glass deposition and surface modification show differing relative intensities of ligand specific-vibrations (Fig. 3.15). The bpy peaks situated at 1030, 1280 and 1320 cm^{-1} have different relative intensities in the spectra of the two MeLLFs. The peaks at 1033 and 1320 cm^{-1} are

almost equivalent in the spectrum from the glass deposited MeLLF whereas the 1035 cm^{-1} peak is the most intense peak with the others at significantly lower intensity in the spectrum from the liquid-liquid analogue. This may be indicative of the complex having a different orientation relative to the surface through the preparation of both the different methods. Overall, the Raman response from the glass deposited MeLLF stained with the $[Re(L1)(CO)_3Br]$ does strongly point to the complex successfully labelling the deposited MeLLF making this a viable method of fabrication.

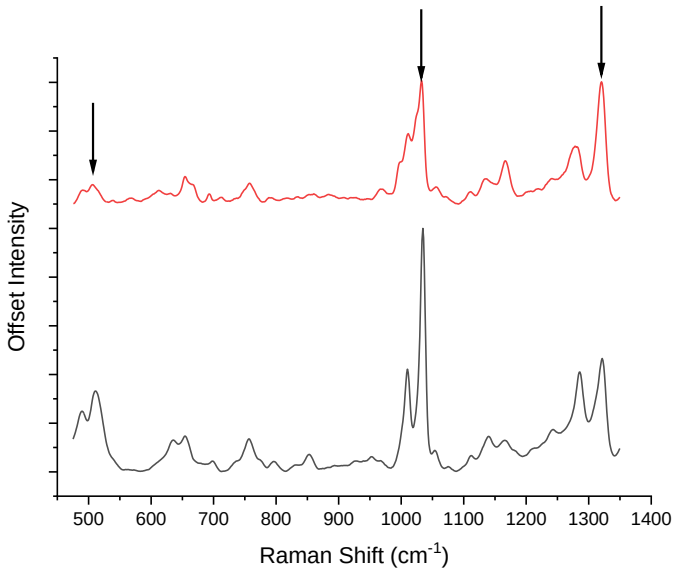

Figure 3.16: *Comparison of the SERS spectra taken from the GD-MeLLF stained with $[Re(L1)(CO)_3Br]$ (–) and the MeLLF formed via nanoparticle modification using $[Re(L1)(CO)_3Br]$ (–). excited at 532nm*

3.4.1.3 Assessments of the Concentration Limits of the Glass-deposited Films Using $[Re(L1)(CO)_3Br]$

The successful recognition of the $[Re(L1)(CO)_3Br]$ complex on the solid films, formed via glass deposition provides an alternative method to form functionalised films. An important difference being that the complex is not required to modify the nanoparticle surface to induce interfacial positioning. It was anticipated that this would allow for the recognition of the complex after staining with concentrations lower than through the complex modified MeLLF formation. To investigate this, glass deposited MeLLFs were

stained with acetonitrile solutions of decreasing concentration of the [Re(L1)(CO)$_3$Br] complex.

The spectra show bpy-specific vibrations are still potentially present at a concentration of 1x10^{-8} M, signified by the ring–ring stretch at 1019 cm^{-1} (Fig. 3.17). Additionally, peaks attributed to the in plane ring and C–H ring deformations at 1486, 1551 and 1608 cm^{-1} can be seen. Surprisingly, the spectrum taken of the film stained with a 1x10^{-14} M [Re(L1)(CO)$_3$Br] solution was still exhibiting peaks that could be attributed to the complex. However the variation in intensity as the concentration decreases does not follow the anticipated trend. An expected result would be the observation of a progressive decrease of the intensity of [Re(L1)(CO)$_3$Br] vibrations as concentration decreases. Unfortunately, the control experiment with the acetonitrile solvent also presented peaks reminiscent of the L1 species which suggests the films are easily contaminated. It is unclear how the contamination occurred as efforts were made to minimise any possible risk of such occurring during the experimental procedure. While this is not ideal when forming labelled surfaces, it does demonstrate the Raman-enhancing capabilities of the films. It is plausible that compounds from the surroundings are able to interact with the films, and if this is occurring, then it can be assumed that any contaminating compounds will be in a very small amount. The recognition of trace amounts the [Re(L1)(CO)$_3$Br] complex may therefore be possible if there was opportunity to produce the films in a cleaner environment.

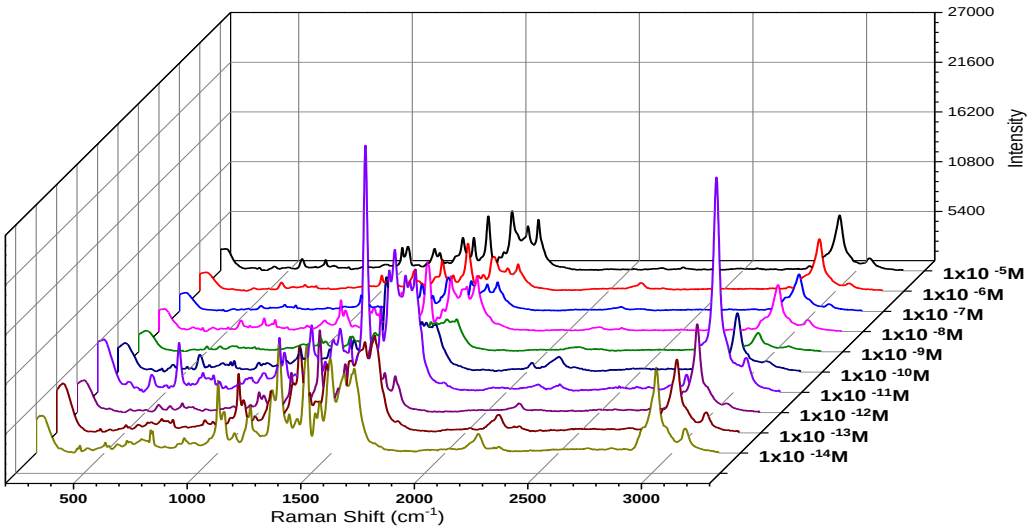

Figure 3.17: *The results from the staining of GD-MeLLFS with decreasing quantities of the [Re(L1)(CO)$_3$Br] in acetonitrile. Excited at 532 nm*

Repeating the experiment with acetone solutions of decreasing concentrations from $1x10^{-5}$ to $1x10^{-14}$ M of the [Re(L1)(CO)$_3$Br] complex presented similar results. The Raman response of a glass deposited MeLLF stained with a $1x10^{-14}$ M complex solution possessed characteristic vibrations owing to the [Re(L1)(CO)$_3$Br] complex. Unfortunately, the control MeLLF slide again presented a similar response, indicating experimental contamination. Despite the possible large enhancement capabilities of the films, further investigation into the fabrication procedure is required before it can be deemed a viable method of film formation. It also illustrates the difficulties of working towards homeopathic concentrations with films designed to bind these reporting groups.

3.4.2 Ag Films Formed Through Photocatalytic Reduction

The generation of a Raman active Ag solid surfaces can also be achieved via the photo-induced reduction of Ag salts using UV radiation. Mills *et al.* describe formation of a SERS active Ag surface by employing the semiconductor photocatalysis using a TiO_2 surface.[23] The initial objectives of this Chapter were to deduced whether the [Re(L1)$(CO)_3$Br] complex could be used to effectively label noble metal nanostructures. The work to this point has involved the use of the [Re(L1)$(CO)_3$Br] as a label for nanoparticles formed through charge stabilisation and it was anticipated that the [Re(L1)$(CO)_3$Br] complex could be used to label a nanostructured surface formed via other methods.

Photo-deposited (PD) Ag films were synthesised using a reported procedure (Chapter 2. Section 2.2.4).[23] The deposition of Ag is apparent due to an observed colour change of the plate surface, and further confirmed using UV-Vis spectroscopy (Fig. 3.18). The absorption spectra of the slides feature a maximum absorption around 360 nm which is in moderate agreement with the literature and is assigned to localised surface plasmon resonance of nanosized silver structures. This provides an indication of their size on the surface and the broad absorbance observed suggests that a variety of structure sizes exist on the surface.[24] Scanning electron microscopy showed these apparent structures on the surface with the lighter grey spots attributed to the Ag nanostructures. (Fig. 3.19). Further analysis with energy-dispersive X-ray (EDX) spectroscopy confirmed the presence of Ag on the surface (Fig. 3.18insert).

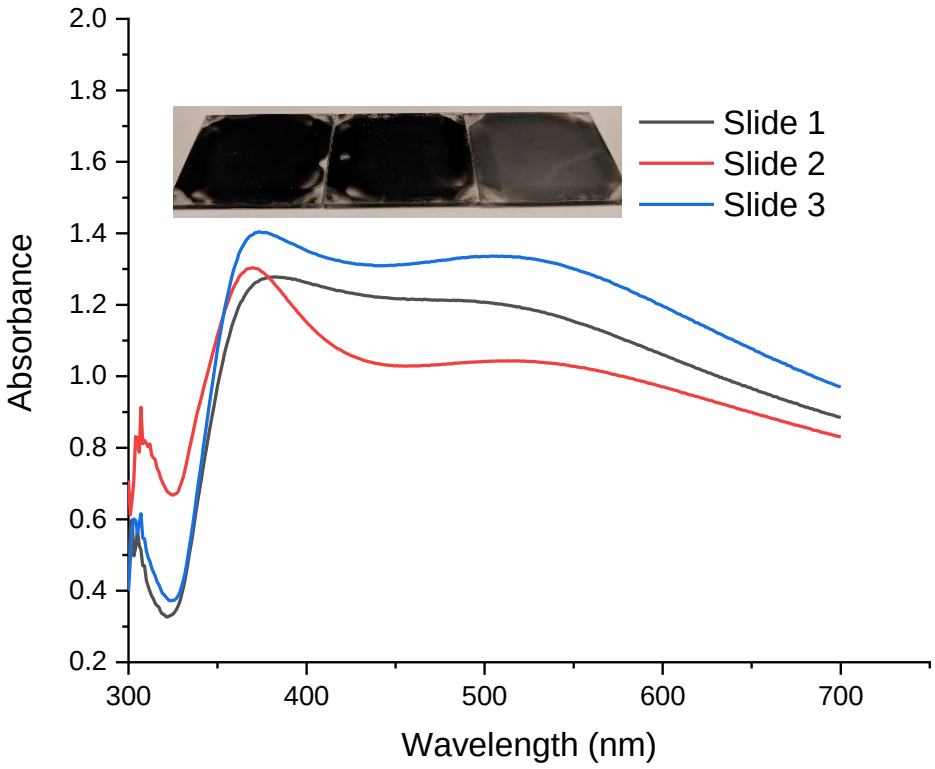

Figure 3.18: *The UV-Vis spectra of the Ag-deposited glass slides, formed via photo-induced reduction of $AgNO_3$. Insert: The Ag glass slides after treatment with $AgNO_3$*

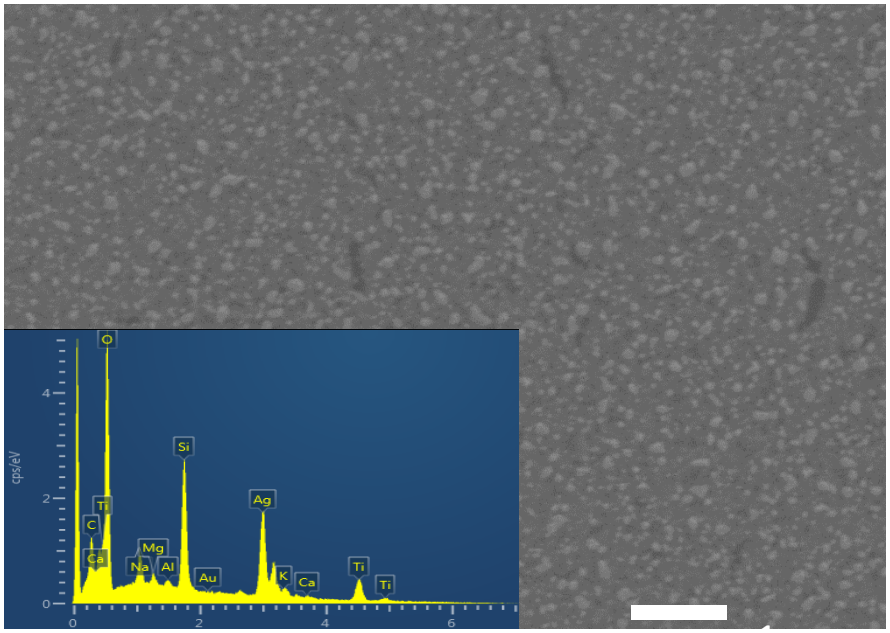

Figure 3.19: *SEM of one of the plates showing Ag structures on the surface. Insert: EDX spectrum showing that elemental Ag was present*

After establishing the presence of Ag structures on the surface, the PD Ag plates were treated with the [Re(L1)(CO)$_3$Br] complex. The plates were partly submerged in a 1 mM solution of the [Re(L1)(CO)$_3$Br] complex and left for several hours before being removed and dried. The SERS spectrum is dominated by features originating from the bpy with the ring–ring stretch at 1024 cm^{-1} and out of phase ring modes visible at 1487, 1562 and 1603 cm^{-1} (Fig. 3.20). The vibrations at 651 and 3069 cm^{-1} may be representative of the dithiolate tail group. Although the vibrations from the bpy allude to the presence of the complex on the surface, the rhenium complex vibrations are not distinguishable.

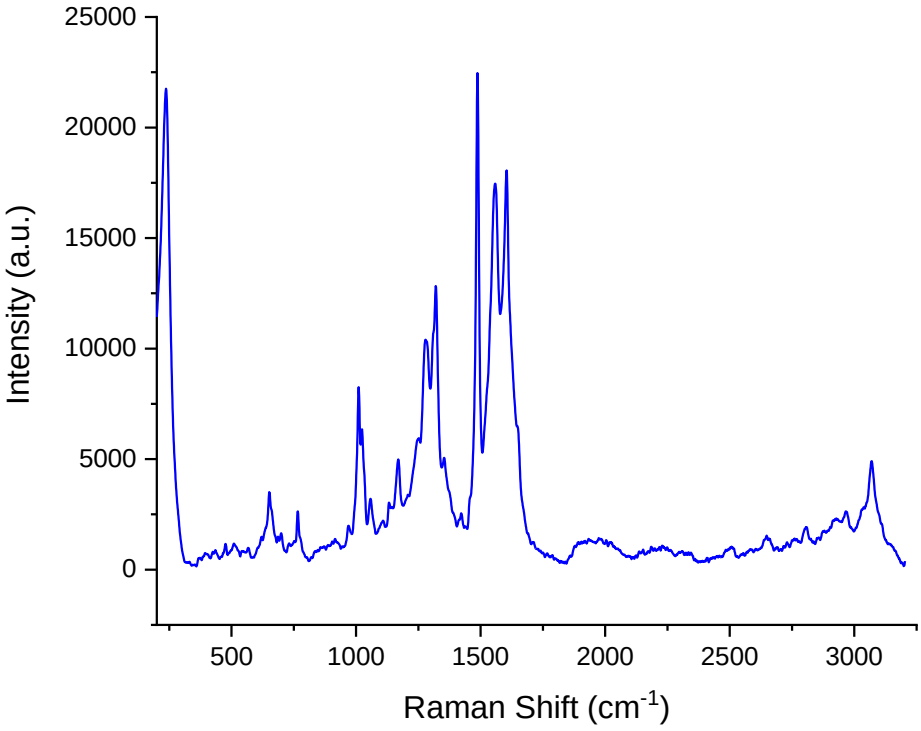

Figure 3.20: *The SERS response from the PD-Ag substrate after staining with a 0.1 mM solution of [Re(L1)(CO)$_3$Br] in acetonitrile. Excited at 532 nm*

To summarise, the use of PD-Ag plates as a possible SERS active substrate for [Re(L1)$(CO)_3$Br] labelling was attempted however, was not developed further. A clear disadvantage of the PD-Ag plates compared to the interfacial films is the difficulty in confirming the presence of the [Re(L1)$(CO)_3$Br] complex on the surface using SERS. It is unclear why staining of the PD-Ag plates with the [Re(L1)$(CO)_3$Br] complex does not appear to show vibrations associated with the Re–CO group. Additionally, the synthetic procedure for the PD-Ag plates is significantly longer and more complex than either the MeLLFs or the SENS. Because of the reasons stated, no further investigation using photocatalytic methods of forming SERS active Ag surfaces were conducted. Overall, the interfacial films prove to be a more suitable substrate for the production of [Re(L1)$(CO)_3$Br] functionalised films.

3.4.3 Surface-Exposed Nanoparticle Sheets

Xu *et al.* have recently demonstrated a new method to isolate NPs from a MeLLF into a reproducible film; surface-exposed nanoparticle sheets or SENS.[25] These are made in a similar manner to MeLLFs in that nanoparticles are either modified or promoted by an additional component resulting in the positioning of the NP at the interface between two immiscible liquids. SENS then rely on the incorporation of a polymer into the organic layer, which creates a robust film upon evaporation. The surface is advantageous as the nanoparticle monolayer is fixed into the polymer leaving one side still chemically accessible.

3.4.3.1 Formation of the SENS using [Re(L1)(CO)$_3$Br]

The modification and interfacial positioning of nanoparticles at a liquid-liquid interface using [Re(L1)(CO)$_3$Br] has been established. The corresponding [Re(L1)(CO)$_3$Br] SENS were formed using the standard procedure using a 0.1 mM acetonitrile of the [Re(L1)(CO)$_3$Br] complex (Chapter 2, Section 2.2.2). The appearance of the films is similar to the MeLLF, having a metallic lustre. They are very flexible upon handling but this is resolved upon the binding of the polystyrene side of the film to sticky tape. SEM characterisation of the films shows the monolayer nature of the surface with NPs in closely arranged 2-dimensional structures (Fig. 3.21c & 3.21d)

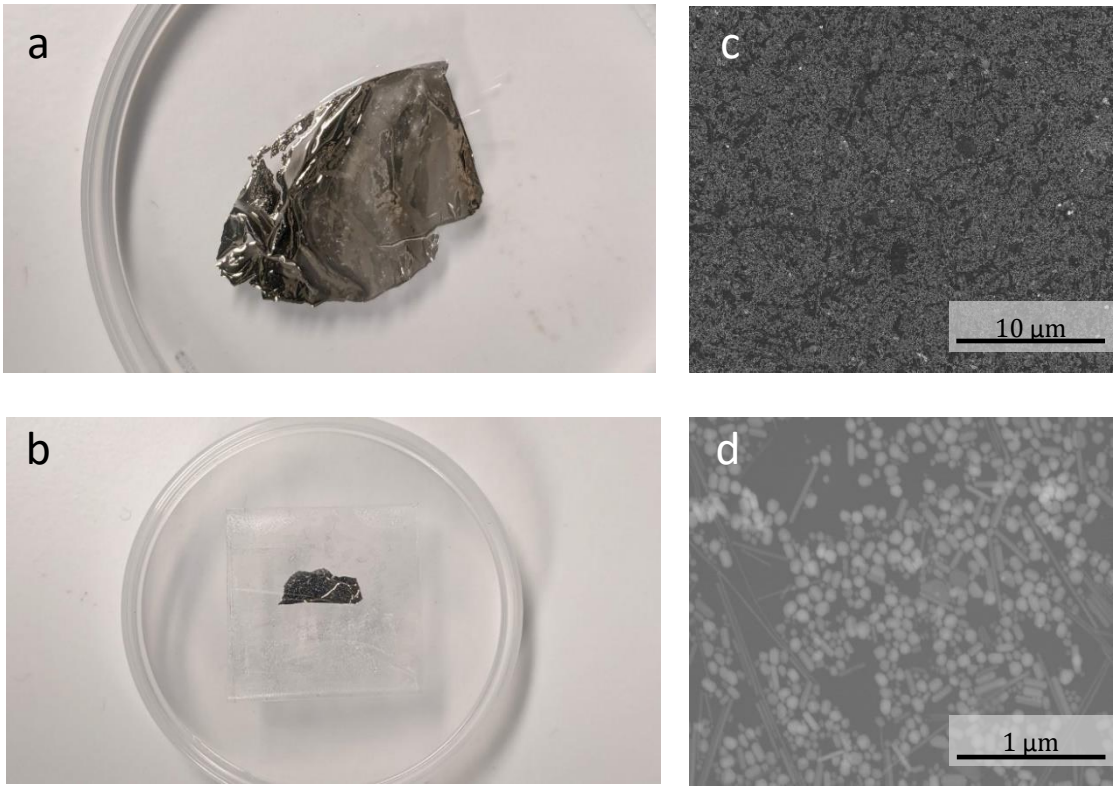

Figure 3.21: *a) A photograph of a SENS formed with 0.1 mM solution of [Re(L1)(CO)$_3$Br] sat on water with the polystyrene layer exposed and b) a section of the SENS isolated on sticky tape with the exposed NP layer. c) Characterisation of the SENS using SEM and d) a closer view of the surface showing the nanoparticles sat at the interface*

The SERS spectrum of the resulting SENS show the Re-CO vibrations are present at 509, 1904 and 2025 cm^{-1} while the C-S mode from the tail at 614 cm^{-1} is visible (Fig 3.22). The ring–ring stretch is evident at 1034 cm^{-1} along with signals associated with the bpy peak and C-S stretch of the tail. The spectrum is similar to the MeLLF spectrum, indicating that the [Re(L1)$(CO)_3$Br] modified nanoparticles are exposed and not encased in the polymer. The absence of vibrations that can be attributed to the polystyrene layer is also noted. The conclusion therefore, is that the [Re(L1)$(CO)_3$Br] complex can successfully generate the SENS materials with an exposed surface that exhibits the SERS spectrum of the [Re(L1)$(CO)_3$Br] complex.

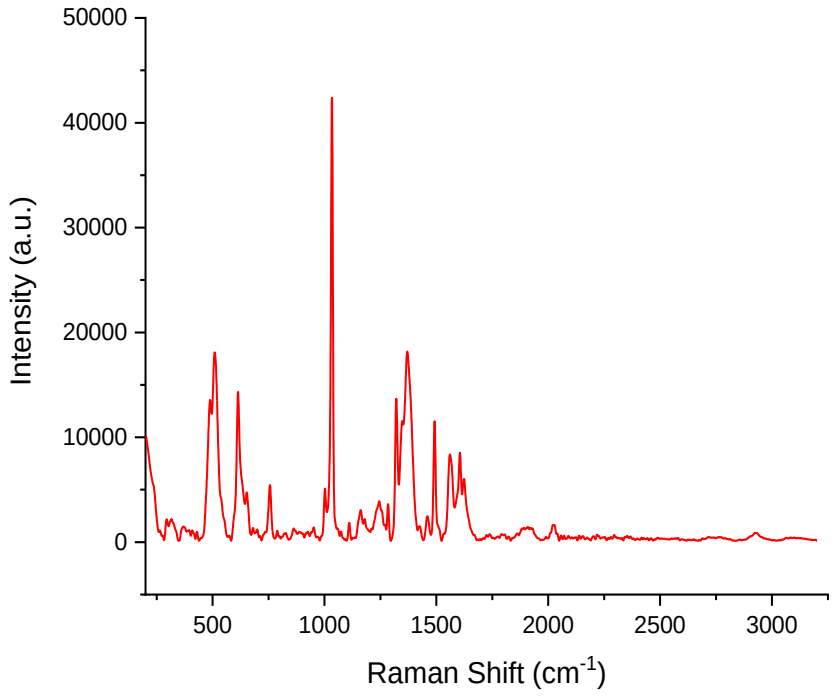

Figure 3.22: *The SERS spectrum of a SENS surface obtained using Ag NPs modified with the [Re(L1)$(CO)_3$Br] complex*

***Table 3.5**: The peak assignments for the SERS spectrum of a SENS formed using Re(L1)(CO)$_3$Br]*

Wavenumber (cm^{-1})	Assignment
509	Re–C str.
654	Aliphatic C–S str.
757	Aliphatic C–S str.
1034	Ring–Ring str.
1285	Ring str. (C–C, C–N) + inter-ring str. + C–H in-plane def.
1321	C–C inter-ring str. + in-plane C–H def.
1492	Ring str. (C–C, C–N) + inter-ring str. + C–H in-plane def.
1558	Ring str. (C–C, C–N)
1606	Ring str. (C–C, C–N)
1623	Ring str. (C–C, C–N)
1901	Re–(C≡O) carbonyl str.
2021	
2932	Alkyl C–H str.
3078	C–H str. (Alkyl + dithiolane ring)

Stretching = str. Deformation = def.

3.4.3.2 Labelling a Promoted SENS using [Re(L1)(CO)$_3$Br]

SENS can be formed via TBA salt promotion as described in the original work by Xu *et al*. generating a SENS surface that would be available for labelling with the [Re(L1)(CO)$_3$Br] complex. An assessment was made on the difference between using *in-situ* modification of colloidal nanoparticles or the labelling of SENS substrate through TBA salt promotion had been produced. A TBA promoted SENS was prepared according to the standard procedure (Chapter 2, Section 2.2.2). After extraction using sticky tape, the SENS was then soaked with a 100 µl droplet of a 0.1 mM solution of [Re(L1)(CO)$_3$Br] and washed with clean acetonitrile. The resulting SERS spectrum contains the typical vibrations of the [Re(L1)(CO)$_3$Br] complex with peaks corresponding to the Re–CO, bpy and tail components visible (Fig. 3.23).

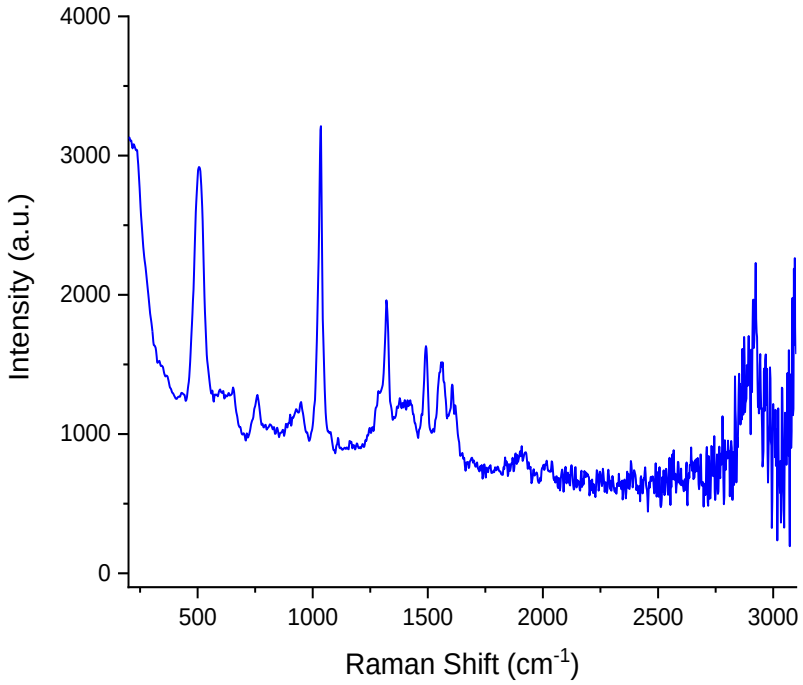

Figure 3.23: *The SERS spectrum of a Ag NP SENS formed via TBA salt promotion and subsequent staining with a 0.1 mM solution of [Re(L1)(CO)$_3$Br] for 30 seconds. Conducted at Queen's University, Belfast using a Perkin Elmer Raman Micro 200 Raman Microscope, excited at 785 nm*

The comparison of the SERS spectra of the SENS formed through the staining of a TBA promoted SENS using [Re(L1)(CO)$_3$Br] solutions (Method 1) and nanoparticle modification (Method 2) shows a dramatic difference in the SERS intensity (Fig. 3.24). The intensity of the Re–C stretch of the SENS formed via method 2 is over 2000% more intense than the Re–C band of the SENS formed via method 1. The modification used in method 2 potentially results in monolayer coverage of the individual nanoparticles which may be an advantage as more of the complex is occupying areas where the nanoparticles are in close proximity. Therefore the observed difference in intensity is an example of "hot spots" (Chapter 1, Section 1.5.1). In the case of the SENS formed via method 1, the interaction of the rhenium label with the surface will be subject to available space on the surface. The presence of a [Re(L1)(CO)$_3$Br] complex on the NP surface may sterically hinder further binding of another molecule, thereby possibly

limiting the coverage on the surface. Furthermore, this may inhibit the binding of complex molecules in these areas that give rise to high SERS intensity.

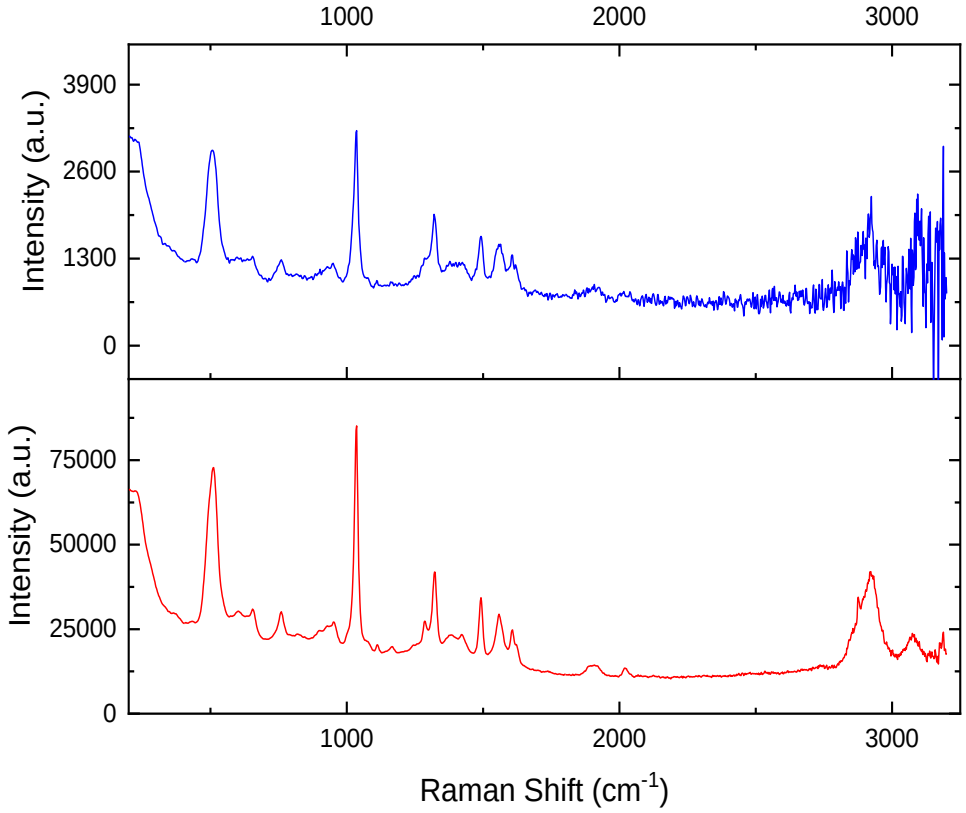

Figure 3.24: *The SERS spectra of the SENS after 30 second soaking with a 0.1 mM solution of [Re(L1)(CO)₃Br] (Method (–) and the SENS formed with via NP modification using [Re(L1)(CO)₃Br] (–). Excited at 785 nm*

Despite the SERS intensity differences of the SENS formed via methods 1 and 2, the results illustrate that the SENS formed via method 2 allows for the recognition of the [Re(L1)(CO)$_3$Br] complex after soaking for 30 seconds. However, this does not suggest that this is the optimal staining time for this particular approach. The formation of a [Re(L1)(CO)$_3$Br] functionalised SENS was again formed via method 2 and the SERS response was taken at 20 second intervals. A sharp increase is initially observed before the intensity plateaus (Fig. 3.25). Some fluctuations are observed at 220 and 400 seconds however the average intensity after almost 10 minutes is still around 4500

counts. This suggests the surface is readily saturated and prolonged exposure to the [Re(L1)(CO)$_3$Br] solution does not greatly affect the observed response. Nonetheless, it still outlines that the staining of a SENS formed through TBA salt promotion can then be functionalised with the [Re(L1)(CO)$_3$Br] complex, offering an alternative method of fabrication.

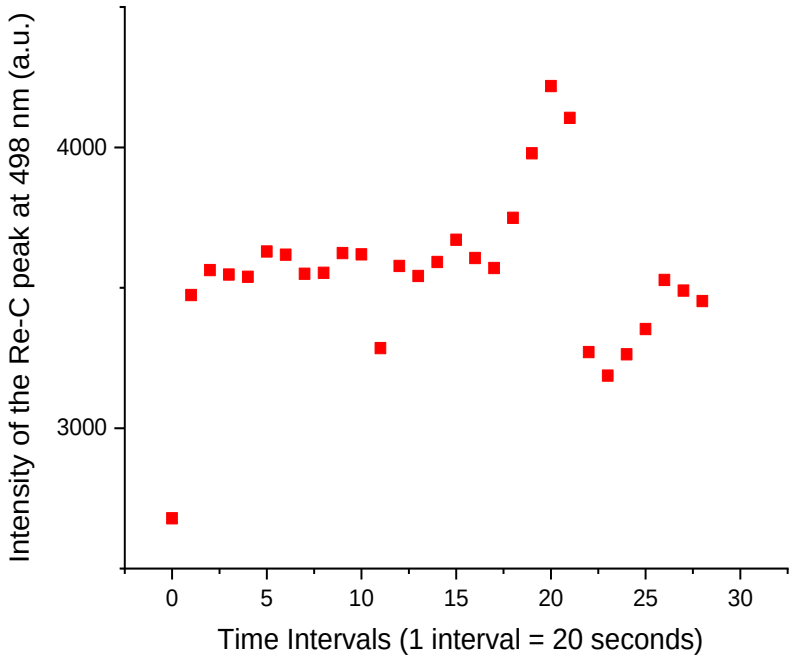

Figure 3.25: *A plot detailing how the intensity of the Re-C vibration changes with time during the soaking of a SENS with a 0.1 M solution of [Re(L1)(CO)$_3$Br]. Each time interval represents a period of 20 seconds*

3.4.3.3 Attempts at Forming Mixed Thiol SENS

Due to the similarity in which both the MeLLFs and the SENS are fabricated, it can be assumed that the constraints of SENS formation are similar to the MeLLFs and therefore dependent on sufficient surface coverage. The results discussed in Section 3.3 describe the ability to form the "picket fence" MeLLFs which achieved recognition of the complex at concentrations lower than the films formed with [Re(L1)(CO)$_3$Br] alone. It

was expected that the same could be replicated with the solid SENS analogues. To investigate this, "picket fence" SENS were formed by combining the procedures for the formation of heptanethiol/[Re(L1)$(CO)_3$Br] MeLLFs and the standard procedure for SENS formation (Chapter 2, Section 2.2). Addition of a $1x10^{-5}$ M solution of [Re(L1)$(CO)_3$Br] and a 1mM solution of $CH_3(CH_2)_6SH$ produced a SENS film. The SERS spectrum does share similarities with the liquid-liquid analogue with the component vibrations of both thiols featuring the Re–C stretch at 509 cm^{-1}, though weak in intensity (Fig. 3.26). Attempts with lower concentrations of the [Re(L1)$(CO)_3$Br] complex proved to be unsuccessful as only vibrations from the heptanethiol are visible. It is unclear why this is the case as the anticipated result was that it would mimic the SERS response seen by the hybrid MeLLF (Section 3.3.2.1). Despite this, the results show that the mixed thiol "picket fence" approach can also be used for the fabrication of the SENS.

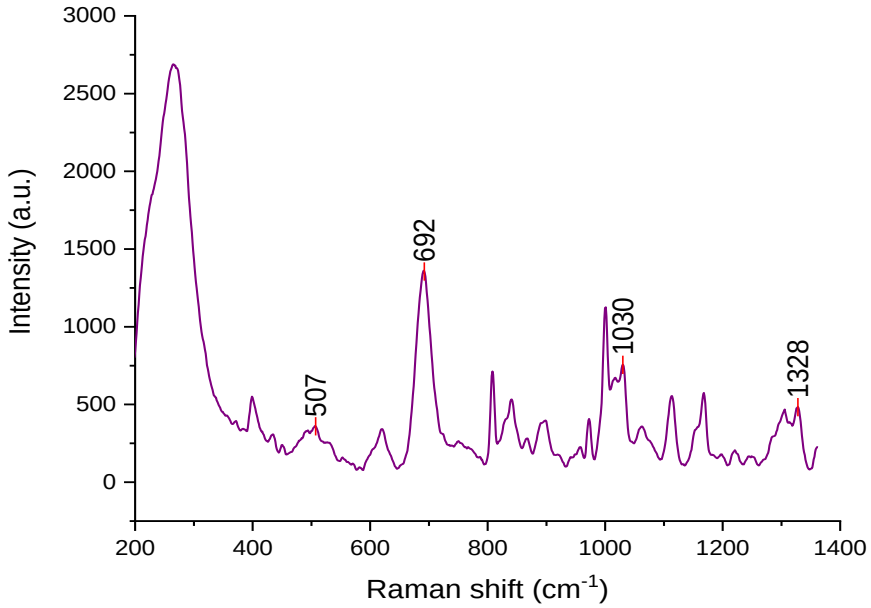

Figure 3.26: *The SERS spectrum of a mixed thiol SENS formed with $1x10^{-5}$ M solution of [Re(L1)(CO)3Br] and 1 mM $CH_3(CH_2)_6SH$*

In summary, the formation of SENS using [Re(L1)$(CO)_3$Br] functionalised nanoparticles builds upon the work of rhenium functionalised MeLLFs (Section 3.2). The SERS response of the [Re(L1)$(CO)_3$Br] SENS displays the characteristic features of the complex while resolving the physical issues associated with the liquid-liquid counterparts. Additional work was conducted to assess the preferred method of labelling a SENS surface with the [Re(L1)$(CO)_3$Br] complex. Both the use of the complex as a modifier and soaking an unlabelled SENS with the complex generates a film that displayed the vibrations inherent to the [Re(L1)$(CO)_3$Br] complex. The SERS response of the SENS formed through the modification of nanoparticles using [Re(L1)$(CO)_3$Br] followed by film formation is distinctly more intense than a film formed via TBA salt promotion and labelled post film formation. This is believed to be a result of the complex being in regions of greater SERS enhancement or “hot spots”. Additionally, the “picket fence” approach can also be used for the formation of mixed thiol SENS. This approach allows for recognition of the [Re(L1)$(CO)_3$Br] complex at a concentration lower than using the [Re(L1)$(CO)_3$Br] complex alone.

3.5 Conclusions on the Development of Rhenium-functionalised Films

The [Re(L1)(CO)$_3$Br] complex can be used to modify noble nanoparticles and induce the interfacial positioning resulting in [Re(L1)(CO)$_3$Br] functionalised MeLLFs. This is confirmed by recognition of complex-specific vibrations on the film using surface-enhanced Raman spectroscopy. This appears to provide a simple and reproducible method of forming a rhenium functionalised surface that possesses a characteristic SERS response. Expanding on this by introducing a polymer to the organic phase allows for more robust films to be produced. The SENS films combine the highly ordered NP monolayer properties of the MeLLFs with the advantages of solid films.

Further studies were also conducted that focused on using mixed thiol layers as a strategy to form both the MeLLF and SENS variants, to identify the lowest concentration of the [Re(L1)(CO)$_3$Br] complex that could be detected by Raman spectroscopy. This mixed thiol system demonstrated a greater degree of sensitivity than using the complex alone as the spectrum of the heptanethiol/[Re(L1)(CO)$_3$Br] MeLLF shows metal-centred vibrations were still observable at a [Re(L1)(CO)$_3$Br] concentration of $1x10^{-6}$ M.

An investigation was also conducted to assess whether MeLLFs could be transferred on to solid substrates. The glass-deposited MeLLFs were shown not to be easily reproducible and had high susceptibility to contamination. Additional work was conducted to see whether simple substrates produced via the photo-induced reduction of Ag(I) could also provide a useful substrate for generating Re(I)-modified surfaces. The procedure for the fabrication of both the glass deposited MeLLFs and the PD Ag

slides were significantly more time consuming than either the interfacial films therefore were judged to be unsuitable approaches for the proposed application.

The [Re(L1)$(CO)_3$Br] functionalised MeLLFs and SENS provide a reproducible surface that offers huge enhancement of the metal-centred and ligand vibrations with the advantage of simple methods of production. It is hoped that such surfaces can now be used to track specific ion-binding interactions using SERS.

3.6 References

1. B. Shan, Y. Pu, Y. Chen, M. Liao and M. Li, *Coord. Chem. Rev.*, 2018, **371**, 11-37.
2. L. Faucher, E. F. Borra and A. M. Ritcey, *J. Nanosci. Nanotechnol.*, 2008, **8**, 3900-3908.
3. G. C. Phan-Quang, X. Han, C. S. L. Koh, H. Y. F. Sim, C. L. Lay, S. X. Leong, Y. H. Lee, N. Pazos-Perez, R. A. Alvarez-Puebla and X. Y. Ling, *Acc. Chem. Res.*, 2019, **52**, 1844-1854.
4. H. J. Montgomery, D. Pelleteret, S. E. J. Bell and N. C. Fletcher, *Inorg. Chem.*, 2011, **50**, 2738-2747.
5. Y. Xu, M. P. Konrad, W. W. Lee, Z. Ye and S. E. Bell, *Nano Lett.*, 2016, **16**, 5255-5260.
6. K. K. Maiti, A. Samanta, M. Vendrell, K.-S. Soh, M. Olivo and Y.-T. Chang, *Chem. Commun.*, 2011, **47**, 3514-3516.
7. M.-J. Li, X. Liu, M.-J. Nie, Z.-Z. Wu, C.-Q. Yi, G.-N. Chen and V. W.-W. Yam, *Organometallics*, 2012, **31**, 4459-4466.
8. V. Gallo, A. Lai, A. Pasquo, S. Almaviva, S. Iacobelli, L. Persichetti, G. Capellini and G. Antonini, *Anal. Bioanal. Chem.*, 2020, **412**, 7659-7667.
9. I. Matulaitienė, Z. Kuodis, O. Eicher-Lorka and G. Niaura, *J. Electroanal. Chem.*, 2013, **700**, 77-85.
10. G. Socrates, *Infrared and Raman characteristic group frequencies: tables and charts*, John Wiley & Sons, 2004.
11. A. Stewart, S. Zheng, M. R. McCourt and S. E. J. Bell, *ACS Nano*, 2012, **6**, 3718-3726.
12. A. Stewart and S. E. Bell, *Chem. Commun.*, 2011, **47**, 4523-4525.
13. M. A. Bryant and J. E. Pemberton, *J. Am. Chem. Soc.*, 1991, **113**, 8284-8293.
14. M. A. Bryant and J. E. Pemberton, *J. Am. Chem. Soc.*, 1991, **113**, 3629-3637.
15. A. Kudelski, *J. Raman Spectrosc.*, 2003, **34**, 853-862.
16. K. T. Carron and L. G. Hurley, *J. Phys. Chem.*, 1991, **95**, 9979-9984.
17. J. Pate, A. Leiden, B. J. Bozlee and R. L. Garrell, *J. Raman Spectrosc.*, 1991, **22**, 477-480.
18. M. A. Bryant, S. L. Joa and J. E. Pemberton, *Langmuir*, 1992, **8**, 753-756.
19. A. Tripathi, E. D. Emmons, S. D. Christesen, A. W. Fountain and J. A. Guicheteau, *J. Phys. Chem. C*, 2013, **117**, 22834-22842.
20. E. Podstawka, Y. Ozaki and L. M. Proniewicz, *Appl. Spectrosc.*, 2004, **58**, 1147-1156.
21. E. Castellucci, L. Angeloni, N. Neto and G. Sbrana, *Chem. Phys.*, 1979, **43**, 365-373.
22. B. Vlckova, S. M. Barnett, T. Kanigan and I. S. Butler, *Langmuir*, 1993, **9**, 3234-3238.
23. A. Mills, G. Hill, M. Stewart, D. Graham, W. E. Smith, S. Hodgen, P. J. Halfpenny, K. Faulds and P. Robertson, *Appl. Spectrosc.*, 2004, **58**, 922-928.
24. M. Kerker, O. Siiman and D. Wang, *J. Phys. Chem.*, 1984, **88**, 3168-3170.
25. Y. Xu, M. P. Konrad, J. L. Trotter, C. P. McCoy and S. E. J. Bell, *Small*, 2017, **13**, 1602163.

Chapter 4:

Metal Cation Sensing using Rhenium-functionalised Films

4.1 Introduction

In Chapter 3, the successful formation of Re-functionalised nanoparticle films using interfacial positioning through surface modification was described. The relatively simple fabrication methods for both MeLLFs and SENS, coupled with the SERS activity of the [Re(L1)$(CO)_3$Br] complex provides an opportunity to explore the development of a "SERS sensing platform". Employing transition metal complexes for SERS-based sensing has seen limited attention although there are examples present in the literature. For example, the work by Kong *et al.* has shown a triosmium complex bound to a gold surface can be used for the detection of glucose.[1]

The sensing of aqueous mercuric ions (Hg^{2+}) using SERS has seen particular focus in recent years with the literature containing numerous examples with the review by Li *et al.* providing a comprehensive overview of the recent developments.[2] The use of labelled sensors, where the SERS response is based on observed changes of a molecule bound to a SERS-active surface, have been used for such purposes. A recent example is the aminothiophenol-functionalised Ag-Au alloy as described by Guo *et al.* in their work on the detection of Hg^{2+} in black tea.[3]

Re(I) complexes, similar in structure to [Re(L1)$(CO)_3$Br] introduced in Chapter 3, have been investigated as a potential sensor for Hg^{2+} in work conducted previously by the Fletcher group (Fig 4.1).[4] It was observed that the introduction of Hg^{2+} to [Re(bpy)$(CO)_3$Br] and [Re(L′)$(CO)_3$Br] gives a "turn-on" fluorescent response and it was proposed that this was facilitated removal of bromide and the subsequent coordination of solvent.

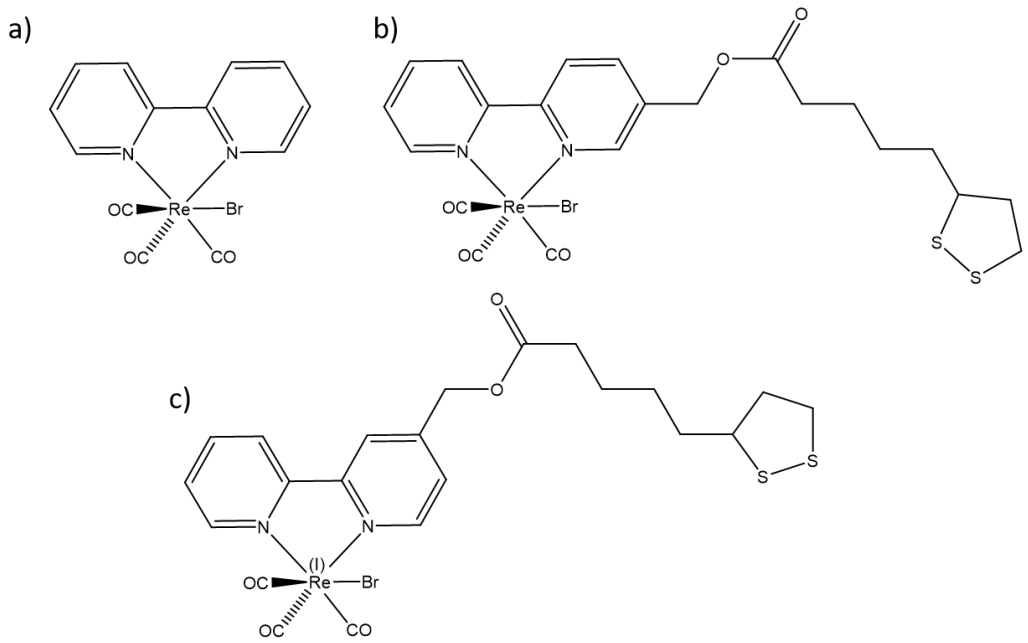

Figure 4.1: *The structures of a) [Re(bpy)(CO)$_3$Br] and b) [Re(L')(CO)$_3$Br] that were investigated for their possible response to the presence of Hg^{2+}along with c) [Re(L1)(CO)$_3$Br].*[4]

The aims of this Chapter are to explore whether rhenium-functionalised interfacial films can be employed for targeted sensing. Additionally, to confirm that the previously observed Hg^{2+} specific behaviour of the similar complex, [Re(L′)(CO)$_3$Br] can also be seen with the [Re(L1)(CO)$_3$Br] and to investigate whether vibrational changes could be observed by Raman spectroscopy and these films can operate as a labelled SERS detecting surface, potentially displaying specific behaviour for cationic mercury.

4.2 Metal Cation Sensing using the Bipyridyl Ligand System, L1

4.2.1 The SERS Response of a MeLLF formed through Bipyridyl-Dithiolate Modification

The bipyridyl-dithiolate species, L1, is a nanoparticle-modifying species that can aid the self-assembly of nanoparticles at an interface (Chapter 3 Section 3.2.2). It has been previously noted that ligand orientation of a similar species on the surface can be controlled by the concentration.[5] At higher concentrations, the density of the ligand surface resulting in the ligand "standing up", with the bpy functional group positioned away from the surface. It was therefore anticipated that a ligand modified NP film would present metal cation sensing capabilities through the coordination of bpy ligands with metal cations.[6] The SERS spectrum of a L1 MeLLF is made up of contributions from both bpy and dithiolate groups (Fig 4.2). The peaks positioned at 997, 1024, 1313, 1445 and 1570 cm^{-1} are all contributions from the bpy while the peaks at 616 and 756 cm^{-1} correspond to the C–S vibrations as discussed in Chapter 3.

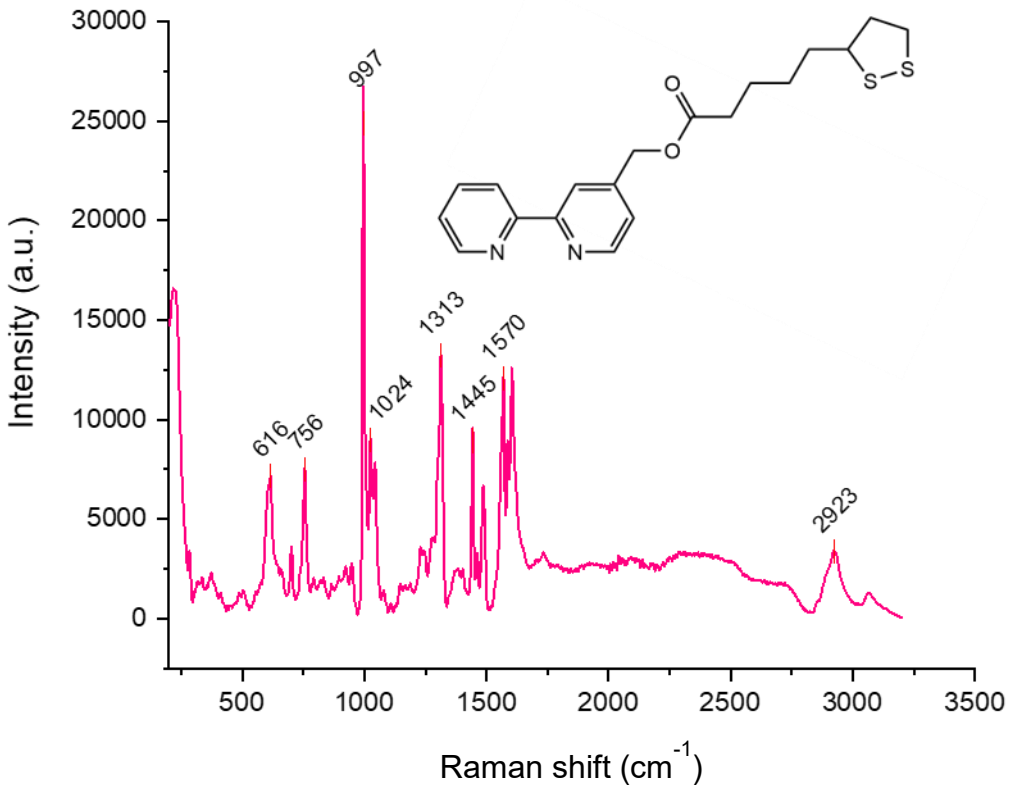

Figure 4.2: *The SERS spectrum of an Ag MeLLF formed using a 1 mM solution of the bpy-thiolate ligand, L1 as a modifier. Excited at 785 nm. Insert: The structure of L1*

4.2.2 SERS Detection of Metal Cations Using L1 MeLLFs

100 µl additions of different 1 mM metal perchlorate salt solutions were made to ligand functionalised MeLLFs and the SERS measurements were made. The introduction of metal cations are seen to induce spectral changes to the bpy contributions between 950 and 1700 cm^{-1} (Fig 4.3). The peak at 995 cm^{-1}, which corresponds to ring breathing, is a point of interest as this vibration responds to the presence of several metal cations. Zn^{2+} causes the appearance of a strong vibration at 1024 cm^{-1} that is of similar intensity to the adjacent 995 cm^{-1} vibration. The addition of Fe^{2+} and Co^{2+} also results in strong vibrations at 1033 and 1023 cm^{-1} respectively, with little or no contribution from the original ring breathing mode. This suggests that the coordination of a metal centre to the bpy species causes a shift in the ring breathing mode and the ring–ring stretch as the

ligand orbitals involved in the metal coordination causes a strengthening of the inter-ring bond.[7] The addition of Hg^{2+} generates a peak at 1008 cm^{-1}, which appears as a shoulder to the original vibration and could be representative of a binding interaction.[8] The addition of Pb^{2+} only appears to cause a very slight decrease in the intensity of the moderate band at 1024 cm^{-1}. Pb^{2+} is the largest of the cations that was screened with the L1-functionalised MeLLF so this limited interaction maybe a result of steric hindrance and reorientation of the bpy group.[9] This may also account for why the interaction with Hg^{2+} also appears to be limited. An additional reason is that the stability of the metal-bpy bond is comparatively weaker than the other cations therefore chelation to the bpy group is hindered.

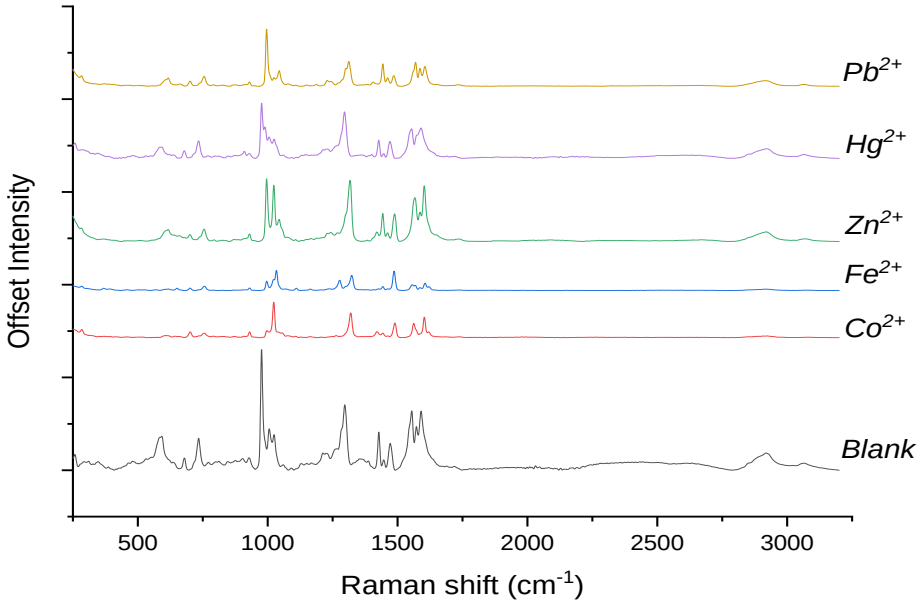

Figure 4.3: *The SERS spectra of the L1-functionalised MeLLFS and the SERS response after the addition of the different metal cations. Excited at 785 nm*

***Table 4.1**: A table showing the impact or metal coordination on selected vibrations of the L1 MeLLF*

Wavenumber (cm^{-1}						Assignment
L1	L1–Co	L1–Fe	L1–Zn	L1–Hg	L1–Pb	
995	995 (w)	995(m)	995	995	995	Ring breathing
1024	1023	1034	1024 (s)	1008	1024 (w)	Ring–Ring stretch
1313	1320	1312	1317	1312	1312	C–C inter-ring stretch and

(w)=weak, (m)=moderate, (s)=strong

This preliminary study using a L1-functionalised MeLLF for the sensing of metal cations in solution suggests that labelled MeLLFs may have wider applications in SERS-active sensing. The observable differences to the spectra of the L1 MeLLFs after the addition of Fe^{2+}, Co^{2+} and Zn^{2+} suggest such films could be used for aqueous metal cationic sensing. Furthermore, similar spectral changes were observed in a study combining the bipyridyl coordination of metal cations and the aggregation of AgNPs.[10] However, the discrimination of the individual cations would be more challenging in the absence of signature vibrations. Cations with larger ionic radii, in this case Hg^{2+} and Pb^{2+} do not illicit the same degree of response. This may be due cation binding being sterically hindered or they do not bind as strongly to the bpy moiety. This does however demonstrate that functionalised interfacial films have possible application within sensitive and selective cation sensing using SERS.

4.3 Solution-based Spectroscopic Studies of Re(L1) and Hg^{2+}

4.3.1 UV-Vis and Emission Spectroscopic Studies of $[Re(L1)(CO)_3Br]$ and Hg^{2+}

Bipyridyl ligands chelated to rhenium centres have UV-vis absorbances attributed to metal-to-ligand-charge-transfer (MLCT) and π-π^* transitions, with emissive characteristics in the visible region. Additionally, a selective Hg^{2+} interaction was previously observed in a complex that is structurally very similar to $[Re(L1)(CO)_3Br]$ in solution.[4] Furthermore, the presence of a dithiolate tail suitably modifies the surface of citrate stabilised nanoparticles, allowing for the formation of the interfacial films. The $[Re(L1)(CO)_3Br]$ complex displays similar photophysical behaviour of analogous $[Re(bpy)(CO)_3Br]$ complexes, with a MLCT absorbance is observed at 372 nm and ligand centred transitions at 251, 293 and 326 nm (Fig 4.4). When excited at 380 nm, an emission is observed at 617 nm (λ_{max}).

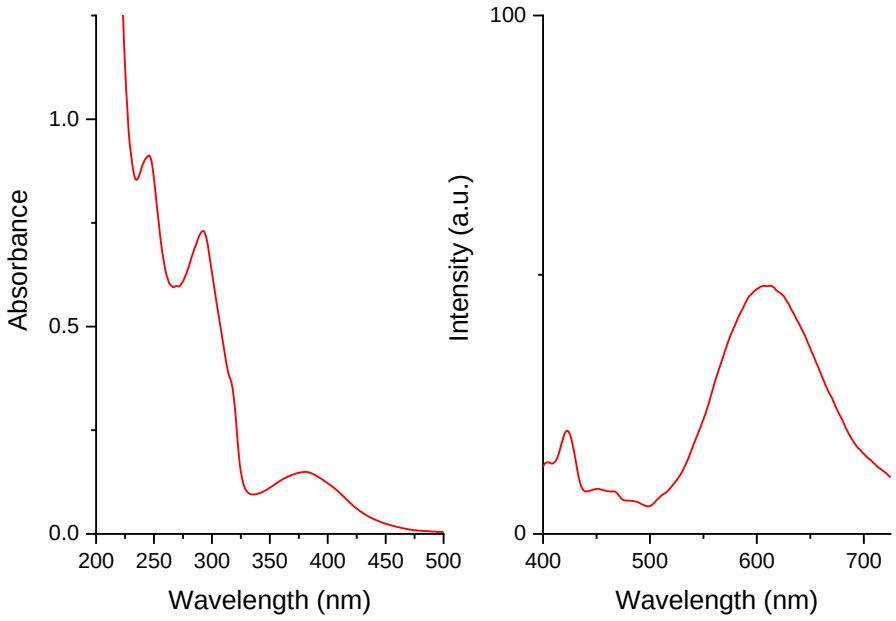

Figure 4.4: *The UV-vis and emission spectra of the $[Re(L1)(CO)_3Br]$ complex in aerated CH_3CN. Sample was excited at 380 nm in aerated acetonitrile at 298 K.*

Table 4.2: *The photophysical properties of the [Re(L1)(CO)$_3$Br] with comparison to the [Re(bpy)(CO)$_3$Br] standard.*

Complex	Absorption[a], λ_{max}/nm				emission[a]	
	LMCT	LC		MLCT	λ_{max}/nm	Φ_{em}[d]
[Re(bpy)(CO)$_3$Br]	244	292	315	366	609[b]	7.8x10^{-3}
[Re(L1)(CO)$_3$Br]	251	293	326	372	617[c]	3.0x10^{-3}

a – in aerated CH_3CN at 298 K at a concentration of 1 x10^{-5} M.
b – excited at 400 nm in aerated CH_3CN at 298 K.
c – excited at 380 nm in aerated CH_3CN at 298 K
d - emission quantum yields (Φ_{em}) were calculated relative to [Re(CO)3Br(bpy)] (Φ_{em} = 7.8 x 10-3)[11] in acetonitrile

To confirm that [Re(L1)(CO)$_3$Br] also displayed similar behaviour when in solution and treated with Hg^{2+}, sequential additions of metal salts in molar equivalent ratios were made to a [Re(L1)(CO)$_3$Br] in aerated acetonitrile. The metal cations of interest were Hg^{2+}, Ag^{+}, Cu^{2+}, Pb^{2+}, Co^{2+}, Cd^{2+}, Ni^{2+}, Zn^{2+} and Fe^{2+}. UV-Vis and emission spectroscopic measurements of the resulting solution were then taken. The sequential addition of 5.0 and 10.0 molar equivalents of a number of metal salts to an acetonitrile solution of [Re(L1)(CO)$_3$Br] do not elicit any particular changes in the optical properties of the complex (Fig 4.5.). The majority of metal cations tested, do not induce an observable change in the UV-vis spectrum of [Re(L1)(CO)$_3$Br]. This is coupled with a slight quenching of the emission with exception of the addition of 5.0 molar equivalents of $Cu(ClO_4)_2$ and $Ni(ClO_4)_2$. Both Cu^{2+} and Ni^{2+} cause a slight increase in emission intensity however to reiterate, this is not coupled with any change in the UV-Vis response.

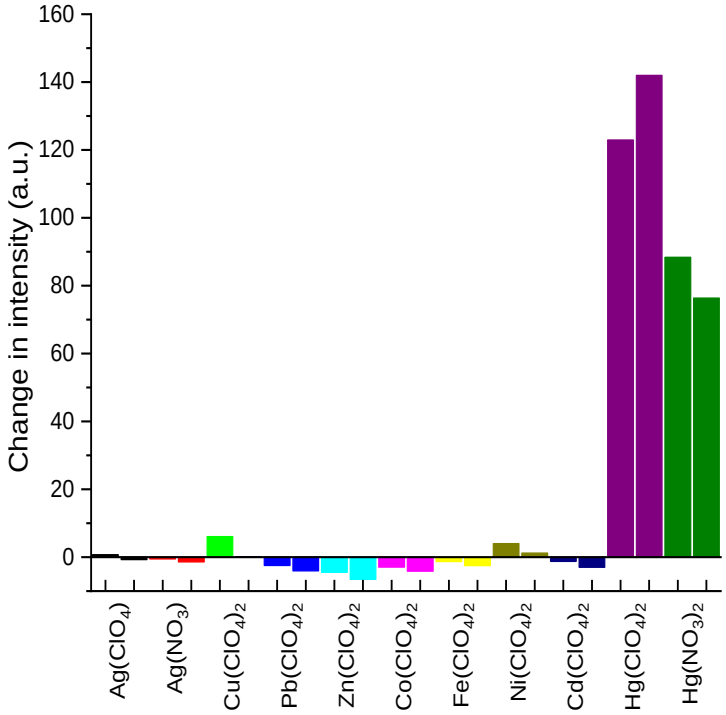

Fig 4.5: *The change in emissive intensity observed upon the addition of 5.0 and 10.0 molar equivalents of various metal salts to a [Re(L1)(CO)$_3$Br] solution.*

The addition of $Hg(ClO_4)_2$ results in notable changes to the UV-Vis spectrum of the [Re(L1)(CO)$_3$Br] complex coupled with changes to the emission intensity (Fig 4.6a). There is a considerable blue shift of the metal-to-ligand charge transfer (MLCT) absorption band from 378 to 341 nm which is accompanied by an intensity increase of the $\pi \rightarrow \pi^*$ transition at 326 nm. There is also a dramatic change in the observed emission spectrum with an increase in the quantum yield coupled with a blue shift from 609 nm to 550 nm (Fig 4.6b). The proposed mechanism is that Hg^{2+} facilitates the removal of the bromide from the metal centre and it is therefore anticipated that the observed spectroscopic changes are representative of this interaction.

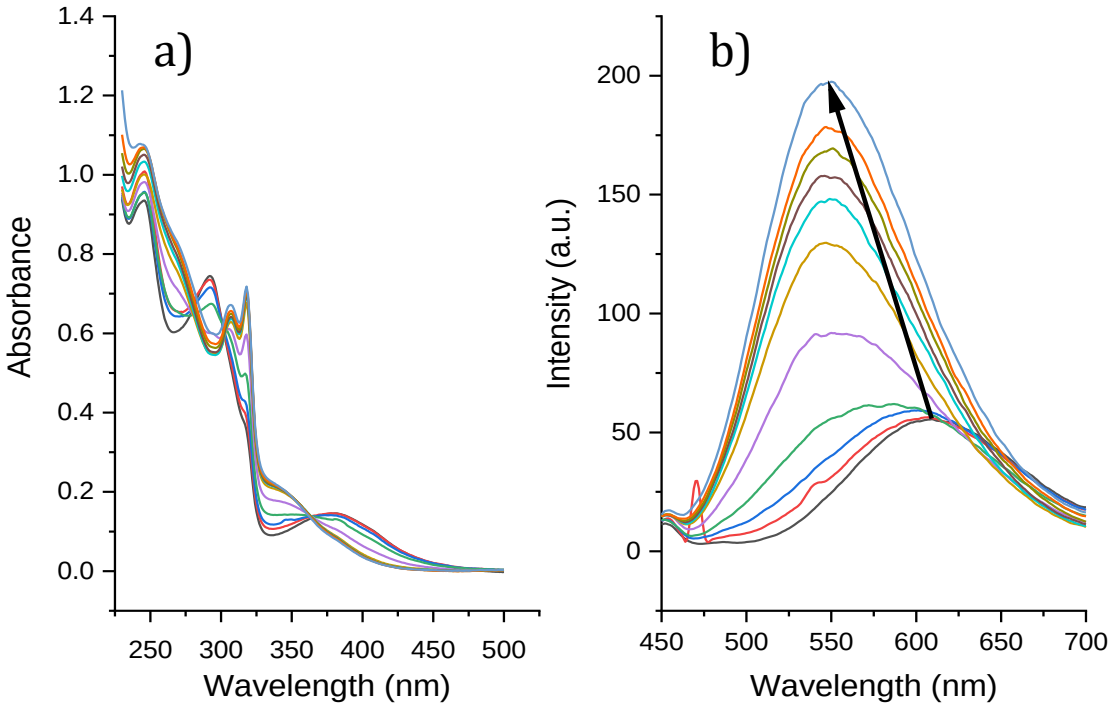

Figure 4.6: *The a) UV-Vis and b) emission response from the titration of the [Re(L1)(CO)$_3$Br] with Hg(ClO$_4$)$_2$ in acetonitrile. Emission excitation conducted at 400 nm. Hg(ClO$_4$)$_2$ molar equivalents 0.0 (–), 0.2 (–), 0.4 (–), 0.6 (–), 0.8 (–), 1.0 (–), 1.5 (–), 2.0 (–), 3.0 (–), 5.0 (–), 10.0 (–). Emission response from sample in aerated acetonitrile and excited at 400 nm at 298 K*

Conducting a similar titration experiment with the addition of Hg(NO$_3$)$_2$ to a [Re(L1)(CO)$_3$Br] solution, induces a similar optical response. The MLCT is blue-shifted from 381 nm to 344 nm and an increased absorbance of the $\pi \rightarrow \pi^*$ transition at 318 nm (Fig 4.7b). Furthermore, there is a similar blue shift that occurs with the λ_{max} of emission moving from 609nm to 547 nm coupled with an increase in quantum yield (Fig 4.7b). There is a subtle difference between Hg(ClO$_4$)$_2$ and Hg(NO$_3$)$_2$, with a slight decrease in the emission intensity once the molar equivalents of Hg(NO$_3$)$_2$ increases beyond 3.0. A possible explanation for this spectroscopic difference is the resultant complex formed after bromide removal. It is anticipated that the coordination of CH$_3$CN into the vacant site occurs. It is at this point that, as the concentration of Hg(NO$_3$)$_2$ increases, the NO_3^- is able to substitute with the coordinated solvent resulting in the

formation of a [Re(L1)$(CO)_3(NO_3)$]. Whereas this does not occur in the case of the perchlorate salt due to its noncoordinating nature.[12]

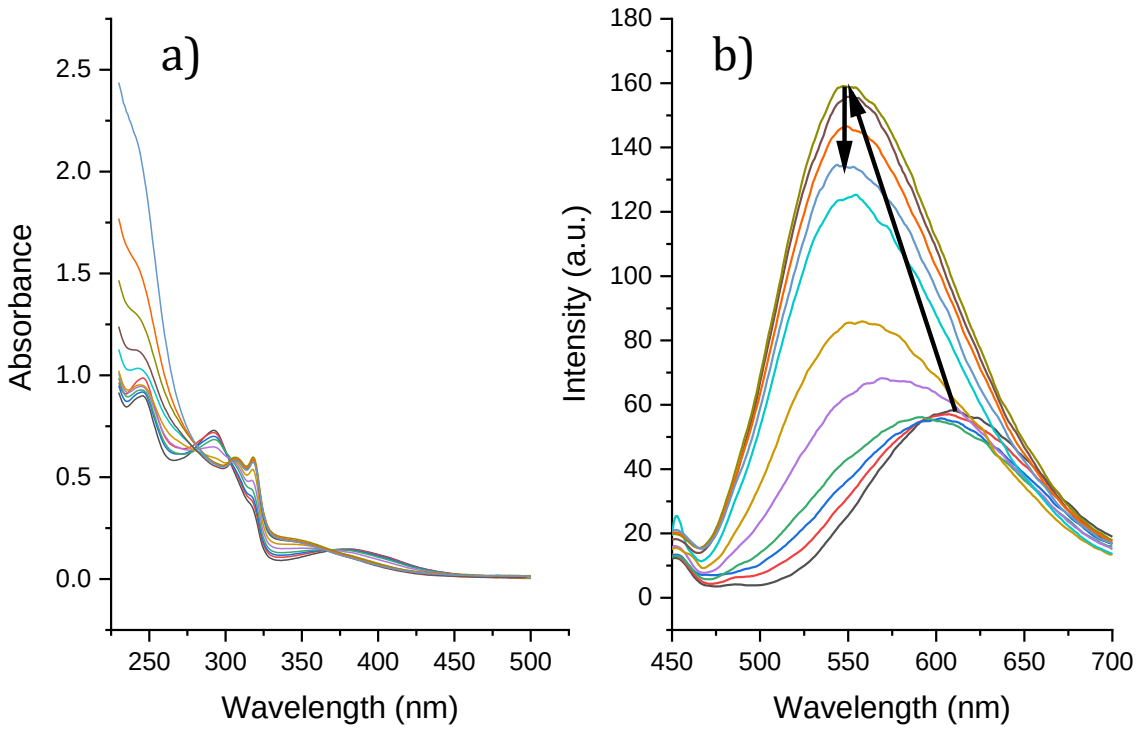

Figure 4.7: *The a) UV-Vis and b) emission spectra from the titration of the [Re(L1)$(CO)_3$Br] with $Hg(NO_3)_2$ in acetonitrile. Emission excitation conducted at 400 nm. $Hg(NO_3)_2$ molar equivalents 0.0 (–), 0.2 (–), 0.4 (–), 0.6 (–), 0.8 (–), 1.0 (–), 1.5 (–), 2.0 (–), 3.0 (–), 5.0 (–), 10.0 (–). Emission response from sample in aerated acetonitrile and excited at 400 nm at 298 K*

4.3.2 ^{1}H NMR Spectroscopy Studies of [Re(L1)$(CO)_3$Br] and Hg^{2+}

Sequential additions of Hg^{2+} salts were made to [Re(L1)$(CO)_3$Br] in acetonitrile-d_3 to investigate the possible structural changes that occur. Addition of $Hg(ClO_4)_2$ results in progressive changes to the NMR spectrum (Fig 4.8). The shift at 5.32 ppm, assigned to the methylene proton, undergoes a gradual decrease in intensity with a new shift appearing at 5.35 ppm as Hg^{2+} concentration increases. Similarly, the peaks assigned to protons 5 and 5′ on the bipyridyl group at 7.62 ppm are lost with a new environment appearing at 7.73 ppm. The same is seen with proton 4′ at 8.21 ppm, proton 6′ at 9.00

and both the 3 and 3′ environments at 8.39 ppm and 8.46 ppm respectively. The changes to the spectrum appear to occur stoichiometrically with the transition from the starting material to the new complex complete after the addition of 0.5 to 0.6 equivalents. This suggests that as the molar equivalents of Hg^{2+} increases, a new complex is formed and that the complex-Hg^{2+} interaction occurs at a 2:1 stoichiometry. This is in good agreement with a previous study.[4]

The addition of $Hg(NO_3)_2$ to a solution of $[Re(L1)(CO)_3Br]$ in acetonitrile-d_3 causes similar behaviour with the slow disappearance of some of the initial peaks growth of new peaks growing as Hg^{2+} concentration increases (Fig 4.9). The shift corresponding to the 5 and 5′ protons at 7.59 and 7.62 ppm decreases with another peak growing in at 7.71 ppm. This initially resembles the response seen with the addition of $Hg(ClO_4)_2$ however once molar equivalence reaches 0.5, a third species begins to grow in. This is most apparent in the 6 and 6′ environments located furthest down field. Addition of greater than 0.5 equivalents causes precipitation of the sample preventing further analysis. A possible explanation is that the $[Re(L1)(CO)_3(CH_3CN)]^+$ is formed initially and as the $Hg(NO_3)_2$ concentration increases, NO_3^- substitutes with the CH_3CN adduct to give a $[Re(L1)(CO)_3(NO_3)]$ complex. This may also explain the observed intensity decrease in both emissive and UV-Vis responses $Hg(NO_3)_2$, however no precipitation in the optical spectroscopic samples was observed.

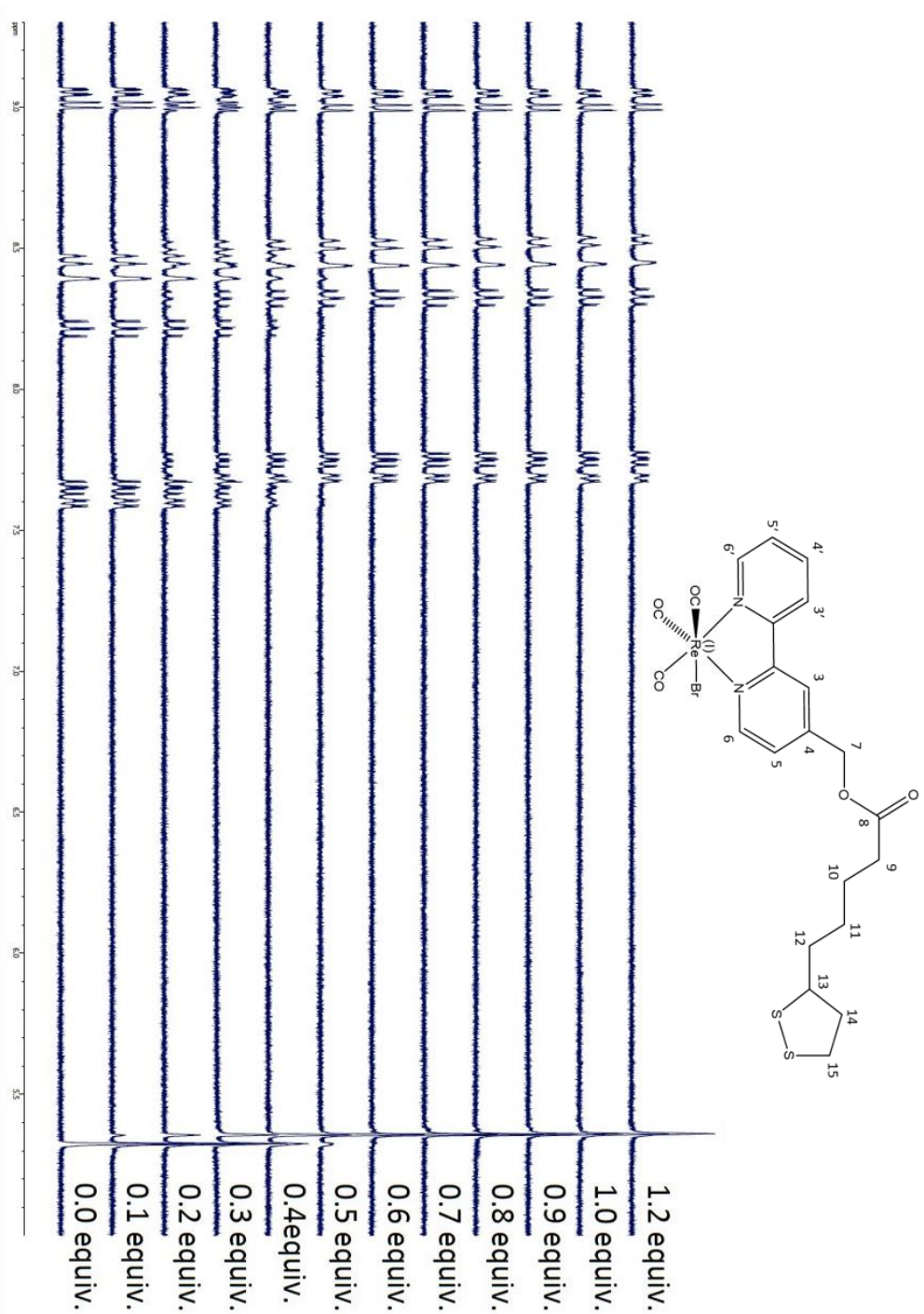

Figure 4.8: *The ^1H NMR titration of $[Re(L1)(CO)_3Br]$ with $Hg(ClO_4)_2$ conducted at 300 MHz at 298 K in acetonitrile-d_3.*

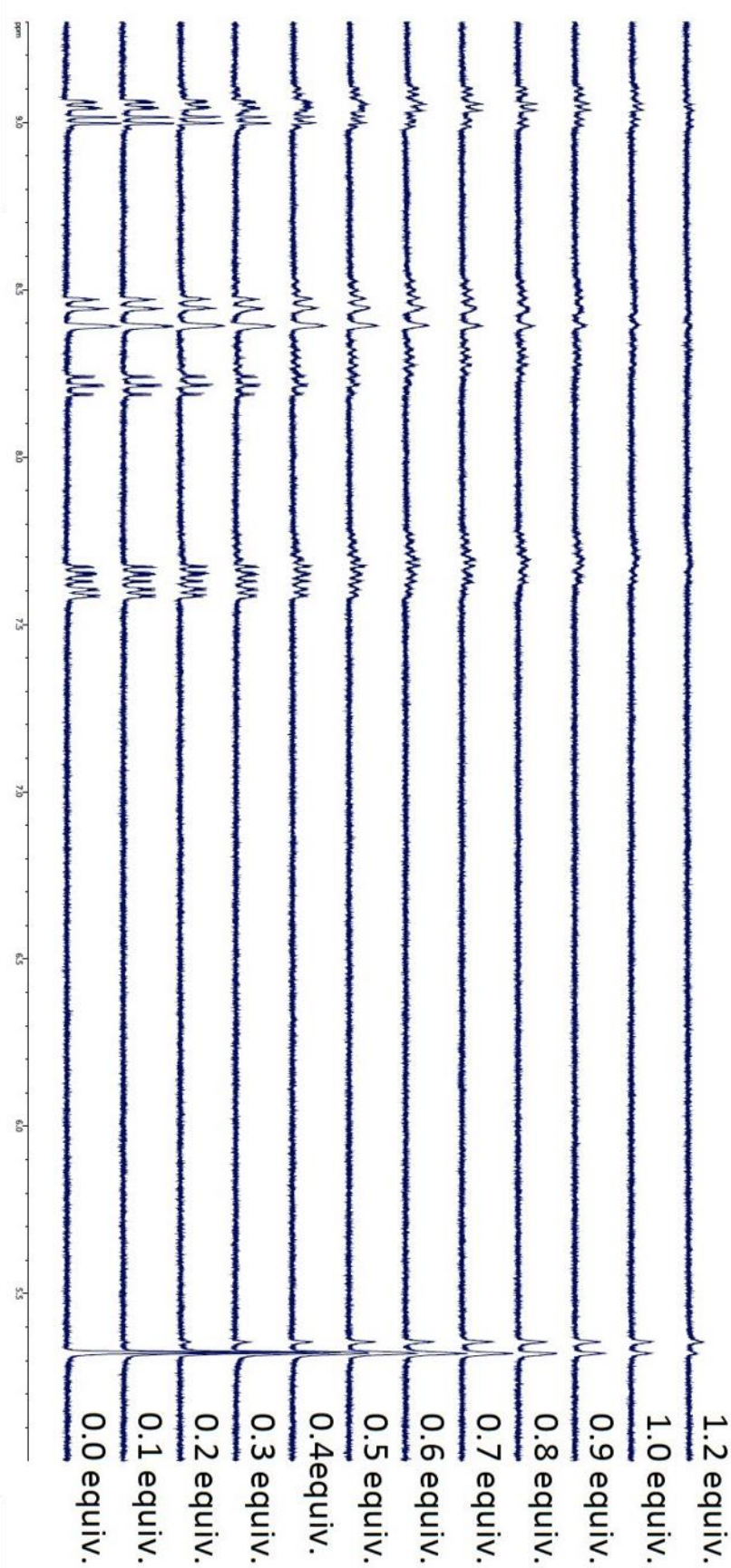

Figure 4.9: *The ^{1}H NMR titration of [Re(L1)(CO)$_3$Br] with Hg(NO$_3$)$_2$ conducted at 300 MHz at 298 K in acetonitrile-d$_3$.*

To summarise, the addition of Hg^{2+} salts to a [Re(L1)$(CO)_3$Br] solution impacts both the optical and structural properties, confirming the observations previously made using [Re(bpy)$(CO)_3$Br] and [Re(L′)$(CO)_3$Br].[ref] The result confirms that the presence of Hg^{2+} facilitates the removal of bromide leading to the weak coordination of solvent in its place (Fig. 4.10). Additionally, the counter ion of the salt appears to also influence the reaction with the presence of NO_3^- seemingly generating a third species, attributed the counter ion replacing the coordinated solvent. The spectroscopic data shows that this small collection of Re(I) complexes have a selective interaction with Hg^{2+} which could be applied for the development of new forms of mercury sensing. There are also possible synthetic implications with Hg^{2+} salts having the ability to facilitate bromide removal. Silver salts are employed for this purpose however Hg^{2+} salts appear to achieve this with the additional advantage that the reaction occurring at room temperature.

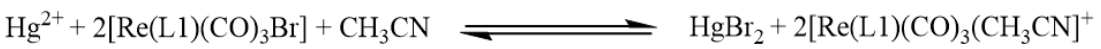

Figure 4.10: *The proposed reaction occurring on the addition of Hg^{2+} to an acetonitrile solution of [Re(L1)$(CO)_3$Br].*

4.4 SERS Sensing of Hg^{2+} Using [Re(L1)$(CO)_3$Br] Interfacial Films

4.4.1 Metal Sensing using [Re(L1)$(CO)_3$Br] MeLLFs

The combination of interfacial film formation and the observed remarkable optical response to Hg^{2+} with [Re(L1)$(CO)_3$Br] could give a SERS-active platform with high sensitivity for this cation. The key Raman vibrations are situated at 506, 1910 and 2025 cm^{-1} which originate from the Re–CO groups, with additional contributions from the bipy and dithiolate tail. It was hoped that the Hg^{2+} induced interaction would cause a sufficient change in the excited state of the molecule to elicit a response from these Re-centred SERS vibrations.

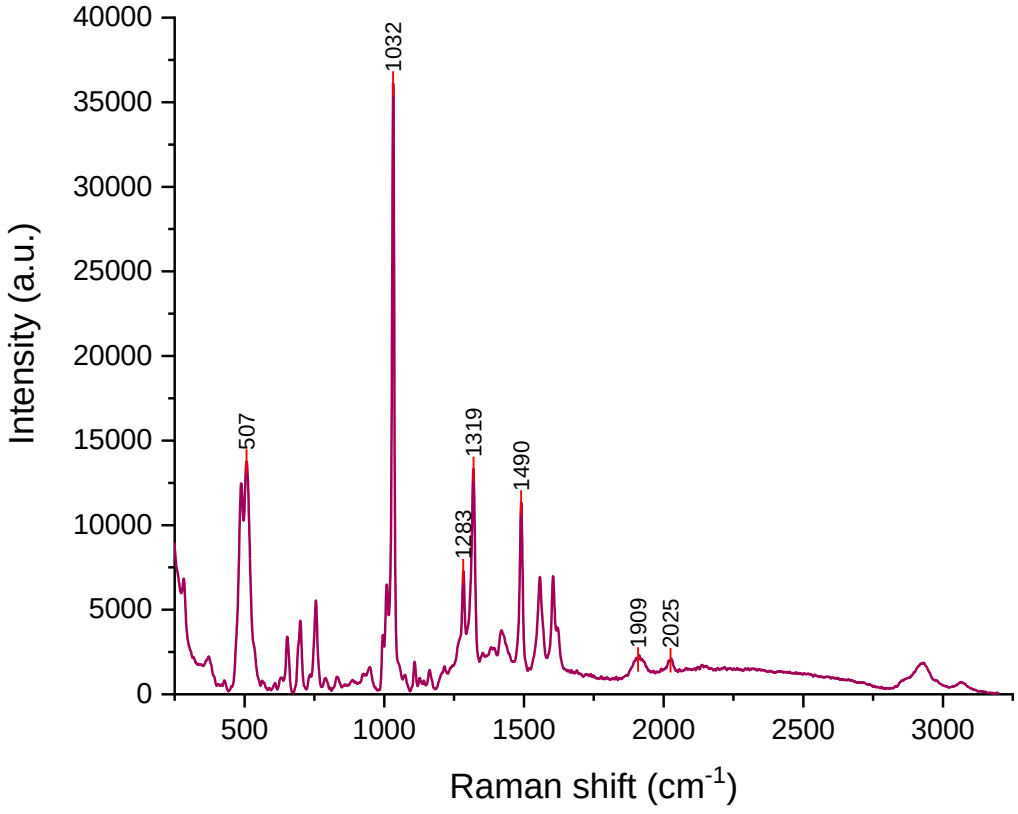

Figure 4.11: *The SERS spectrum of a [Re(L1)$(CO)_3$(Br)] MeLLF (Chapter 3. Section 3.2.2.3)*

The MeLLFs were fabricated using the [Re(L1)(CO)$_3$(Br)] complex using the standard procedure, followed by the addition of acetonitrile solutions of metal salts (Chapter 2, Section 2.2.1). The cations used for testing were Hg^{2+}, Ag^{+}, Cu^{2+}, Pb^{2+}, Co^{2+}, Cd^{2+}, Ni^{2+}, Zn^{2+} and Fe^{2+}. The SERS response of the resulting MeLLFs suggest that the majority of cations do not induce significant changes to the Re–C stretch (Fig 4.12). The presence of Ag^{+}, Hg^{2+} and Fe^{2+} do appear to cause a decrease in the SERS intensity of the complex as a whole. However, in the case of both Ag^{+} and Fe^{2+}, the shape of the Re–C stretch at 510 cm^{-1} strongly resembles the observed vibration of the untreated [Re(L1)(CO)$_3$Br] MeLLF. As neither cation induced a change to the emissive response of the complex according to the spectroscopic study so this suggests the nature of their interaction with the [Re(L1)(CO)$_3$Br] surface may not be a result of cation-complex interactions (Fig 4.5). It is possible that Ag^{+} could interfere with the metal centre, as Ag salts are commonly employed for the synthetic removal of bromide from rhenium centres in ligand substitution reactions although these require heating.[13-15]

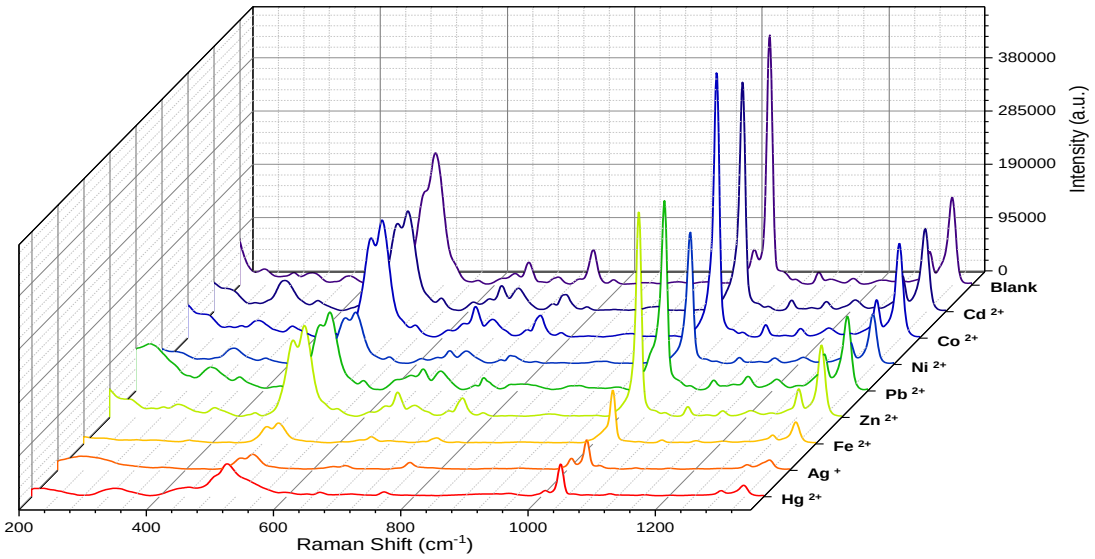

Figure 4.12: *The SERS response of [Re(L1)(CO)$_3$Br]-functionalised MeLLFs and the response after the individual addition of 1 mM solutions of different metal perchlorate salts untreated response for comparison. Excited at 785 nm*

Addition of Hg^{2+} appears to change the appearance of the Re-C vibrational mode situated at 510 cm^{-1} with the appearance of shoulders at 490 and 530 cm^{-1} and an increase in intensity of the original mode (Fig. 4.13). This could be a direct result of the interaction that occurs between Hg^{2+} and the Re–Br group. The nature of the interaction is not yet fully understood though an expectation is that the electronic distribution of the rhenium centre would be affected if the Re–Br bond was disrupted in some way. It is possible that this would also have implications for the Re–C bonding mode. Addition of Hg^{2+} also results in the appearance of a broad vibration centred at 330 cm^{-1}. This vibration was initially attributed to some form of Hg–Br interaction however, published data on the Raman response of mercuric halide salts report the $HgBr^+$ and $HgBr_2$ stretches occurring in a range between 200 and 250 cm^{-1} depending on the source.[16, 17]

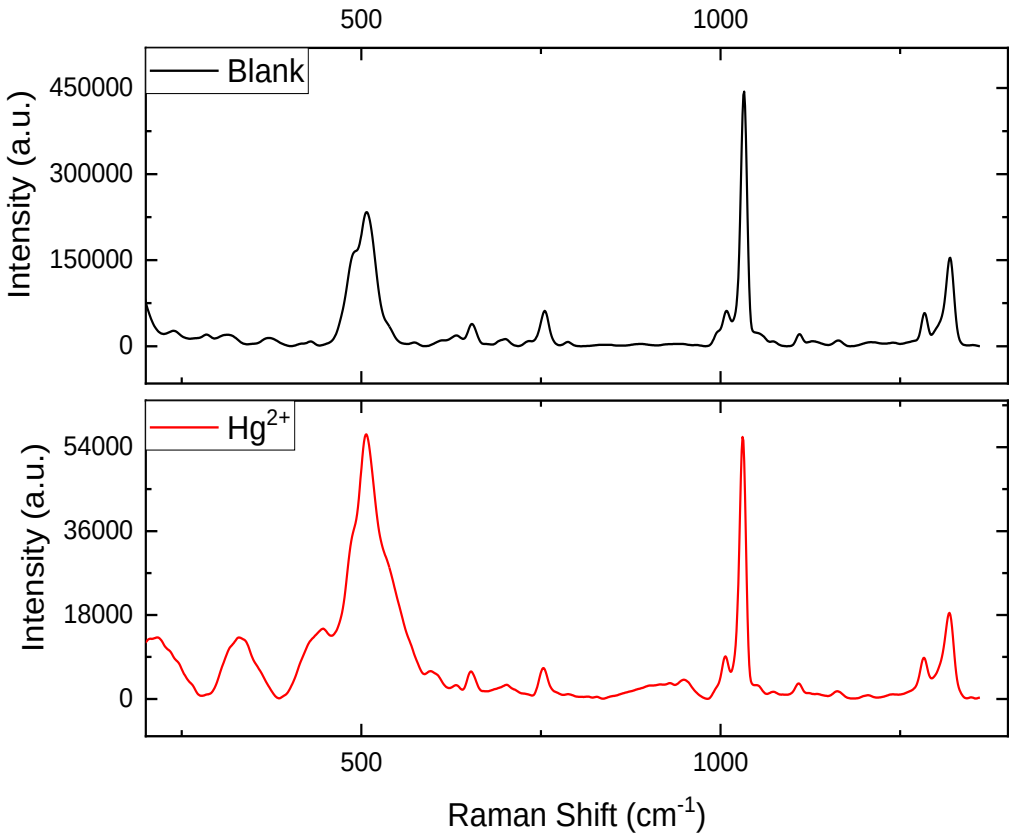

Figure 4.13: *The SERS spectrum of a MeLLF formed using a 1 mM solution of [Re(L1)(CO)$_3$Br] (–) and the resulting spectrum after addition of a 1 mM solution of Hg(ClO$_4$)$_2$ (–). Excited at 785 nm*

Another possible argument is that if the Hg-facilitated removal of bromide is occurring, then the solvent may occupy the vacant site. The expectation would therefore be to observe the vibrations associated with the coordinated solvent. The assumed identity of the peak at 330 cm^{-1} is possibly therefore, a Re–X vibration belonging to the coordination of solvent (Fig 4.14). The characterisation of the solvent binding mode is challenging as MeLLFs require two immiscible solvents to be present for formation. One assumption is that the interaction occurring on the MeLLF surface is similar to the observed interaction in solution. This would mean the acetonitrile is replacing the bromide as it is removed but this is also appears not to be the case as vibrations attributed to CH$_3$CN are not observed.[18] Water soluble Re(I) complexes with water coordinated in place of the halide exist in the literature and Raman studies on hexaaqua

metal ions do show M–OH_2 stretching vibrations occuring.[19,20] Unfortunately however, no conclusive experimental evidence that provides a value for the vibrational frequency a Re-OH_2 mode is available so any conclusions drawn remain tentative.

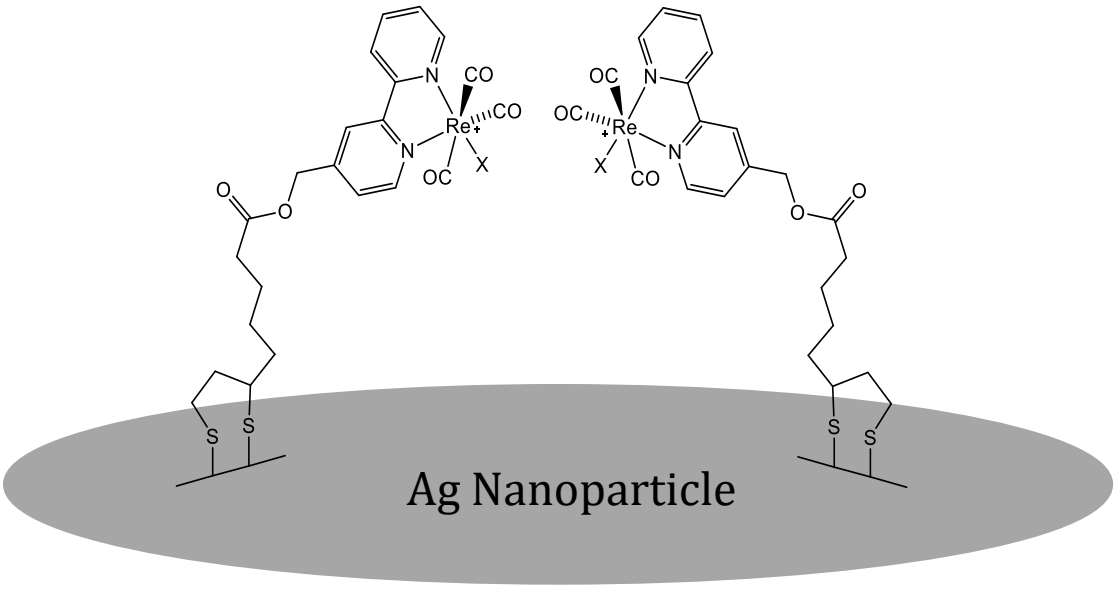

Figure 4.14: *A representation of the charged species that occurs upon the addition of Hg^{2+} to a [Re(L1)$(CO)_3$Br]-functionalised MeLLF.*

4.4.2 Hg^{2+} Concentration Limits of [Re(L1)$(CO)_3$Br] MeLLFs

To assess the Hg^{2+} concentration limitations of the films further, concentrations of Hg^{2+} were decreased sequentially. The addition of a 0.1 mM Hg^{2+} solution appears to show a decreased level of intensity with the peak at 506 cm^{-1} at approximately 60% intensity of the peak from the untreated [Re(L1)$(CO)_3$Br] MeLLF (Fig 4.15). This is not coupled with the perturbation of the Re–C stretch as seen with 1 mM Hg^{2+}. The addition of solutions with a concentration below 0.1 mM does not appear to affect the SERS response in an observable way, suggesting this is the concentration limit of the [Re(L1)$(CO)_3$Br] MeLLFs. This can be explained the addition of lower concentrations of Hg^{2+} will result in less of the [Re(L1)$(CO)_3$Br] being affected. It is possible that the Hg^{2+} is interacting with the surface, however the SERS response is dominated by

unaffected [Re(L1)$(CO)_3$Br]. Attempting to map the surface to assess whether such small-scale interactions were occurring were difficult due to the fluid nature of the MeLLFs.

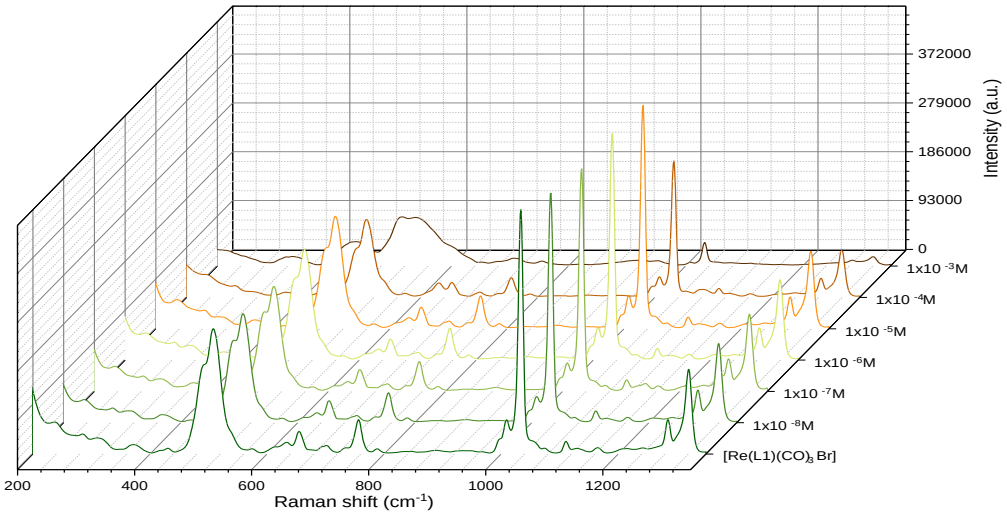

Figure 4.15: *The observed responses of [Re(L1)$(CO)_3$Br] MeLLFs upon additions of Hg^{2+}solutions with decreasing concentration. Excited at 785 nm.*

4.5 Cationic Sensing with the [Re(L1)(CO)$_3$Br] SENS

The fluid nature of MeLLFs does present challenges, an example being that the interfacial surface can move during SERS measurements. A possible solution to these issues are the surface-exposed nanosheets or SENS, formed through the modification of citrate stabilised nanoparticles with the [Re(L1)(CO)$_3$Br] (Chapter 2, Section 2.2.2). The SENS are a solid analogue of the MeLLFs, formed in an almost identical manner via interfacial positioning. The slight difference being the polymer incorporated in the organic layer that isolates the nanoparticle layer upon drying. The SERS response of the [Re(L1)(CO)$_3$Br] SENS is comparable to the MeLLF therefore the expectation was that the SENS would also display a spectroscopic response when exposed to Hg^{2+} in solution.

4.5.1 Metal Selectivity of [Re(L1)(CO)$_3$Br] SENS

The [Re(L1)(CO)$_3$Br] SENS were treated with aliquots of acetonitrile solutions containing metal salts to determine whether they would display similar behaviour to the MeLLFs. The metal selectivity exhibited by both the complex in solution and the [Re(L1)(CO)$_3$Br]-labelled MeLLFs is also observed (Fig. 4.16). A dramatic reduction in SERS intensity belonging to the complex is only seen with the presence of Hg^{2+}. The intensity of the SENS treated with Cu^{2+} also sees a decrease in intensity with the Re–C vibration appearing at 34% of the original intensity. It is believed that this is a separate interaction that is occuring between the [Re(L1)(CO)$_3$Br] surface and Cu^{2+} as the only a marginal increase in the emission spectrum was observed (Fig. 4.5). It is possible that this is interference of the Ag–S binding resulting in the removal of the [Re(L1)(CO)$_3$Br] species from the surface. However, this is speculative as there is no evidence available

to support this and no further investigation was conducted. Both the emissive and SERS responses were not comparable to what was observed with Hg^{2+} so it was concluded to be a separate interaction.

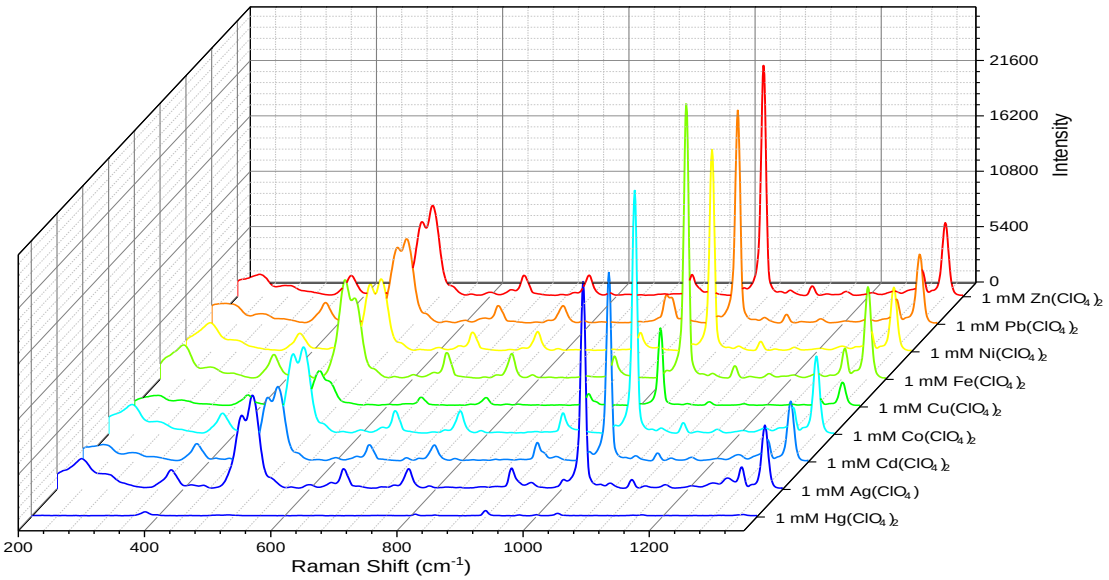

Figure 4.16: *The SERS spectra after screening of [Re(L1)(CO)$_3$Br] SENS with different metal perchlorate solutions all at a concentration of 1 mM. Excited at 785 nm*

4.5.2 SERS Detection of Hg^{2+} using [Re(L1)(CO)$_3$Br] SENS

The addition of Hg^{2+} to the [Re(L1)(CO)$_3$Br] SENS causes a dramatic reduction in the SERS intensity of the complex which differs from the liquid-liquid counterparts. The distinct increase in intensity of the original 510 cm^{-1} vibration and the shoulder peaks at 490 and 530 cm^{-1} are not visible. Several new vibrational modes are observed at 380 and 920 cm^{-1} which can be assigned to the acetonitrile C–C ≡ N bending and C–C stretching modes respectively (Fig. 4.17).[21] The Re–C and bpy stretches at 510 and 1030 cm^{-1} are still apparent which suggests the complex is still present at the SENS surface in some form. Several other peaks are observed at 809 and 972 cm^{-1} which may originate

from the resulting species generated after the Hg^{2+} interaction. This is speculative as the peaks cannot be confidently assigned as they do not resemble previously reported $Hg(ClO_4)_2$ vibrations and do not belong to the original $[Re(L1)(CO)_3Br]$ complex.[22] There is also the loss of the moderate peaks that can be attributed to the bipy-dithiolate tail, specifically the vibrations that stem from the Ag-dithiol surface. It is unclear as to whether the emergence of the acetonitrile contributions is due to coordination with the Re centre or, as a result of the removal of the complex from the surface.

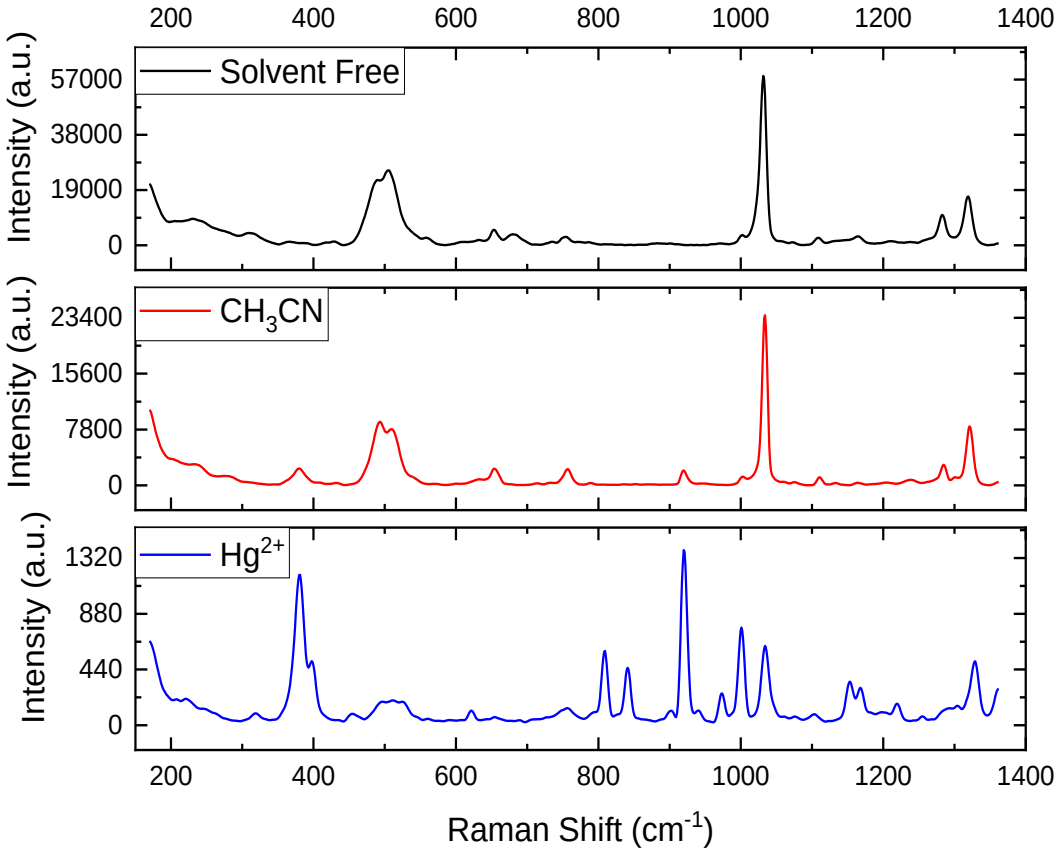

Figure 4.17: *The SERS response of the $[Re(L1)(CO)_3Br]$ SENS after treatment; a) blank (–), b) CH_3CN (–), c) Hg^{2+}(–). Excited at 785 nm*

A possible explanation for the change to the spectrum is the proposed bromide removal and solvent coordination which results in a charged species. This $[Re(L1)(CO)_3(X)]^+$ complex (where X=solvent adduct), undergoes either orientation away from the surface or dissociates entirely. The dominance of the acetonitrile peaks could be representative

of this as the same peaks are weakly apparent when the [Re(L1)(CO)$_3$Br] SENS are treated with pure acetonitrile but become more prominent when the SENS are treated with Hg^{2+}. Additional evidence that suggests a change on the surface is found at higher wavenumbers. The typical response of the [Re(L1)(CO)$_3$Br] SENS includes two peaks at 2932 and 2942 cm^{-1}, assigned to the asymmetric acyclic C–H and symmetric C–H stretching from the bpy-dithiolate tail. The addition of Hg^{2+} sees the disappearance of the 2932 cm^{-1} vibration (Fig. 4.18). An expectation is that in the event of either dissociation or orientational change there would be a corresponding change to the vibrational modes that originate from the bipy-thiolate tail. The combined loss of both the dithiol surface binding group and acyclic C–H stretches strongly suggests that the [Re(L1)(CO)$_3$(X)]$^+$ dissociates from the surface.

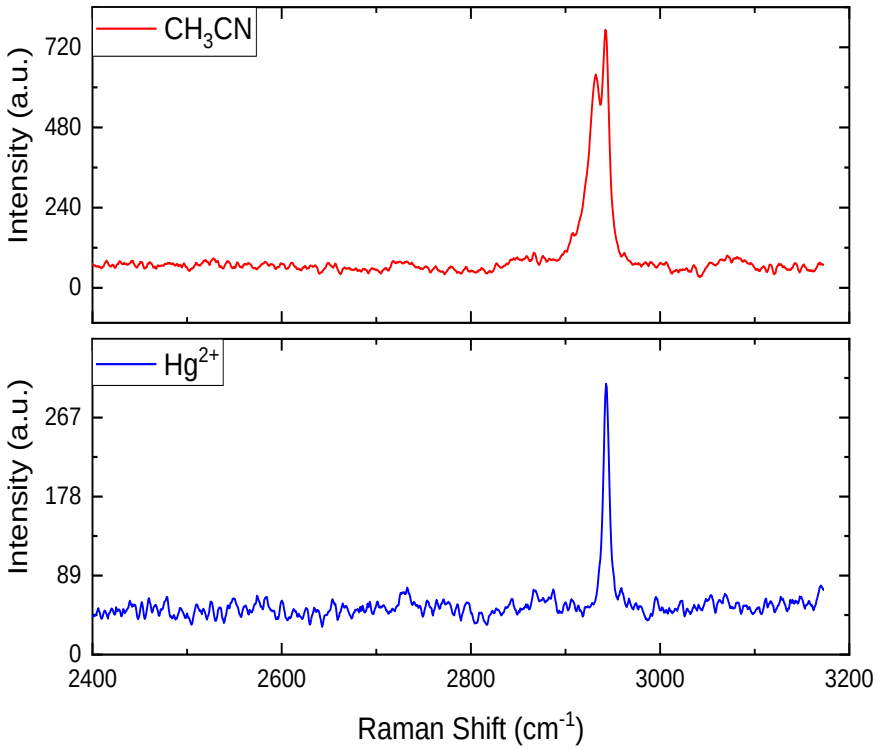

Figure 4.18: *The SERS response of the [Re(L1)(CO)$_3$Br] SENS after treatment at higher frequencies; a) CH_3CN (–), b) $Hg(ClO_4)_2$ (–). Excited at 785 nm*

An assessment was also made on the Hg^{2+} concentration limits of the SENS system to see if decreasing the surface area of the sensing film would improve the limits of detection. [Re(L1)$(CO)_3$Br] SENS were treated with small portions of $Hg(ClO_4)_2$ solutions in decreasing concentrations in a manner similarly conducted with the analogous MeLLFs. The MeLLFs showed only a marginal change at 0.1 mM whereas the [Re(L1)$(CO)_3$Br] SENS show a notably greater response (Fig 4.19). There is a perceivable decrease in the relative intensity of the [Re(L1)$(CO)_3$Br] SERS response when the SENS is treated with a 0.01 mM solution of Hg^{2+}. While the decrease is minimal, approximately 10%, it suggests that recognition at low concentrations could be achievable. However, in this specific case, there is little indication that sensing of Hg^{2+} is achieved below this concentration. This suggests that the solid film and the ability to better control surface area has the potential to improve the sensing capabilities of the [Re(L1)$(CO)_3$Br] films.

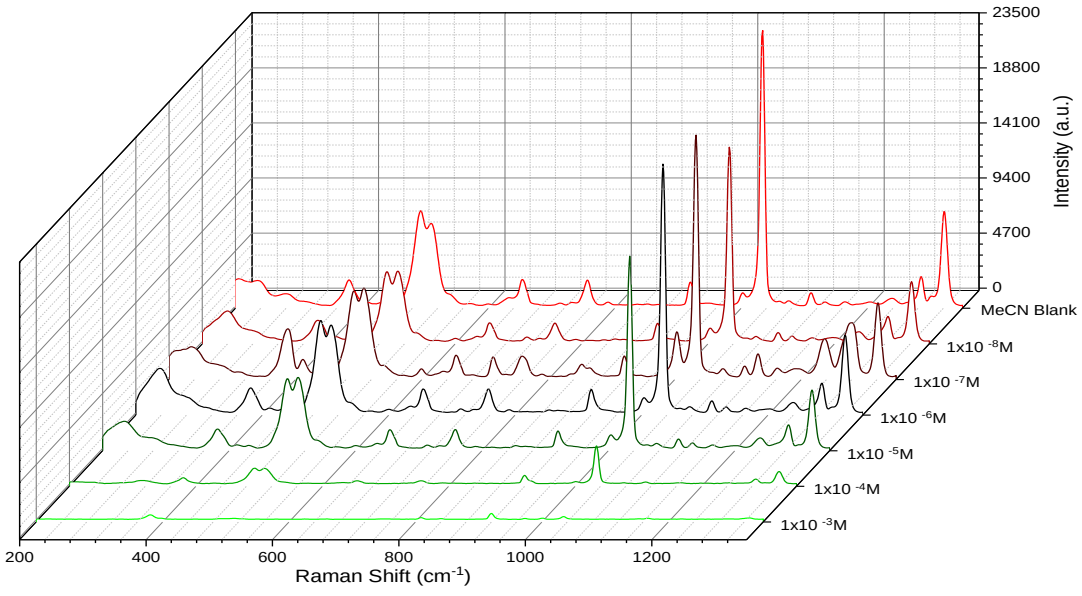

Figure 4.19: *The assessment of sensitivity of the [Re(L1)$(CO)_3$Br] SENS to acetonitrile solutions of Hg^{2+} in decreasing concentrations. Excited at 785 nm*

4.5.3 Hg^{2+} Detection in Aqueous Solvent

Previous studies using the [Re(L′)$(CO)_3$Br] complex concluded that the interaction also had a dependency on the solvent environment as different emissive behaviours were seen when conducting Hg^{2+} in acetone and acetonitrile.[4] This suggested that the Raman behaviour would also be susceptible to the presence of different solvents. A desired characteristic of SERS sensors is the ability to detect the target species in aqueous environments. To explore this, 1 mM aqueous solutions of the metal salts were dropped onto the [Re(L1)$(CO)_3$Br] SENS formed via standard procedure (Chapter 2, Section 2.2.2). The addition of Hg^{2+} prompts a response that is similar to those observed in acetonitrile with a sizeable loss of the overall intensity of the Re complex (Fig. 4.20). This is not the case when the solutions of the other metal cations are present. This would suggest that Hg^{2+} detection in aqueous media could well be possible using the [Re(L1)$(CO)_3$Br] SENS.

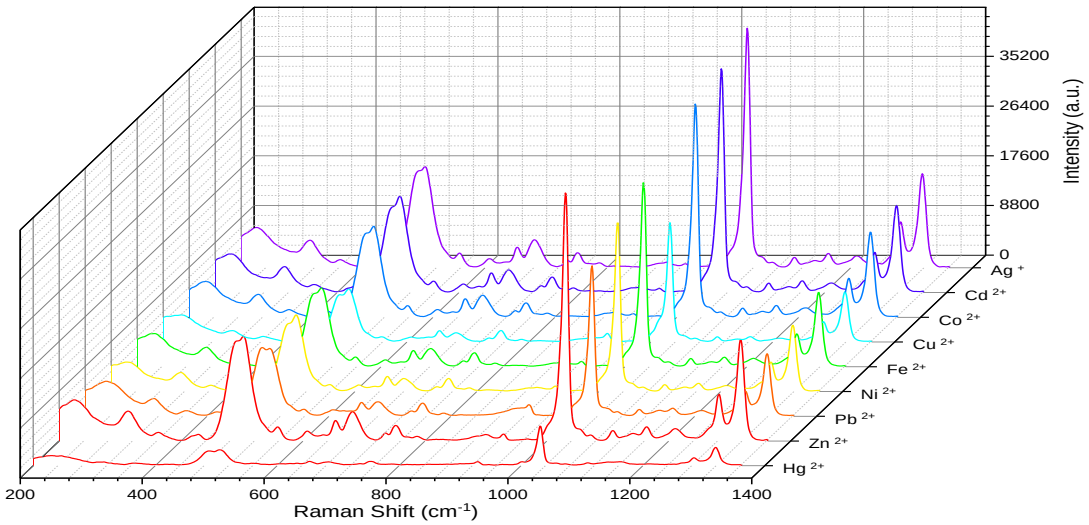

Figure 4.20: *The SERS spectra of the [Re(L1)$(CO)_3$Br] SENS after screening with 1 mM aqueous metal perchlorate solutions. Excited at 785 nm*

4.6 Conclusions for Metal Cation Sensing using Interfacial Films formed via Rhenium Complex Modification

The objectives of this chapter were the investigation of whether [Re(L1)(CO)$_3$Br] functionalised films could be employed for SERS based sensing. Spectroscopic titrations of the [Re(L1)(CO)$_3$Br] complex was confirmed to show the same optical and structural behaviour when subjected to Hg^{2+} as observed with the [Re(L′)(CO)$_3$Br] in an earlier study.

Initial experiments using the uncoordinated L1 species to form MeLLFs showed that vibrational changes occurred upon the binding of metal cations to an exposed bpy group, confirming that interfacial films for SERS sensing was possible. The addition of aqueous metal salts to a [Re(L1)(CO)$_3$Br] MeLLF displays a sensitive and selective response to the presence of Hg^{2+}, resulting in a considerable change to the Re-C vibration. This is accompanied by the addition of a new peak which is thought to represent the coordination of solvent to the site vacated by the bromide. This change is not observed upon the addition of any other metals. Assessment of the concentration sensitivity of the [Re(L1)(CO)$_3$Br] MeLLFs suggests that recognition of Hg^{2+} is not possible at concentrations below 0.1 mM.

The Hg^{2+} selective behaviour is also observed with the [Re(L1)(CO)$_3$Br] SENS with the observed response differing from the liquid-liquid counterparts. A sizeable reduction in the overall SERS intensity of the complex and the disappearance of vibrations that stem from the bpy-dithiol binding tail suggests the complex has orientated differently or, more likely, dissociated from the surface. In comparison with the MeLLFs, the SENS showed a greater concentration sensitivity as the SENS showed

a clear response to the presence of 0.1 mM solutions. Additionally, that for this particular Re-functionalised surface, there is a Hg^{2+} specific interaction in aqueous media.

The results demonstrate that interfacial films formed with [Re(L1)$(CO)_3$Br] offer a unique method of detecting and show the feasibility of such surfaces for SERS detection. This allows for further investigation into the use of rhenium complexes coordinated to ligands that possess other binding capabilities for targeted detection.

4.7 References

1. K. V. Kong, Z. Lam, W. K. O. Lau, W. K. Leong and M. Olivo, *J. Am. Chem. Soc.*, 2013, **135**, 18028-18031.
2. W. Ji, L. Li, Y. Zhang, X. Wang and Y. Ozaki, *J. Raman Spectrosc.*, 2021, **52**, 468-481.
3. Z. Guo, A. O. Barimah, C. Guo, A. A. Agyekum, V. Annavaram, H. R. El-Seedi, X. Zou and Q. Chen, *Spectrochim. Acta, Part A*, 2020, **242**, 118747.
4. H. J. Montgomery, PhD Thesis, Queen's University Belfast, 2011.
5. H. J. Montgomery, D. Pelleteret, S. E. J. Bell and N. C. Fletcher, *Inorg. Chem.*, 2011, **50**, 2738-2747.
6. W. R. McWhinnie and J. D. Miller, in *Advances in Inorganic Chemistry and Radiochemistry*, eds. H. J. Emeléus and A. G. Sharpe, Academic Press, 1970, vol. 12, pp. 135-215.
7. H. C. Garcia, R. Diniz, M. I. Yoshida and L. F. C. de Oliveira, *CrystEngComm*, 2009, **11**, 881-888.
8. Y. Du, R. Liu, B. Liu, S. Wang, M.-Y. Han and Z. Zhang, *Anal. Chem.*, 2013, **85**, 3160-3165.
9. R. D. Shannon, *Acta Crystallogr. A*, 1976, **32**, 751-767.
10. J. Docherty, S. Mabbott, W. E. Smith, J. Reglinski, K. Faulds, C. Davidson and D. Graham, *Analyst*, 2015, **140**, 6538-6543.
11. E. Wolcan, G. Torchia, J. Tocho, O. E. Piro, P. Juliarena, G. Ruiz and M. R. Féliz, *J. Chem. Soc., Dalton Trans.*, 2002, 2194-2202.
12. N. M. N. Gowda, S. B. Naikar and G. K. N. Reddy, in *Adv. Inorg. Chem.*, eds. H. J. Emeleus and A. G. Sharpe, Academic Press, 1984, vol. 28, pp. 255-299.
13. F. L. Thorp-Greenwood, J. A. Platts and M. P. Coogan, *Polyhedron*, 2014, **67**, 505-512.
14. D. B. MacQueen and K. S. Schanze, *J. Am. Chem. Soc.*, 1991, **113**, 7470-7479.
15. V. Wing-Wah Yam, V. Chor-Yue Lau and L.-X. Wu, *J. Chem. Soc., Dalton Trans.*, 1998, 1461-1468.
16. J. R. Ferraro, in *Low-Frequency Vibrations of Inorganic and Coordination Compounds*, Springer US, Boston, MA, 1971, pp. 111-189.
17. J. W. Macklin and R. A. Plane, *Inorg. Chem.*, 1970, **9**, 821-827.
18. W. J. Casteel, D. A. Dixon, N. LeBlond, P. E. Lock, H. P. A. Mercier and G. J. Schrobilgen, *Inorg. Chem.*, 1999, **38**, 2340-2358.
19. A. Nakada and O. Ishitani, *ACS Catal.*, 2018, **8**, 354-363.
20. J. Mink, C. Németh, L. Hajba, M. Sandström and P. L. Goggin, *J. Mol. Struct.*, 2003, **661-662**, 141-151.
21. P. Neelakantan, *Proceedings of the Indian Academy of Sciences - Section A*, 1964, **60**, 422-424.
22. M. M. Jones, E. A. Jones, D. F. Harmon and R. T. Semmes, *J. Am. Chem. Soc.*, 1961, **83**, 2038-2042.

Chapter 5

Anionic Sensing Using Rhenium-functionalised Films with Attempts at Biological Sensing

5.1 Introduction

The [Re(L1)(CO)$_3$Br] system used in Chapter 3 provided a proof of concept that interfacial nanoparticles films functionalised with the [Re(L1)(CO)$_3$Br] complex have potential as novel SERS sensors. This means that different rhenium complexes could be investigated to sense a diverse range of analytes by changing the ligand functionality. For example, the detection of phosphate is a subject of interest due to its diverse biological relevance, being an important component in a number of biomolecular structures, the most notable being DNA and RNA, while also it plays a key role in biochemical energy transfer processes.[1] It also has great relevance in agriculture and farming with widespread use in fertilisers and animal feeds. Having an ability to interact with phosphate-containing molecules allows for greater understanding of both biological features and environmental contamination.

The design of polypyridyl species and their coordination to transition metal centres for anion-based sensing has been prevalent for several years.[2, 3] The popularity of transition metal anion sensors arises from their luminescent properties which are susceptible to anionic interactions, driven via hydrogen bonding and electrostatic mechanisms with numerous Re(I) complexes investigated.[4] A recent example is the Schiff-base Re(I) complex described by Ramdass *et al.* which has a "turn-on" sensing of fluoride however it is also receptive to $H_2PO_4^-$.[5]

This Chapter focuses on the development of a rhenium complex that can effectively bind phosphate and can also functionalise nanoparticles and form interfacial films. The aim is to understand whether this functionalised SERS surface can be used to detect any potential phosphate interactions. Additionally, the platform will be screened with DNA

to assess whether the platforms can be applied in a biological setting. The hope is that this will demonstrate that tailored functionalities, coordinated to a rhenium centre can be used for targeted detection and therefore providing an example of a modular approach to the design of labelled SERS sensing devices.

5.2 Development of a Hydrogen Phosphate Sensing Rhenium Complex

The origins of this work stem from observations made by other members of the Fletcher group in their work with polypyridyl ruthenium complexes. A bis-benzimidazole bipyridyl (L2) ligand coordinated to ruthenium metal centre, generating the complex, $[Ru(bipy)_2(L2)]^{2+}$ displays an emissive response when treated with TBA dihydrogen phosphate (Fig 5.1).[6] It was anticipated that a $[Re(L2)(CO)_3Br]$ derivative complex would elicit a similar response to TBA dihydrogen phosphate, with the hope that this interaction could be tracked using SERS and potentially, SERRS.

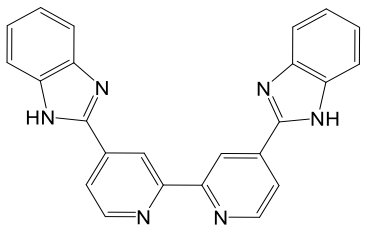

Figure 5.1: *The structure of the bis-benzimidazole bipyridine ligand, L2*

Once coordinated to a metal centre, the structure of L2 does not possess a suitable nanoparticle binding functionality and therefore the introduction of another surface binding ligand was explored. The removal of bromide from the rhenium tricarbonyl centre is well documented, proceeding via transmetalation with silver salts. The resulting $[Re(L2)(CO)_3X]^+$ where X is either a solvent adduct or weakly coordinating

anion, can then undergo further reaction through substitution of the desired ligand, R, to give $[Re(L2)(CO)_3R]^+$.[7-9] An additional benefit is that the resulting complex would be a charged species so formation of interfacial films could also be achieved via the promotion mechanism. $[Re(L2)(CO)_3(pyr)](PF_6)$ was synthesised initially through reaction of the $[Re(L3)(CO)_3Br]$ precursor in pyridine, in the presence of silver triflate. This was followed by reaction of the $[Re(L2)(CO)_3Br]$ with N-(4-pyridylmethyl)lipoamide, L3, formed via the acyl chloride of thioctic acid and 4-picolylamine (Fig. 5.2). It was theorised that L3 would suitably coordinate to the rhenium centre and modify the surface of the nanoparticle sufficiently for MeLLF formation.

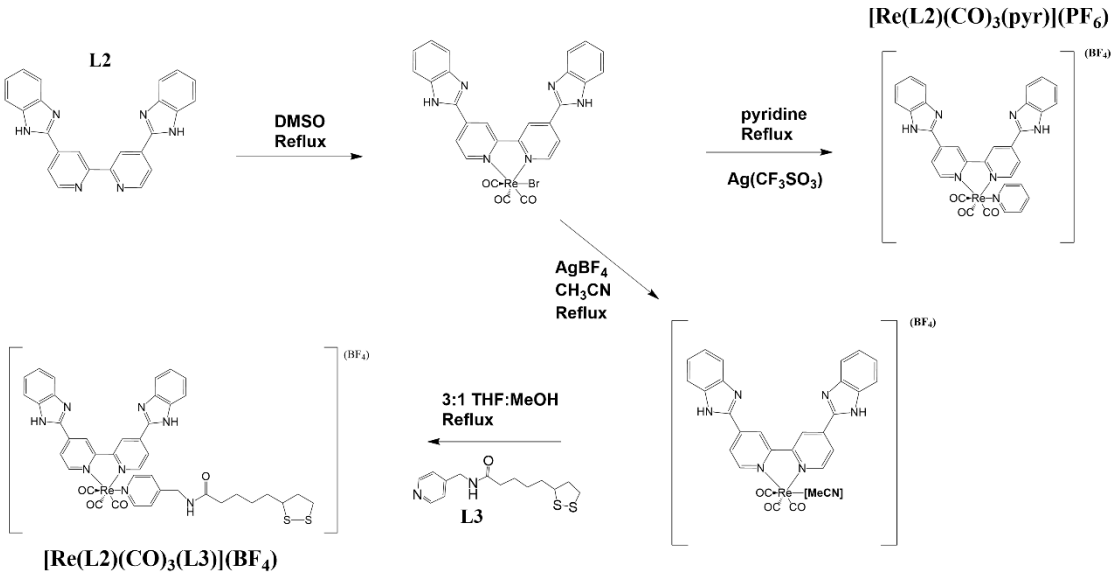

Figure 5.2: *The reaction scheme for the synthesis of $[Re(L2)(CO)_3(pyr)](PF_6)$ (Yield 41%) and $[Re(L2)(CO)_3(L4)](BF_4)$ (Yield 23.6 %) complexes*

$[Re(L2)(CO)_3(pyr)](PF_6)$ was successfully synthesised and characterised through ^1H NMR spectroscopy. However, the synthesis of the $[Re(L2)(CO)_3(L3)](BF_4)$ did present a number of challenges, mainly arising from the very poor solubility of the L2 ligand. To successfully coordinate L2 to the rhenium centre, the ligand and $Re(CO)_5Br$ were reacted in hot DMSO and the complex precipitated out on addition of water. Difficulties

were found during the subsequent transmetallation and ligand substitution, arising from the poor solubility of the neutral [Re(L2)$(CO)_3$Br] complex. Reaction of [Re(L2)$(CO)_3$Br] with both silver triflate and tetrafluoroborate in CH_3CN gave a brown insoluble solid, assumed to be AgBr signifying that the reaction had gone through to completion, leaving the intermediate in solution, assumed to be the acetonitrile intermediate, Re(L2)$(CO)_3(CH_3CN)]^+$. Attempts at observing this using ^{1}H NMR spectroscopy provided was inconclusive. There is a possibility that the intermediate could have also coordinated to DMSO remaining from the preceding step due to possible coordination of DMSO in the preceding step. Coordination the pyridyl amide ligand, L3 should be favoured in the later steps. After the addition of L3, the crude showed the presence of 2 products in the ^{1}H NMR spectrum and attempts at purification using both silica and size-exclusion chromatography were unsuccessful. A potential reason for poor coordination of the ligand and subsequent purification could be due to π-stacking interactions from the planar L2 structure which inhibits coordination of the ligand to the vacant site. Another possible outcome is that the nitrogens of the benzimidazole are able to bind to the vacant site and forming a dimeric type species thereby preventing the binding of L4 however this has been difficult to confirm due to the separation issues.

5.3 Spectroscopic Studies of the [Re(L2)(CO)$_3$(pyr)](PF$_6$) Species

5.3.1 The Optical Properties of [Re(L2)(CO)$_3$(pyr)](PF$_6$)

The [Re(L2)(CO)$_3$(pyr)](PF$_6$) complex in acetonitrile displays the anticipated UV-Vis absorption and luminescent behaviour (Table 1). An MLCT d–π^* transition is observed at 370 nm with ligand π–π^* transitions at 296 and 324 nm, and there is a slight perturbation of the spectrum at 217 nm which may correspond to a transition associated with the pyridine group (Fig. 5.3). Excitation of [Re(L2)(CO)$_3$(pyr)](PF$_6$) at 370 nm results in fluorescence with a λ_{max} of 585 nm with a relative emission quantum yield of 1.2×10^{-2}.[10] Comparison to the [Re(bpy)(CO)$_3$Br] standard shows that the λ_{max} of [Re(L2)(CO)$_3$(pyr)](PF$_6$) is blueshifted and the quantum yield of emission is significantly greater. This correlates with behaviours observed of similar pyridyl substituted rhenium complexes.[11, 12]

Table 5.1: *The photophysical properties of the [Re(L2)(CO)$_3$(pyr)](PF$_6$) with comparison to the [Re(bpy)(CO)$_3$Br] standard.*

Complex	Absorption[a], λ_{max}/nm				emission[a]	
	LMCT	LC		MLCT	λ_{max}/nm	Φ_{em}[d]
[Re(bpy)(CO)$_3$Br]	244	292	315	366	609[b]	7.8x10^{-3}
[Re(L2)(CO)$_3$(pyr)]$^+$	217	296	324	370	585[c]	1.2x10^{-3}

a – in aerated CH$_3$CN at 298 K at a concentration of 1 x10^{-5} M.

b – excited at 400 nm in aerated CH$_3$CN at 298 K.

c – excited at 370 nm in aerated CH$_3$CN at 298 K

d - emission quantum yields (Φ_{em}) were calculated relative to [Re(CO)$_3$Br(bpy)] (Φ_{em} = 7.8 x 10-3)[10] in acetonitrile

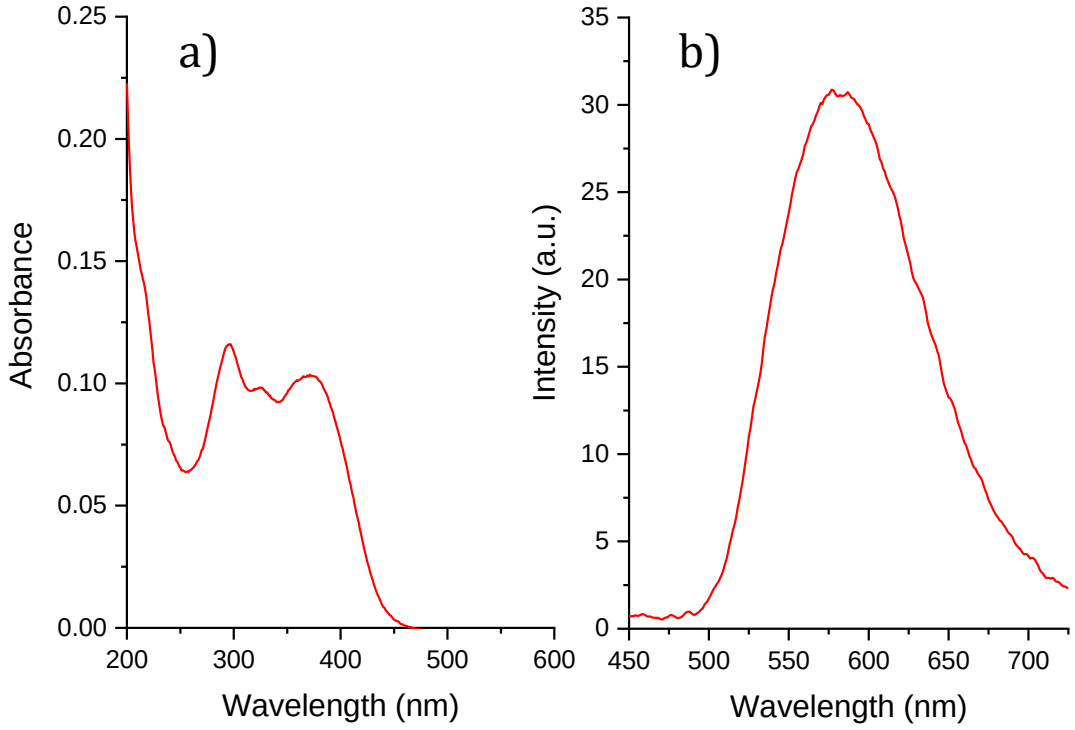

Figure 5.3: *a) The UV-Vis spectrum of [Re(L2)(CO)$_3$(pyr)](PF$_6$) in aerated CH$_3$CN and b) the emission spectrum of [Re(L2)(CO)$_3$(pyr)](PF$_6$). Excited at 370 nm*

5.3.2 Spectroscopic Studies of Anionic Interactions with $[Re(L2)(CO)_3(pyr)](PF_6)$

Titrations were conducted to assess the possible photophysical responses of the $[Re(L2)(CO)_3(pyr)]^+$ complexes when in the presence of common anions, specifically, Br^-, Cl^-, HSO_4^-, OAc^-, NO_3^- and $H_2PO_4^-$. The experiment, similar to the metal salt titrations used in the previous Chapter, involved the sequential addition of tetrabutylammonium (TBA) salts to aerated acetonitrile solutions of the $[Re(L2)(CO)_3(pyr)](PF_6)$ complex followed by UV-Vis and emission spectroscopic measurements.

The presence of Cl^- and NO_3^- did not appear to influence the optical behaviour of $[Re(L2)(CO)_3(pyr)](PF_6)$, suggesting no observable interaction with the complex. The introduction of HSO_4^- causes a marginal quenching of the fluorescence coupled with a marginal increase in absorbance at 360 nm in the UV-Vis spectrum. The addition of Br^- also results in a decrease in emission intensity with no discernible shift in wavelength (Fig. 5.4). It is possible that this is due to heavy atom quenching, caused by overlap of the orbitals from the excited $[Re(L2)(CO)_3(pyr)](PF_6)$ complex with outer orbitals of Br^-, as there is no significant change in the UV-visible spectrum that one would anticipate for ligand exchange. It is unlikely that the fluorescence quenching is occurring through a binding interaction between the complex and Br^-.

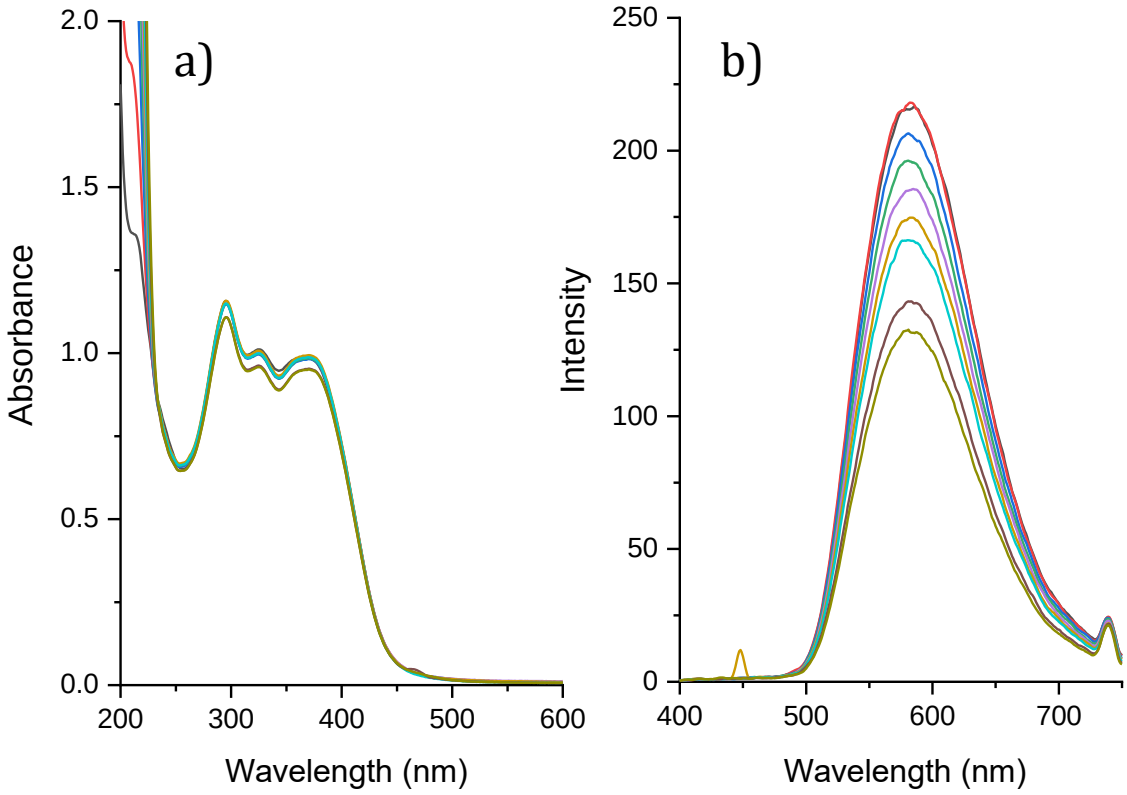

Figure 5.4: *a) The UV-Vis and b) emission spectra from the titration of [Re(L2)(CO)3(pyr)](PF6) with TBA Br in acetonitrile and excited at 370 nm. Molar equivalents 0.0 (-), 0.5 (-), 1.0 (-), 1.5 (-), 2.0 (-), 2.5 (-), 3.0 (-), 4.0 (-) and 5.0 (-)*

The addition of TBA dihydrogen phosphate induces changes to both the UV-Vis absorption and emission spectra. The absorption spectrum sees a notable shift in the MLCT transition from 371 to 386 nm upon the addition of two molar equivalents (Fig. 5.5a). As the molar ratio increases beyond two, the absorbance of the MLCT transition increases until a maximum is reached at 6 molar equivalence. This observed change in the visible absorption is accompanied by a change in the emissive response (Fig. 5.5b). Between 0 and 1.6 molar equivalents, there is a slight blue shift of λ_{max} from 585 nm to 570 nm with a progressive quenching. Increasing molar equivalents above 1.6 sees a continuation of the quenching however, there is no further shift in wavelength and agrees with the observations seen when conducting similar experiments $[Ru(bipy)_2(L2)](PF_6)_2$.[6]

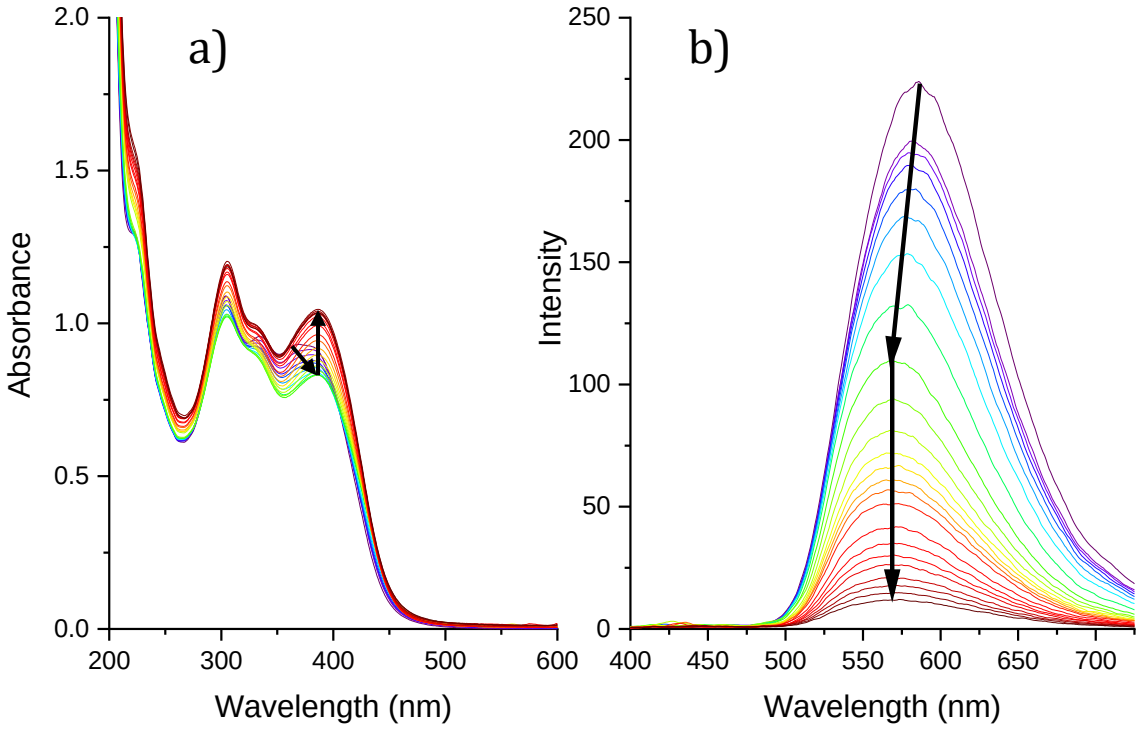

Figure 5.5: *a) The UV-Vis and b) emission spectra from the titration of [Re(L2)(CO)$_3$(pyr)](PF$_6$) with TBA H_2PO_4 in acetonitrile and excited at 370 nm. Molar equivalents 0.0 (-), 0.2 (-), 0.4 (-), 0.6 (-), 0.8 (-),1.0 (-), 1.2 (-), 1.4 (-), 1.6 (-), 1.8 (-), 2.0 (-), 2.2 (-), 2.4 (-), 2.6 (-), 2.8(-), 3.0 (-), 3.5 (-), 4.0 (-), 4.5 (-), 5.0 (-), 6.0 (-), 7.0 (-), 8.0 (-), 10.0 (-)*

The interaction between [Re(L2)(CO)$_3$(pyr)](PF$_6$) and dihydrogen phosphate is thought to be a result of hydrogen bonding of the anion to the N–H of the benzimidazole although it is possible that the interaction is also stabilised by interactions with the bpy protons situated in the 3 position of the bipyridyl group. The subtle changes that occur at 1.6 molar equivalents may be an indication of the binding of a second phosphate anion and could indicate that a cooperative binding interaction is occurring (Fig. 5.6). A similar two-step change to fluorescence behaviour has been reported by Blackburn *et al.* using dirhenium(I) complexes with a bridging thiourea species showing a similar interaction with $H_2PO_4^-$.[13] They also observed a subtle blue shift of the luminescence although the change to the luminescent intensity was significantly different. Their conclusions suggest that a cooperative binding mechanism occurs with two anions interacting with a single thiourea group via a proton transfer. It is possible that a similar

mechanism is occurring in this instance with the L2 with a sigmoidal response in both absorption and emission behaviour.

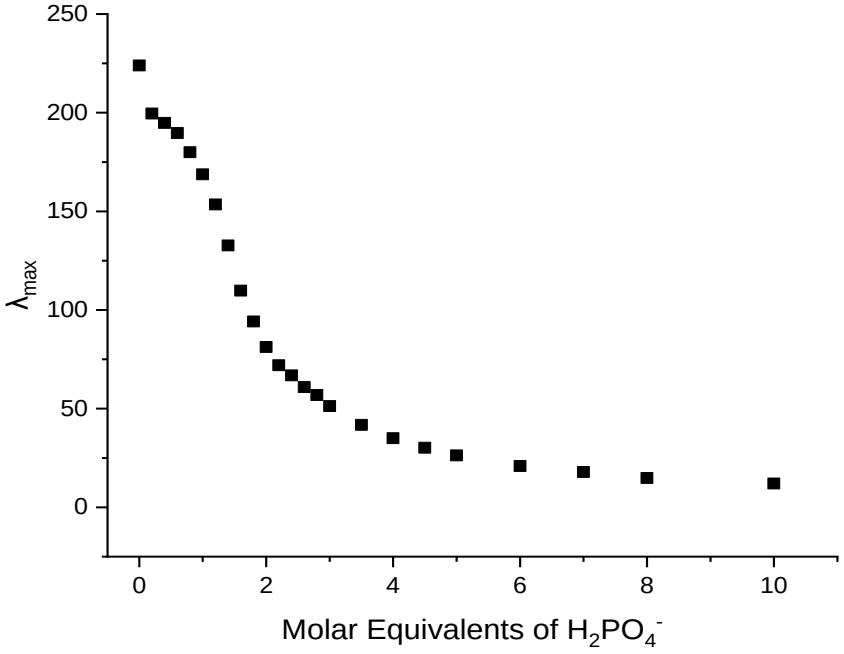

Figure 5.6: *A graph showing how the λ_{max} of emission of the [Re(L2)(CO)$_3$(pyr)](PF$_6$) complex, changes as molar equivalence of TBA H_2PO_4 increases*

The addition of OAc^- to the [Re(L2)(CO)$_3$(pyr)](PF$_6$) complex in an acetonitrile solution also results in changes to both absorbance and emissive response. A marginal shift in the MLCT absorption band from 371 to 383 nm (Fig. 5.7a) coupled with an almost immediate quenching in the fluorescence upon addition of the anion (Fig. 5.7b). There is evidence of similar compounds exhibiting OAc^- interactions as Shao *et al.* describe two phenanthroline systems that use di-substituted chains containing benzimidazole for anionic recognition that present quenching upon the addition of OAc^-. They concluded that deprotonation was occurring, allowing for the free rotation of the benzimidazole units as .[14] OAc^- is very basic in comparison to the other anions screened and is known to induce fluorescence changes via deprotonation. However in this instance, the addition of OAc^- sees only a slight increase of the d–π^* MLCT transition

in the UV-Vis spectrum, suggesting this is not the case.[15] If deprotonation was occurring then a noticeable shift to the absorption of the complex would be expected. [16, 17] A possible explanation for the observed change maybe a high degree of proton exchange occurring between L2 and OAc^-. The work by Blackburn *et al.* also described interactions between their reported thiourea bridged compounds and OAc^-, concluding that proton exchange was occurring in a similar manner to the $H_2PO_4^-$. It is feasible that the size of the OAc^- anion is able to form multiple binding interactions within the cleft of the ligand L2, causing the quenching in emission. Similar behaviour has also been observed with the aforementioned $[Ru(bipy)_2(L2)]^{2+}$ species, suggesting that the observed changes of the emission are representative of interactions between L2 and the anion.[6]

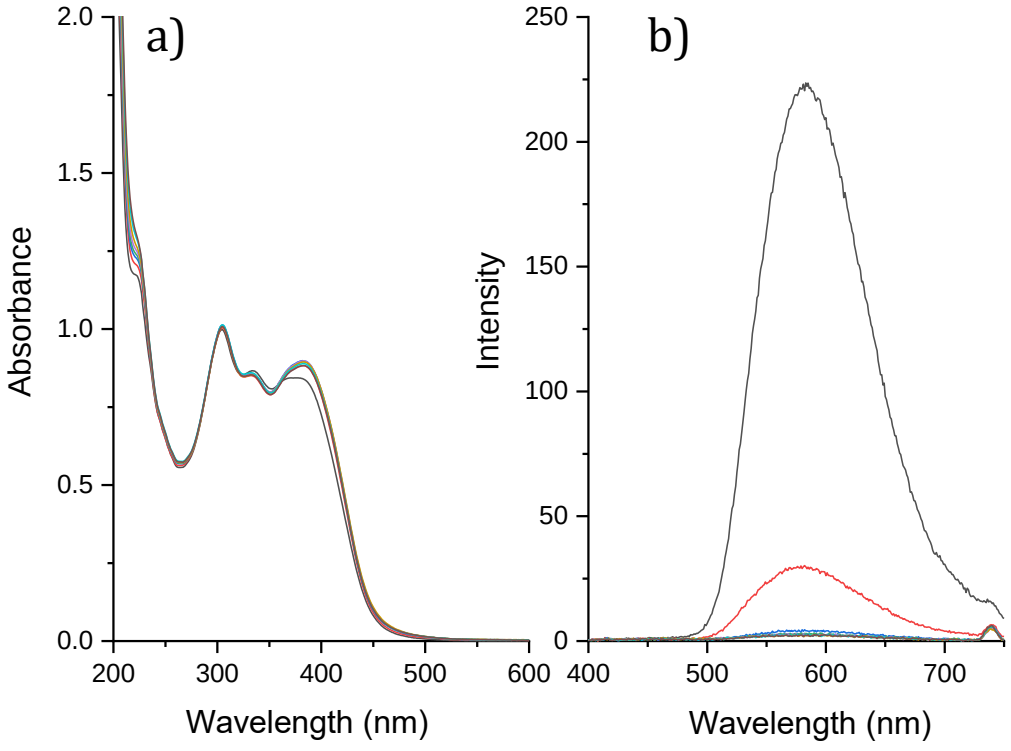

Figure 5.7: *a) The UV-Vis and b) emission spectra from the titration of $[Re(L2)(CO)_3(pyr)](PF_6)$ with TBA OAc in acetonitrile and excited at 370 nm. Molar equivalents 0.0 (-), 0.5 (-), 1.0 (-), 1.5 (-), 2.0 (-), 3.0 (-), 4.0 (-), 5.0 (-)*

The observed spectroscopic response of $[Re(L2)(CO)_3(pyr)](PF_6)$ to the addition of both $H_2PO_4^-$ and OAc^- suggests a recognition response is occurring through binding of the ligand, L2 to the respective anions. $H_2PO_4^-$ induces a sequential quenching in emission while OAc^- induces an almost complete "switch off" of fluorescence, strongly suggesting an L2-anion interaction in each case. The presence of two significant changes in both the UV-vis and emission spectra upon the addition of $H_2PO_4^-$ is suggestive of a cooperative binding mechanism. Unfortunately, there has not been the opportunity to track the anion interactions with the $[Re(L2)(CO)_3(pyr)](PF_6)$ using ^1H NMR spectroscopy. It is expected that this have provided more information on the nature of the binding mechanisms of occurring. Despite this, the results demonstrate that the coordination of the L2 ligand to a rhenium centre generates a complex with both dihydrogen phosphate and acetate selective interactions in solution which can be tracked spectroscopically. This indicates that the use of $[Re(L2)(CO)_3(R)]^+$ to form interfacial films, may also allow for the SERS detection of both dihydrogen phosphate and acetate.

An additional titration was conducted to investigate whether the ligand L3 would interact with the individual anions. In order to confirm this, the $[Re(bpy)(CO)_3(L3)](BF_4)$ complex with the notable absence of an anion-binding functionality. Additions of five molar equivalents of the anions was made to 0.1 mM acetonitrile solutions of a $[Re(bpy)(CO)_3(L3)](BF_4)$ complex followed by UV-Vis and emission measurements. No significant changes were observed with Br^-, Cl^-, NO_3^-, HSO_4^-, OAc^- and $H_2PO_4^-$, suggesting there is no interaction between the L3 tail and the anions.

5.4 Interfacial Film Formation and SERS Response

5.4.1 Formation and SERS Response of $[Re(L2)(CO)_3(R)]^+$ MeLLFs

Attempts were made to form MeLLFs using the $[Re(L2)(CO)_3(R)]^+$ complexes, where R represents either the pyr or the ligand, L3, to determine whether the complexes could induce interfacial positioning. The complex resulting from bromide removal and substitution of either pyr or L3 are charged and that interfacial positioning of Ag NPs may be possible via the charge screening, promotion mechanism. To explore this, a MeLLF was formed according to the standard procedure for MeLLF formation using a 1mM acetonitrile solution of the $[Re(L2)(CO)_3(pyr)](PF_6)$ complex (Chapter 2, Section 2.2.1). Successful film formation was confirmed with the formation of as the metallic lustre, characteristic of the MeLLFs, indicating nanoparticles were positioned at the interface. By using the $[Re(L2)(CO)_3(pyr)](PF_6)$ it ensures that there is no functionality capable of binding to the Ag nanoparticle surface. Therefore it is assumed that this complex achieves film formation via charge screening and not through surface modification.

SERS measurements taken from the MeLLF formed with $[Re(L2)(CO)_3(pyr)](PF_6)$ demonstrate that the complex is present on the surface (Fig. 5.8). The peaks stemming from the Re–CO group are visible at 497, 1920 and 2033 cm^{-1} respectively. The intense peaks in the range between 1000 and 1650 cm^{-1} can be assigned to overlapping vibrations from both bpy and benzimidazole groups with the peaks at 1439, 1488 and 1621 cm^{-1} attributed to C=C and C=N ring vibrations.[18, 19] The ring–ring stretching mode can be seen at 1032 cm^{-1}. Features specific to L2 can also be seen with the vibration at 1554 cm^{-1} attributed to the N–H in-plane bending of the benzimidazole and

at 1280 cm^{-1} to the in plane bending of the C–H and ring vibrations of the aromatic group on the benzimidazole.[18,20] The spectrum demonstrates that charged rhenium complexes have the ability to sufficiently negate the surface charge of citrate stabilised Ag nanoparticles allowing controlled interfacial aggregation. It is thought that the $[Re(L2)(CO)_3(pyr)](PF_6)$ complex is amphiphilic, enabling the nanoparticle to be stabilised on either side of the interface, in a similar fashion to TBA salts as illustrated in the original publication by Xu *et al.* (Chapter 1, Section 1.5.4).[21]

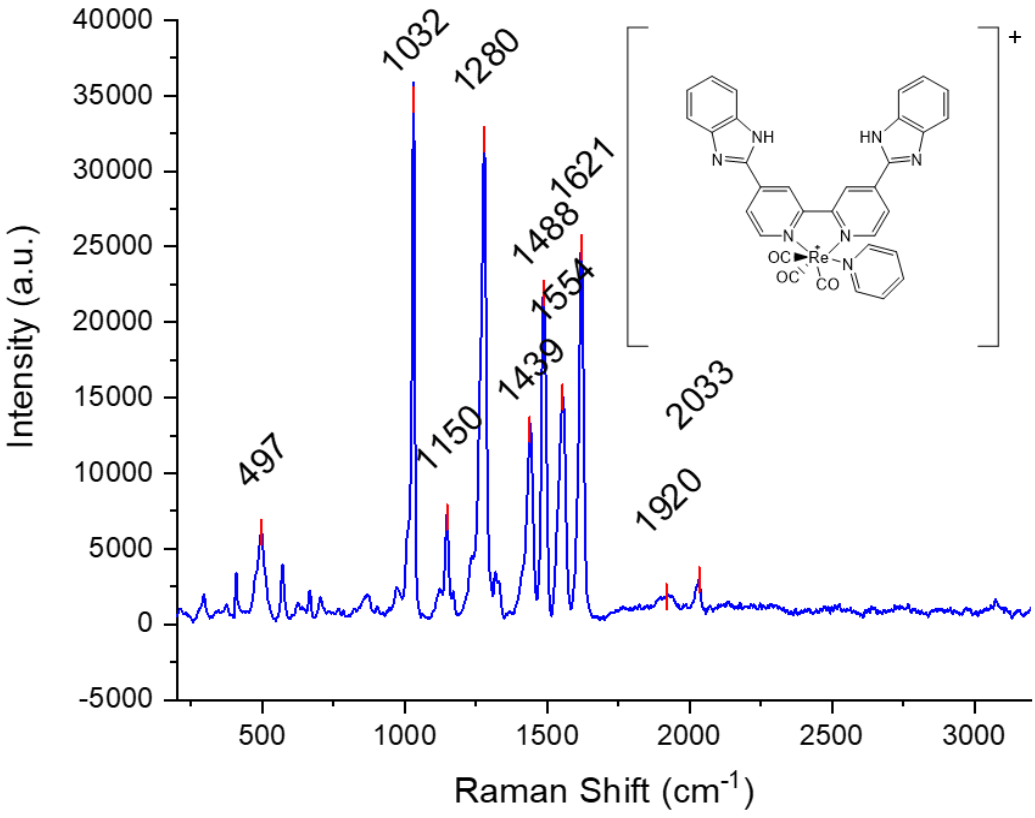

Figure 5.8: *The SERS spectrum of the MeLLF formed using $[Re(L2)(CO)_3(pyr)]$ (PF_6) complex as a promoting species, excited at 532 nm. Insert: The structure of $[Re(L2)(CO)_3(pyr)](PF_6)$*

***Table 5.2**: The peak assignments for the SERS spectrum of a MeLLF formed using [Re(L2)(CO)$_3$(pyr)](PF$_6$)*

Wavenumber (cm^{-1})	Assignment
408	unknown
497	Re–C str.
571	unknown
1031	Ring–Ring str.
1150	C–H def. (pyridine)
1280	In-plane C–H bending (benzimidazole)
1439	Ring str. (C–C, C–N)
1488	Ring str. (C–C, C–N) + inter-ring str. + C–H in-plane def.
1536	Ring str. (C–C, C–N) (sh)
1554	N–H in-plane bending (benzimidazole)
1621	Ring str. (C–C, C–N)
1920	Re–(C≡O) carbonyl str.
2033	

Stretching = str. Deformation = def. (sh)=shoulder

The bipyridyl thiolate ester, L1, as featured in Chapters 2 and 3, showed that a lipoic acid-based ligand could be coordinated to a rhenium complex enabling modification of Ag NPs and subsequent interfacial film formation. In the case of [Re(L2)(CO)$_3$(Br)], the L2 functionality occupies the same coordination site as L1 in the earlier work and does not possess a group capable of binding to the nanoparticle surface. Coordination of the pyridyl amide dithiolate, L3, via removal of the bromide was done to incorporate a surface modifying group. The standard procedure for MeLLF formation using a 0.1 mM acetonitrile solution of the [Re(L2)(CO)$_3$(L3)](BF$_4$) resulted in a MeLLF, signified by the formation of a reflective metallic surface (Chapter 2, Section 2.2.1). The SERS spectrum of the resulting film possesses the vibrations of the Re–C bond, assigned to the peak at 495 cm^{-1} (Fig. 5.9). The vibrational modes of the bpy and benzimidazole are almost identical to the SERS spectrum from the [Re(L2)(CO)$_3$(pyr)](PF$_6$) MeLLF. The ring–ring stretch of the bpy at 1032 cm^{-1} with the in-plane breathing modes of the ring systems of both bpy and benzimidazole are visible at similar wavenumbers to the [Re(L2)(CO)$_3$(pyr)](PF$_6$) complex. It is possible that binding to the surface is

represented by the peak at 238 cm^{-1} corresponding to a Ag–S interaction and therefore implying the $[Re(L2)(CO)_3(L3)](BF_4)$ complex has bound to the surface. However, instrument limitations means that this conclusion is only tentative.

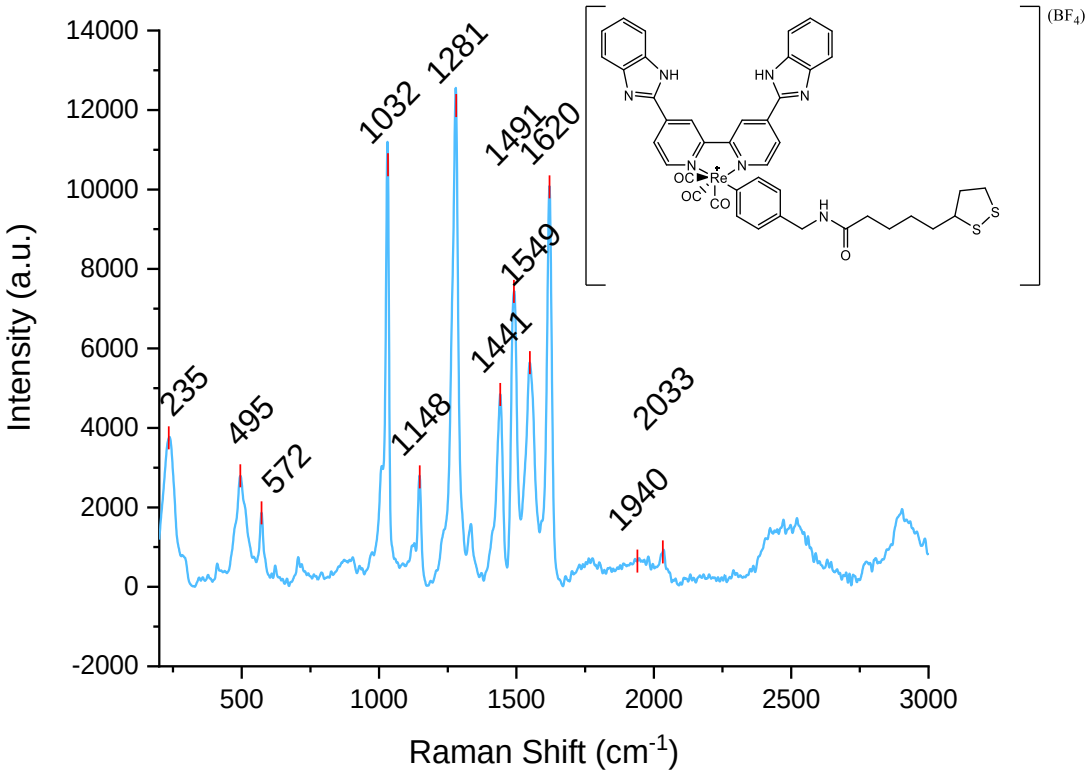

Figure 5.9: *The SERS spectrum of the MeLLF formed using $[Re(L2)(CO)_3(L3)]$ complex excited at 532 nm. Insert: The structure of $[Re(L2)(CO)_3(L3)](BF_4)$*

***Table 5.3**: The peak assignments for the SERS spectrum of a MeLLF formed using [Re(L2)(CO)$_3$(L3)](BF$_4$)*

Wavenumber (cm^{-1})	Assignment
495	Re–C str.
572	unknown
705	C–S str. (dithiolane ring)
1031	Ring–Ring str.
1148	C–H def. (pyridine)
1281	In-plane C–H bending (benzimidazole),
1441	Ring str. (C–C, C–N)
1491	Ring str. (C–C, C–N) + inter-ring str. + C–H in-plane def.
1531	Ring str. (C–C, C–N) (sh)
1549	N–H in-plane bending (benzimidazole)
1620	Ring str. (C–C, C–N), C=O str.
1940	Re–(C≡O) carbonyl str.
2033	
2903	Alkyl C–H str.

Stretching = str. Deformation = def. (sh)=shoulder

Both the [Re(L2)(CO)$_3$(pyr)](PF$_6$) and the [Re(L2)(CO)$_3$(L3)](BF$_4$) complexes demonstrate an ability to form interfacial nanoparticle films that present a characteristic SERS response attributed to the individual complexes. Both films represent the first time in which charged rhenium complexes have been employed for the formation of SERS active interfacial films. The wider implications for this are that other charged organometallic complexes used for molecular sensing may also possess the ability to form a SERS responsive films. This in turn, would present new avenues of investigation for the use of other organometallic sensors with the application of SERS sensing.

5.4.2 Formation and SERS Response of $[Re(L2)(CO)_3(R)]^+$ SENS

Positioning of Ag NPs at the interface between two immiscible liquids using the $[Re(L2)(CO)_3(R)]^+$ complexes, where R represents either the pyr or the ligand L3, was demonstrated in the previous section. From this, it was expected that the surface-exposed nanosheets or SENS, could also be formed using the $[Re(L2)(CO)_3(R)]^+$ complexes. This was achieved using a 0.1 mM acetonitrile solution of both the $[Re(L2)(CO)_3(pyr)](PF_6)$ and $[Re(L2)(CO)_3(L3)](BF_4)$ complexes, in the standard procedure for SENS formation (Chapter 2, Section 2.2.2). Interfacial positioning was confirmed through the appearance of a metallic-like film at the interface. The film was dried and extracted onto sticky tape and the SERS response was taken.

During the formation of the SENS films using both the $[Re(L2)(CO)_3(pyr)](PF_6)$ and $[Re(L2)(CO)_3(L3)](BF_4)$ complexes, visible differences were observed which are attributed to their variation in structure. The SENS made using the $[Re(L2)(CO)_3(pyr)](PF_6)$ was significantly smaller in size than that formed with the $[Re(L2)(CO)_3(L3)](BF_4)$. Additionally, using the $[Re(L2)(CO)_3(pyr)](PF_6)$, there were nanoparticles that remained aqueous colloidal suspension. Whereas with the $[Re(L2)(CO)_3(L3)](BF_4)$ complex, the aqueous layer appeared colourless after film formation, suggesting a greater percentage of the nanoparticles were positioned at the interface. This was reflected when viewing the film at x50 objective under the Raman microscope (Fig. 5.10). The SENS formed with $[Re(L2)(CO)_3(pyr)](PF_6)$ is cracked and incomplete whereas the SENS formed with the $[Re(L2)(CO)_3(L3)](BF_4)$ gives complete coverage. The differences of the two films would suggest that the presence of the L3 ligand results in a greater number of nanoparticles being successfully positioned at the interface, and a potentially more responsive surface.

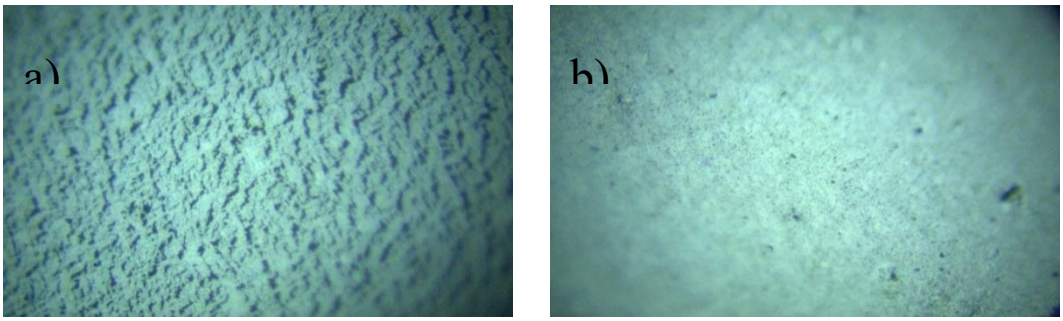

Figure 5.10: *Images of the SENS films taken using the Raman microscope, formed using a) [Re(L2)(CO)$_3$(pyr)](PF$_6$) and b) [Re(L2)(CO)$_3$(L3)](BF$_4$) complexes at x50 objective*

The SERS responses of both films illustrate that the respective rhenium complexes are present on the surface (Fig. 5.11). The Re–C vibrations are seen at 497 cm^{-1} in both spectra, along with the metal centred carbonyl vibrations at 1915 and 2033 cm^{-1}. The contributions of both the bpy and benzimidazole of L3 are also observed in the fingerprint region, with the presence of the ring–ring stretch at 1029 cm^{-1} and the N–H bending of the benzimidazole at 1443 cm^{-1}.

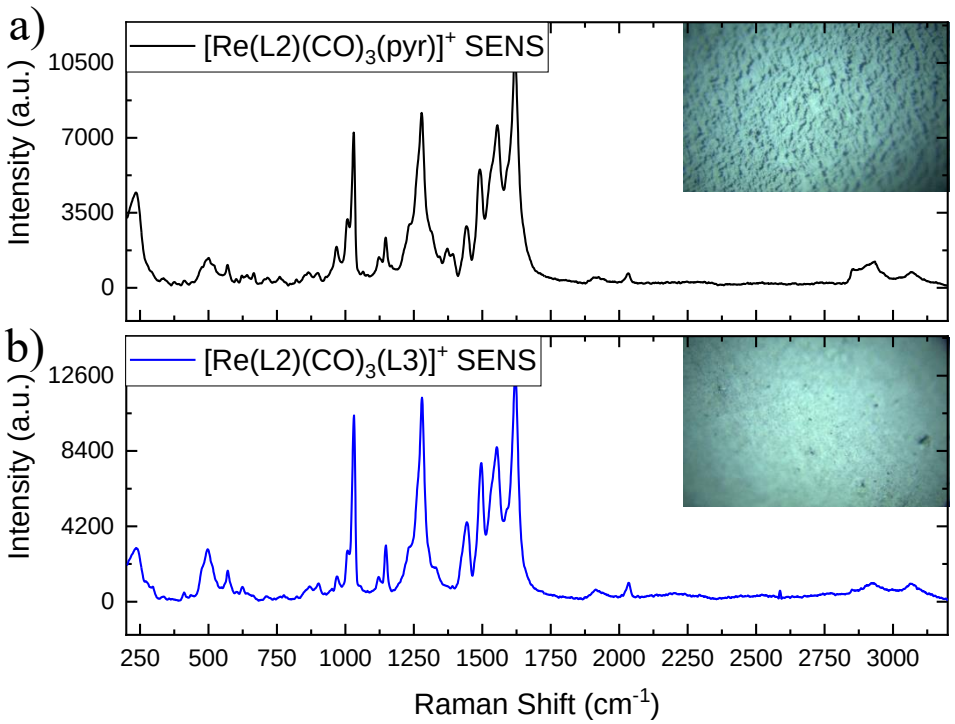

Figure 5.11: *The SERS spectrum from the SENS formed using a) [Re(L2)(CO)$_3$(pyr)](PF$_6$) and b) [Re(L2)(CO)$_3$(L3)](BF$_4$). Excited at 532 nm*

5.5 Tracking Anion Interactions Using $[Re(L2)(CO)_3(R)]^+$ Interfacial Films

5.5.1 Attempts at Anion Tracking Using $[Re(L2)(CO)_3(R)]^+$ MeLLFs

Both the $[Re(L2)(CO)_3(pyr)](PF_6)$ and $[Re(L2)(CO)_3(L3)](BF_4)$ complexes are able to generate the interfacial films that show a SERS fingerprint response and $[Re(L2)(CO)_3(pyr)](PF_6)$ shows a spectroscopic response upon the addition of $H_2PO_4^-$. This may allow for the SERS detection of $H_2PO_4^-$ using the $[Re(L2)(CO)_3(R)]^+$ functionalised interfacial films. MeLLFs were formed following the standard procedure using a 1 mM acetonitrile solution of $[Re(L2)(CO)_3(pyr)](PF_6)$, followed by the addition of 1 mM aqueous solution of TBA dihydrogen phosphate (Chapter 2, Section 2.2.1).

The fingerprint of the $[Re(L2)(CO)_3(pyr)](PF_6)$ is visible with the presence of the Re–CO vibrations at 500 cm^{-1} suggesting that the complex is responsible for MeLLF formation and not the TBA salt (Fig. 5.12). An expectation was that the binding of $H_2PO_4^-$ would result in the possible appearance of bands corresponding to the anion, coupled with noticeable differences in the peaks corresponding to the complex. However, there were no distinguishable differences that could be attributed to any possible interaction between the complex and phosphate. There are no additional peaks that could be attributed to the presence of $H_2PO_4^-$. The is a slight change in the appearance of the Re–CO vibration it is not possible to attribute this to an anion-complex interaction.

A plausible explanation for this result could be the interfacial nature of the MeLLF. Film formation requires an aqueous layer so it is possible that the presence of water in the system prohibits the desired H-bonding interaction between the target anion and the complex. The [Re(L2)(CO)$_3$(pyr)](PF$_6$) MeLLFs were not tested with any other anions as it was assumed that the inherent problems believed to inhibit phosphate sensing would be present in the iterations conducted with the other anions.

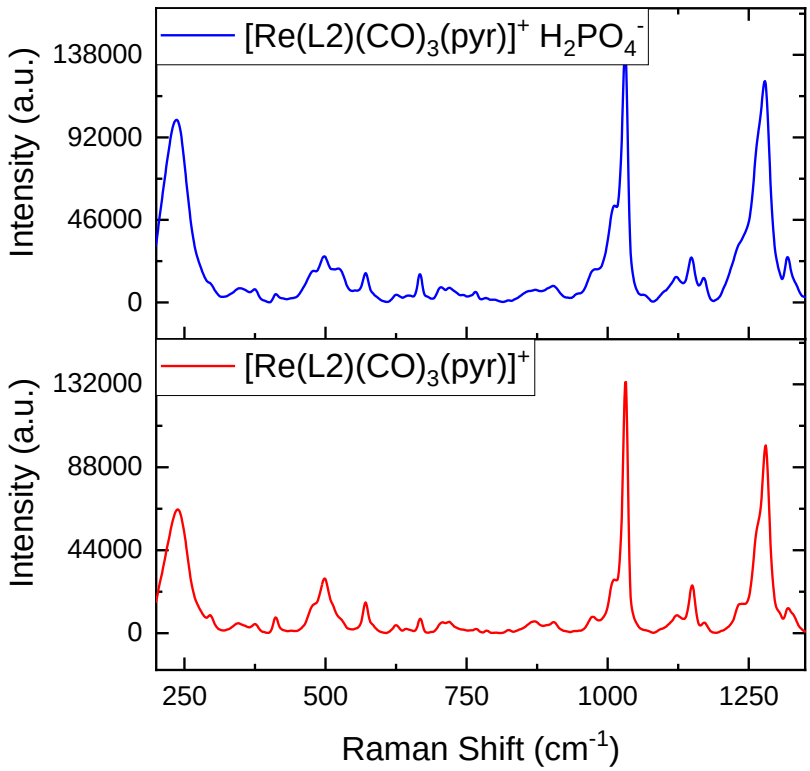

Figure 5.12: *The SERS spectrum of the MeLLF formed with [Re(L2)(CO)$_3$(pyr)](PF$_6$) treated with H$_2$PO$_4^-$(-) and a MeLLF formed with [Re(L2)(CO)$_3$(pyr)](PF$_6$) only (-). Excited at 532 nm*

5.5.2 Anion Detection using $[Re(L2)(CO)_3(L3)](BF_4)$-functionalised SENS in Organic Media

5.5.2.1 The Addition of TBA Salts to $[Re(L2)(CO)_3(L3)](BF_4)$-functionalised SENS

It was hoped that using the functionalised SENS as the sensing platform, would allow for the observation of the interaction between the $[Re(L2)(CO)_3(pyr)](PF_6)$ complex and the TBA anions. The reason being that sensing could potentially take place outside of an aqueous environment therefore li. Anions were introduced to the SENS formed with $[Re(L2)(CO)_3(L3)](BF_4)$ with the assumption that any interaction between the complex and the anions would stem from the L2 ligand (Sect. 4.4.2). 1 mM acetonitrile solutions of the following TBA salts, $H_2PO_4^-$, OAc^-, NO_3^-, Br^-, Cl^- and HSO_4^- were made to SENS formed via the standard procedure using a 0.1 mM solution of the $[Re(L2)(CO)_3(L3)](BF_4)$ complex (Chapter 2, Section 2.2.1).

In view of the fact that addition of TBA OAc to $[Re(L2)(CO)_3(pyr)](PF_6)$ in acetonitrile results in an observed change in the UV-vis absorption and with quenching of emission, the addition of OAc^- to a $[Re(L2)(CO)_3(L3)](BF_4)$ SENS may generate a detectable change in the SERS spectrum. This is confirmed with the appearance of a vibration at 924 cm^{-1}, corresponding to the C–C stretching of the OAc^- anion (Fig. 5.13).[22] This presence of this vibration does not necessarily confirm that binding has occurred with the metal complex but the lack of any perceived vibrations owing to the TBA^+ counterion would suggest it is not a result of an interaction between the surface and the salt.

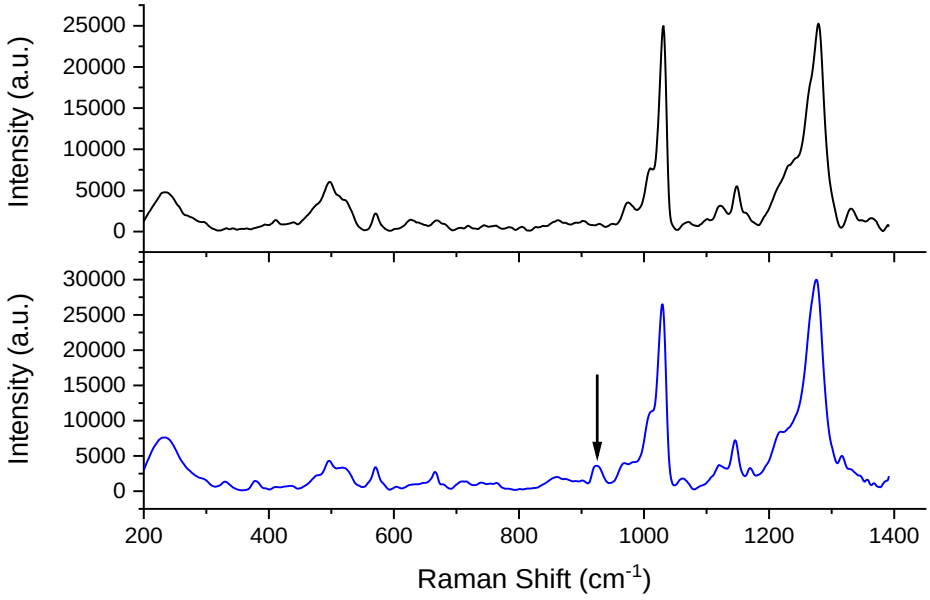

Figure 5.13: *The SERS spectrum of the [Re(L2)(CO)$_3$(L3)](BF$_4$) SENS (-) and the resulting spectrum after treatment with OAc$^-$ (-) excited at 532 nm. The arrow indicates the new vibration at 924 cm^{-1}*

The SERS response at higher wavenumbers may be more suggestive that a hydrogen bond is present. The addition of OAc$^-$ causes the prominent aromatic ligand vibrations at 1279, 1490 and 1619 cm^{-1}, attributed to C-H bending and the C=C and C=N breathing modes to shift to lower wavenumbers (Fig. 5.14). Additionally, there is a shift and the appearance of a shoulder at the peak at 1550cm^{-1} which is attributed to the N–H bending of the benzimidazole group. There is some evidence to suggest that the hydrogen bonding of an analyte can cause deviations in an observed Raman peak. For example, Zhuang *et al.* describe a change in several prominent vibrations in 2-nitro-5-mercaptobenzoic acid label on addition of melamine, which they conclude to be a result of hydrogen bonding induced charge transfer.[23] The shift of the ring centred bands of the [Re(L2)(CO)$_3$(L3)](BF$_4$) complex may be indicative of a similar charge transfer interaction. Coupled with the appearance of the OAc$^-$ stretch at 924 cm^{-1}, this would

strongly suggest that the $[Re(L2)(CO)_3(L3)](BF_4)$ bound to a SERS surface can recognise OAc^-.

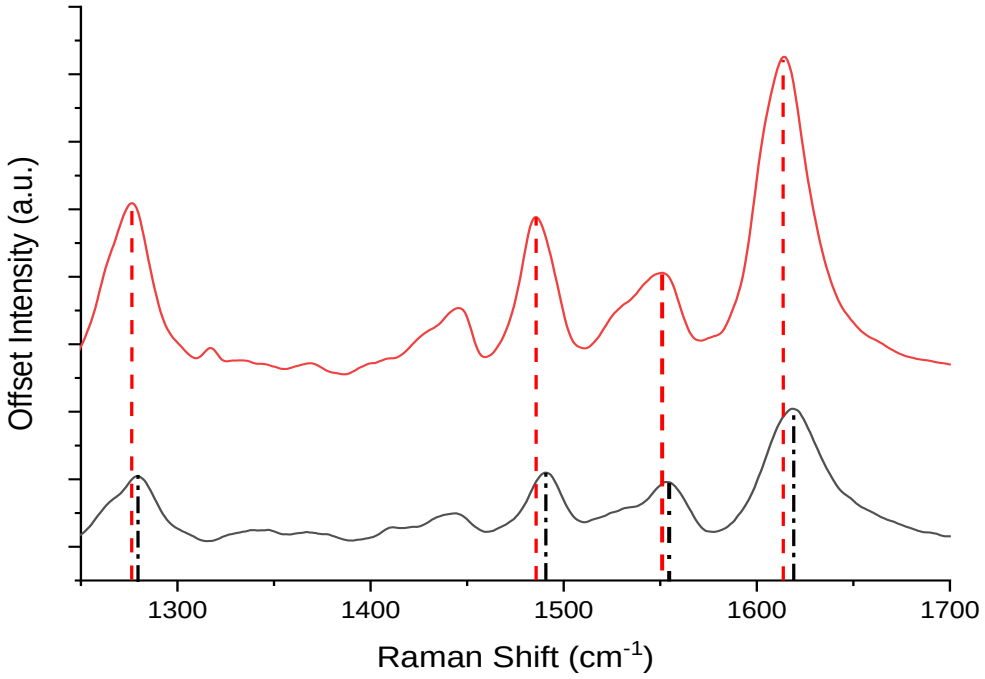

Figure 5.14: *The SERS spectrum of $[Re(L2)(CO)_3(L3)](BF_4)$ (-) and the response after treatment with OAc^- (-). The dashed lines indicate how the peak centre is shifted to a lower frequency*

The addition of TBA Br to the $[Re(L2)(CO)_3(L3)](BF_4)$ SENS also exhibited a dramatic change in the SERS response. The vibrations owing to $[Re(L2)(CO)_3(L3)](BF_4)$ are enhanced and appear better resolved after addition of Br^- comparison with the response of the untreated $[Re(L2)(CO)_3(L3)](BF_4)$ SENS (Fig. 5.15). Halide salts have been employed previously to improve the SERS recognition of analytes as highlighted by Xu *et al.* in their work on protein recognition using iodide-modified nanoparticles. They concluded that a low concentration of iodide acts as a competitive surface binder with the nanoparticle, repelling any surface impurities.[24] A similar process may be occurring in this instance with the bromide removing surface impurities, leaving the complex, $[Re(L2)(CO)_3(L3)](BF_4)$ present on the surface. It is unlikely that the complex is easily

displaced from the surface as it is assumed that the complex is anchored to the surface via Ag–S bonds.

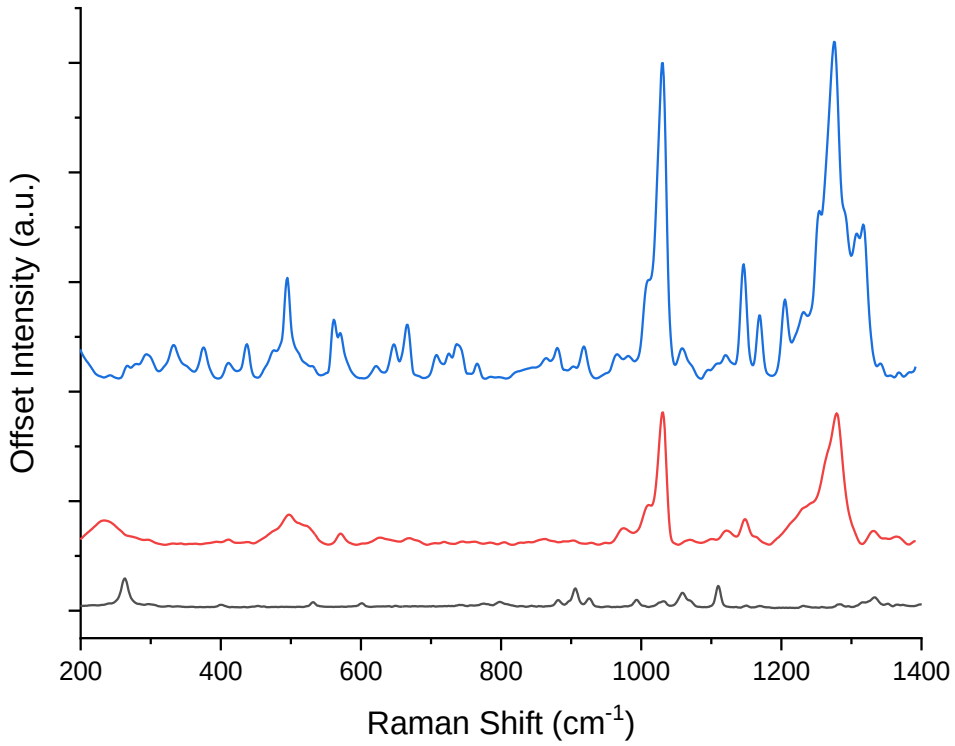

Figure 5.15: *The SERS spectra of the [Re(L2)(CO)$_3$(L3)](BF$_4$) SENS in the presence of TBA Br (-), [Re(L2)(CO)$_3$(L3)](BF$_4$) control (-) and the Raman spectra of TBA Br (-). Excited at 532 nm*

The SERS response of the [Re(L2)(CO)$_3$(L3)](BF$_4$) SENS to the presence of the other anions was also assessed (Fig. 5.16). There is little change in the spectrum of the complex in the presence of TBA HSO$_4$. The addition of TBA NO$_3$ and TBA Cl results in prominent peaks at 667, 1169 and 1316 cm^{-1}. The UV-Vis absorption and emission titrations of [Re(L2)(CO)$_3$(pyr)](PF$_6$) with molar equivalents of nitrate and chloride showed no spectroscopic changes therefore it is thought that these three peaks are unlikely to be a be a result of a complex-anion interaction. These observed peaks are present in both the individual responses so it is possible that the peaks are not anion-specific and perhaps a result of salt interactions with the Ag surface. It is unlikely that

the vibrations belong to the TBA^+ cation as they do not correlate to Raman spectra of TBA salts.

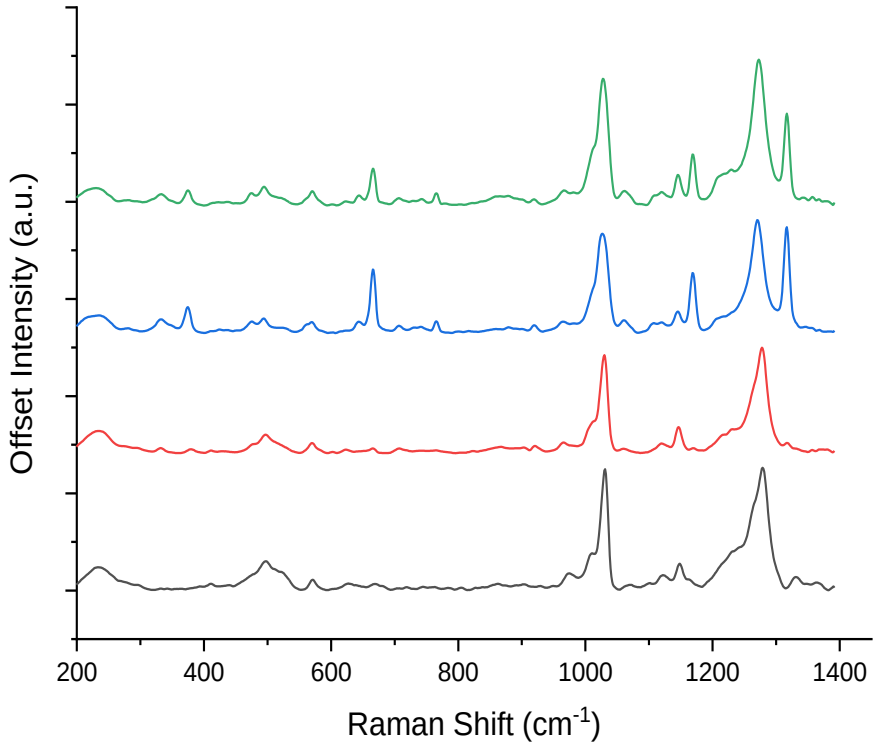

Figure 5.16: *The SERS spectra of the [Re(L2)(CO)$_3$(L3)](BF$_4$) SENS in the presence of TBA NO_3^- (-), Cl^- (-), HSO_4^- (-) and the [Re(L2)(CO)$_3$(L3)](BF$_4$) control (-). Excited at 532 nm*

5.5.2.2 Phosphate Sensing Using [Re(L2)(CO)$_3$(L3)](BF$_4$)-functionalised SENS

The addition of TBA dihydrogen phosphate to a [Re(L2)(CO)$_3$(L3)](BF$_4$) SENS has a notable influence on the SERS response from the film. The most prominent addition is a peak situated at 900 cm^{-1} which could be attributed to the $P(OH)_2$ symmetric vibrations (Fig. 5.17). Studies of the Raman response of the dilute solutions of phosphoric acid solutions have detailed that this particular vibrational mode is observed at of 877 cm^{-1}.[25] This is slightly shifted from the observed peak seen in this instance which is tentatively attributed to the assumed hydrogen bonding interaction that is thought to occur between [Re(L2)(CO)$_3$(L3)](BF$_4$) and $H_2PO_4^-$. As stated previously,

hydrogen bonding is known to induce a change in the Raman shift of prominent bands and it is possible the same is occurring here.[23] There is also a visible decrease of the intensity of the peak at 1148 cm^{-1}, attributed to the C–H bending mode of the aromatic protons, relative to the ring–ring stretch of the bpy at 1030 cm^{-1} and the N–H bending at 1274 cm^{-1}. It could be that the hydrogen bonding of the $H_2PO_4^-$ anion limits the possible bending modes that occur on these aromatic protons. It may also be indicative of cooperative binding that has been observed in the absorption and emission titrations. This is thought to be stabilised by the protons situated on both the benzimidazole and the bipyridyl groups of L2 which would align with the changes to the aforementioned modes.

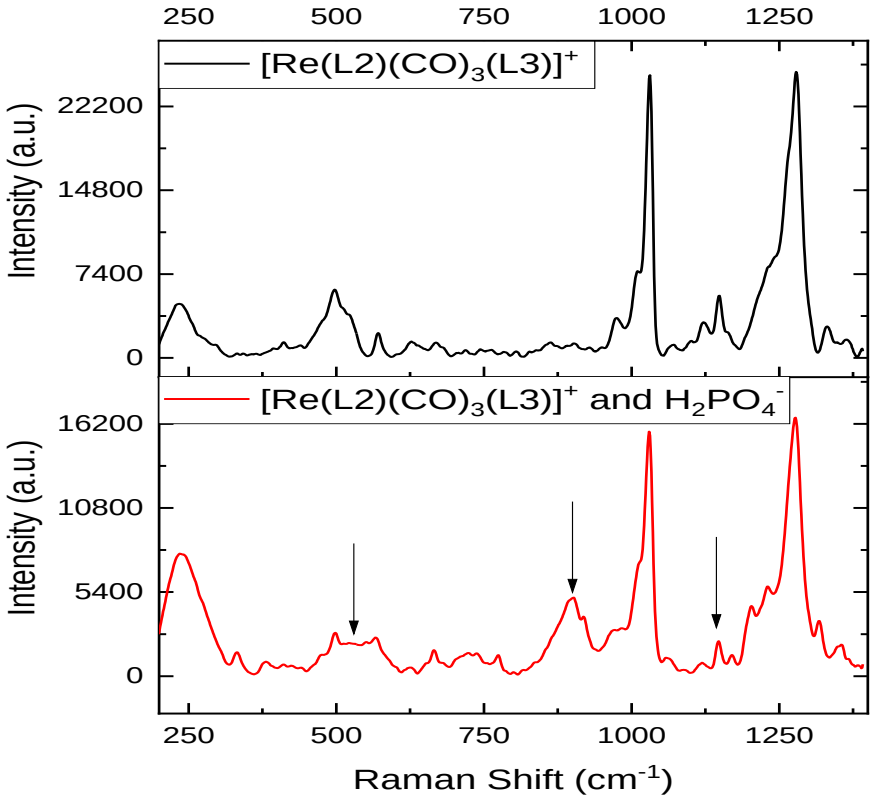

Figure 5.17: *The SERS response of the [Re(L2)(CO)₃(L3)](BF₄) SENS (-) and the response after treatment with TBA $H_2PO_4^-$ (-). Excited at 532 nm*

Addition of $H_2PO_4^-$ to the [Re(L2)$(CO)_3$(L3)](BF_4) functionalised SENS also causes a noticeable change in the region between 500 and 600 cm^{-1}, attributed to the Re–C stretch. If $H_2PO_4^-$ is binding into the cleft of the L2 ligand, an expectation is that it would induce a change in the electronic polarizability of the molecule. The possible hydrogen bond interaction that can occur between $H_2PO_4^-$ and L2 would disrupt the charge distribution of the ligand which in turn, could impact the metal centre. The metal centred carbonyls are capable of forming hydrogen bonds as illustrated by Pelleteret *et al.* so it is plausible that the Re–CO of this complex is in involved in the interaction with dihydrogen phosphate.[26]

The UV-Vis absorption and emission response of [Re(L2)$(CO)_3$(pyr)](PF_6) to the presence of $H_2PO_4^-$ is noticeably different from OAc^-, suggesting the binding interaction is also different. This is reflected in the SERS response of the [Re(L2)$(CO)_3$(L3)](BF_4) SENS to both anions. Addition of $H_2PO_4^-$ only induces a slight change in the ligand centred vibration at 1490 cm^{-1}, whereas OAc^- induces shifts in a number of vibrations (Fig. 5.18). Furthermore, the response of the [Re(L2)$(CO)_3$(L3)](BF_4) SENS to OAc^- shows an overall increase in SERS intensity relative to the untreated [Re(L2)$(CO)_3$(L3)](BF_4) SENS. However, the response of the SENS to $H_2PO_4^-$ is of similar intensity to the control (Fig. 5.18.). The nature of the two interactions are still unclear however, it is apparent that the differences can be tracked using SERS. Computational studies and investigations using ^1H NMR spectroscopy would provide a better insight into the binding of the particular anions with the [Re(L2)$(CO)_3$(L3)](BF_4) complex.

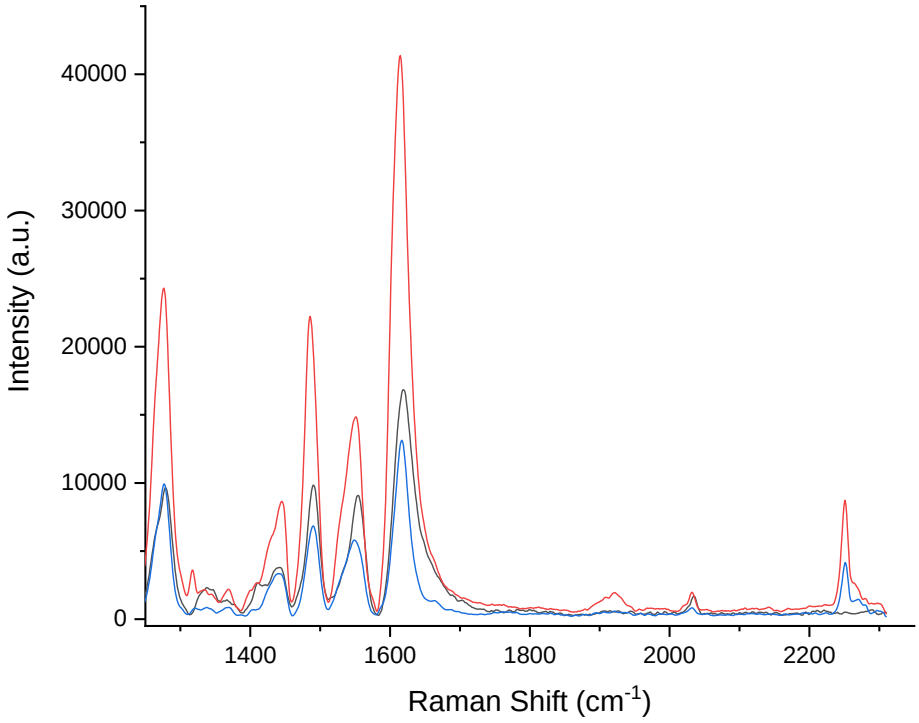

Figure 5.18: *The SERS response of the [Re(L2)(CO)$_3$(L3)](BF$_4$) SENS (–) and the response after treatment with $H_2PO_4^-$ (–) and OAc^- (–). Excited at 532 nm*

5.5.3 Anionic Sensing using [Re(L2)(CO)$_3$(L3)](BF$_4$)-functionalised SENS in Aqueous Media

To this point, the data has described the efforts to track anionic interactions using interfacial films through the modification of citrate stabilised nanoparticles with [Re(L2)(CO)$_3$(L3)](BF$_4$). Initial attempts using the [Re(L2)(CO)$_3$(pyr)](PF$_6$) MeLLFs did not show any recognizable changes in the SERS response upon the introduction of dihydrogen phosphate, attributed to the presence of water. The [Re(L2)(CO)$_3$(L3)](BF$_4$) functionalised SENS with acetonitrile solutions of the TBA salts show that the interactions of the complex with both OAc^- and $H_2PO_4^-$ could be tracked via observable changes in the SERS response. It was postulated that dropping aqueous solutions of TBA salts directly onto [Re(L2)(CO)$_3$(L3)](BF$_4$) functionalised SENS could show a visible change to the SERS response.

[Re(L2)(CO)$_3$(L3)](BF$_4$) functionalised SENS synthesised using the standard procedure for functionalised SENS were treated with 1 mM aqueous solutions of TBA salts, specifically, $H_2PO_4^-$, HSO_4^-, NO_3^-, OAc^-, Cl^- and Br^- (Chapter 2, Section 2.2.2). The addition of aqueous solutions containing either TBA acetate or dihydrogen phosphate did not yield any perceivable changes in the SERS response of the [Re(L2)(CO)$_3$(L3)](BF$_4$) SENS (Fig. 5.19). The distinguishable differences seen when treating the SENS with acetonitrile solutions of the respective anions are not apparent in this instance. It is likely that the proposed hydrogen bonding that was thought to inhibit anion sensing in the MeLLFs, is occurring here.

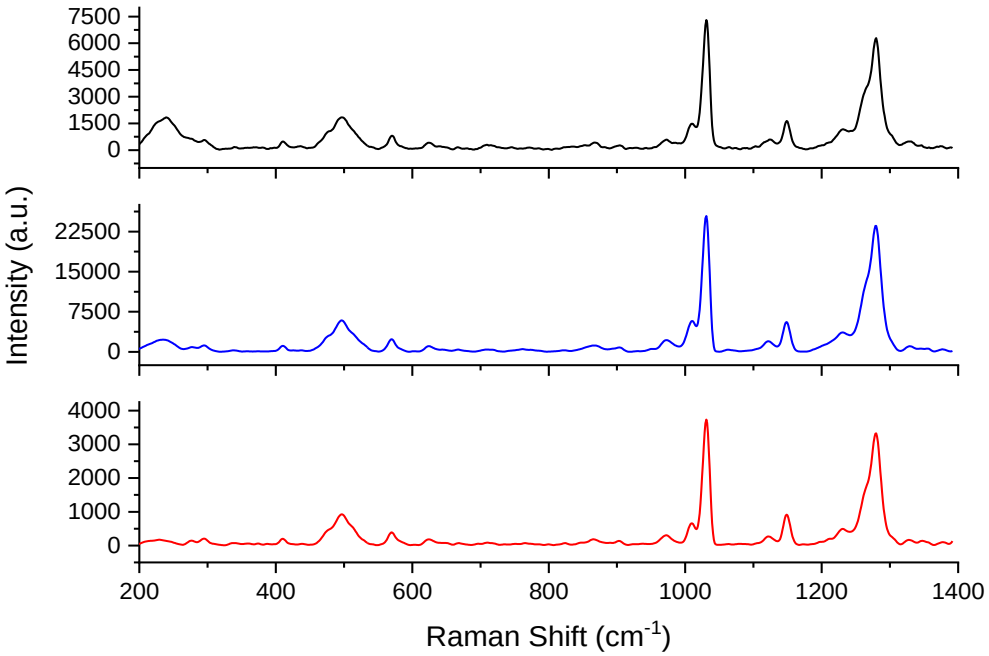

Figure 5.19: *SERS Spectra of the [Re(L2)(CO)$_3$(L3)](BF$_4$) SENS (-), after treatment with $OAc^-_{(aq)}$ (-), and $H_2PO_4^-{}_{(aq)}$ (-). Excited at 532 nm*

5.6 Biomolecular Sensing using $[Re(R)(CO)_3(L3)]^+$ Interfacial Films.

The overall aims as described in the introductory Chapter were to design a functionalised platform that would allow SERS based detection of large molecules with biological significance. The work of this Chapter to this point has demonstrated that the $[Re(L2)(CO)_3(L3)](BF_4)$ functionalised SENS show an ability to track phosphate interactions in the absence of water. The benzimidazole moiety is known to interact with a variety of biological molecules with a number of derivatives demonstrating pharmaceutical activity.[27] They possess an ability to act as a DNA minor groove binding species which has led to their incorporation in transition metal complexes for anti-cancer applications.[28, 29] The aim is therefore to assess whether the $[Re(L2)(CO)_3(L3)](BF_4)$ functionalised SENS would have an ability to effectively bind DNA and allow for SERS based sensing.

In addition to the bis-benzimidazole bipyridine ligand (L2), dipyridophenazine or L4 (L4) has also been the subject of considerable interest for its ability to intercalate into DNA.[30] L4 chelated to a rhenium centre has been previously reported and shown to bind with DNA (Fig. 5.20).[31, 32] The complex $[Re(L4)(CO)_3(L3)](BF_4)$, was synthesised with a view to form the SENS films in a similar vein as the $[Re(L2)(CO)_3(L3)](BF_4)$ functionalised SENS. The aim of this is to evaluate whether DNA-complex interactions could be observed and would the different binding mechanisms of the L4 and L4 ligands present differently in the observed SERS response.

Polypyridyl Re(I) complexes for DNA binding studies have been previously reported by Lo and Tsang in which0 they describe a Re(I) complex coordinated to both L4 (L4) and a biotin moiety.[33] The complex in question was shown to bind to DNA via intercalation with the planar L4 molecule stacking between base pairs. However, L4-containing complexes have not been investigated as possible SERS labels and similar to the bis-(benzimidazole)-4,4′-bipyridine, L4 does not possess a functionality that will bind to a nanoparticle surface. To assess whether such applications could be realised, $[Re(L4)(CO)_3Br]$ was used in a ligand substitution reaction in the presence of silver tetrafluoroborate in acetonitrile to give the adduct, $[Re(L4)(CO)_3[CH_3CN]](BF_4)$. This was then further reacted with the ligand, L3 to give $[Re(L4)(CO)_3(L3)](BF_4)$ at 64% yield (Fig. 5.20).

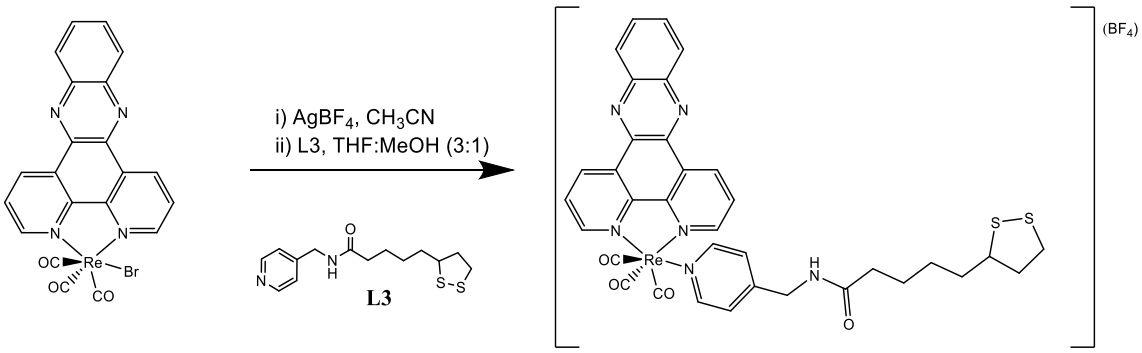

Figure 5.20: *The reaction scheme for the synthesis of* $[Re(L4)(CO)_3(L3)](BF_4)$

5.6.1 Formation of the $[Re(L4)(CO)_3(L3)](BF_4)$-functionalised SENS

To ensure that interfacial film formation was possible using the $[Re(L4)(CO)_3(L3)](BF_4)$ complex, 100 µl of a 1 mM acetonitrile solution of the $[Re(L4)(CO)_3(L3)](BF_4)$ was used to form a MeLLF via the described standard procedure (Chapter 2, Section 2.2.1). Successful formation was signified by the appearance of the metallic lustre associated with such films. The resulting SERS

spectrum from the MeLLF displays the characteristic vibrations belonging to the Re–CO group (Fig. 5.21a). The peak at 499 cm^{-1} is attributed to the Re–C stretch with the CO vibrations at 1930 and 2035 cm^{-1}. The component vibrations of the L4 are also visible with the most prominent vibrations situated at 1316, 1408 and 1448 cm^{-1}.[34, 35] The formation of the $[Re(L4)(CO)_3(L3)]^+$ SENS was also successful with the SERS response being notably similar to that of the MeLLF analogue (Fig. 5.21b) (Chapter 2, Section 2.2.2).

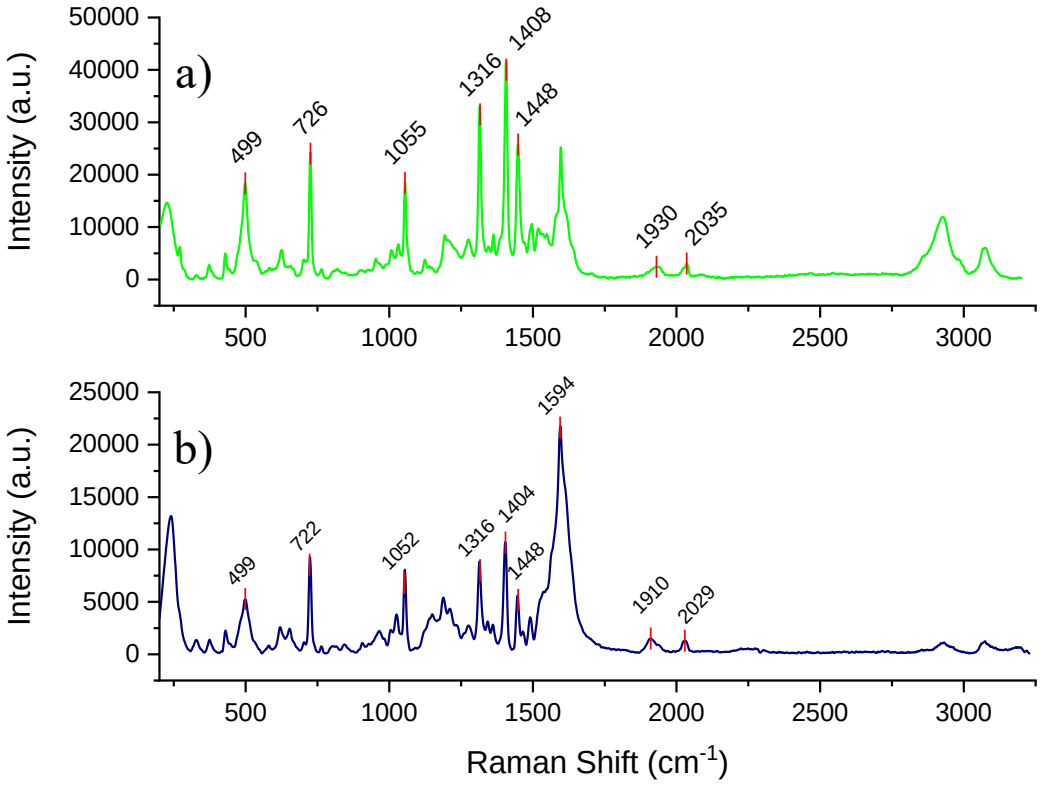

Figure 5.21: *The SERS spectrum of the a) $[Re(L4)(CO)_3(L3)](BF_4)$ MeLLF and b) $[Re(L4)(CO)_3(L3)](BF_4)$ SENS. Excited at 532 nm*

***Table 5.2**: The peak assignments for the SERS specta obtained from the[Re(L4)(CO)$_3$(L3)](BF$_4$) MeLLF and [Re(L4)(CO)$_3$(L3)](BF$_4$) SENS*

Wavenumber (cm^{-1})		Assignment
MeLLF	*SENS*	
499	499	Re–C str.
726	722	Aliphatic C–S str.
1055	1052	Ring–Ring str.
1194	1188	C–H bending (L4)
1275	1275	(C–C, C–N) str. (L4)
1316	1316	C–C inter-ring str. + in-plane C–H def.
1408	1404	C–C str. (L4)
1448	1448	Ring str. (C–C, C–N) + inter-ring str. + C–H in-plane def.
1495	1495	C–C str. (L4)
1559		Ring str. (C–C, C–N)
1597(br)	1596(br)	Ring str. (C–C, C–N)
1624		Ring str. (C–C, C–N)
1930	1910	Re–(C≡O) carbonyl str.
2035	2029	
2927	2927	Alkyl C–H str.
3074	3074	C–H str. (Alkyl + dithiolane ring)

Stretching = str. Deformation = def. (br)=broad

5.6.2 Attempts at DNA Sensing from Solution using [Re(R)(CO)$_3$(L3)]$^+$ SENS

To assess whether the binding of DNA to the [Re(L2)(CO)$_3$(L3)](BF$_4$) and [Re(L4)(CO)$_3$(L3)](BF$_4$) SENS was possible, initial studies were conducted where 100 µl droplets of a DNA solution at a concentration of 127 µm per base pair, was dropped onto SENS formed via complex modification of Ag NPs with the respective complexes. Initial attempts at DNA detection using the [Re(L2)(CO)$_3$(L3)](BF$_4$) SENS showed no variations in the SERS response which suggests no observable interactions were occurring (Fig. 5.22).

The anticipated interaction of the $[Re(L2)(CO)_3(L3)](BF_4)$ complex with DNA is expected to be via minor groove binding or through interaction with sugar phosphate backbone. The results describing attempts at anion sensing in aqueous media, (Section 4.5.3) indicate that the L2-$H_2PO_4^-$ interaction was not observed due to competitive hydrogen bonding. It is thought likely that the same issue is occurring here with the aqueous environment inhibiting binding.

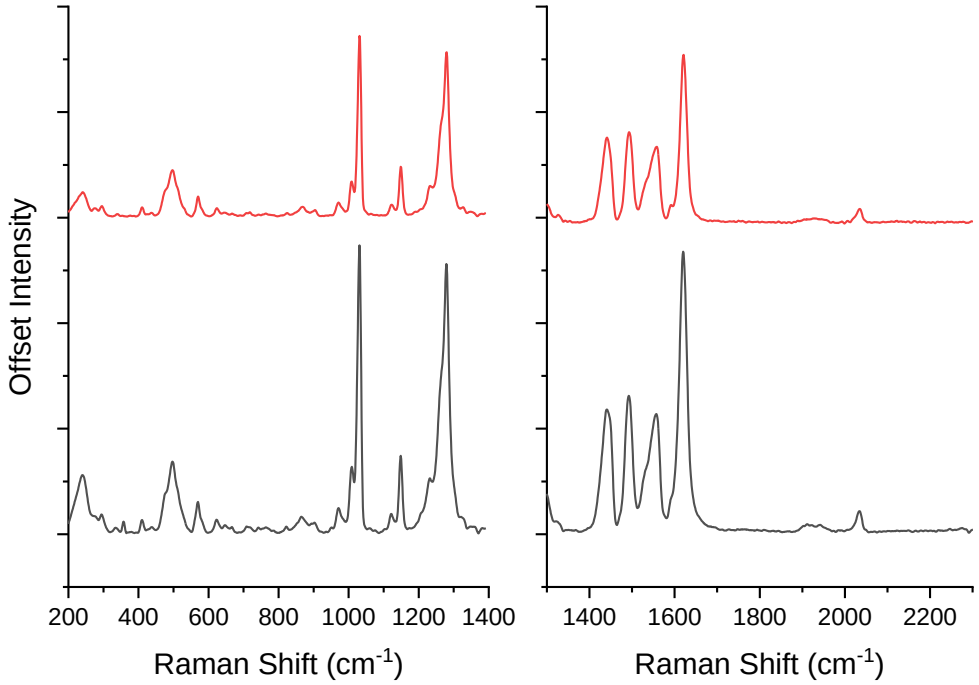

Figure 5.22: *The SERS spectra of the $[Re(L2)(CO)_3(L3)](BF_4)$ SENS treated with aqueous tris buffer (–) and after treatment with an aqueous tris buffer DNA solution (127 μM per base pair) (–). Excited at 532 nm*

Additions of the DNA tris buffer solutions (127 μM) were also made to the $[Re(L4)(CO)_3(L3)](BF_4)$ SENS. The relative SERS intensity of the complex on the film after treatment with DNA is approximately double when compared with a similar film treated with just the buffer solution (Fig. 5.23). There is a subtle variation in the metal centred carbonyl vibration with a more prominent peak appearing, slightly shifted at

1902 cm^{-1}. There are no features that can be attributed to the direct presence of the DNA which suggests that it is not present on the surface.[36] It is not apparent if these changes are a result of DNA binding to the reporting unit as the anticipated result was expected to impact vibrations of the complex. Studies on the resonance Raman of L4-containing ruthenium complexes and their interaction with DNA described a loss of Raman intensity of the complex after binding which is not observed here.[37] It is possible that the variations in the SERS response of the SENS are a result of DNA-complex interaction however further investigation is necessary before any conclusions can be made.

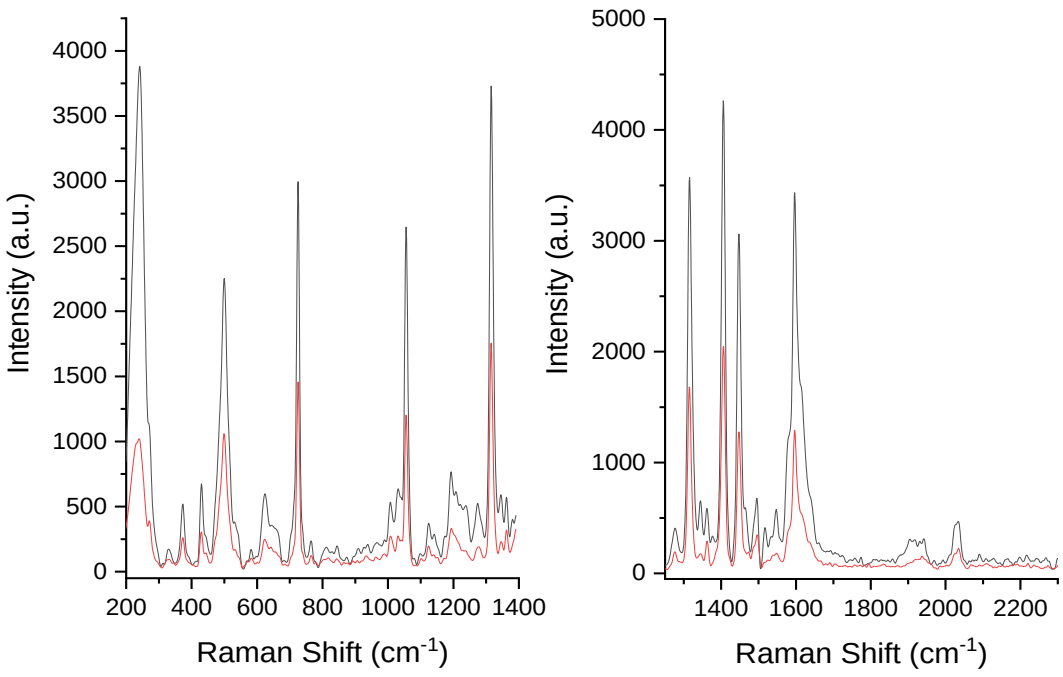

Figure 5.23: *The SERS spectra of the [Re(L4)(CO)$_3$(L3)](BF$_4$) SENS (-) and after treatment with DNA (127 μM per base pair) (-). Excited at 532 nm*

Testing using a higher concentration of DNA in tris buffer (127 mM) on the [Re(L4)(CO)$_3$(L3)](BF$_4$) SENS did show a decrease in SERS intensity of the complex. The intense bands of the complex are still visible at 498, 724, 1053 and 1314 cm^{-1} however the signal to noise ratio does not allow for identification of any of the other

bands including any vibrations associated with DNA. As such, it is difficult to conclude whether or not binding has occurred. Accurately focusing on the SENS surface was found to be more difficult with the higher concentrated DNA solution in comparison with the tris buffer reference spectrum. The observed poor Raman intensity of the $[Re(L4)(CO)_3(L3)](BF_4)$ SENS is consequently thought to be a result of the viscosity of the DNA sample and not as a result of binding.

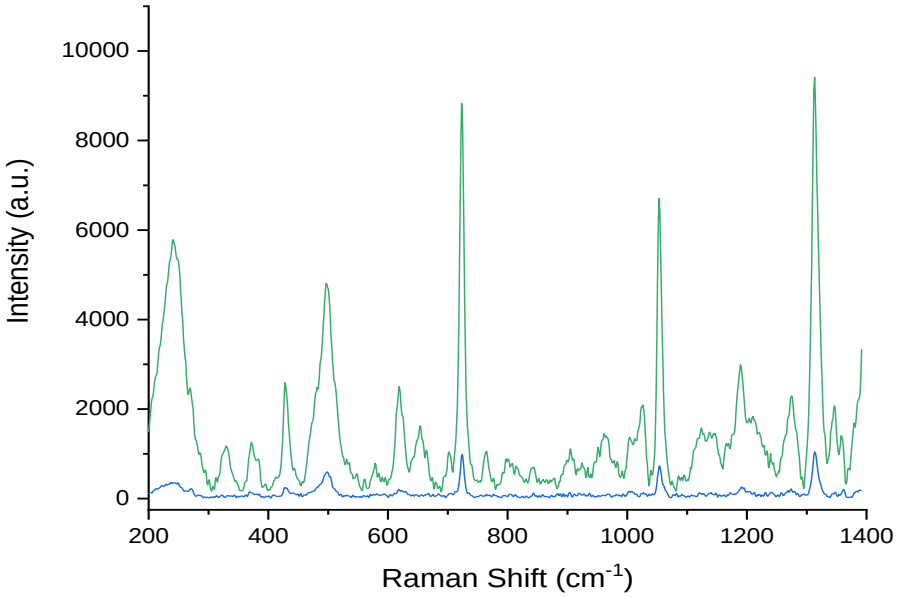

Figure 5.24: *The SERS spectrum of the $[Re(L4)(CO)_3(L3)](BF_4)$ treated with tris buffer (–) and treated with the higher concentration of DNA (127 mM per base pair) (–). Excited at 532 nm*

Overall, the preliminary attempts at DNA sensing using rhenium functionalised interfacial films appear to not be successful in the current format. A possibility is that the pre-fabricated films are unsuitable for use in this manner however, Chapter 2 indicated that rhenium complexes could be used as labels that bind to an unlabelled SENS film. Any future investigation could explore the possibility of labelling the DNA with the preferred Re complex and seeing whether DNA detection could be achieved via this route.

5.7 Conclusions

The incorporation of the bis-(benzimidazole)-4,4′-bipyridine, L2 to the rhenium centre was investigated for possible detection of dihydrogen phosphate in solution. Absorption and emission titrations of the $[Re(L2)(CO)_3(pyr)](PF_6)$ complex with a number of different TBA salts confirmed an observable interaction with dihydrogen phosphate. This is a stepwise quenching of emission and demonstrates cooperative binding, achieved via hydrogen bonding in the cleft of the L2 ligand. The same complex also displays a hydrogen bonding interaction with acetate and a "turn off" fluorescence quenching.

Both the charged rhenium complexes, $[Re(L2)(CO)_3(L3)](BF_4)$ and $[Re(L2)(CO)_3(pyr)](PF_6)$ demonstrate an ability to form MeLLFs through both the promotion and the modification of Ag NPs. The $[Re(L2)(CO)_3(pyr)](PF_6)$ complex does not possess a functional group that can appropriately bind to the nanoparticle surface. Therefore, it is assumed the positive charge sufficiently neutralises the charge that stabilises the colloid in a similar manner to the TBA salts described in Chapter 1 and 2. The incorporation of the pyridyl tail ligand, L3, appears to form the interfacial films more efficiently as fewer nanoparticles remained in the aqueous layer after film formation.

Preliminary attempts at the detection of $H_2PO_4^-$ using $[Re(L2)(CO)_3(pyr)](PF_6)$ functionalised MeLLFs were deemed to be unsuccessful due to disruption from the aqueous environment. However, the $[Re(L2)(CO)_3(L3)](BF_4)$ SENS does display SERS response to the presence of both $H_2PO_4^-$ and OAc^- in acetonitrile. With $H_2PO_4^-$, there are visible changes to the vibration attributed to the Re–C stretch with a slight wavenumber shift of one of the ring centred vibrations. This is also coupled with the

appearance of a vibration at 900 cm^{-1} which is attributed to the $P(OH)_2$ stretching. The response to OAc^- is a significant shift of a number of the ring centred vibrations to lower wavenumbers. Additionally, a peak is observed at 924 cm^{-1} which strongly correlates to the C-C stretching of OAc^-. Subsequent testing of the $[Re(L2)(CO)_3(L3)](BF_4)$ SENS with aqueous solutions of both anions appears to confirm that the hydrogen bonding interaction is obscured by solvent.

The overall aim of this work was to develop a SERS platform that would interact with large molecules of biological importance. The complexes, $[Re(L2)(CO)_3(L3)](BF_4)$ and $[Re(L4)(CO)_3(L3)](BF_4)$ containing the bis-(benzimidazole) bipyridine (L2) and dipyridophenazine (L4) are likely to bind to DNA, through minor groove and intercalation respectively. Both complexes also possess the ability to form the interfacial SENS films however attempts at DNA binding in solution using these films did not present any observable changes to the SERS spectra. DNA binding using the $[Re(L2)(CO)_3(L3)](BF_4)$ is thought to be susceptible to the same hydrogen bonding issues observed in the attempted sensing of dihydrogen phosphate in aqueous conditions. The binding of DNA is incapable of displacing water from the cleft of L2. With respect to the $[Re(L4)(CO)_3(L3)](BF_4)$ complex, it is possible that binding is sterically hindered by the complex being in close proximity to the surface. The packing of the complex on the surface means that intercalation between the base pairs may not be possible. Despite not achieving the desired result, there are further avenues that could be explored that could employ Re labels and interfacial films for DNA detection.

5.8 References

1. C. Fernández-García, A. J. Coggins and M. W. Powner, *Life*, 2017, **7**, 31.
2. P. D. Beer and J. Cadman, *Coord. Chem. Rev.*, 2000, **205**, 131-155.
3. R. Hein, P. D. Beer and J. J. Davis, *Chem. Rev.*, 2020, **120**, 1888-1935.
4. K.-C. Chang, S.-S. Sun and A. J. Lees, *Inorg. Chim. Acta*, 2012, **389**, 16-28.
5. A. Ramdass, V. Sathish, M. Velayudham, P. Thanasekaran and S. Rajagopal, *ChemistrySelect*, 2018, **3**, 2277-2285.
6. C. L. Howells and N. C. Fletcher, unpublished work.
7. K. K.-W. Lo, *Acc. Chem. Res.*, 2015, **48**, 2985-2995.
8. F. L. Thorp-Greenwood, J. A. Platts and M. P. Coogan, *Polyhedron*, 2014, **67**, 505-512.
9. V. Wing-Wah Yam, V. Chor-Yue Lau and L.-X. Wu, *J. Chem. Soc., Dalton Trans.*, 1998, 1461-1468.
10. E. Wolcan, G. Torchia, J. Tocho, O. E. Piro, P. Juliarena, G. Ruiz and M. R. Féliz, *J. Chem. Soc., Dalton Trans.*, 2002, 2194-2202.
11. F. E. Kühn, J.-L. Zuo, F. Fabrizi de Biani, A. M. Santos, Y. Zhang, J. Zhao, A. Sandulache and E. Herdtweck, *New J. Chem.*, 2004, **28**, 43-51.
12. M. Rajkumar, J. Bhuvaneswari, M. Velayudham, E. Rajkumar and S. Rajagopal, *J. Fluoresc.*, 2011, **21**, 1729-1737.
13. A. L. Blackburn, N. C. A. Baker and N. C. Fletcher, *RSC Adv.*, 2014, **4**, 18442-18452.
14. J. Shao, Y. Qiao, H. Lin and H. Lin, *J. Fluoresc.*, 2008, **19**, 183.
15. V. Amendola, M. Boiocchi, L. Fabbrizzi and A. Palchetti, *Chem. Eur. J.*, 2005, **11**, 120-127.
16. S. P. Mahanta and P. K. Panda, *J. Chem. Sci.*, 2017, **129**, 647-656.
17. E. Badaeva, V. V. Albert, S. Kilina, A. Koposov, M. Sykora and S. Tretiak, *PCCP*, 2010, **12**, 8902-8913.
18. N. Sundaraganesan, S. Ilakiamani, P. Subramani and B. D. Joshua, *Spectrochim. Acta, Part A*, 2007, **67**, 628-635.
19. G. Socrates, *Infrared and Raman characteristic group frequencies: tables and charts*, John Wiley & Sons, 2004.
20. M.-S. Kim, M.-K. Kim, C.-J. Lee, Y.-M. Jung and M.-S. Lee, *Bull. Korean Chem. Soc.*, 2009, **30**, 2930-2934.
21. Y. Xu, M. P. Konrad, W. W. Y. Lee, Z. Ye and S. E. J. Bell, *Nano Lett.*, 2016, **16**, 5255-5260.
22. E. Spinner, *J. Chem. Soc.*, 1964, 4217-4226.
23. H. Zhuang, W. Zhu, Z. Yao, M. Li and Y. Zhao, *Talanta*, 2016, **153**, 186-190.
24. L.-J. Xu, C. Zong, X.-S. Zheng, P. Hu, J.-M. Feng and B. Ren, *Anal. Chem.*, 2014, **86**, 2238-2245.
25. W. W. Rudolph, *Dalton. Trans.*, 2010, **39**, 9642-9653.
26. D. Pelleteret, N. C. Fletcher and A. P. Doherty, *Inorg. Chem.*, 2007, **46**, 4386-4388.
27. G. Yadav and S. Ganguly, *Eur. J. Med. Chem.*, 2015, **97**, 419-443.
28. G.-B. Jiang, W.-Y. Zhang, M. He, Y.-Y. Gu, L. Bai, Y.-J. Wang, Q.-Y. Yi and F. Du, *Polyhedron*, 2019, **169**, 209-218.
29. S. Liu, W. Cao, L. Yu, W. Zheng, L. Li, C. Fan and T. Chen, *Dalton. Trans.*, 2013, **42**, 5932-5940.
30. T. Phillips, I. Haq, A. J. H. M. Meijer, H. Adams, I. Soutar, L. Swanson, M. J. Sykes and J. A. Thomas, *Biochemistry*, 2004, **43**, 13657-13665.
31. F. L. Thorp-Greenwood, M. P. Coogan, L. Mishra, N. Kumari, G. Rai and S. Saripella, *New J. Chem.*, 2012, **36**, 64-72.
32. V. Wing-Wah Yam, K. Kam-Wing Lo, K.-K. Cheung and R. Yuen-Chong Kong, *J. Chem. Soc., Dalton Trans.*, 1997, 2067-2072.
33. K. K.-W. Lo and K. H.-K. Tsang, *Organometallics*, 2004, **23**, 3062-3070.

34. M. B. James, F. Amar, P. M. I. James, A. Christopher, P. D. Lee and G. K. Christopher, *Bull. Chem. Soc. Jpn.*, 2002, **75**, 933-942.
35. R. J. Kessler, M. R. Fisher and G. N. R. Tripathi, *Chem. Phys. Lett.*, 1984, **112**, 575-579.
36. A. Barhoumi, D. Zhang, F. Tam and N. J. Halas, *J. Am. Chem. Soc.*, 2008, **130**, 5523-5529.
37. W. Chen, C. Turro, L. A. Friedman, J. K. Barton and N. J. Turro, *J. Phys. Chem. B*, 1997, **101**, 6995-7000.

Conclusions

The work detailed in this thesis describes a novel, modular approach that generates Re(I)-labelled silver substrates for sensing using surface-enhanced Raman spectroscopy (SERS). The method described herein, demonstrates the first example of SERS sensing using functionalised interfacial films using Re(I) complexes that possess both a chemical sensor and a nanoparticle binding moiety. The complexes featured, can be used to label the SERS surface for detection which is achieved by observable changes to the Raman fingerprint of the complex after interacting with the analyte.

Chapter 3 evaluated the use of interfacial nanoparticle self-assembly and photocatalytic reduction of Ag salts for the formation of Re(I) labelled SERS surfaces. Ag substrates fabricated using photoreduction were successfully formed with nanostructures visible on the surface. However, attempts at labelling were inconclusive due to difficulties confirming the presence of the [Re(L1)$(CO)_3$Br] complex. The surface modification of citrate-stabilised silver nanoparticles was achieved using a 0.1 mM solution the [Re(L1)$(CO)_3$Br] coimplex, generating both the metal liquid-like films (MeLLFs) and the surface-exposed nanosheets (SENS). SERS measurements of both surfaces display the Raman fingerprint of the complex, highlighted by the Re–CO vibrations at 510, 1909, 2025 cm^{-1}. Further investigation was conducted using a mixed thiol approach to assess whether interfacial films could be formed using lower concentrations of the complex. This was successful as MeLLFs formed using a combination of 1 mM heptanethiol and 0.01 mM [Re(L1)$(CO)_3$Br] in solution, formed a film with the fingerprint vibrations of the complex. An investigation was conducted into the deposition of unlabelled MeLLFs onto glass plates which was deemed unsuccessful as recognition of the complex was difficult, as vibrations owing to the complex are masked by other peaks likely caused by contamination. Despite this, the response of the glass-deposited MeLLFs highlight the sensitivity of these films.

MeLLFs formed through modification using the ligand L1, showed a SERS response to Fe^{2+}, Co^{+2} and Zn^{2+} evidenced by changes to vibrations attributed to metal coordination to the bipyridyl group. The $[Re(L1)(CO)_3Br]$ complex shows a sensitive and selective response to the presence of Hg^{2+} shown by sequential changes to both absorption and emission response with structural changes also observed using ^1H NMR spectroscopy. The spectroscopic responses also showed that the counterion influences the nature of the interaction as $Hg(ClO_4)_2$ and $Hg(NO_3)_2$ induce different changes to the spectrum. Hg^{2+} is thought to facilitate the removal of the bromide from the metal centre followed by the coordination of solvent. The interaction was also observable via SERS using $[Re(L1)(CO)_3Br]$ functionalised MeLLFs through changes to the Re–CO vibration at 510 cm^{-1} coupled with the addition of a broad peak at 330 cm^{-1}. Recognition of Hg^{2+}-induced changes using the MeLLFs were possible at 1 mM concentrations of Hg^{2+}. SERS sensing of Hg^{2+} was also possible using $[Re(L1)(CO)_3Br]$ functionalised SENS. Addition of Hg^{2+} causes a reduction of overall intensity of the SERS response of the complex on the surface with greater sensitivity than the MeLLFs. The $[Re(L1)(CO)_3Br]$ SENS showed a larger sensitivity to the presence of Hg^{2+} with recognizable changes observed at 0.1 mM.

The $[Re(L2)(CO)_3(pyr)](PF_6)$ complex shows a selective response to both dihydrogen phosphate and acetate via hydrogen bonding to the L2 ligand. $H_2PO_4^-$ causes sequential changes to the absorption and emissive response of $[Re(L2)(CO)_3(pyr)](PF_6)$ resulting in fluorescence quenching while OAc^- causes an almost immediate “switching off” of fluorescence. The fluorescence response to $H_2PO_4^-$ is sigmoidal, suggesting cooperative binding. The complexes, $[Re(L2)(CO)_3(pyr)](PF_6)$ and $[Re(L2)(CO)_3(L3)](BF_4)$ demonstrated form the interfacial films, illustrating that charged complexes can also induce interfacial positioning. Selective sensing of the anions is possible using $[Re(L2)(CO)_3(L3)](BF_4)$ SENS. $H_2PO_4^-$ interactions are evidenced by the

appearance of a vibration at 900 cm^{-1}, attributed to the $P(OH)_2$ vibration and an additional peak in the Re–CO region. OAc^- binding causes the observation of a peak at 924 cm^{-1} coupled with wavenumber shifts of the ring centred vibrations.

Attempts at SERS sensing of DNA using $[Re(L2)(CO)_3(L3)](BF_4)$ and $[Re(L4)(CO)_3(L3)](BF_4)$ functionalized SENS were also conducted. This was deemed unsuccessful as no discernable differences to Raman fingerprint of either complex was observed. Changes in overall intensity were observed using the $[Re(L4)(CO)_3(L3)](BF_4)$ complex however, it is not clear that is resulting from a complex-DNA interaction.

This work provides a proof of concept that suitably functionalised transition metal complexes can be employed for both targeted sensing and inducing self-assembly of nanoparticles. The result being a labelled SERS-active sensing surface possessing a tailored interaction for a specific molecule. Future studies could aim on refining the method, with a view to improving the sensitivity of the system so that ultrasensitive detection can be fully realised. Further work could also look to use this as a framework to investigate other transition metal complexes for SERS based sensing as chemical sensors are not limited to Re(I) complexes. With regards to possible applications, investigating the detection of molecules of biological importance could lead to sensors that may be beneficial to areas such as drug delivery and diagnostics. These devices provide a new gateway for the development of new SERS-based sensing platforms which could help take ultrasensitive detection out of the lab, and into the real world.